A Thesis Submitted for the Degree of PhD at the University of Warwick

http://go.warwick.ac.uk/wrap/57652

Metal window electrodes for organic photovoltaics

by

Helena Maria Stec

A thesis submitted for the degree of

Doctor of Philosophy

The University of Warwick

Supervised by Dr. Ross A. Hatton

Department of Chemistry

University of Warwick

March 2013

Abstract

The work presented in this thesis focuses on the development ultra-thin metal film electrodes for organic photovoltaics (OPVs) with the aim of boosting device performance, lowering the cost and/or extending the range potential application.

Chapter 1 gives a general overview of OPVs, including the materials used for their fabrication and the fundamental processes underpinning OPV's operation. The experimental techniques and equipment used are described in Chapter 2. Chapter 3 describes the development of a solvent free method for the fabrication of highly transparent ultra-thin Au films on glass based on co-deposition of a mixed molecular adhesive layer prior to Au thermal evaporation. By integrating microsphere lithography into the fabrication process the transparency could be improved *via* the incorporation of a random array of micron-sized circular apertures into the film. In Chapter 4 it is shown that these films are amenable to rapid thermal annealing to realise highly crystalline window electrodes with improved transparency and conductivity. By capping these films with a very thin transition metal oxide layer their thermal stability can be dramatically improved, whilst at the same time improving their far field transparency. In Chapter 5 the molecular adhesive method for the fabrication of ultra-thin Au films on glass is translated to the technologically important flexible substrates and extended to the lower cost coinage metals Ag and Cu. In Chapter 6 a lithography-free approach to fabricating thin Au and Ag films with a dense array of sub-wavelength apertures is reported. These electrodes support surface plasmon resonances which couple strongly with visible light concentrating it near to the electrode surface, thereby increasing light harvesting. Chapter 7 shows how the electrodes developed in Chapter 3 can be used to investigate a fundamental question of importance in OPV research and indicates the direction of future work. The results of chapters 3, 5 and 6 have been published in peer reviewed scientific journals.

Table of contents

Declaration

The work presented in this thesis has been conducted at the Department of Chemistry at The University of Warwick in Coventry except the X-ray photoelectron spectroscopy (XPS) measurements, which were carried out in UK National Physical Laboratory in London. Assistance with XPS data collection and analysis was provided by Mr. Steve Spencer and Dr. Alex Shard. Assistance with XRD data collection was provided by Dr. David Walker. All data collection was performed by me, except the characterisation of the Au films on MPTMS derivatised glass and optimisation of MPTMS treatment time. These measurements were performed by Rebecca J. Williams and are presented in Figure 3.3 and are included in her Master level report, which was submitted to the University of Warwick. I confirm that none of the work included has previously been submitted for a higher degree.

Parts of the work have been patented, published in scientific journals and were presented at conferences and Supergen Consortium meetings.

Acknowledgements

Firstly, I would like to thank my supervisor Dr. Ross Hatton for the great opportunity to carry out research in his group and for all his support, guidance, countless ideas and encouragement I could always count on.

I would like to thank my colleagues in Hatton Group; Lara-Jane Pegg, Oliver Hutter and Martin Tyler for helpful discussions, support and lovely company. Many thanks to Master project and summer placement students; in particular Rebecca J. Williams, whose summer project gave foundations to my PhD as well as Ying Wang, Germaine Kok and Kristian Roberts.

I would like to thank Professor Tim Jones, Professor Julie Macpherson and Professor Patrick Unwin and their research groups for allowing me the access to their instrumentation and providing equipment training. I am grateful to Mr. Steve York from the Physics Department for assistance and training on SEM, Dr. David Walker from the Physics Department for assistance and training on XRD, Mr. Steve Spencer and Dr. Alex Shard from NPL for their help with collection and analysis of XPS data.

I met here many wonderful people, who gave me their support, friendship and made this beautiful country feel like home; Huilin, Ada, Evelyn, Dorota, Asia, Romina, Polina, Claudia, Andrzej, Edgar and Orestis – thank you all! Many thanks to my friends in Poland; Ola, Agnieszka, Przemek, Judyta, Karolina and Patrycja – for their lasting friendship despite the distance and changing circumstances.

I wish to thank my family; my parents, my sister, my brother in law and my wonderful nephews; for their love, support and warm home where I always gladly return. Finally, I would like to thank Massimo for being my best friend and a great partner.

List of publications and presentations

Publications:

- **H. M. Stec**, R. Williams, T. S. Jones, R. A. Hatton, *Ultra-thin Transparent Au Electrodes for Organic Photovoltaics fabricated using a Mixed Mono-Molecular Nucleation Layer*, Advanced Functional Materials, **2011,** *21* (9), 1709-1716.
- **H. M. Stec**, R. A. Hatton, *Widely Applicable Coinage Metal Window Electrodes on Flexible Polyester Substrates Applied to Organic Photovoltaics*, ACS Applied Materials & Interfaces, **2012**, *4* (11), 6013-6020.
- **H. M. Stec**, R. A. Hatton, *Plasmon-Active Nano-Aperture Window Electrodes for Organic Photovoltaics*, Advanced Energy Materials, **2013,** *3* (2), 193-199.

Patents:

- R. A. Hatton, H. M. Stec, T. S. Jones, Transparent electrodes for semiconductor thin film devices, PCT/GB2011/051245, granted
- R. A. Hatton, H. M. Stec, xxx, xxx, filed
- R. A. Hatton, H. M. Stec, xxx, xxx, filed

Conferences

- MRS Fall 2009, San Francisco (USA), April 2011, Talk
- HOPV12, Uppsala (Sweden), May 2012, Poster
- Postgraduate Research Symposium 2010, University of Warwick, June 2012, Talk
- Supergen Consortium meetings, 2009-2012

List of symbols and abbreviations

A	absorption
AFM	atomic force microscopy
AM	air mass
A_S	electron affinity
B_E	binding energy
BHJ	bulk heterojunction
C_B	conduction band
CPS	counts per scan
CNT	carbon nanotubes
D	diffusion coefficient
DSSC	dye-sensitised solar cell
E_F	Fermi level
E_g	energy bandgap
EQE	external quantum efficiency
E_{EXB}	electron-hole binding energy in exciton
F	electric field
FF	fill factor
HOMO	highest occupied molecular orbital
HOPG	highly oriented pyrolytic graphite
HRXPS	high resolution X-ray photoelectron spectroscopy
I_p	ionisation potential
J	current density
J_{mp}	current at maximum power point

J_{ph}	photogenerated current
J_{sc}	short circuit current
k_B	Boltzmann constant
L_D	exciton diffusion length
LUMO	lowest unoccupied molecular orbital
OLED	organic light emitting diode
(O)PV	(organic) photovoltaic
P_{mp}	maximum power point
P_{inc}	incident radiant power
r.p.m.	revolutions per minute
R_{rms}	root mean square roughness
R_s	series resistance
R_{sheet}	sheet resistance
R_{shunt}	shunt resistance
QCM	quartz crystal microbalance
SEM	scanning electron microscopy
TCO	transparent conductive oxide
UV	ultraviolet light
V	voltage
V_B	valence band
V_{CPD}	contact potential difference equal to work function difference
vis	visible light
V_{mp}	voltage at maximum power point
VL_s	vacuum level at the surface
V_{oc}	open circuit voltage

XRD	X-ray diffraction
ε	dielectric constant
ε_f^{vac}	change in energy between the electrode E_f and the vacuum level at the surface
η	power conversion efficiency
λ	wavelength

List of chemical compounds

APTMS	3-aminopropyl(trimethoxysilane)
BCP	2,9-dimethyl-4,7-diphenyl-1,10-phenanthroline (bathocuproine)
CIGS	copper indium gallium selenide
CuPc	copper phthalocyanine
C_{60}	Buckminster fullerene
ITO	indium tin oxide
MPTMS	3-mercaptopropyl(trimethoxysilane)
MoO_x	molybdenum oxide
PCBM	[6,6]-phenyl C_{61} butyric acid methyl ester
PCDTBT	poly[N-9'-heptadecanyl-2,7-carbazole-alt-5,5-(4',7'-di-2-thienyl-2',1',3'-benzothiadiazole)]
$PC_{60}BM$	[6,6]-phenyl C_{61} butyric acid methyl ester
$PC_{70}BM$	[6,6]-phenyl C_{71} butyric acid methyl ester
PEDOT:PSS	poly(3,4-ethylenedioxythiophene) : poly(styrenesulfonate)
PEN	polyethylene naphthalate
PET	polyethylene terephthalate

PTCDA	perylene-3,4,9,10-tetracarboxylic-3,4,9,10-dianhydride
P3HT	poly(3-hexylthiophene)
SubPc	boron subphthalocyanine chloride
TiO_x	titanium oxide
WO_x	tungsten oxide

Chapter 1.

Introduction

This chapter gives a general overview of organic photovoltaics (OPV). The first section describes the demand and prospects for sustainable energy sources, with a particular emphasis on photovoltaics. Then, the properties of organic semiconductors are discussed and compared to inorganic semiconductors, followed by an outline of the principles of OPV operation and key device performance parameters. The next section focuses on transparent electrodes for OPV, which is the main subject on this thesis, with a review of the state-of-art and the requirements which need to be met for commercial application. The following section covers characterisation of materials used for OPV fabrication. The final part describes different types of PV and the history of OPV development.

1.1 Sustainable Energy Demand

World energy demand is expected to grow by ~ 20% over the next decade, mainly due to the industrialisation of developing countries.[1] Fossil fuels (coal, oil and natural gas) are predicted to remain the main energy source at least until 2050,[2,3] despite serious drawbacks: *(i)* The heavy dependence of the global economy on fossil fuels - 80% of global energy consumption in 2010 came from this source[4] - which are unevenly distributed throughout the world (>75% of proven oil reserves are situated on territory of 12 countries belonging to the Organization of the Petroleum Exporting Countries[5]) - leads to political and economic tension.; (*ii*) Burning fossil fuels also releases a variety of carbon based gases into the atmosphere, which pollute the environment and are responsible for global warming.[6] For these reasons carbon free energy sources are urgently required, with nuclear power and a number of renewable energy technologies emerging as viable candidates. The latter, namely; solar photovoltaic and solar thermal, wind, biomass, wave power, tidal power, hydroelectric and geothermal are, by definition, inexhaustible and relatively easily-accessible energy sources. Nevertheless, many technologies developed to exploit renewable sources of energy require great capital investments that are out of the reach of poor countries: In 2001 65% of the investments in renewable energy capacity were made by developed countries, with 12% in Germany alone.[4, 7] In reality, only those technologies capable of generating electricity at a cost that competes with electricity generated from coal (i.e. the cheapest fossil fuel due to its abundance), can change the industrial policy of developing countries which, in the near future, will be the biggest energy consumers. Access to cheap, renewable energy not only helps to protect the planet but also brings economic and social development to the poorest parts of the World, many of which are trapped in the vicious circle of poverty.

The energy delivered from the sun to the earth hugely exceeds the demand for energy by humanity and is, in large parts of the world, a potentially practical source of electrical energy as well as heat and light. Photovoltaics (PVs) enable sunlight to be converted directly into electric current and so have great potential to be a low cost means of generating electricity at the point of use.

The amount of energy generated by PV technologies globally grew from 1.5 GW in 2000 to 67 GW in 2011.[8] Whilst those countries with the largest solar resource, such as those at low latitude (e.g. equatorial regions) and high altitude (e.g. Southern Andes and the Himalayas), have the greatest potential for electricity generation from solar,[9] 70% of PV electricity is generated in European Union countries with Germany remaining an undisputable leader.[10] A number of European countries have invested heavily in PV infra-structure based on existing technologies and research into innovative new concepts for PV technologies creating a good environment for research in emerging fields such as OPV, which have not as yet achieved market requirements.

1.2 Organic semiconductors

'Organic semiconductors' is a generic name given to highly conjugated organic molecules, which can be divided into two classes; small molecule[11,12,13] and polymeric[14,15,16] semiconductors. Their electronic and optical properties depend on their structure and number of conjugated bonds and hence they can be engineered to match application requirements.[17,18] In recent years, technologies based on thin films (10– 100 nm) of organic semiconductors have developed rapidly, offering the tantalising prospect of truly flexible, ultra-lightweight and low-cost electronic devices, which can be disposed of in a sustainable way at the end-of-use.[19,20,21]

1.2.1 Basic concept of solid state physics

The content of this section is based on information taken from references [22,23,24,25]. An atom consists of a nuclei surrounded by an electron cloud. The discrete energy of electrons is characterised by atomic orbitals. When an atom forms a chemical bond, the atomic orbitals undergo hybridisation and a bonding and anti-bonding molecular orbital is formed; as the number of atoms participating in the bond increases, a high density of degenerate bonding and anti-bonding orbitals merge forming bands (see Figure 1.1.).

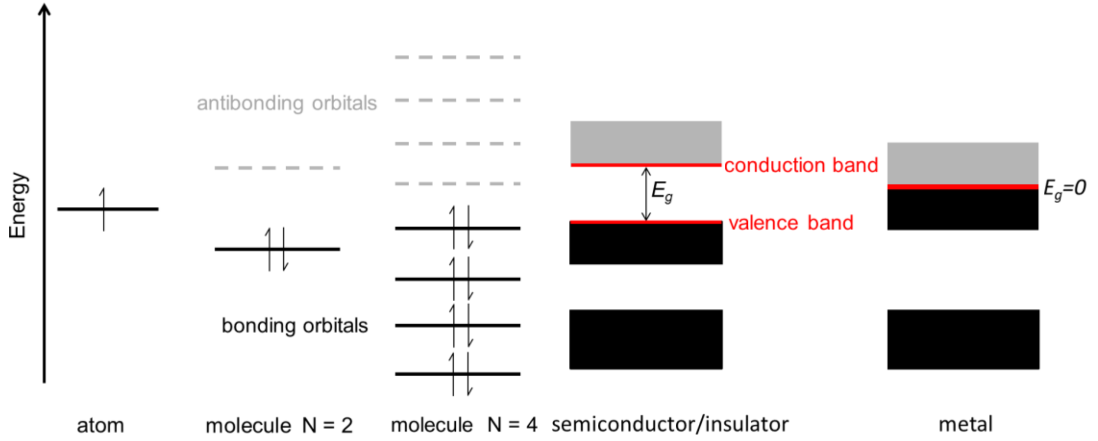

Figure 1.1: Orbitals in an atom and in molecules. The gaps between discrete energy levels decrease with increasing number of atoms, N, participating in the bond formation. For crystals with an approximately infinite number of atoms the energy levels merge into continuous bands; empty C_B and filled with electrons V_B.

The highest energy band occupied with electrons in a crystal is called the valence band (V_B) and the unoccupied band with the lowest energy is referred to as the conduction band (C_B). Inorganic semiconductors comprise equivalent atoms (e.g. Si), or are compounds of two or three elements (e.g. GaAs) that are bound through strong chemical bonds in a continuous lattice. Consequently the C_B and V_B are wide (of the order of eV) and extend throughout the solid.

In metals the transition between the VB and the CB is continuous (Eg = 0 on Figure 1.1), since the top band is half filled and so electrons can move under the influence of an applied electric field which makes these materials easily conduct electricity and heat. In the case of semiconductors and insulators there is a band gap (Eg > 0) between the CB and VB and so at absolute zero the VB is completely full and the CB completely empty. Materials with Eg > 4 eV are classified as insulators and do not conduct electricity. In very small E_g semiconductors elevated temperature can make semiconductors conduct electricity. In the case of doped semiconductors impurity states in E_g can make semiconductors conduct electricity without the requirement of low E_g.

This property is exploited in PVs to harvest energy from the sunlight. Thermalisation in the band is extremely rapid and so the band gap in a semiconductor material also serves to delay recombination of the electron and hole, giving time for them to be separated from one another. In organic semiconductors E_g varies from 1.1 – 3.1 eV,[26,27] which corresponds to the wavelength range from 1000 nm and 400 nm. This range of wavelengths contains 70% of the solar irradiance. The E_g depends strongly on the chemical structure of the molecule [28, 29] and can hence be modelled in organic semiconductors,[30] and tuned in order to maximise absorbed energy.

1.2.2 Molecular solids

In molecular solids only the intra-molecular bonds (ionic, covalent) are strong whilst the inter-molecular bonding is weak van der Waals bonding. As a result the bands formed are narrow (< 0.1 eV)[31,32] and only form in highly crystalline organic semiconductors.[33,34] As an analogy to the inorganic crystal V_B corresponds to the highest occupied molecular orbital (HOMO) in organic semiconductor, while C_B corresponds to lowest unoccupied molecular orbital (LUMO). As defects and disorder in molecular crystals lead to a further reduction in the bandwidth down to $\sim k_BT$ (where k_B is the Boltzmann constant) the band model is not applicable to the majority of molecular solids, where the electronic structure is better described by the potential box model (Figure 1.2). According to this model the electronic structure of each molecule in a molecular solid is largely preserved due to the weak interactions between adjacent molecules. As a result the electrons occupy molecular orbitals localised in deep potential wells and in order to hop to another molecule they need to overcome the potential barrier between molecules.[31]

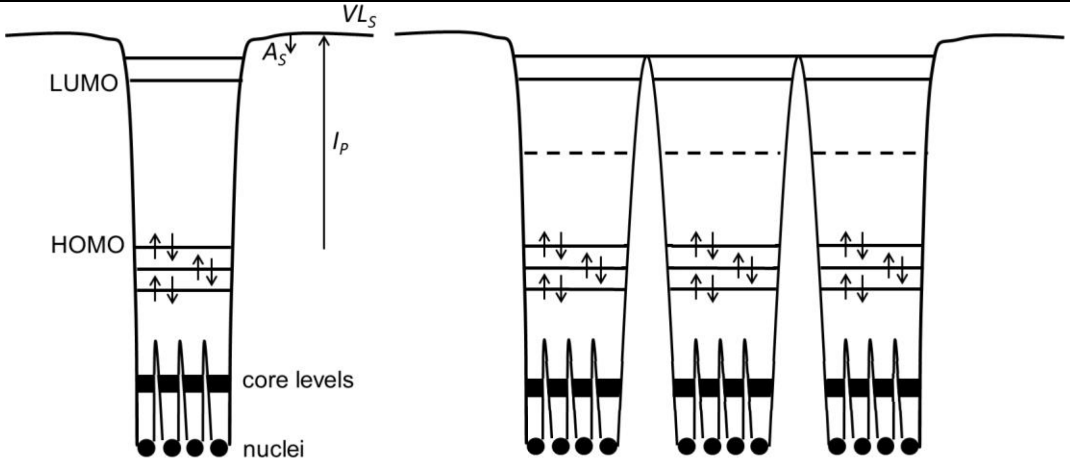

Figure 1.2: The potential box model for an isolated molecule and a molecular solid.

The energy of electrons in the atom/molecule/crystal is taken to equal zero at the vacuum level (VL_s) – which corresponds to a region just outside the solid surface where the electron is at rest. The energy of an electron at an infinite distance from the solid surface is defined as $V_{L\infty}$ and is substantially different from VL_s, as the electron no longer experiences the potential created by the dipolar layer that exists at all solid surfaces.[31,35,36] In molecular solids the ionisation potential (I_p), the electron affinity (A_S) and E_g are greatly reduced, as compared to isolated molecule, due to polarisation stabilisation effects[37,32] as the ions are stabilised by dipoles induced in the surrounding molecules. This stabilisation is a function of the degree of crystallinity, since more closely packed structures provides stronger dipole interaction (Figure 1.3).

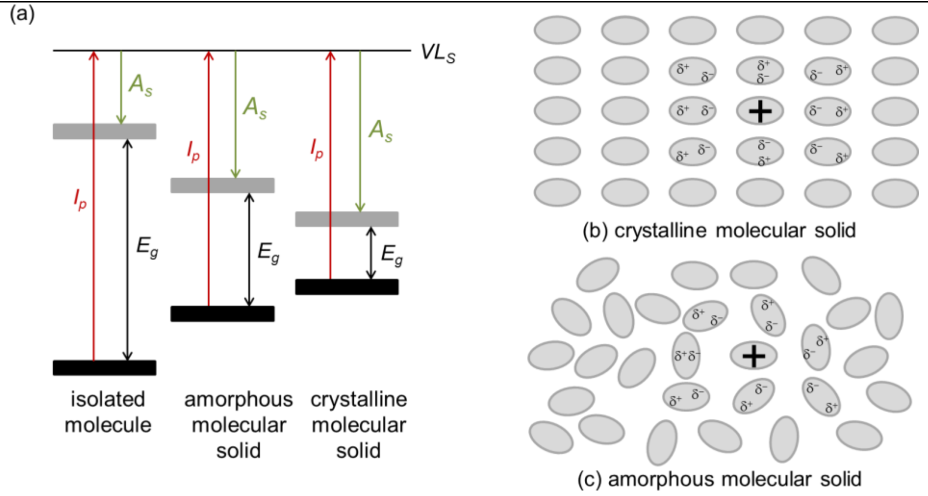

Figure 1.3: (a) HOMO (black) and LUMO (grey) in a molecular semiconductor in isolated molecule and stabilised in crystalline (b) and amorphous (c) molecular solid.

Polarisation stabilisation may vary in the material due to spatial and energetic disorder.[38] As a consequence of this disorder the frontier orbitals have a distribution of energies as schematically depicted in Figure 1.4.

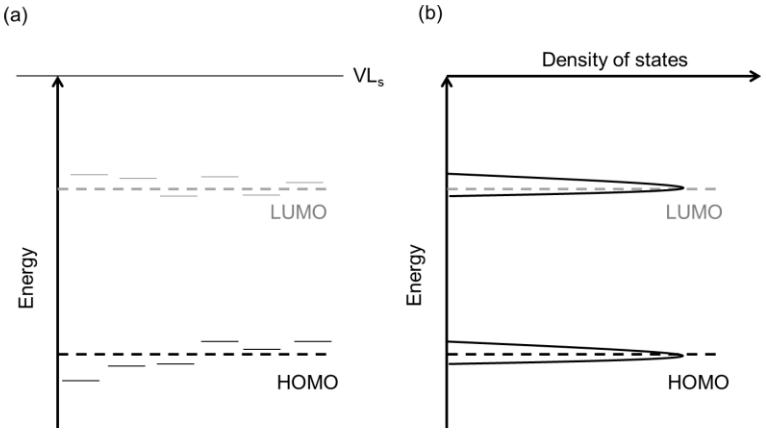

Figure 1.4: (a) Schematic of HOMO and LUMO energy spread resulting from spatial and energetic disorder in molecular semiconductors. (b) Schematic of the density of states distribution of HOMO and LUMO energies.

1.2.3 Excitons in semiconductors

The differences in the bond strength between the repeat units of organic and inorganic semiconductors results in significant differences in their properties. When a quantum of light is absorbed in a semiconductor an electron is excited from the V_B (HOMO) to an excited state in the C_B (LUMO). The system immediately relaxes to an excited state with the lowest possible energy called an exciton which is a hydrogen-like quasi-particle with an electron-hole binding energy E_{EXB}. If the electron-hole pair Bohr radius is smaller than the unit cell dimension (i.e. ≤ 1 nm) the exciton is referred to as Frenkel exciton (Figure 1.5 (a)).[39] Excitons with a Bohr radius significantly larger than one unit cell are called Wannier-Mott excitons.[40] In a molecular solid when the electron and hole reside on adjacent molecules the exciton is referred to as a charge transfer exciton[40] (Figure 1.5 (b) and (c)).

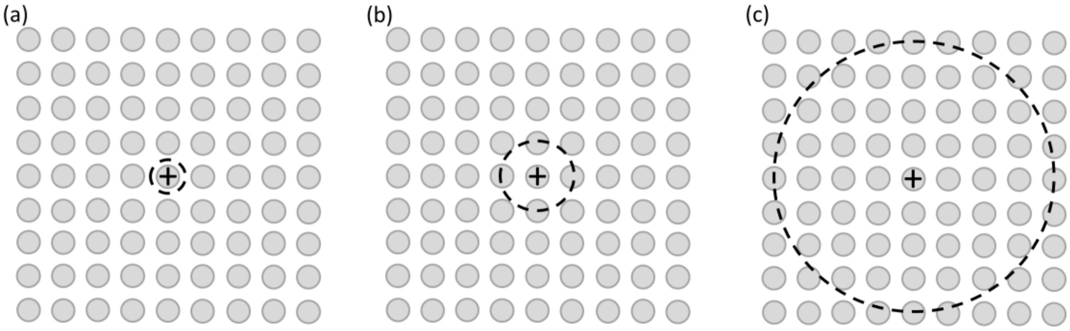

Figure 1.5: Interaction ranges for (a) Frenkel, (b) charge – transfer, (c) Wannier-Mott exciton.

The E_{EXB} depends mainly on the extent of charge screening and scales inversely with the dielectric constant of the material; ε.[39] In inorganic semiconductors ε is typically > 10, but can be as high as 20,[41] which results in the formation of Wannier-Mott type excitons with binding energies of 15 - 40 meV.[42,43] Since this energy range is ~ k_BT at room temperature, excitons in inorganic materials are not stable and dissociate easily into a free electron and a hole. Conversely, organic semiconductors are characterised by a low relative dielectric constant ($\varepsilon < 4$) and so have very high exciton binding energies in the range 150 – 1400 meV.[44,45,46] Excitons in conductive polymers have typically an $E_{EXB} < 400$ meV.[47] As a result, even with the application of a large electric field, the electron and hole remain trapped together in a deep potential well and so excitons in organic semiconductors are very stable and do not spontaneously dissociate. After time τ, depending on the strength of the exciton energy exchange interaction between molecules, the excitons decay.[32] An exciton formed solely by absorption of a quantum of light, with the electron retaining its spin and orbital momentum, is called a singlet exciton. A singlet exciton can undergo an intersystem crossing through a spin-orbital coupling with a phonon, which causes it to relax to a triplet state. As the recombination of a triplet exciton requires again an electron-phonon interaction, it is much less efficient than for singlet states and hence triplets exhibit much longer lifetimes than singlet states.[48]

Since excitons are neutral species they are not influenced by an electric field, but diffuse randomly in organic semiconductors. The transport of excitons is described by hopping theory, in which the coulombically bound electron and the hole move together from one molecule to another in a lossless process.[49] In these non-radiative processes the exciton is transferred to the neighbouring molecule *via* a long-range dipole-induced dipole process coupling (< 10 nm) - Förster transfer or electron exchange in Dexter transfer (< 2nm).[48, 49]

1.2.4 Charge carrier transport

The charge transport in organic semiconductors is best described by a thermally activated hopping process.[50] As such, the charge carrier mobility μ is proportional to the square root of the electric field according to the Poole-Frenkel relation:[51,52] The charge carrier mobility depends on the material and may vary by a few orders of magnitude for the same material depending on crystallinity, purity and processing conditions.

1.3 Interfacial energy alignment

1.3.1 Fermi level and work function

The population of electrons of energy E is related to the density of states and the probability that these states are occupied. The latter is described by Fermi-Dirac distribution function f(E,T):

$$E(E,T) = \frac{1}{e^{(E-E_F)/k_B T} + 1} \qquad \textit{(Eqn. 1.01)}$$

where; E is electron energy, T is temperature, E_F is the Fermi level. E_F is a useful quantity for describing the concentration of electrons and holes at different energies in a semiconductor. It is evident from Equation 1.01 that E_F is the energy at which the probability of finding an electron is equal to 0.5. At T = 0 K all states above E_F are empty and all below are fully occupied; in this special case E_F is called the Fermi energy. At T > 0 K E_F is called the Fermi Level.[24] The effect of the temperature on the *f(E,T)* is shown in Figure 1.6.

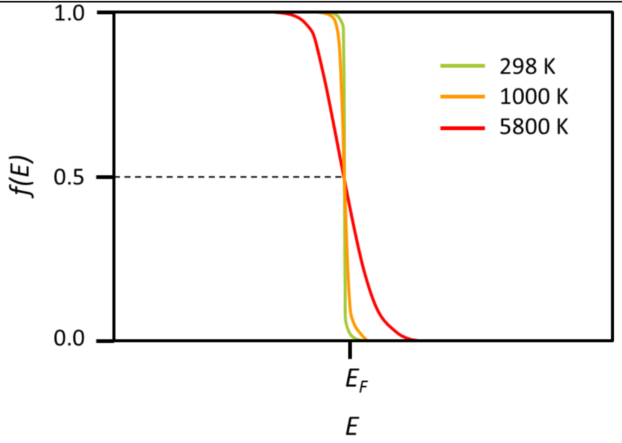

Figure 1.6: The Fermi-Dirac distribution function depicting the probability of occupancy of states for different temperatures.

The energy required to bring an electron from the E_F to the VL_s is defined as the work function (ϕ) and is an important quantity in electrode design for OPVs:

$$\phi = V_{LS} - E_F \qquad (Eqn.\ 1.02)$$

ϕ comprises two components:

$$\phi = \mu + \chi \qquad (Eqn.\ 1.03)$$

where; $\boldsymbol{\mu}$ is the bulk chemical potential originating solely from the potential of the lattice, while χ is the surface potential resulting from the dipole layer at the solid surface. The latter depends on the arrangement and number density of surface atoms (Figure 1.7).[53,35]

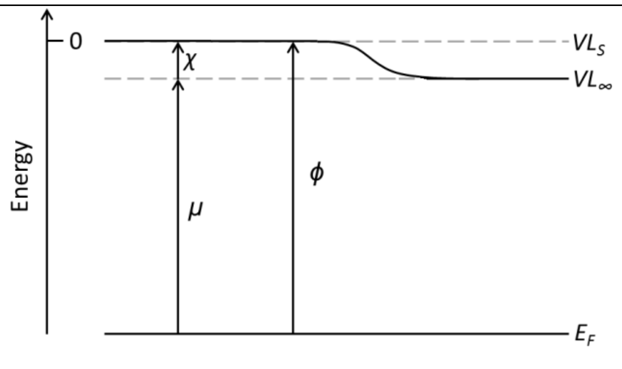

Figure 1.7: Schematic representation of ϕ components in relation to VL_s and $V_{L\infty}$.

The surface composition and crystal structure determines χ and so the ϕ measurements are extremely sensitive to changes in surface electronic structure. For example the difference of ϕ between crystal faces of Au vary by ~0.2 eV (Figure

1.8)[54,55] and by > 0.5 eV between (110) and (111) faces of W.[31] E_F is common within the solid and so differences in ϕ arising from the variation in VL_S. Large changes in measured ϕ can occur due to surface contamination and a chemisorbed molecular monolayer, a phenomenon particularly characteristic for Au, where a physisorbed organic monolayer may reduce ϕ to as low as 4.5 eV.[56,57]

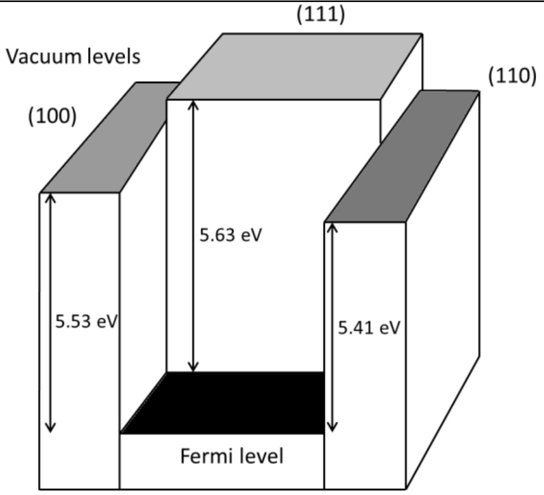

Figure 1.8: Differences in VL_S for the different crystal faces for Au single crystal and the impact on ϕ. The values taken from a theoretical study performed by Fall *et al.*[54]

The E_F of the bulk material, which determines $\boldsymbol{\mu}$, can be altered by doping the material in order to introduce negative (*n*-type) and positive (*p*-type) charge carriers. While organic semiconductors are not usually intentionally doped, significant levels of impurities acting as dopants may affect ϕ of these materials.

In case of metals the E_F is situated at the edge of V_B and C_B. For intrinsic semiconductors E_F lies in the middle of E_g between the V_B and C_B (Figure 1.9). In the case of *p*-doped semiconductors ionisable impurities are introduced in E_g creating positive charge carriers in the V_B resulting in an E_F shift towards the $V_{B.}$ Conversely, the impurities in *n*-doped semiconductors create negative charge carriers in C_B shifting the E_F towards C_B and reducing the ϕ.[25]

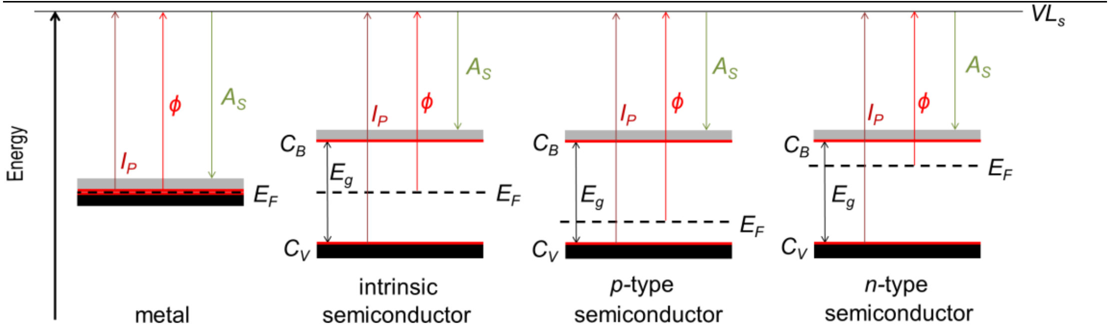

Figure 1.9: Band diagrams of metal, and intrinsic, *p*-doped and *n-doped* semiconductor, with specified I_p, A_S and ϕ.

To measure ϕ of solid materials two methods are usually employed: the Kelvin probe method and Ultraviolet Photoelectron Spectroscopy. The Kelvin probe technique is a non-contact method based on measurement of potential difference between the sample and the probe of known ϕ. This technique can probe OPV device thicknesses (>10 nm). The Kelvin probe, used in this study, is discussed in more detail in Chapter 2. In UPS, the surface of the sample is irradiated with UV photons and the kinetic energy of ejected photoelectrons is measured. The measurements, performed with respect to E_f of the sample being in electrical equilibrium with the detector, provide information about the valence energy level structure and ϕ.

1.3.2 Interfaces in OPVs

The interfaces involving organic semiconductors are: *(i)* electrode/organic, *(ii)* organic/organic and *(iii)* organic/electrode.[31,35,58] There is a significant difference in the electrical characteristic between interfaces of type *(i)* and *(iii)* arising from chemical reactions occurring when hot metal atoms arrive at the soft organic film.[31]

The surface potential plays an important role in determining the interfacial energetics at electrode/organic semiconductor contacts. In a solid, electrons are confined in a potential well of finite depth and so, at the edge of the solid the electron density spills into the vacuum. The dipole layer that exists at the surface of all solids originates from this spilling of electron density into the vacuum, since there is a tail of electron density on the vacuum side of the interface and a region of positive charge of equal magnitude on the solid side as shown in Figure 1.10. The change in electron potential moving through this dipole layer towards the vacuum is equal to the dipole energy (Figure 1.10 (b)).[31,32] Once an electron has passed through the dipole layer it reaches a region of constant electrostatic potential VL_s which extends several microns into the vacuum. The size of the surface dipole depends on the electron density and confinement and is larger on metals than semiconductors.

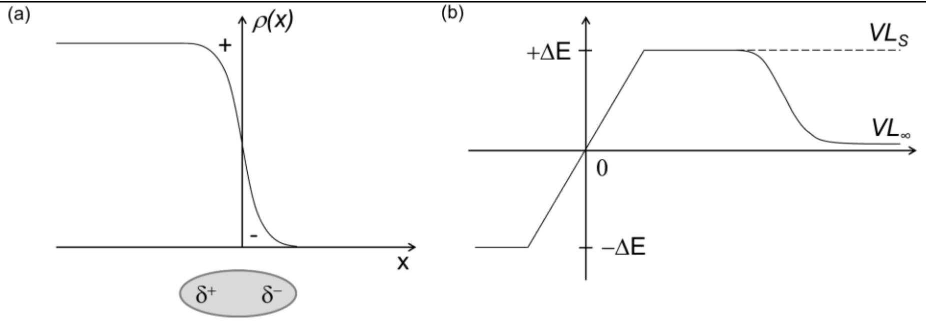

Figure 1.10: (a) Electron density distribution *ρ(x)* as a function of distance from the metal surface, *x*. (b) The potential energy step across a dipole layer.

When a molecule is adsorbed on a solid surface, its electron cloud repels the electron cloud of the solid reducing the extent to which it spills into the vacuum. As a result the size of surface dipole is reduced and so is ϕ. This phenomenon is known as the *push-back* effect (Figure 1.11).[31, 35]

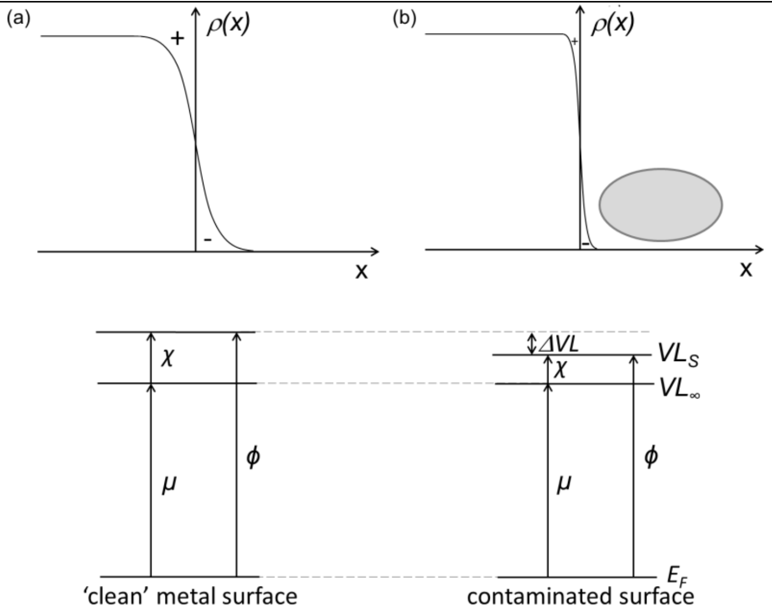

Figure 1.11: Upper: Electron density distribution $\rho(x)$ as a function of distance from the metal surface (x) for a clean metal surface (a) and a surface with a physisorbed overlayer (b).; Lower: Corresponding energy level diagrams.

The *push-back* effect is believed to be the origin of the ϕ reduction observed in metals exposed to the laboratory environment,[56, 59] since a mixture of low mass hydrocarbons and siloxanes is readily physisorbed onto its surface. The *push-back* effect also plays an important role at metal/organic semiconductor interfaces in OPVs, since the organic semiconductor is physisorbed to at least one of the electrodes. Upon organic material deposition the electron density is redistributed across the interface so that the surface of the metal electrode and organic interfacial region become charged (Figure 1.12) and an abrupt shift in VL_s at the interface is observed. Vacuum level shifts are typical for metal/organic interface and are less common at organic/organic interfaces due to the absence of large intrinsic surface dipoles.[31, 35, 60]

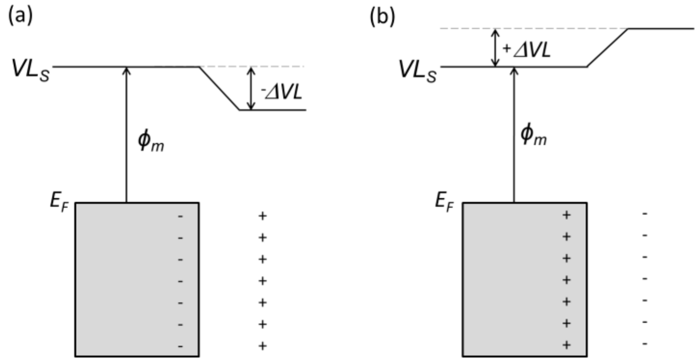

Figure 1.12: The vacuum level shift occurring upon metal/organic contact formation when electrons are transferred to (a) and from (b) the electrode.

A positive vacuum level shift (i.e. electrons moving from the metal to the organic) is less common and may occur when: *(i)* the adsorbate molecules possess an appropriately oriented permanent dipole and all of the molecules are bound to the surface in approximately the same orientation (e.g. self-assembled monolayers); *(ii)* the organic materials is a powerful electron acceptor, which results in formation of an interfacial layer dipole due to partial charge transfer.

Chemical bond formation also induces a charge density rearrangement at the interface since the substrate molecule bond normally has an associated dipole, but due to the close proximity between the two materials the *push-back* effect will also play a role.[31, 35]

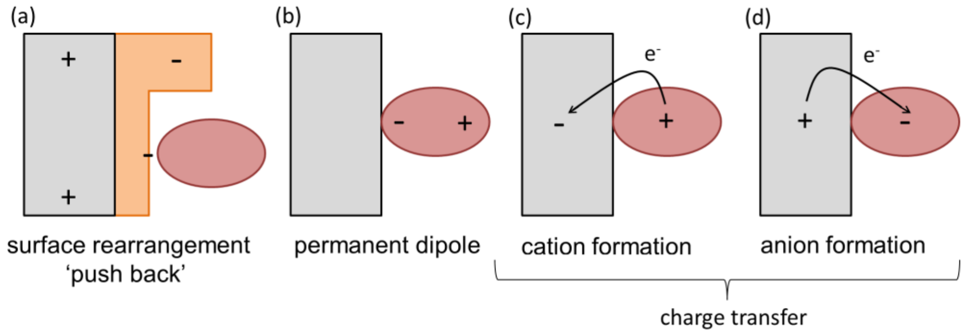

Figure 1.13: The possible factors affecting the interfacial dipole layer: (a) the *push-back* effect; (b) a molecule with permanent dipole; (c) and (d) charge transfer between surface and adsorbate.

1.3.3 Electrode/organic semiconductor contacts

In OPV architectures, where the organic semiconductor and electrode form a direct contact the electrode properties such as ϕ, surface energy and surface roughness play crucial role in the OPV performance. The electrode ϕ controls the process of charge carrier extraction because electrons flow towards lower energy states until E_F alignment is achieved. The abundance of dopant states in E_g of conventionally doped semiconductors either provide or accept electrons so that spontaneous ground state electron transfer can occur from the semiconductor to the electrode if $\phi_{electrode} > \phi_{semiconductor}$ or from the electrode to the semiconductor if $\phi_{semiconductor} > \phi_{electrode}$. In these cases a space charge region (depletion region) is formed in the semiconductor adjacent to the metal electrode as depicted in Figure 1.14.

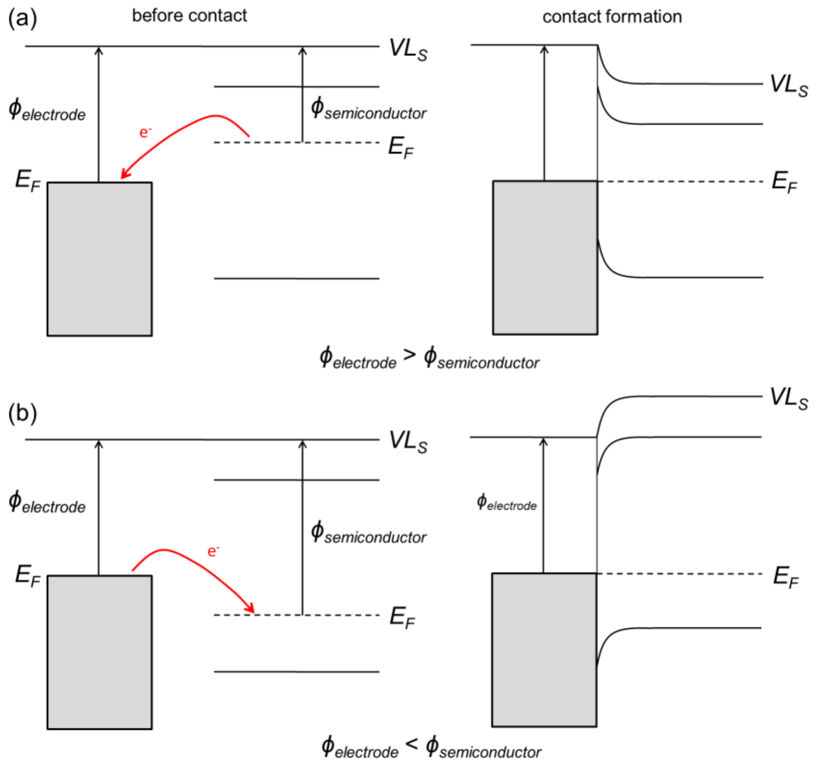

Figure 1.14: The energy level diagram of electrode and semiconductor before (left) and after (right) contact formation; the red arrow indicates the direction of electron transfer.

In OPVs the organic semiconductors layers are typically very thin (10-200 nm) and can have extremely low dopants density ($<10^{14}$ cm^{-3}). As a result there are often insufficient ionisable impurities to reach thermodynamic equilibrium across the interface.[31, 35, 61]

1.4 Principles of operation

The simplified energy diagram of a bi-layer heterojunction OPV is depicted in Figure 1.15. The cell consists of two metal electrodes; an anode with a high work function (ϕ_a) and a cathode with low work function (ϕ_c). At least one of the electrodes needs to be optically transparent to let light into the device. The photoactive organic heterojunction is sandwiched between the electrodes and comprises an electron donor and electron acceptor. For the dissociation of an exciton in the donor material to be thermodynamically favourable the LUMO of the acceptor must be lower lying than that of the donor. Conversely for the dissociation of an exciton in the acceptor the HOMO of the acceptor must be lower lying than that of the donor.

The process of converting light into electric current in OPVs can be sub-divided into four key processes: (1) Photon absorption in the photoactive layer resulting in exciton formation; (2) Exciton diffusion to the donor/acceptor interface; (3) Exciton dissociation at the heterojunction leading to formation of free charge carriers; (4) charge transport and extraction to the external circuit *via* the electrodes.

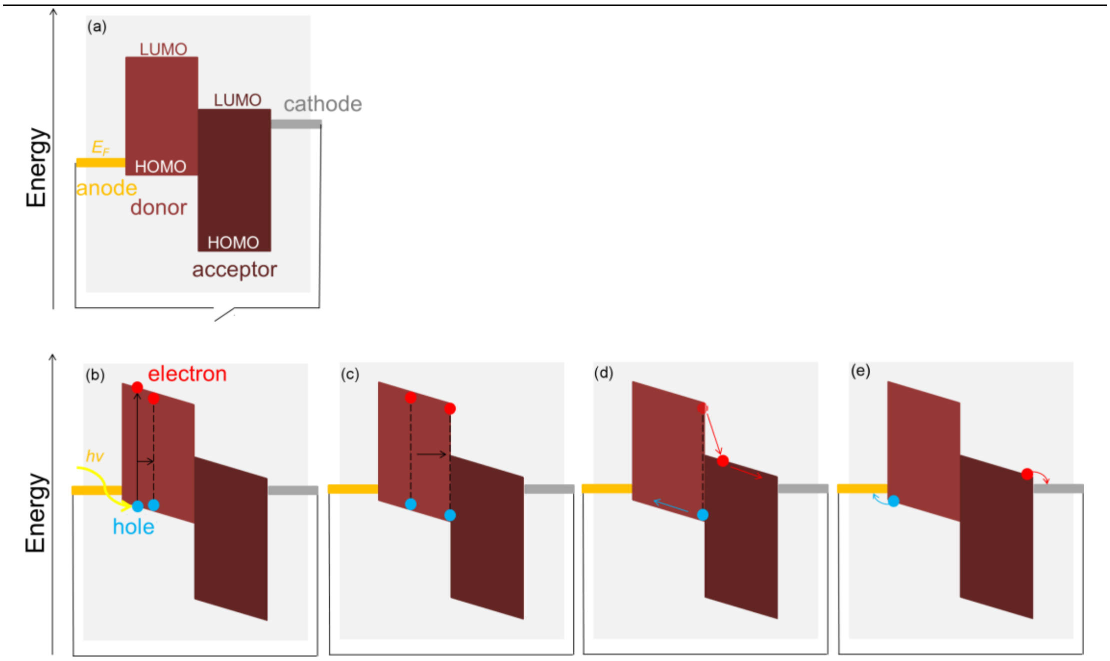

Figure 1.15: A schematic diagram of an OPV in open (a) and closed circuit conditions ((b)-(e)) depicting the basic operation stages; (b) light absorption and the exciton formation; (c) exciton diffusion; (d) exciton dissociation at the donor/acceptor interface; (e) charge extraction and collection at the electrodes.

1.4.1 Absorption

An electron enters the OPV through the semi-transparent electrode and is absorbed in the photoactive layer. If the photon energy is greater than or equal to the HOMO-LUMO gap of the photoactive material - which in organic semiconductors typically corresponds to the visible region of the spectrum - it is absorbed. Excitation of an electron from the HOMO to the LUMO results in the formation of a Frenkel exciton. The absorption efficiency, η_{abs}, describes the fraction of incident photon flux absorbed in the photoactive layer and can be measured through external quantum efficiency (EQE) measurements (section 2.2.6.2).[62] Inadequate absorption of the solar spectrum remains one of major factors limiting the efficiency of OPVs. Whilst the EQE can be as high as 80% over a limited range of wavelengths in the visible part of the spectrum it is typically very low in the near infra-red wavelength range.[62,63] η_{abs} depends on the properties of the transparent electrode, device geometry and the photoactive layer thickness, as well as the absorption coefficient of the organic semiconductor layer.

The amount of light entering the photoactive layer depends strongly on the far-field transparency of the window electrode, although increasing the transparency without compromising the sheet resistance of the electrode is extremely difficult. However η_{abs} can be improved by using plasmon-active structures which increase the light path length through the photoactive layer[64] without increasing the far field transparency, or by employing microcavity effects (e. g. using two reflective metal electrodes[65]) or optical spacers to optimise the optical geometry of the cell.[66]

The capability of a material to absorb incident light is described by the Lambert-Beer law, where the absorption coefficient, α, is defined by following equation:

$$I = I_0 e^{-\alpha\lambda} \qquad (Eqn.\ 1.04)$$

where; I and I_0 is the transmitted and incident photon flux respectively, λ is the wavelength. Since the thickness of the photoactive layer is limited by the exciton diffusion length and the requirement to minimise material usage and cost, α should be as large as possible. For materials used in OPVs α must exceed 10^5 cm^{-1}, [67,68] so that a path length of only 100 nm is sufficient to absorb nearly 100% of the light.

1.4.2 Exciton diffusion

Excitons diffuse randomly through the photoactive layer, unaffected by electric field or concentration gradients. The exciton lifetime (τ) and diffusion speed (described by diffusion coefficient D) are material specific parameters and determine the average distance an exciton can diffuse before recombining (L_D). These three parameters are related by the equation:

$$L_D = \sqrt{D\tau} \qquad (Eqn.\ 1.05)$$

The exciton diffusion length, L_D, limits the thickness of the photoactive layer, since the probability of an exciton formed at a distance greater than L_D from the heterojunction reaching the donor/acceptor interface is low. The efficiency of this process, η_{diff}, can be distinguished from other factors affecting the overall efficiency by photoluminescence measurements.[69]

The exciton diffusion length of conjugated polymers is in the range of 5 to 20 nm,[70,71] but is significantly higher in many small molecules (e.g. 30 nm in phthalocyanines[72]) and is reported to be as high as 65 nm in the pentacene.[73] Indeed it has been proposed that it may be possible to achieve exciton diffusion lengths in the μm range in highly ordered molecular crystals.[74]

1.4.3 Exciton dissociation

To generate free negative and positive charge carriers (i.e. electrons and holes respectively) excitons must be dissociated. Due to the very high exciton binding energy in most molecular solids the thermal energy of the electron at room temperature (~ 25 meV) is too low for exciton dissociation into free charges, even with the assistance of the large built-in electric field in OPVs. To overcome the exciton binding energy the exciton must arrive at a discontinuity in frontier orbital energies larger than the E_{EXB}, which can be achieved at the interface between dissimilar molecules and crystal defects.[75] Exciton dissociation can be described as a two-step process: *(i)* a Frenkel exciton at the heterojunction is dissociated to form a charge-transfer exciton across the junction, where the electron in the LUMO of the acceptor and a hole in the HOMO of the adjacent donor molecule are bound coulombically with an energy ~0.1 eV.;[76] *(ii)* The geminate pair can then either recombine to the ground state or dissociate into free charge carriers.[76] This splitting process depends on the electric field across the junction, which is determined by the built-in potential[77] and external voltage.[78] In practice a frontier orbital energy offset of ~ 0.3 eV is typically required for exciton dissociation. The efficiency of this charge transfer process, η_{ct}, may approach 100% in optimised device structures.[79]

1.4.4 Charge transport and extraction

The final process is charge carrier transport to the external circuit *via* the electrodes to supply a direct current to the load. The separated electrons and holes are transported in the LUMO (C_B) and HOMO (V_B) respectively and their velocity depends on the external electric field strength E and charge carrier mobility;

$$\mu = -\frac{q\tau}{m}E \qquad (Eqn.\ 1.06)$$

where; q is the particle charge, m is the particle mass, τ is the average scattering time.

The efficiency of this process, η_{cc}, depends on the mobility of the charges through the organic layers and the efficiency of their extraction to the external circuit by the electrodes. In the context of an OPV a significant variation in electron and hole mobility can lead to imbalanced charge carrier extraction resulting in a build-up of space charge that adversely affects the potential distribution in the device reducing device efficiency.[80] Unfavourable molecular orientation, polycrystallinity, crystal defects and traps can also reduce the efficiency of this step.

When charges approach the electrodes they are extracted to the external circuit, a process that is facilitated by the built-in electric field and, in the case of bilayer device architectures, by diffusion current. The nature of electrode/organic semiconductor interface is complex and the subject of a great deal of scientific research.[56] Ideally for OPVs the E_F of the electrode should align closely to the energy of the relevant frontier orbital in the adjacent organic semiconductor to maximise the built-in electric field. The deposition method used, order of deposition, contamination at the electrode surface, interfacial oxide layers and chemical reactions can all strongly affect the alignment of the organic frontier electronic levels with the respect to electrode E_F and so affect the charge extraction efficiency.[81] Charge carrier collection is often facilitated using molecular interlayers[82] to improve the energy level alignment and block exciton quenching. Also electrode structuring may improve the efficiency of this process by increasing charge collection area and local electric field.[83]

The overall EQE of these four processes gives the ratio of incident photons transformed into electrons delivered to the external circuit and is given by the product η_{abs}. η_{diff}. η_{ct}.η_{cc}.

1.4.5 *J-V* characteristics

The *J-V* characteristics of a PV device in the dark and under illumination are shown in Figure 1.16. In the dark under reverse bias the current saturates at the reverse saturation current; J_0. J_0 is a recombination current and is a function of the minority carrier concentration. J_{sc} is the current density at the short circuit condition (i.e. when $V = 0$ and the load resistance (R_l)= 0 (see Figure 1.17)). In an ideal OPV the current density under illumination is independent of the applied voltage under negative bias and J_{sc} is equal to J_{ph}. For very small area devices J_{sc} may be falsely increased due to edge effects when the area surrounding the geometric area of the top electrode is not masked.[84] V_{oc} is the maximum potential difference across the electrodes and is achieved at open circuit conditions, when $J = 0$ (i.e. $R_l = \infty$). In an ideal cell V_{oc} depends on J_{ph} and J_0.[22]

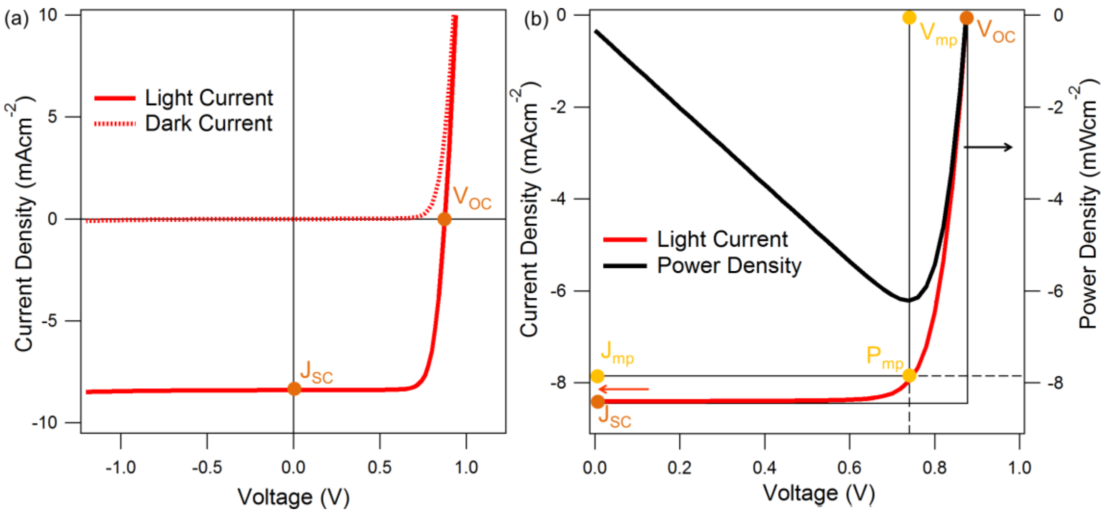

Figure 1.16: (a) *J-V* curve of an ideal PV in the dark (dotted line) and under illumination (solid line); (b) *J-V* characteristic and power density curve of a PV with P_{mp} , J_{mp}, J_{sc}, V_{mp} and V_{oc} labelled.

In an OPV the difference in potential between a hole in the HOMO of the electron donor and an electron in the LUMO of the electron acceptor represents, to a good approximation, the maximum theoretical V_{oc},[26,75] although V_{oc} also depends on materials properties[85] and device geometry,[86,87] and so this maximum value is not always achieved. The electrode ϕ is reported to play a minor role in determining $V_{oc.}$[88] Cook *et al.* have shown that provided ϕ_a of the hole extracting electrode exceeds the ionisation potential of the of the electron donor V_{oc} is maximised.[89] An additional wide band-gap interfacial layer may be used between the electrode and the photoactive material, which enables selective extraction of one carrier type (i.e. electrons or holes). When such a layer is used the V_{oc} is typically increased, which is attributed to a reduction in J_0.

The power produced by an OPV, $P = JV$, is shown in Fig. 1.16 (b). The maximum power is generated at the maximum power point (P_{mp}), where the product $J \times V$ is at a maximum. The relation between P_{mp}, J_{sc} and V_{oc} is given by fill factor (*FF*);

$$FF = \frac{J_{mp}V_{mp}}{J_{sc}V_{oc}} \qquad (Eqn.\ 1.07)$$

The theoretical maximum for FF is 0.8, but empirically rarely exceeds 0.7.

An ideal PV can be modelled as a current source connected in parallel with a rectifying diode, as depicted in Figure 1.17 (solid lines). In this case the J-V characteristic is described by the Shockley equation:[22]

$$J(V) = J_{ph} - J_0\left(e^{\frac{qV}{k_BT}} - 1\right) \qquad (Eqn.\ 1.08)$$

where; V is voltage, $J(V)$ is the voltage dependent current density.

OPVs exhibit non-ideal J-V characteristics due to defects arising from the fabrication process, material properties and the cell architecture. An equivalent circuit diagram for a non-ideal PV is given in Figure 1.17 (solid and dashed lines). In a non-ideal diode there are 2 additional components as compared to an ideal diode that affect device performance; namely, the series resistance (R_s) and shunt resistance (R_{shunt}). R_s is depicted on Figure 1.17 as a resistance between the current source and the load, and describes losses arising from mechanisms affecting charge transport through the device layers. The contributions to series resistance are; *(i)* the low charge carrier mobilities in the organic layers; *(ii)* the contact resistance and low rates of charge transfer at the electrode interfaces. In an ideal device R_s would be 0

Ω. R_{shunt}, is a resistance parallel to the load and in an ideal device would be infinitely large, but is reduced due to pin holes and recombination mechanisms across the device.

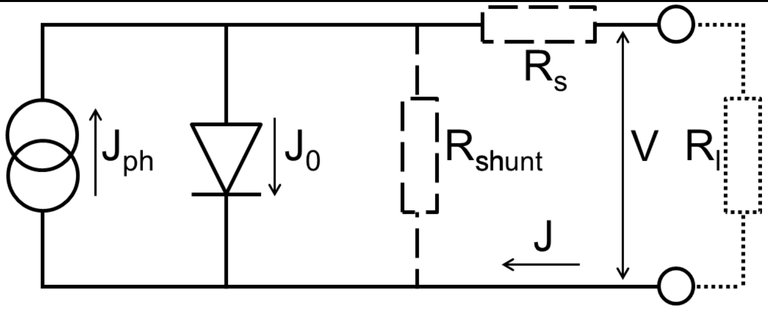

Figure 1.17: A schematic circuit equivalent of an ideal (without dashed lines) and non-ideal (with dashed lines) photovoltaic device.

When the values of R_{shunt} and R_s deviate from the ideal, the shape of the *J*-*V* characteristic changes as shown in Figure 1.18. A reduction in R_{shunt} and increase in R_s results in a reduction in *FF* and hence lower J_{mp}, V_{mp} and efficiency. In practice the *J*-*V* curve of a real device is often modelled by fitting to the modified Shockley equation;[90]

$$J = \frac{R_{sh}}{R_s + R_{sh}} \left\{ J_0 \left[\exp\left(q\left(\frac{V - JR_s}{nk_BT} \right) \right) - 1 \right] + \frac{V}{R_{shunt}} \right\} - J_{ph} \qquad (Eqn.\ 1.09)$$

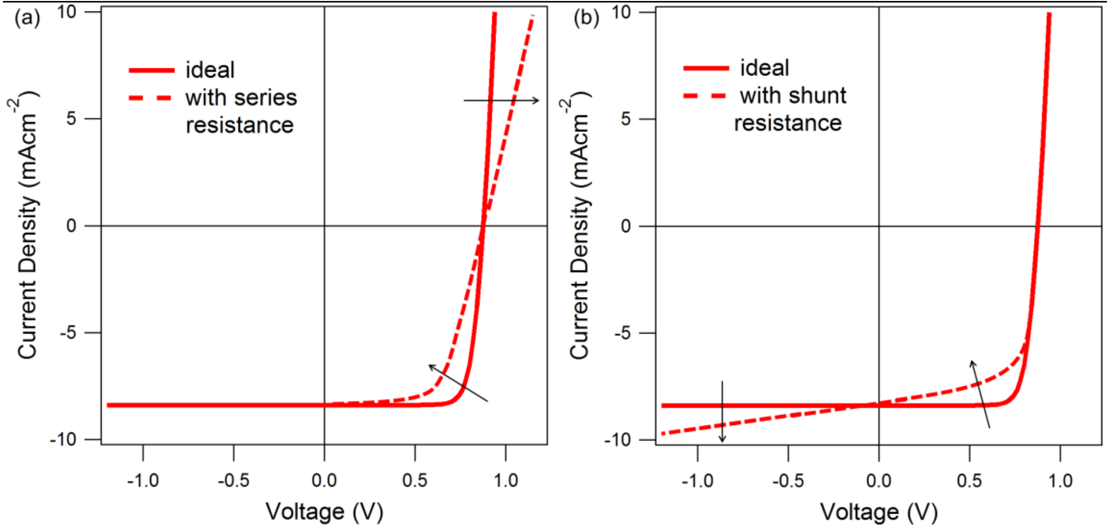

Figure 1.18: The effect of series (a) and shunt (b) resistance on the *J-V* characteristic of the OPV. The arrows indicate the trend in changes of *J-V* curve.

The power conversion efficiency of a PV device (η) is defined as:

$$\eta = \frac{P_{mp}}{P_{inc}} = \frac{J_{sc}V_{oc}FF}{P_{inc}} \qquad (Eqn.\ 1.10)$$

where; P_{inc} is the incident radiant power. Since η is proportional to J_{sc}, V_{oc} and FF all three of these parameters must be maximised and it is not meaningful to increase one at the expense of another. η, J_{sc}, V_{oc} and FF are the 4 key parameters used for characterising PV performance.

1.5 Transparent electrode

1.5.1 Indium Tin Oxide (ITO)

Doped metal oxides have been used as materials for transparent electrodes since the start of the 20th century and they are now widely employed in a variety of applications due to their combination of good transparency and high conductivity.[91] Indium-tin oxide (ITO) and fluorine doped tin oxide (F:SnO_2), are almost universally employed as the transparent electrode in the current generation of OPV. ITO coated glass, with an optimal In:Sn atomic ratio of 9:1, has a mean transparency of ~ 85% across the visible spectrum, a ϕ of between 4.4-5.5 eV – depending on the method of surface cleaning - and a sheet resistance below 15 Ω sq^{-1}.[92] These properties have made ITO coated glass the transparent electrode of choice for years of preliminary OPV research focused on device efficiency and architecture. However, as OPV technology approaches commercially viable power conversion efficiencies the need for electrode flexibility, extended device lifetime, low cost and large area fabrication capability has grown. In these respects ITO has a number of series of drawbacks, but there remains a lack of a viable alternative.

ITO is a complex ternary oxide and its optical, electrical and surface properties depend strongly on the In:Sn ratio[93] and the method of deposition.[94,95] The electrical and topographic inhomogeneity of its surface combined with its chemically ill-defined nature are particularly problematic for organic optoelectronic devices, since organic semiconductors are susceptible to damage resulting from localised heating and/or unintentional doping by metal ions leaching from the electrode.[96,97] ITO is also poorly compatible with plastic substrates; in order to achieve a low sheet resistance (i.e. $< 15\ \Omega\ sq^{-1}$) it must be annealed at temperatures ≥ 300 °C,[98] a process that is incompatible with low cost, highly transparent, flexible plastic substrates such as polyethylene naphthalate (PET) and polyethylene terephthalate (PEN). As a result the sheet resistance of commercially available ITO films supported on plastic substrates is typically > 35 Ω sq^{-1}, which is 3-4 times higher than on glass. Additionally, ITO is only sufficiently electrically conductive at thicknesses of ~ 100 nm,[99] rendering it prone to cracking upon bending.[100,101]

One of the most serious shortcomings of ITO glass for OPV applications is the limited global supply of indium, which is expected to fall short of projected demand in the coming years creating a bottleneck to the proliferation of OPVs once performance targets for market entry are met. Indeed in a recent independent study the substrate cost was identified as the most important factor in the manufacturing cost of OPVs.[102] In recent years other transparent and conductive metal oxides (TCOs) have been widely investigated as replacements for ITO. Whilst many of these oxides offer lower materials cost than ITO they still require high energy processing and their properties remain inferior to ITO.[103] The main groups of alternative electrodes to transparent conducting oxides are briefly described in the following section.

1.5.2 Alternative transparent electrodes

Transparent conductive polymers such as chemically doped polyacetylene, polyaniline and poly(3,4-ethylenedioxythiophene) (PEDOT) are the organic equivalents of TCOs and have been used in place of TCOs in some applications. Particularly PEDOT doped with poly(styrenesulfonate) (PSS) (described in detail in section 1.6.2) is the most widely used organic conductor due to its high ϕ (5.2-5.3

eV),[104] which renders it stable towards oxidation and its relatively high transparency at low thickness. PEDOT:PSS was first used as an anti-static material, then as an interfacial layer in organic light emitting diodes (OLEDs) and most recently in OPVs where its use is now widespread. As new methods for improving the conductivity of PEDOT have been developed it has been used as an independent electrode in small area OPVs. PEDOT:PSS is a low cost electrode material[105] which can be processed using existing commercial large area coating technologies.[106,107] Despite its advantages as compared to TCOs PEDOT:PSS has a number of drawbacks for OPV applications: *(i)* the instability of the doped state;[91] *(ii)* its hydrophilic nature makes it susceptible to water uptake which results in degradation of the polymer-photoactive layer interface;[108] *(iii)* poor long term stability;[109,110] *(iv)* the high conductivity required for large area electrode applications is only achieved by the transparency trade-off. For example, the mean transparency across the visible spectrum is only > 80% when the sheet resistance is > 50 Ω sq^{-1},[111] which is too high for efficient large area efficient OPV.[112]

Nano-structured organic and inorganic hybrid electrodes are an emerging class of transparent electrodes, which enable both high conductivity and high transparency. Carbon nanotubes (CNTs) have been successfully introduced into OPV structures as transparent electrodes. CNTs are exceptionally conductive and can be processed from solution to form large area networks.[113] Recently graphene has also been investigated as the transparent electrode in OPVs.[114] These carbon electrodes suffer from a series of drawbacks including high surface roughness, poor adhesion to the substrate and additional processing requirements in order to achieve higher conductivity. However the main drawbacks are the high production cost (the cost of

CNT electrodes is currently a few times that of ITO)[105] and the high sheet resistance (> 20 Ω sq^{-1}) at thicknesses that provide good transparency.[113,114,115]

Metal nano-structures such as nano-wires and nano-fibres are currently much cheaper than CNTs and graphene,[105] and can be solution processed on a large scale.[116] Their processing also results in reduced material losses as compared to TCO deposition methods such as sputtered films. Cu and Ag are typically the metals of choice for this type of electrode due to their high electrical conductivity. However their high surface to bulk ratio renders them susceptible to oxidation, including sulfidation by low levels of H_2S, OCS, SO_2, and CS_2 in air.[117] Electro-migration is also a concern for long-term electrode stability.[118] Moreover, the random array of micron length[119] metal nano-wires needed to achieve high conductivity significantly increases electrode roughness which can have a detrimental effect on the performance of very thin devices, such as OPVs, by increasing the likelihood of shunts. Metals are also very reflective and so high transparency is only obtained for lower coverage, which results in high sheet resistance.[116]

Metal grid electrodes are widely used in conventional PVs and may exhibit transparency comparable to, or superior to ITO glass.[120] However the large grid spacing (700 nm[121]) required for high transparency greatly increases free carrier recombination losses in OPVs. Conversely, reducing the gaps between grid lines inevitably increases losses due to light absorption.[91] The high surface roughness of metal grid and random nanowire electrodes necessitates coating with a planarising conducting polymer layer which reduces the transparency, adds to the complexity of fabrication and causes these hybrid electrodes to suffer from the drawbacks associated with the use of conducting polymers.

As a result very few of these electrodes have yielded devices with performance comparable to those utilising ITO glass. Indeed, the small area OPVs (<< 1 cm^2) usually fabricated for research purposes to demonstrate new concepts often mask the detrimental effect of electrode sheet resistance, which needs to be ≤ 15 Ω sq^{-1} in order to be useful for practical applications. It is also notable that very few of the aforementioned studies demonstrate the performance of OPVs on flexible substrates after repeated bending and those that do relate to device areas much smaller than the radius of bend curvature.[113,122,123] As a result, it is not yet clear as to whether they are suitable for use in OPVs with cell areas greater than a few millimetres square. Another increasingly important consideration for OPVs is the stability and chemical make-up of the substrate electrode surface. As device efficiencies approach values suitable for commercialisation the importance of device stability is taking centre stage in OPV research.[124,125] With the drive towards thinner and more complex device architectures, it is essential that the substrate electrode is chemically well-defined, stable and smooth, since the interfaces at the electrodes are critical determinants of device performance.[82, 91] Chemically and structurally well-defined substrate electrodes are also a prerequisite to engineering reproducible, energetically optimised interfaces.

1.5.3 Thin metal films

The oldest category of electrode materials is that of unpatterned thin metal films, which offer the advantages of inherent flexibility, chemical homogeneity and established manufacturing infrastructure for large area roll-to-roll evaporation in the packaging industry.[126,127] O'Connor *et al.* have provided general guidelines for the design of this class of electrode for OPV applications, and show that for film thicknesses below 10 nm the high absorption of metals as compared to ITO can be partly offset by micro-cavity effects which result in a greater photocurrent than expected on the basis of the far-field transmittance.[128] Indeed, by optimising the thickness of the photoactive layer O'Connor *et al.* show that it is possible to achieve comparable device performance in molecular OPVs employing an ultra-thin Ag electrode to that on an ITO glass electrode,[128] which serves to highlight the need for full optoelectronic modelling when screening candidate window transparent electrodes for OPVs. However, this class of electrode has received relatively little attention to date since there is the perception that ultra-thin metal films are prohibitively resistive, discontinuous, prone to oxidation - thus incompatible with long life applications - and extremely fragile due to poor adhesion with the substrate.[91]

1.5.3.1 The role of interfacial adhesion layers

Realising robust sub-10 nm metal films on glass is difficult, particularly for noble metals, and requires the use of an interfacial adhesion layer owing to the intrinsically low energy of adhesion between many metals and glass.[129] One established class of adhesive layer for this purpose is an ultra-thin (1-10 nm) film of a transition metal such as Ge,[130] Cr or Ta[131] although, in the context of optically thin metal films, this thickness is sufficient to contribute to the film absorption. The other way to circumvent this issue is to derivatise the substrate with a layer of molecules designed to enhance metal nucleation by interacting strongly with both the substrate and the incoming metal atoms (i.e. a molecular adhesive), thereby suppressing surface diffusion and promoting the growth of continuous metal films at low thickness.[132,133] Methoxysilanes form strong covalent bonds to the surface of glass by reaction with native hydroxyl groups and, unlike metal adhesion layers, do not contribute to light absorption by the electrode making this type of adhesion layer well suited to the fabrication of highly transparent metal films. Thiol functionalised silanes have previously been investigated for the preparation of Au films on glass, since thiols have a strong affinity for Au, whilst organosilanes couple with native hydroxyl groups on a variety of substrate materials[134,135] to form strong siloxane bonds. Hatton *et al.* has previously reported the viability of this approach for optically thin Au films on glass using a thiol functionalised molecular adhesive layer and demonstrated application in organic light-emitting diodes.[133] However, the method reported is not amenable to scale-up because of the requirement to use large amounts of solvent and the potential for methoxysilanes to polymerise when deposited from a dilute solution.[135,136] A few reports have also investigated the possibility of utilising amine functionalised silanes to promote the growth of Au films on silicon and glass, although not for the purposes of fabricating highly transparent films and all using solvent assisted deposition methods.[137,138,139]

1.5.3.2 Flexible metal electrodes

For the full potential of OPVs to be realised they must be fabricated on flexible substrates to enable rapid roll-to-roll fabrication, although there are very few reports relating to the use of unpatterned metal films on flexible substrates as the window electrode for OPV. Kim *et al.* have recently demonstrated OPVs fabricated on 15 nm thick Au wrinkled electrodes on PET with a cell area of 0.18 cm^2 and a power conversion efficiency of 1.8%.[140] Yambem *et al.* have demonstrated small area OPV employing flexible 19 nm Ag electrodes evaporated onto PET with power conversion efficiency of 2.3%.[123] Optically thin Cu films sandwiched between oxide layers are also emerging as a promising electrode materials for OPVs; Perez Lopez *et al.* have recently demonstrated 18 nm Cu films sandwiched between the MoO_x layers in 0.22% efficient OPVs on glass,[141] although unpatterned copper films have not yet been used as window electrodes in flexible OPV. Again an adhesion interfacial layer between flexible substrates and metals is required to make these electrodes suitable for truly flexible purposes. For example, Wu *et al*. reported that 20 nm thick Cu films prepared by sputtering onto flexible poly(dimethylsiloxane) fail catastrophically when bent through an 8 mm radius,[119] which is caused by poor adhesion between the metal and the substrate.

1.5.3.3 Absorption enhancement

To date the most efficient polymer based OPVs are based on bulk heterojunction (BHJ) concept, where co-deposited electron-donor and electron-acceptor type organic semiconductors spontaneously phase-separate into domains, which helps to address the excitonic diffusion bottleneck that occurs in bi-layer OPVs. However, recombination losses during charge carrier transport through the complex network of donor and acceptor phases can limit the thickness of the photoactive layer to less than the optimal for light absorption.[142] By analogy, the very short mean free path of charge carriers in amorphous silicon and quantum dot photovoltaics also imposes a limitation on the thickness of the semiconductor layer. At the same time it is also desirable to reduce the semiconductor thickness without reducing device efficiency in order to reduce materials cost, increase the fabrication speed and reduce electrical losses.[64]

It is possible to increase light absorption without increasing the thickness of the photoactive layer using light trapping strategies including the use of optical spacers[66] and structures to scatter the incident light.[64, 143] An electrode-centric approach that is well suited to metal film electrodes, involves establishing a resonant microcavity to trap those wavelengths not efficiently absorbed by the photoactive layer in an optical cavity between the opaque electrode and a partially reflective front electrode.[144] Sergeant *et al.* have recently demonstrated this approach using a highly transparent tri-layer electrode comprising a 6 nm Ag film sandwiched between two ultra-thin molybdenum oxide layers.[65] Besides improving device geometry, metal oxide/metal/metal oxide multilayers significantly improve the far field transparency because the high refractive index metal oxides, between which the metal is sandwiched, induce multiple reflection reducing overall metal reflectivity.[145]

1.5.3.4 Plasmon-active structures in OPVs

Surface plasmons are collective oscillations of the conduction band electrons at the surface of a metal. In noble metals these resonances occur in the visible spectrum. Plasmon active noble metal nano-structures have been investigated for a plethora of applications ranging from molecular sensors to the treatment of cancer.[64] Plasmonic effects can be also exploited to concentrate the optical field in the photoactive layer using plasmon-active metal nano-structures,[146] or to increase the effective path length through the photoactive layer either using metal nano-structures as scattering elements, or by trapping the incident solar flux in surface plasmon polaritons at the photoactive layer - metal electrode interface.[147] In the latter approach the electrode surface must be suitably nano-structured so that the incident light is efficiently coupled into the plane of the electrode.[64] The most widely used plasmon-active metals are Au and Ag since they support surface plasmon resonances that couple strongly with light and are relatively stable towards oxidation. To date, plasmonics have been exploited in OPVs in two ways: *(i)* Incorporation of plasmon active metal nanoparticles with diameters < 100 nm either at the electrode interfaces[148,] or dispersed within the photoactive layer itself;[149] *(ii)* Utilisation of electrodes comprising networks of plasmon-active metal nanowires[147] or metal films patterned with arrays of apertures with sizes in the range 80-300 nm[150,151] or gratings[152] (see Figure 1.19). Due to the low thickness of the semiconducting layer in OPVs (< 200 nm), incorporating metal nanoparticles or nanowires into these devices greatly increases the risk of short-circuiting,[153] although in metal film electrodes with apertures or surface gratings this is not a concern. In the latter case the majority of studies have focused on the use of regular periodic structures,[154,155] and so modelling can be used to predict the structure – property relation as so identify optimised designs.[152,156] Conversely a random array of sub-wavelength apertures is more amenable to scaling than a periodic array, although such structures are inherently more difficult to model. Indeed, the possible plasmon activity in metal films with a high density of randomly arranged apertures becomes increasing complex as the film becomes optically thin (i.e. < 15 nm) since efficient coupling between surface plasmon polaritons on the front and back of the metal film can occur - due to the film thickness being smaller than the penetration depth of the surface plasmons - and there is significant ordinary transmission of light. These effects are in addition to coupling between adjacent apertures[157] and the effect of light concentration at aperture edges,[158] that are features of optically thick metal films with a random array of sub-wavelength apertures.

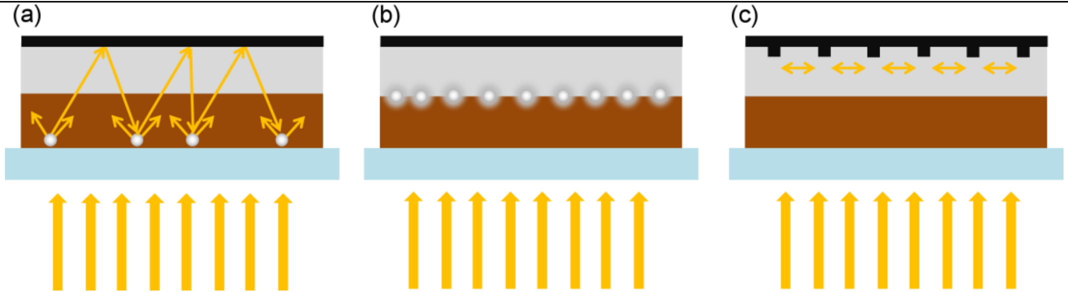

Figure 1.19: Strategies for plasmon enhanced light-trapping in OPVs; (a) plasmon-active metal nanoparticles at the electrode scatter light entering the cell increasing the path length; (b) plasmon-active metal nanoparticles distributed in the photoactive layer concentrate the light in localised surface plasmon resonances increases absorption in the semiconductor within ~10 nm of the nanoparticle surface; (c) an electrode with a surface grating interacts strongly with the incident light coupling it into surface plasmon polaritons which increase light absorption in the adjacent semiconductor layer.[64]

The first report of plasmon-active metal film electrodes in OPVs was by Reilly *et al.* who have shown that OPVs utilising an Ag metal electrode with a random arrangement of circular apertures outperform identical devices without apertures in the electrode.[150] In that work the Ag electrode was relatively thick (30 nm) and the random array of 92 nm diameter circular apertures was formed using nanosphere lithography. Whilst the relative improvement in performance was large, 1.03% to 1.22%, the absolute performance was at least a factor of three lower than achieved in the same device structure using a conventional ITO electrode. Reilly *et al.* have also shown that when using lithographic techniques to form apertures in a 40 nm Ag film the sheet resistance increases by 150% when 20% of the metal film is removed to make way for 92 nm diameter apertures,[159] which makes it difficult to realise a high number density of apertures in much thinner metal films with a higher transparency. A further disadvantage of microsphere lithography is the need to remove 100% of the microspheres prior to deposition of the organic semiconductor and top metal contact. It is therefore clear that for practical implementation this class of window electrode must be shown to perform as well as conducting oxide electrodes in efficient OPVs. For practical implementation, low-cost, scalable methodologies for the fabrication of optically thin metal electrodes with a high density of sub-wavelength apertures and low sheet resistance must also be forthcoming. In practice the sheet resistance must be $< 15\ \Omega\ \text{sq}^{-1}$ to be low enough for OPV applications.[160] Finally, to help guide the design of these electrodes it is necessary to determine whether the sub-wavelength apertures need to have a tight size and shape distribution for plasmon-mediated light concentration to be useful.

1.5.3.5 Thermal stability

For many applications it is also desirable that the electrode surface is structurally well-defined, which for metal films can be achieved by thermally annealing.[161] The ability to withstand elevated temperatures also greatly increases the number of potential applications. For example, for PV applications the processing temperatures can reach up to 500 °C.[162,163] Intuitively a single layer of organic molecules with a thickness less than 0.8 nm[137] would not be expected to be stable at high temperature, particularly above 350 °C, which is the temperature at which these molecules are known to desorb or degrade.[164,165] Encouragingly Wanunu *et al.* have shown that 15 nm Au films on (3-aminopropyl)-trimethoxysilane (APTMS) derivatised glass can be annealed at 200 °C for 20 hours to realise a smooth (111) textured surfaces with an average transparency across the visible spectrum of 32%.[166] Ghandi *et al.* reported that 50 nm copper films supported on (3-methoxypropyl)-trimethoxysilane (MPTMS) derivatised silicon substrates and capped with 150 nm Ta were remarkably resistant to fracture along even after annealing to 700 °C, which resulted in toughening of copper films.[167] Notably the thermal stability of optically thin (<10 nm) continuous noble metal films has not been reported.

1.6 Materials

1.6.1 Photoactive layer

The photoactive layer in OPVs comprises an electron donor and electron acceptor molecules arranged in a bilayer structure or an interpenetrating network: a BHJ (see Figure 1.20). The bilayer architecture is the oldest heterojunction OPV architecture and is used in OPVs employing small molecules characterised by exceptionally large L_D and α. The concept of BHJ partially addresses the exciton diffusion bottleneck in the bilayer architecture, since the photo-active layer thickness can be much greater than L_D in either the acceptor or donor materials. In a BHJ the active materials are mixed together forming a randomly distributed interpenetrating network of donor and acceptor phases, where the dimensions of each phase are comparable to L_D. In effect the surface area of the heterojunction is greatly increased as compared with the bilayer structure. The BHJ architecture is most common in OPV employing solution processed blends of conductive polymer and soluble fullerene, which spontaneously phase separate into domains when spin-cast. However it has also been successfully adapted to small molecule devices and can be formed either *via* thermal co-evaporation[11] or spin-casting.[13] In both cases the deposition process is typically followed by an annealing step which furthers phase separation and can be used to tune the domain size. The shortcoming of the BHJ architecture is the presence of isolated domains, which lead to charge trapping and recombination, reducing η_{cc}. Further improvement in photoactive layer architecture requires engineering controlled three-dimensional interpenetrating donor/acceptor network, e. g. through nanosphere lithography[168] or introducing nanorods.[169,170]

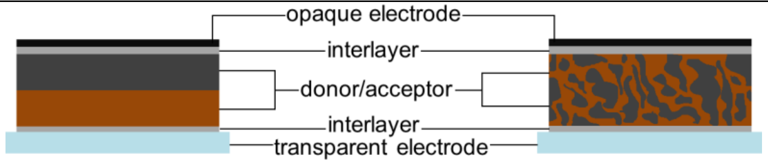

Figure 1.20: Schematics of an OPV device with a bilayer junction (left) and BHJ (b).

The chemical structures of photoactive material used in this work are depicted in Figure 1.21.

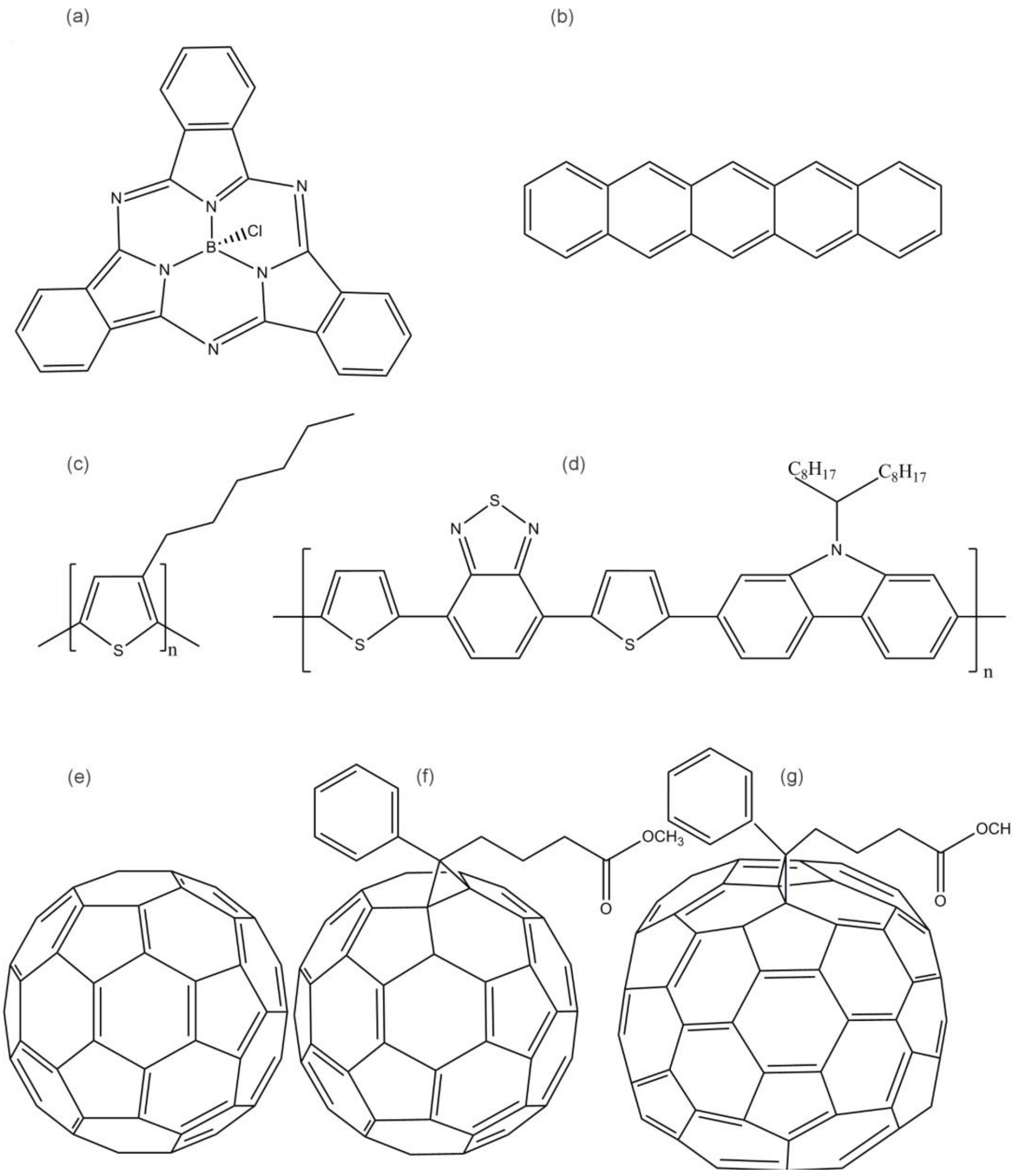

Figure 1.21: Chemical structures of the organic semiconductors used in the work reported in this thesis: (a) SubPc; (b) pentacene; (c) P3HT; (d) PCDTBT; (e) C_{60}; (f) PCBM; (g) $PC_{70}BM$.

1.6.1.1 Electron donors

Boron-subphthalocyanine chloride

Boron-subphthalocyanine chloride (SubPc) is a small molecule semiconductor consisting of 3 N-fused diiminoindole rings forming a 14 π-conjugated electron system with the isoindoline amine groups coordinating to a boron atom with a Cl substituent. This molecular semiconductor strongly absorbs light with an absorption coefficient over the wavelength range 500 – 650 nm exceeding 2×10^5 cm^{-1}.[171] However it also has a relatively low L_D of < 20 nm[172] and so in bilayer OPVs typically its thickness does not exceed 20 nm. It has a relatively large HOMO-LUMO gap and LUMO and HOMO energies of 3.6 eV and 5.6 eV below VL_s respectively. The large ionisation potential means that when used in combination with C_{60} as an electron acceptor a V_{oc} close to 1.1 V can be achieved.[83, 173]

Pentacene

Pentacene is a small molecule organic semiconductor consisting of 5 linearly fused benzene rings, which form 11 π-conjugated electrons. The higher number of conjugated electrons as compared with naphthalene and anthracene results in a red-shift in the absorption spectrum.[28] Pentacene has a broad absorption band in the 540 – 690 nm range ($\alpha > 10^5$ cm^{-1}) resulting from complex multiple transitions, the origins of which have been extensively studied.[174] The large L_D of pentacene (~ 65 nm),[73] allows for the use of thicker layers in bilayer OPV architectures (40 - 50 nm). The HOMO and LUMO energies of pentacene are 4.9 eV and 3.0 eV respectively. The relatively small ionisation potential means that OPV based on a C_{60} electron acceptor achieve a V_{oc} of only 0.4 V.[73, 175]

Poly(3-hexylthiophene)

Poly(3-hexylthiophene) (P3HT) is the most widely studied polymer used in OPVs and consists of long chains of repeating 3-hexylthiophene units. For OPV applications long[176,177] and highly ordered[178] polymer chains are most beneficial, since intra-molecular transport along kink free polymer chains is more efficient that intermolecular transport. The hole mobility in P3HT can reach $10^{-2}cm^{2}V^{-1}s^{-1}$,[179] although is usually lower in a BHJ due to scattering at the domain boundaries. The role of the hexyl chain is to improve the solubility of the polymer in organic solvents and promote crystallinity in the solid state. The maximum absorption of P3HT occurs in the range 450 – 600 nm ($\alpha > 10^{5}$ cm^{-1}) although in high regioregularity P3HT this can be red-shifted.[180] Regioregularity is a measure of chain asymmetry, describing the percentage of polymer units derived from the same monomer (Figure 1.22). Regioregularity plays a crucial role in the OPV performance as polymer chain twists and folding affect the π-conjugated system and so affect the η_{ct}. For OPV applications P3HT is typically processed from solution with either PCBM or $PC_{70}BM$ as electron acceptor in a 1:1 ratio. The two materials spontaneously phase-separate into nano-crystalline domains[181] with dimensions comparable to the exciton diffusion length in each material to realise a BHJ of 100 – 250 nm optimal thickness.[180, 182, 183] The choice of solvent and a post-deposition annealing step have a large effect on the formation of donor and acceptor domains of optimal dimensions.[182,183,184] P3HT has HOMO of 5.0 – 5.2 eV and LUMO of 3.0 eV to 3.3 eV below the VL_s which in devices with PCBM results in V_{oc} of ~ 0.65. [176, 180,185]

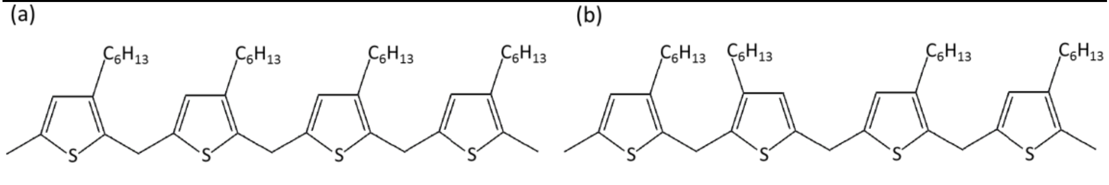

Figure 1.22: P3HT chain with: (a) 100 % regioregularity and (b) 75 % regioregularity.

Poly[N - 9' – heptadecanyl - 2, 7 – carbazole – alt - 5, 5 - (4', 7' – di – 2 – thienyl - 2',1',3' - benzothiadiazole)] (PCDTBT)

PCDTBT is a relatively new conjugated polymer, capable of delivering OPV efficiencies of 6 - 7%[186,15] and operating lifetime of 6 years when used as the electron donor.[187] The carbazol unit provides stiffer backbone than in P3HT improving intra-molecular hole transporting properties. On the other hand, PCDTBT has higher energetic disorder than P3HT[188] and the intermolecular transport is impeded by short range intermolecular interaction and abundance of hole trap states resulting from amorphous structure of the polymer.[16] With hole mobilities of $\sim 6 \times 10^{-5}\text{cm}^2\text{V}^{-1}\text{s}^{-1}$ [16] the optimal thickness of the polymer layer is reduced to ~ 70 nm in BHJ. PCDTBT has a broad absorption band with two peaks at 400 nm and 570 nm. In order to obtain pure material domains in the context of a BHJ, which are necessary for efficient exciton dissociation, PCDTBT is mixed with an excess of fullerene derivative,[189] which forms crystalline domains sufficient for effective exciton diffusion. PCDTBT has LUMO of 3.5 eV and HOMO of ~ 5.3 eV,[188] which, when employed in an OPV device with $PC_{70}BM$ results in a $V_{oc} > 0.85$ V.[15, 186]

1.6.1.2 Electron acceptors

C_{60}

C_{60} is a fullerene composed of 60 carbon atoms forming a spherical-shaped molecule composed of 12 pentagons and 20 hexagons. This large conjugated system in which, to a good approximation, all carbon atoms have sp^2 hybridisation is an excellent electron acceptor providing ultra-fast electron transfer from the photoexcited polymer and a long lifetime of the charge separated state.[190] Due to its high symmetry C_{60} absorbs visible light weakly ($\alpha > 10^5$ cm^{-1} only below 300 nm) and has wide absorption band extending from UV to 500 nm ($\alpha > 10^4$ cm^{-1})[191] and long L_D ~ 35 nm.[192] C_{60} has a HOMO of ~-6.1 eV and LUMO of -4.5 eV,[193] below VL_s, which makes it a suitable acceptor for many small molecule donor systems.

[6,6]-phenyl-C_{61}-butyric acid methyl ester (PCBM) and [6,6]-phenyl-C_{71}-butyric acid methyl ester ($PC_{70}BM$)

Since C_{60} is poorly soluble in most organic solvents, its functionalised derivative; [6,6]-phenyl C_{61} butyric acid methyl ester (PCBM) is the most commonly used fullerene electron acceptor in BHJ OPVs. PCBM has a similar absorption characteristic to C_{60}; a strong absorption band below 360 nm ($\alpha > 10^5$ cm^{-1}) tailing off towards 600 nm.[67] PCBM has a relatively high electron mobility of 10^{-2}cm^{2}V^{-1}s^{-1} and HOMO and LUMO energies of 6.2 eV and 3.7 eV below VL_s, respectively. [193, 194] PCBM in combination with P3HT is now widely regarded as the model efficient BHJ OPV system, which provided first efficient (~ 4.5%) OPVs.[195] In the research laboratory the mixture is most typically spin-cast from a 1,2-dichlorobenzene solution forming a well-defined nano-crystalline structure of pure P3HT and pure PCBM domains; their dimensions can be tuned *via* the processing conditions.

$PC_{70}BM$ is the analogous derivative of C_{70}. C_{70} contains 70 sp^2 hybridised carbon atoms which combined into 25 hexagons and 12 pentagons to form an elongated cage, much less symmetric than C_{60}. BHJ devices employing $PC_{70}BM$ show improved V_{oc} by ~ 0.03 V and J_{sc} by over 1 mAcm^{-2} as compared with PCBM.[196] $PC_{70}BM$ is a state-of-art electron acceptor used in most efficient OPVs (>6%), employing both polymer[186] and small molecule[197] donors.

1.6.2 Interfacial layers

Interlayers at the electrode/photoactive layer interfaces – are important parts of efficient OPV devices, which greatly improve the performance. They are typically 1-20 nm thick and wide band gap materials comprising metal oxides, polymers or small molecules. In addition to having electronic functionality they can be used as optical spacers in order to improve η_{abs} and barrier layers preventing interlayer atom/molecule diffusion to enhance OPV stability. However their main role is to improve charge carrier collection and selectivity (i.e. extraction of only one carrier type) by the electrodes. When spontaneous ground state charge transfer is possible at the electrode – interlayer and organic semiconductor - interlayer interfaces the E_F of the electrode and interfacial layer are aligned and pinned near to the relevant frontier orbital in the organic semiconductor,[35, 198] improving charge transport across the interface. The interlayers can also block exciton recombination at the electrode and give flexibility in device design enabling the realisation of inverted device architectures, in which the substrate electrode operates as the low work function electrode and the top metal electrode can also be a relatively low work function metal (Figure 1.23).

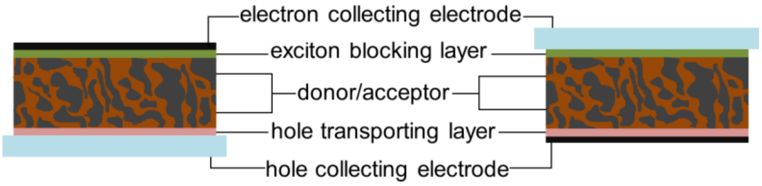

Figure 1.23: ‘Standard’ and inverted OPV architecture. The transparent electrode can be used as an anode or as a cathode depending on the choice of the interfacial layer.

Poly(3,4-ethylenedioxythiophene) doped poly(4-styrenosulfonate) (PEDOT:PSS)

The structures of PEDOT and PSS are shown in Figure 1.24. PEDOT is one of the most successful conjugated polymers to be used commercially, exhibiting exceptionally high stability in the doped state combined with very high electrical conductivity (0.1-10^2 Sm^{-1}). However PEDOT is insoluble and for processing purposes it is normally mixed with insulating PSS, with which it forms a stable dispersion in water. PEDOT:PSS dispersion is typically spin-cast or spray-deposited and is widely used as hole conductor in OPVs[106] and also as an electrode in its own right.[111] The thickness of PEDOT:PSS films used in OPVs is typically a few tens of nm which ensures the film has high transparency (>90%). PEDOT:PSS has a high ϕ ~5.2 eV[104,199] and an abundance of deprotonated sulfonyl groups for selective hole transport.

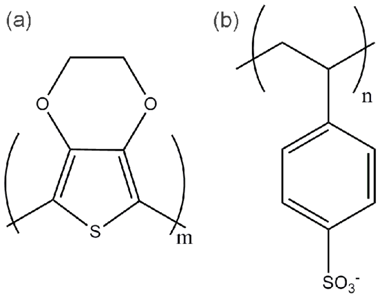

Figure 1.24: Chemical structures of PSS (a) and PEDOT (b).

Metal oxides

Transition metal oxides are an important class of interfacial layers, particularly oxides of Mo, W and Ti, all of which are used in this thesis. Oxides of Mo and W can be deposited either from solution[200,201,202] or by thermal evaporation[203,204] allowing thickness tuning and making them particularly versatile. Conversely, PEDOT:PSS can only be deposited easily onto hydrophilic surfaces, otherwise the fabrication process gains extra complexity with surface pre-treatment steps. No such restrictions applied for evaporated oxide films. Mo, W and Ti oxides are nearly 100% transparent above 400 nm;[205] moreover they can significantly reduce the reflectivity of metal films[145] which make them suitable as an interlayer at the organic semiconductor - transparent electrode interface. The wide band gap also helps to prevent exciton quenching by the electrode; MoO_x ~ 3.0 eV,[206,207] WO_x ~ 3.2 eV,[204,208] TiO_x ~ 3.2 eV.[207] Metal oxides can be *p*-type or *n*-type and so can be successfully used as either hole or electron transport layers.

The properties of metal oxides depend on the oxide stoichiometry,[209] particularly WO_x which only becomes electrically conductive when the metal to oxide ratio increases beyond a certain point. The stoichiometry of evaporated films varies for WO_3 and MoO_3 especially as the amount of oxygen is reduced e. g. during pre-heating for thermal evaporation. This phenomenon is very well pronounced in tungsten oxide which has a pale-blue colour that changes to black after annealing due to formation of trap states. The defects and trap sites result from the oxygen reduction and are desired since they improve charge transport,[210] so the OPV efficiency is quite high even for thicker buffer layers.

MoO_x is the most widely studied metal oxide interlayer in OPV. This high work function material is strongly *n*-type due to electron rich Mo(V) atoms / oxygen array vacancies, which act as electron donors.[198] When MoO_x is deposited onto ITO or Au (Figure 1.25) electron transfer from the electrode to the C_B of the oxide induces a very large positive vacuum level shift aligning the electrode E_f with the Fermi level in the MoO_x. The same process occurs at the organic semiconductor, resulting in pinning of the HOMO of the organic semiconductor near to the defect band and the C_B of MoO_x.[198, 210] As a result the electrode E_f is closely aligned to the HOMO of the organic semiconductor and charge transport across the oxide is mediated by the C_B and/or the defect band in the oxide.

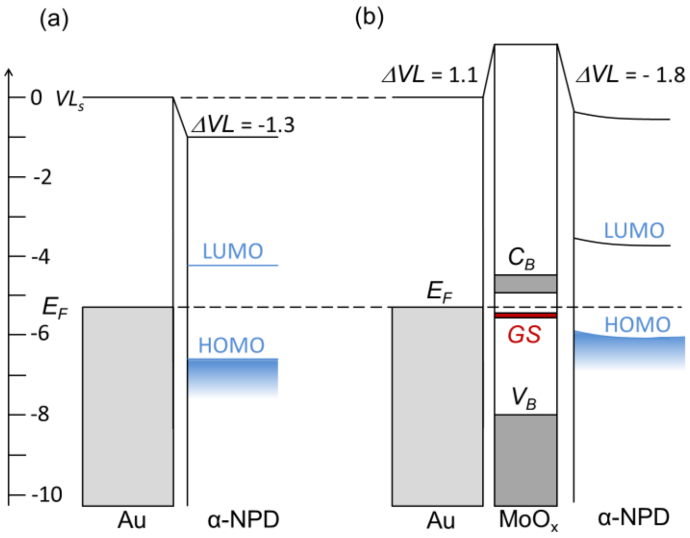

Figure 1.25: Schematic energy level alignment of the Au/ *N,N'* – di[(1-naphthyl)-*N,N'*-diphenyl]-*1,1'*-biphenyl-4 ,4'-diamine (α-NPD) and Au/MoO_x/α-NPD junction (based on Kroeger *et al.* Kanai *et al.*).[198,210]

Bathocuproine

Bathocuproine (BCP) - 2,9-dimethyl-4,7-diphenyl-1,10-phenantroline (Figure 1.26) is widely used in conjunction with an Al electron-extracting electrode in OPVs. It has a wide band gap of ~ 3.5 eV with a LUMO energy of -3.5 eV below the VL_S,[211,212] which prevents exciton quenching by the Al electrode. BCP is typically used in standard OPV device architecture where the BCP layer is deposited by evaporation with thickness of 8 - 10 nm followed by evaporation of the top metal electrode. The BCP layer protects the photoactive layer from the damaging impact of the evaporated Al and increases the built-in potential by helping to align the electrode E_F with the LUMO of the electron acceptor, which results in higher V_{oc} in OPVs.[213] The evaporation of the Al layer plays also an important role in rendering BCP conductive towards electron transport by introducing defect states which allow efficient charge transport across the otherwise strongly insulating layer.[212]

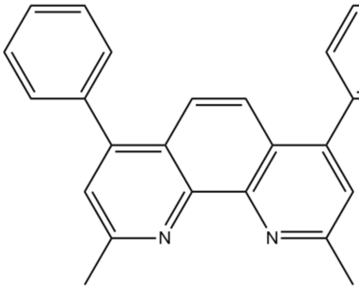

Figure 1.26: Chemical structure of BCP.

1.6.3 Opaque electrodes

The top electrode in an OPV is typically a relatively thick (50-150 nm) layer of Ag or Al. The ϕ of Ag and Al are 4.3 eV - 4.7 eV[214] and ~4.3 eV[215] respectively and so in architectures with interlayers such as LiF, BCP (in the case of the cathode) or MoO_3, WO_3 (in the case of the anode) they can be successfully used as either the anode or cathode. Al is usually the electron-extracting electrode material of choice, due to its relatively low cost, low evaporation temperature and reduced risk of organic layer damage by light atoms compared to Ag. In the standard architecture the Al electrode is typically evaporated onto a BCP layer, although a 10 nm Ca electrode capped with a thick Ag layer without any interfacial layer is sometimes used. Ca is a metal of small atomic weight, so at low rates it can be evaporated directly onto organic material without the risk of penetrating into the organic layer too much. Ca has a very low ϕ of ~ 2.9 eV, which makes it a suitable material for the cathode.

Indeed it can be also used as an interfacial layer to render a high ϕ electrode material suitable as an electron extracting electrode: an optically thin (~ 0.5 nm) Ca can be evaporated onto ITO which may then act as a cathode in inverted OPV architecture.[216] Despite this advantages Ca is not used very often because it is prone to oxidation and difficult to handle due to its high reactivity.

1.7. PV generations

The PV effect was discovered by Becquerel in 1839, who measured a photocurrent across platinum electrodes coated with AgBr/AgCl in aqueous solution upon illumination. However, it wasn't until the 1950's that PVs become extensively studied, when the first crystalline silicon PV device was developed at Bell Laboratories.[217] The first generation of commercial PVs was based on single crystalline silicon grown by the Czochralski method. This was followed in the 1980s by technology for polycrystalline cells fabricated by die-casting.[22] In both cases the thicker and lightly doped *p*-type layer is diffusively doped with phosphorus forming a thin *n*-type region; as the E_F of *p*- and *n*- doped regions align a space charge region is formed at the junction. Free charge carriers generated drift towards the edge of the depletion region and then diffuse across the neutral region to the electrodes. In crystalline silicon PVs only ~30% of the solar irradiance is harvested, resulting in a maximum achievable power conversion efficiency of ~ 25%;[22] this efficiency was achieved in Sandia Test Centre in 1999.[218]

Since Si is an indirect band gap semiconductor across most of the visible spectrum (direct bandgap at 3.4 eV)[219] it does not absorb the solar spectrum efficiently, particularly at longer wavelength. The large thickness of crystalline Si required for crystalline Si PVs increases their cost and has triggered a technology race to find lower cost PV technologies. This has led to the development of second generation PVs which use much thinner semiconductor layers to harvest the incident light. The Si thickness in second generation PV has been reduced to ~ 10 microns, since amorphous silicon has a direct band gap of 1.4-1.6 eV. Second generation PV can also be made from non-silicon semiconductors such as cadmium telluride which has a band gap of 1.44 eV and is often used in conjunction with sulphur telluride which has a 2.4 eV band gap to form *p-n* junction PV only few µm thickness.[22] Other materials used in second generation PVs include various compounds of rare elements from groups III and V in the periodic table, with gallium arsenide and indium phosphide being two of the most well-known. These PVs can be tailored by choice of materials with different absorption regions to maximise the photocurrent and power conversion efficiency up to nearly 30%.[218] This can be further enhanced to 30 – 40% as multi-junction PV are build, employing as many as 30 individual semiconductor layers. [218, 220]

The principle of operation of third generation PVs differs from the previous two generations which are based on a *p-n* junction: In the third generation PV a tightly bound exciton is generated upon light absorption in the photoactive layer which can only be dissociated into free charge carriers at an abrupt hetero-interface, hence this class of PVs are called excitonic PVs. Third generation PVs were developed to find an even lower cost alternative to second generation PV by employing conjugated organic molecules or polymers instead of inorganic semiconductors to harvest light. Excitonic PVs can be divided into two main categories; dye-sensitized solar cells (DSSC) and OPVs. The DSSC was first reported in the 1980s and soon after cell efficiencies of 8% were reached.[221] DSSCs consist of two electrodes, one of which comprises a mesoporous inorganic semiconductor, typically TiO_2 (Figure 1.27 (c)). The latter is usually sintered onto a conducting oxide electrode and impregnated with a monolayer of organic dye; the space between these electrodes is filled with an electrolyte to facilitate charge transport. The organic monolayer can be designed to achieve very broad band absorption by using mixtures of co-adsorbed dyes with complimentary absorption[222] or dyes with an exceptionally wide absorption band (e.g. the black dye[223]) to boost cell efficiency to 11%.[224] Since the dyes used can be derived from natural pigments, DSSCs promise a green and cheap energy source. The best efficiencies of DSSCs have remained around 10 – 11%,[218] for two decades although this is sufficient for them to be commercialised.

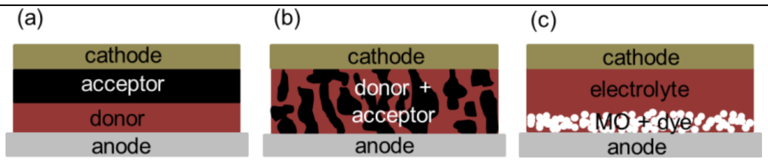

Figure 1.27: A schematic illustration of different OPV architectures; (a) a flat bilayer heterojunction; (b) a bulk heterojunction (c) Dye-Sensitized Solar Cell (DSSC).

Another emerging group of third generation PVs, which is related to the DSSC is the hybrid PV, which comprises an organic photoactive *p*-type material forming a heterojunction with an *n*-type semiconductor. However the efficiencies of such hybrid structures is still very low (<1%).[225]

1.8 OPV history

Whilst photoconductivity in organic molecules was reported by Pochettino as early as 1906 the first OPVs were not fabricated until the late 1950s. Early OPVs were based on *p*-type molecular organic layers (usually phthalocyanines[226] or polyacenes[227]) sandwiched between two electrodes and exhibited very low efficiency. In these early OPVs exciton dissociation occurs at a Schottky-contact which forms at the interface between the organic semiconductor and a low ϕ electrode although the separation efficiency was very low (< 0.1%). Vacuum deposition of molecular materials was an important technological advance and rapidly became a popular method of fabricating OPVs.[228,229] Many years of investigation have shown that the efficiency of OPVs employing only one type of organic semiconductor is low because they rely on the built-in electric field to dissociate the excitons formed in the organic semiconductor. Excitons in organic semiconductors are particularly tightly bound and so inherently difficult to dissociate into free charge carriers. As a result it is not possible to achieve built-in electric field strengths large enough to efficiently dissociate excitons. An important advance, which dramatically boosted the efficiency of Schottky OPV, was the introduction of a thin interfacial oxide layer on the low work function metal surface which provided improved energy level alignment and selective carrier extraction, which resulted in an improvement in V_{oc} and overall device performance.[230]

In 1986 Tang reported the first OPV based on a heterojunction between electron donor and electron acceptor type molecules, which were arranged in a bilayer structure. The heterojunction comprised copper phthalocyanine as the electron donor and 3,4,9,10-perylenetetracarboxylic bis-benzimidazole as the electron acceptor and achieved a power conversion efficiency of 0.95% under 1 sun irradiance.[231] This was a major advance in OPV performance since free charge carriers were generated at the organic/organic interface independent of the built-in electric field strength, which resulted in a large enhancement in *FF* and efficiency.

Another important advance in the development in OPVs came soon after the discovery of C_{60} in 1985.[232] Thermally evaporated layers of C_{60} are employed in bilayer OPVs as the electron acceptor in conjunction with electron donors such anthracenes and oligothiophenes. Sariciftci *et al.* reported that in blends of C_{60} and conjugated polymers dissociation of excitons formed in the polymer phase upon absorption of light is extremely efficient in comparison to single component systems. This is due to ultra-fast electron transfer from the photo-excited polymer to the C_{60} and the long lifetime of the charge separated state.[190] Since Sariciftci *et al.* reported this phenomenon in 1992[233] the field of polymer-fullerene blend science has rapidly advanced and led to the development of the BHJ device architecture, which was another crucial point in OPV development. The first reported BHJ was based on a co-evaporated mixture of *n*-type perylene tetracarboxylic derivative acceptor and *p*-type metal free phthalocyanine donor.[234] In 1995 a solution processed blend of poly[2-methoxy-5-(2-ethylhexyloxy)-phenylenevinylene] and PCBM was also used as the basis for a BHJ.[235] In the latter case the donor and acceptor phases spontaneously phase separate into nano-scale domains of polymer and PCBM, which was the starting point for the development of today's high efficiency BHJ OPVs.[67] The state-of-the-art in the field of OPVs is currently represented by bulk heterojunction OPVs based on P3HT, PCDTBT and the fullerenes PCBM and $PC_{70}BM$.[236]

Whilst organic semiconductors for OPVs have been intensively investigated over the past two decades, relatively little research attention has focused on the transparent electrodes used in OPV. ITO was first used in Si solar cells[237] and adopted as the transparent anode material for OPVs, due to its high transparency, low sheet resistance and high ϕ. However, it is unsuitable for OPVs primarily owing to the high cost of indium and its incompatibility with low cost flexible substrates.

Chapter 2.

Experimental techniques

Summary

This chapter is divided into three sections. In the first section methods of fabricating ultra-thin metal films on glass and flexible substrates are described, followed by the second part which focuses on OPV fabrication and testing. The third part describes the different techniques used to characterise thin metal films.

2.1 Ultra-thin metal film fabrication

2.1.1 Substrates

Thin metal films were prepared on three different substrates: (1) 1.2 mm thick glass microscope slides (Menzel-Gläser); (2) 100 µm thick polyethylene terephthalate (PET) - Hostaphan GN 4600 (Mitsubishi Polyester Film GMBH); (3) and 125 µm thick polyethylene naphthalate (PEN) - Teonex® (DuPont Teijin Films UK Ltd). It is important that substrates supporting transparent electrodes for OPV applications don’t absorb light themselves in the 350-1100 nm wavelength range, since it is this wavelength range that is harvested by the photoactive layer. The transparency of the glass and plastic substrates used in this thesis is shown in Figure 2.1. Glass has the highest transparency at ~ 90% above 300 nm. The remaining 10% is reflected. PET and PEN are ~ 5% less transparent than glass at wavelengths > 500 nm and absorb strongly below 350 nm and 400 nm respectively, blocking highly energetic UV radiation. This is an advantage for OPVs since UV-photons can have a detrimental effect on OPV lifetime.[238]

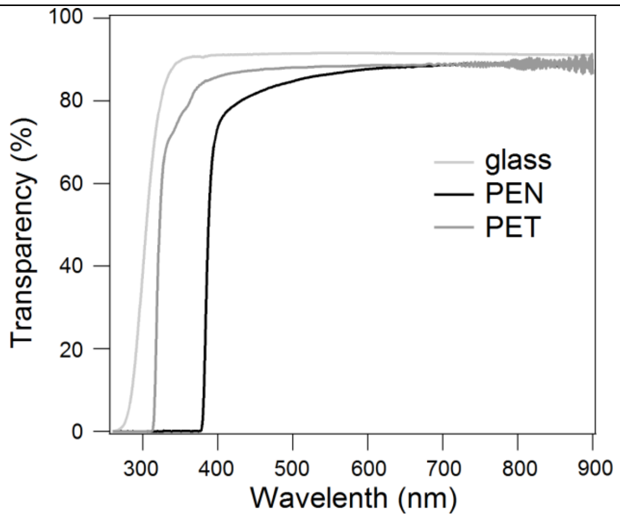

Figure 2.1: The far-field transparency spectra of substrates used to support the thin metal films described in this thesis.

Due to the low thickness of the semiconductor layer in OPVs (70-200 nm) an important property, which has to be taken into consideration when choosing substrates, is the surface roughness. In this thesis the metal films have a thickness of 5-12 nm and so the roughness of the underlying substrate needs to be very low to avoid variations in metal distribution and/or discontinuities in the film which adversely affect both the transparency and conductivity. Throughout this thesis, unless otherwise stated, the surface roughness is described in terms of the root mean square roughness R_{rms} over a 5 × 5 µm sample area as measured using atomic force microscopy (AFM) (section 2.3.1.) For glass the R_{rms} is ~ 0.4 nm, while for PET and PEN it is almost twice as high at ~ 1.0 nm. PET substrates with roughness exceeding 6 nm were found to be unsuitable, resulting in poor metal film quality in terms of both sheet resistance and transparency.

Pre-patterned ITO coated glass with a sheet resistance of 15 Ω sq^{-1} was purchased from Psiotech Ltd. ITO coated PET with a sheet resistivity 45 Ω sq^{-1} was purchased from Aldrich.

2.1.2 Substrate cleaning

ITO coated glass substrates were received with a protective photo-resist layer which was removed by rinsing with acetone. Unless stated otherwise, the following cleaning procedure was applied to all transparent substrates, including ITO coated glass and those substrates used for metal electrode fabrication:

(i) Rinsing in deionised water;

(ii) Ultra-sonic agitation in dilute Decon Neutracon solution in deionised water for 15 minutes;

(iii) Rinsing in deionised water;

(iv) Rinsing in isopropyl alcohol;

(v) Ultra-sonic agitation in isopropyl alcohol for 15 minutes;

(vi) 10 seconds exposure to hot acetone vapour.

Solvents were purchased from Fisher Scientific. With the exception of the acetone, which was analytical grade, all other solvents were HPLC grade purity. Water was either purchased from Fisher Chemicals or purified with using a Purite Select HP purifier. After the wet cleaning process, the substrates were UV/O_3 treated.

2.1.3 UV/O_3 treatment

UV/O_3 treatment was performed using a Novascan PSD-UVT. In this instrument substrates are exposed to UV light from a Hg lamp (185 nm and 254 nm, 20 mW/cm^2) at a distance of 25 mm from the substrate in a sealed air-filled chamber. Photons with a wavelength of 185 nm are absorbed by atmospheric oxygen which forms O_3. 254 nm wavelength photons are absorbed by both O_3 and hydrocarbons resulting in their decomposition. The atomic oxygen formed as a result of O_3 decomposition is a very reactive species and is the main oxidising agent.[239] UV/O_3 treatment improves substrate surface wettability by increasing the surface energy and removes carbon residues.[240] However in this study it was also used as a means of introducing bound hydroxyl and other reactive oxygen containing species onto the surface of glass and plastic substrate surfaces.[239, 241,242] For this reason the time of exposure to UV/O_3 varied depending on its use: 5 minutes for ITO on glass and plastic substrates; 15 minutes for glass substrates; and 5 minutes or less minutes for flexible substrates. The treatment was followed by a 15 min dark period, during which time the O_3 levels fall away.

2.1.4 Oxygen Plasma treatment

Plasma treatment was performed using a Plasma Asher EMITECH K1050X. This treatment involves exposure of the sample to an oxygen plasma generated by radio frequency irradiation of O_2. The high frequency radiation strips electrons from the O_2 molecules generating electrons and ions which can react to form O_3 and a variety of excited species such as O_2^-, O_2^+, O^+ and O with strongly oxidative properties.[243] Similar to UV/O_3 treatment, plasma etching is a very efficient method of removing hydrocarbon contamination, increasing wettability and introducing hydroxyl groups onto the surface.[244] This method is however much more intrusive due to the flux of reactive species as compared to UV/O_3. Even very short exposure results in significant modification of the surface structure and morphology.[93] For this reason plasma-ashing was used only in the context of the work described in Chapter 3, where micron-sized polystyrene spheres distributed on a substrate were shrunk in size by plasma oxidising the outer polymer layers.

2.1.5 Monolayer deposition

Glass and plastic substrates were derivatised with a monolayer of thiol and/or amine functionalised tri-methoxysilanes prior to metal deposition. Methoxysilanes bind strongly to native hydroxyl groups at solid surfaces,[135, 137] whilst thiols and primary amines have a high affinity for coinage metals. These monolayers therefore improve metal-substrate adhesion and increase the number of nucleation centres thereby reducing the metal island coalescence threshold.[133, 137, 138]

After oxidative treatment the substrates were immediately transferred to a dessicator, where they were exposed to the vapour of (3-aminopropyl)-trimethoxysilane (APTMS), (3-methoxypropyl)-trimethoxysilane (MPTMS) or APTMS:MPTMS under reduced pressure (see Figure 2.2): A few drops of liquid molecular adhesive were placed in the vial in the vicinity of the substrates. The substrates and the vial were placed in a beaker, in a dessicator and pumped down. The time of exposure and background pressure were used to tune the monolayer density as described in chapter 6. After monolayer deposition substrates were immediately transferred to the N_2-filled glovebox for metal deposition by thermal evaporation.

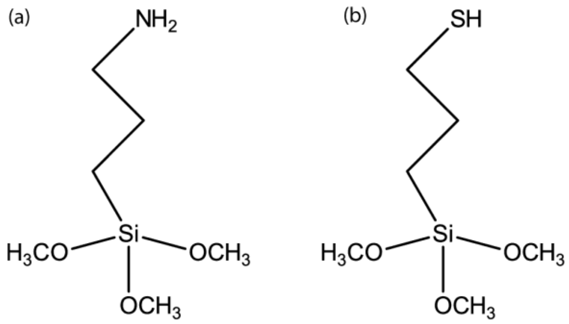

Figure 2.2: The chemical structures of APTMS (a) and MPTMS (b).

2.1.6 Thin film fabrication

2.1.6.1 Vacuum deposition system

The Mbraun evaporation system was used to deposit metal electrodes and small molecule organic semiconductors with low solubility. The evaporation system was situated in a N_2 filled glove box with H_2O and O_2 levels remaining below 1 ppm. An electro-pneumatic controlled bell-jar forms the vacuum chamber in the lowered position, while in the lifted position it allows access to the evaporation sources and materials. A two stage pump system is used to achieve and maintain high vacuum. In the first stage rough vacuum is achieved with a backing pump. When a pressure of 0.1 mbar is achieved a turbo-molecular pump reduces the pressure further to a working pressure of ~ 4 10^{-6} mbar. The evaporation unit is shown in Figure 2.3. It consists of two thermal sources (for metal/metal oxide deposition) and two organic sources. The evaporation sources are equipped with shutters which are closed when the sources are not in use. The rotating sample holder helps to ensure homogeneous material deposition. The sample is obscured from the sources by a shutter, opened only for material deposition. The deposition rate may have a major impact on the structure/properties of the deposited films and so the sample shutter allows optimisation of the material flux before it is deposited onto the substrates. The thickness of evaporated films is monitored by two quartz crystal microbalance (QCM), placed next to the sample holder (although not obscured by the shutter). The SQM monitoring unit was used to control the metal deposition rate and a Creaphys Controller with Eurotherm temperature monitoring was used to control the small molecule deposition rate.

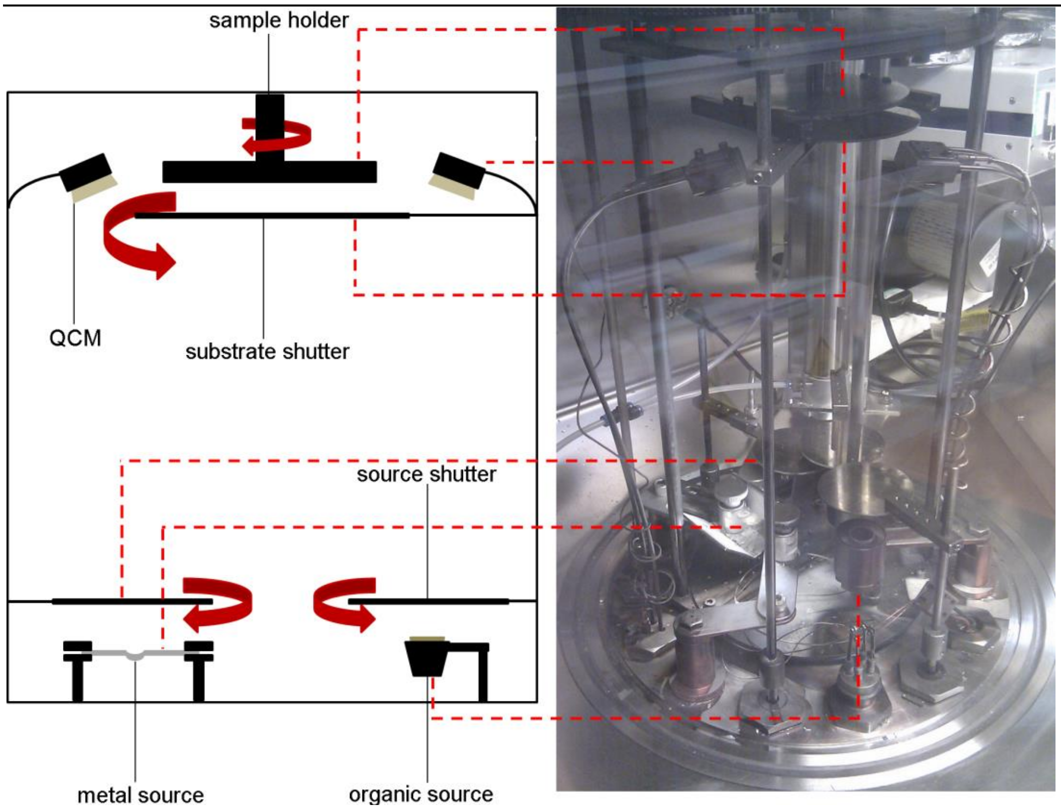

Figure 2.3: A schematic diagram (left) and a photograph (right) of the evaporation unit; red dotted lines indicate respective parts.

2.1.6.2 Film thickness measurement – Quartz crystal microbalance (QCM)

The thickness of deposited materials was controlled with sub-nm accuracy using a quartz crystal microbalance (QCM). QCM is a highly sensitive technique enabling in-situ thickness measurement in real time. An oscillating electric field is applied to a thin quartz crystal *via* Au electrodes inducing an acoustic wave propagating perpendicular to the crystal surface.[245] Changes in oscillation frequency occur when mass is accumulated on the crystal surface as shown by Sauerbrey *et al.,*[246] from which the thickness of material deposited can be determined, provided the density and shear modulus of the deposited material are known. The evaporated material is incident simultaneously on the sample and QCM, which is positioned at the same height, allowing detection of very small change in deposition rate and thickness. In case of thin films, particularly of new organic materials required physical properties are often unknown and an ex-situ thickness calibration is necessary. It also helps to reduce the measurement errors arising from distance between the sample and QCM sensor.

2.1.6.3 Film thickness measurement: Tooling factor determination

An accurate method of determining the tooling factor for the QCM is step edge analysis performed using tapping mode AFM (Figure 2.4): The film of the investigated material is evaporated onto a hard substrate with sub-nm surface roughness and the thickness precisely measured using a QCM (usually 20 – 40 nm) located next to the substrate. Then the film is partially removed by scoring with a sharp needle forming a well-defined edge. An AFM image of the step edge can then be used to determine the actual thickness of the film. This is most precisely determined from a statistical height distribution (2.4 (b)), because it averages across the investigated area. However some materials may pile up at the edges of the score while being removed, which results in more complex height distribution spectrum and/or wider peaks. In this case the cross-section method is more reliable and the film thickness is calculated from the difference between the flat areas in the step profile such as that in Figure 2.4 (c). The ratio of thickness measured by the QCM to that determined from AFM step edge analysis is then used in QCM operating software as a tooling factor.

This method is also used to determine the thickness of thin film deposited from solution.

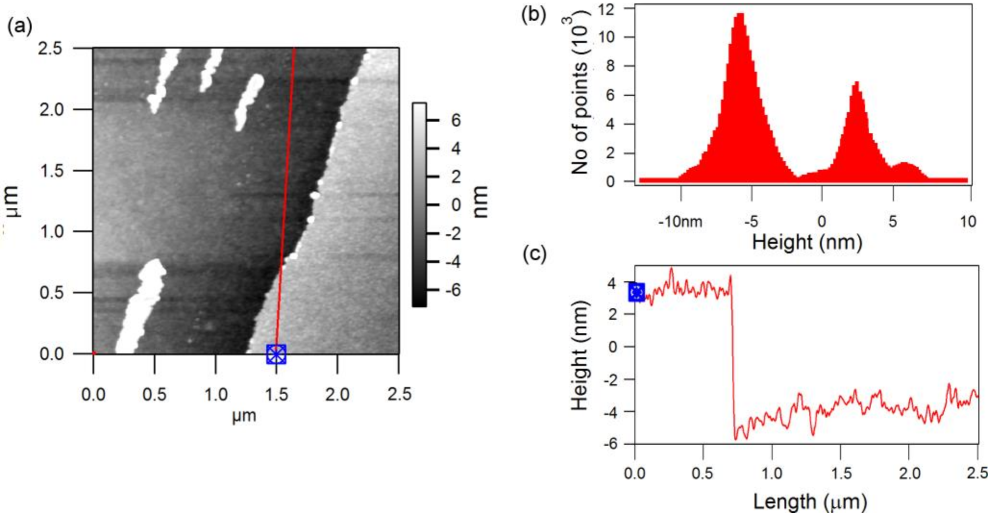

Figure 2.4: (a) Step edge AFM image of an Au film (b) statistical height distribution analysis and c) cross-section height.

2.1.6.4 Metal deposition

Metal electrodes were evaporated onto glass, PET and PEN substrates derivatised with molecular adhesive layers. Au, Ag, Cu (K J Lesker, 99.99%) were deposited at a rate of 0.1 nm s^{-1} from tungsten evaporation boats (Testbourne Ltd.). For bi-layer electrodes the metal layers were deposited one after the other without breaking the vacuum.

2.2 Device fabrication and testing

2.2.1 Thermal evaporation of molecular semiconductors

Thermal evaporation is a deposition technique used to grow thin films of small molecule organic semiconductors, many of which sublime in high vacuum.[247,248] This method is particularly convenient for thermally stable materials with low solubility, such as the phthalocyanines and acenes and allows precise control over layer thickness.

Materials were deposited from resistively heated boron nitride crucibles (Testbourne Ltd.) which can be heated in the range 30 °C – 450 °C. Prior to crucible filling the empty crucible was placed in the evaporation source and gradually annealed to 400 °C for outgassing and removing impurities. The purified material was then placed in the crucible and the outgassing process repeated up to a temperature just below the material sublimation/evaporation temperature. To reach the desired deposition rate the temperature is controlled using a thermocouple and, after achieving a stable flux at desired rate, the sample shutter was opened. The deposition temperatures and rates for different materials are given in Table 2.1.

Table 2.1. Material sublimation temperatures and rates.

Material	Temperature (°C)	Rate (nm s^{-1})
BCP	140 -150	0.05 – 0.1
C_{60}	380 - 450	0.01 – 0.04
ClAlPc	370 - 390	0.1
CuPc	400 – 420	0.1
pentacene	180 - 200	0.01
PTCDA	300 - 320	0.1
SubPc	180 - 210	0.2

2.2.2 Deposition of metal oxides

Metal oxides (WO_x, MoO_x) were deposited from metal sources (Figure 2.3). WO_x was deposited from a resistively heated tungsten boat (Testbourne Ltd.), while MoO_x was deposited from a boron nitride crucible metal holder-boat (Testbourne Ltd.), due to turbulent outgassing when heated. Both metal oxides were outgassed just below the sublimation temperature prior to deposition and deposited at relatively low rates: MoO_x 0.02 – 0.03 nm s^{-1}; WO_x 0.01 nms^{-1}.

2.2.3 Spin-casting

Spin-casting is a convenient method for the deposition of thin films of organic semiconductors from solution over small areas. It is particularly well established for the deposition of bulk heterojunction thin films, like poly(3-hexylthiophene) : [6,6]-phenyl C_{61} butyric acid methyl ester (P3HT:PCBM) on a laboratory scale. However, this method is not amenable to scaling-up where it must be replaced by spray coating, or screen printing. Spin-casting can be used for any material which forms a concentrated solution in a suitable solvent and in this work was used to obtain thin films of the polymer blends P3HT:PCBM, PCDTBT:$PC_{70}BM$, PEDOT:PSS and the metal oxides; TiO_x and MoO_x from solution. A substrate on which the thin film is to be formed is placed on a rotating stage, equipped with vacuum suction to hold the substrate in place. The substrate surface may be completely covered with material solution before rotation starts, or dropped on once the sample is spinning. The deposition of a single very small drop whilst the sample is already moving allows fabricating of very thin films without aggregations and is particularly suitable when using very volatile solvents. However this method makes uniform coverage of larger samples more difficult. The choice of solvent, concentration and the spinning speed are important parameters in controlling films thickness and crystallinity. For metal oxides higher spin speeds are used to realise very smooth surfaces. For examples the R_{rms} roughness of TiO_x films is ~ 0.5 nm when spun at 2000 r.p.m. If a greater thickness is needed, a more concentrated solution can be used. In the case of P3HT:PCBM and $PCDTBT:PC_{70}BM$ BHJ films the drying process controls the formation of donor and acceptor domains which adds complexity to the optimisation process.[249]

2.2.4 Device structure

As described in Chapter 1 the basic structure of an OPV is an anode, cathode and photoactive organic semiconductor layer - either a bilayer or BHJ - sandwiched between them. An electron (or hole) blocking layer and exciton blocking layer may also be incorporated at the photoactive layer/electrode interfaces. These additional layers are usually included in the most efficient devices. To show the versatility of ultra-thin metal films as window electrodes in OPVs they were incorporated into a range of devices with different architectures. The processing of the materials used is described in the following sections.

2.2.4.1 Hole transporting / Electron blocking layer

The hole extraction layer PEDOT:PSS (Sigma-Aldrich) was filtered using an 0.4 µm syringe filter to remove aggregates and spin-cast at 6000 revolutions per minute (r.p.m.) for 60 seconds followed by annealing at 110 °C for 10 minutes in air.

The interfacial layer perylene-3,4,9,10-tetracarboxylic-3,4,9,10-dianhydride (PTCDA - Sigma-Aldrich, 97%), typically used at thickness of 1 nm, was thermally deposited at temperature of 300 – 320 °C.

The transition metal oxides MoO_x and WO_x (both 99.99% purity from Sigma-Aldrich) were thermally evaporated to form layers of thickness 5 nm and 7.5 nm respectively unless otherwise stated. Alternatively 1M solution of MoO_x powder in 30% H_2O_2 was refluxed for 2 hours and cooled to room temperature for 24 hours in air.[200] Such mixture could be stored up to a week and was spin-cast at 3000 r.p.m. for 60 s and annealed at 350 °C for 30 minutes.

2.2.4.2 Photoactive layer

Bulk heterojunction (BHJ)

P3HT (Rieke Metals) and PCBM (Solenne) were combined in a 1:1 ratio at a concentration of 20 mg ml^{-1} each in anhydrous 1,2-dichlorobenzene. The blend was stirred for two days at 40 °C before filtering through a 0.2 µm polytetrafluoroethylene filter. P3HT:PCBM BHJ films were spin-cast at 600 r.p.m. for 2 minutes and allowed to dry at room temperature under nitrogen for 40 minutes, before annealing at 120 °C for 20 minutes to drive off residual solvent and promote further phase separation.

PCDTBT (Ossila Ltd.) and $PC_{70}BM$ (Ossila Ltd.) were combined in a 1:3 ratio at a concentration 16 mg ml^{-1} in anhydrous chloroform. The blend was stirred for 1 hour at 65 °C before filtering using a 0.45 µm polytetrafluoroethylene filter. $PCDTBT:PC_{70}BM$ films were spin-cast at 6000 r.p.m. for 60 seconds and annealed at 80 °C for 30 minutes.

Solution preparation and spin-casting was processed under N_2 atmosphere in the glovebox containing evaporation unit.

Bilayer OPVs

In bilayer OPVs two types of small molecule electron donors were used: SubPc (Sigma Aldrich, 85%) and pentacene (H. W. Sands, 99.99%) with film thicknesses of 14 nm and 40 nm respectively unless stated otherwise. Pentacene was supplied with very high purity, having been triply sublimed by the supplier, and SubPc was purified once by gradient thermal sublimation prior to evaporation. Gradient thermal sublimation involves heating the material to be purified to its sublimation temperature at the end of long glass tube with a temperature gradient along its length under reduced pressure (~10^{-5} mbar). The material to be purified is at the hottest end of the tube. The temperature gradient causes the material and impurities to condense at different places along the tube provided they have different sublimation temperatures.

C_{60} (Nano-C Inc.) is an electron acceptor commonly used for small molecule OPV with a layer of thickness 40 nm unless stated otherwise. Because C_{60} has a very high evaporation temperature (~ 400 °C) there is no need for material purification as most impurities are removed during material degassing at lower temperatures.

2.2.4.3 Exciton blocking layer

A thermally evaporated 8 nm thick BCP layer was used in the majority of device architectures as an exciton blocking layer at the interface between the electron acceptor and the electron-extracting electrode (Al or Ag). It also acts as a protective layer against highly energetic metal atoms since the electron extracting electrode is typically evaporated as a top electrode and can damage the sensitive photoactive layer.

For devices with an inverted architecture a thin layer of TiO_x was used as the exciton blocking layer. Titanium(IV) isopropoxide (Sigma-Aldrich, 99.99%) was mixed with *n*-butanol (Sigma-Aldrich, 99.8%) in ratios ranging from 1:5 to 1:40 in order to obtain different film thicknesses; from 5 nm to 20 nm. The precursor solution was spin-cast at 2000 r.p.m. followed by annealing at 450 °C for at least 30 minutes under nitrogen.

2.2.4.4 Opaque electrode

100 nm films of Al (99.99%, K. J. Lesker) was typically used as the opaque top electrode, evaporated at a rate of 0.1 nm s^{-1}. To minimise the possibility of damage to the photoactive layer (which creates traps) the opaque metal electrode wasn't deposited straight onto the photoactive layer but onto BCP or metal oxide (in case of inverted device structure). Alternatively a Ca (99.99%, Sigma-Aldrich)/Ag bilayer was used as an opaque electrode, both of which were evaporated at 0.1 nm s^{-1} to form a 20 nm/50 nm bilayer.

2.2.5 Device layout

The different device layouts used in this thesis are depicted in Figure 2.5: (a) a 6-pixel layout, each pixel with an active area of 0.06 cm^2; (b) a 3-pixel layout with an l area of 0.16 cm^2 per pixel; (c) a 2-pixel layout with an active area of 0.35 cm^2 per pixel; and (d) a 1-pixel device with an active area of 1.00 cm^2 per pixel. Device layouts with a higher number of pixels are more convenient for preliminary studies giving a good statistical spread. They are also used for fundamental studies focusing on comparative studies of devices with different properties rather than absolute device performance. However devices with very small areas (<<1 cm^2) are known to mask the contribution of electrode resistivity[160] and exhibit higher current densities due to the edge effects[84]. Large area devices (1 cm^2) were therefore used for optimised device structures to demonstrate their practical applicability. Contacts to external probes were improved with conductive silver paint (RS Components Ltd.) to minimise the contact resistance with the probe apparatus (i.e. the device holder for *J*-*V* and external quantum efficiency (EQE) analysis).

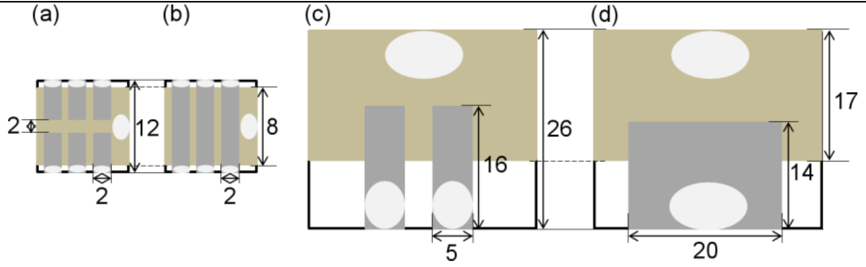

Figure 2.5: Schematic diagrams of; (a) 6-pixel device; (b) 3-pixel device; (c) 2-pixel device; (d) 1-pixel device. The dimensions are given in mm. The transparent electrode area is represented with beige. The opaque electrode area is represented with grey and silver paint contacts with pale grey. The organic material layers are sandwiched between two electrodes and are not specified with colour as covering virtually whole device area. The active area is formed between the opaque and transparent electrodes.

2.2.6 OPV current density-voltage (*J*-*V*) analysis

J-*V* measurements made under 1 Sun simulated solar irradiance and in the dark, together provide crucial information about OPV performance and the potential for application. The complexity of factors influencing OPV performance makes it difficult to predict the *J-V* characteristic. Hence, electrodes fabricated as part of this thesis were all incorporated into OPVs to truly estimate their potential. *J-V* measurements of fabricated devices were all made under N_2. The testing equipment was located next to the evaporator chamber so that devices could be tested immediately after fabrication without exposure to the air. Devices were mounted into holders designed for testing small (Fig. 2.5 (a) and (b)) and large (Fig. 2.5 c and d) area OPVs. The voltage sweep (typically -1 V to 1 V) was performed with a Keithley 2400 source meter and the data recorded using a LabView interface.

2.2.6.1 Solar simulator

The performance (efficiency & lifetime) of OPVs depends on the wavelength and intensity of the radiation to which the device is subjected. While it would be ideal to test cells under direct sunlight, changing weather conditions, altitude, latitude and levels of atmospheric pollution cause a significant time dependent variation in the solar power density. Hence a normalised light source mimicking the solar spectrum is used to enable direct comparison of OPVs fabricated in different laboratories throughout the world.

The sun radiates a great deal of energy over a broad range of wavelengths between 300 nm and 2300 nm. The temperature at its core is estimated to be 10^7 K, although this decreases to 6000 K at its surface (the photosphere). The distribution of wavelengths radiated from the sun can be described by that of black body at 6000 K. The emission spectrum of a black body at 6000 K, given by the Planck equation, is a good match to the empirically measured extra-terrestrial spectrum shape of the sun between 340 nm – 2300 nm (see Figure 2.6);[250]

$$E(\lambda,T)=\frac{2\pi hc^{2}}{\lambda^{5}\left(e^{\frac{hc}{\lambda k_{B}T}}-1\right)} \qquad (Eqn.\ 2.01)$$

where; E(λ,T) is the spectral emissive power, λ is the wavelength, h is Planck's constant, k_B is Boltzmann's constant, c the speed of light and T the blackbody temperature in degrees Kelvin.

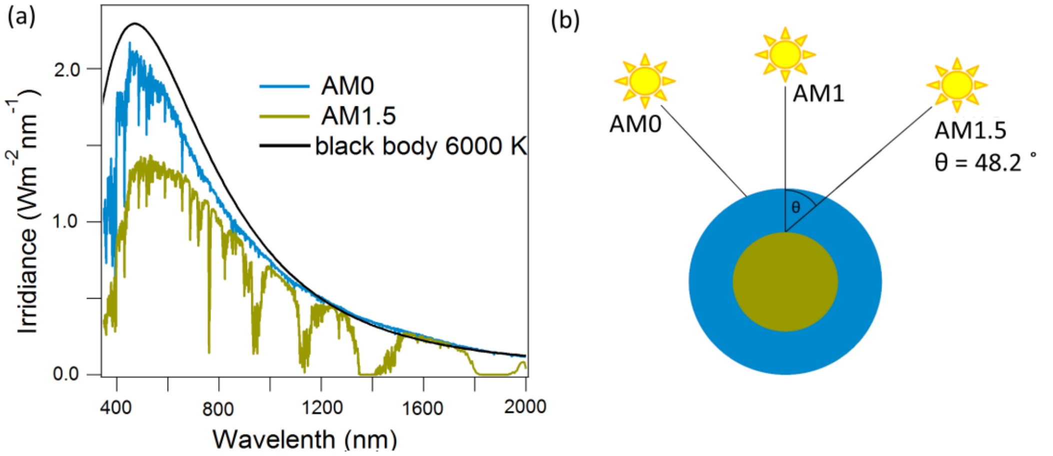

Figure 2.6: (a) Spectral power density of sunlight; AM0 (extra-terrestrial); AM1.5 (terrestrial for Japan, Europe, North America), typically used for OPV testing; (b) AM dependence on angle θ between actual solar radiation and zenith; AM0 measured outside the atmosphere.

While travelling through the Earth's atmosphere - which extends to altitudes of upwards of a thousand kilometres above the surface - the solar radiation is partially absorbed, reflected and scattered. Collectively these effects cause attenuation of the spectrum across the whole wavelength range, but also local spectral minima (see Fig. 2.5 (a)) attributed to vibrational and electronic excitation of atmospheric gases, most notably O_3, H_2O, O_2 and CH_4.[250] The degree of attenuation depends on the distance travelled through the atmosphere and hence the latitude and time of day. The 'thickness' of atmosphere through which the light is attenuated is described in terms of the 'air mass (AM)'. AM1 is equivalent to the thickness of atmosphere when the sun is at its zenith and the extra-terrestrial irradiance is described as AM0 (Figure 2.6 (b)), since there is no attenuation by the atmosphere. When the solar radiation forms an angle θ to the zenith, the air mass is given by;

$$AM = \cos(\theta)^{-1} \qquad \textit{(Eqn. 2.02)}$$

AM1.5 corresponding to θ of 48.2°, which results in a total incident light intensity of 100 mW cm^{-2} at the surface of the Earth and the spectrum is used as a standard for OPV testing.

J-V curves were measured in the dark and under 1 sun simulated solar illumination: 100 mW cm^{-2}; AM1.5. LOT Oriel GmbH & Co. KG solar simulator was used with Xenon short arc lamp and AM 1.5 filters. A PV Measurements Inc. silicon photodiode was used to calibrate the beam intensity of 100 $mWcm^{-2}$. The intensity was checked before each measurement to avoid uncertainties due to light intensity fluctuations.

2.2.6.2 External Quantum Efficiency (EQE)

Whilst for practical purposes the performance of a PV is described by J_{sc}, V_{oc}, FF, η, measurements of the quantum efficiency (QE) are required to understand the underlying factors contributing to the photocurrent and hence model and improve OPV properties. The external QE is defined as the ratio of number of electrons generated in the external circuit to the incident photon flux at a specific wavelength impinging on the cell surface;[22]

$$EQE(\lambda) = \frac{J_{sc}(\lambda)}{qN(\lambda)} = \frac{J_{sc}(\lambda)}{J_{ph}(\lambda)} \qquad (Eqn.\ 2.03)$$

where; $N(\lambda)$ is the incident photon flux density at given wavelength and q is the electronic charge. J_{sc} can be calculated from the $EQE(\lambda)$ and $N(\lambda)$ by integrating over the whole wavelength spectrum;[90]

$$J_{sc} = \int_{\lambda_0}^{\lambda_1} \frac{q\lambda}{hc} EQE(\lambda) S(\lambda) d\lambda \qquad (Eqn.\ 2.04)$$

where; $S(\lambda)$ is the spectral irradiance of the incident light, λ_0 and λ_1 determine the wavelength range, usually not exceeding 300 nm to 900 nm.

EQE is correlated to the absorption spectrum of the photoactive material and allows determination of the contribution of photocurrent generated in different materials in an OPV. It is also particularly useful in investigating optical phenomena such as plasmonic effects, which give rise to a strongly wavelength dependent enhancement in photocurrent and so can be easily distinguished from changes in the charge carrier extraction efficiency or microcavity effects using EQE measurements.

EQE measurements were performed using Sciencetech solar simulator equipped with a white light xenon arc lamp and computer controlled AM1.5 monochromatic filters. The monochromatic light intensity was calibrated with a Si photodiode (818UV, Newport) each time the equipment was used. The current generated in the device was measurement as a function of wavelength with a current-voltage amplifier (Femto DHPCA-100) and lock-in amplifier (Stanford Research SR830 DSP).

2.3 Thin film analysis

OPVs comprise a series of thin films ranging from few nm to few hundred nm in thickness. In this thesis the emphasis is on the development of the thin metal film electrodes and so the remaining device components were usually used as previously described in the literature. There are six features of the transparent electrode which need to be carefully chosen and optimised for OPV applications: *(i)* morphology; *(ii)* electrical conductivity; *(iii)* transparency; *(iv)* ϕ; *(v)* surface chemical composition; *(vi)* and surface structure. In this thesis tapping mode AFM was used to investigate thin film morphology and conductive mode AFM to determine the electrical homogeneity of the sample and to measure conductivity in the light and the dark. The resistance of the samples was determined using four point probe for the determination of sheet resistance. Far-field transparency measurements were performed using ultraviolet-visible light (UV-Vis) spectroscopy. Film crystallinity, an important factor affecting morphology, conductivity and transparency of the samples was measured using X-ray diffraction (XRD). ϕ was measured using the Kelvin probe technique. The density and composition of molecular monolayer was determined using high resolution X-ray photoelectron spectroscopy (HRXPS).

2.3.1 Atomic Force Microscopy (AFM)

AFM is a type of scanning probe microscope, invented in 1986 by Binning and Quate to investigate surfaces at the atomic scale.[251] AFM is very versatile because measurements can be performed in the air and in liquids, and on both conductive and insulating samples; both hard (e.g. metals) and soft (organic semiconductors and biological samples). A variety of derivative methods have also been developed including for the measurement of sample conductivity and surface potential. These advantages, along with the simplicity and relatively short time of the actual measurement make AFM a convenient tool for measuring the morphology of thin metal films.

A schematic illustration of AFM is depicted in Figure 2.7 (a). The instrument core comprises a cantilever probe with a sharp tip. The probe is mounted on a head, which can be lowered mechanically to preliminary approach the sample surface. The head is equipped with a piezoelectric crystal to control surface – tip separation with sub-nm precision. The head is placed above the sample on a base equipped with piezoelectric *x*-*y* scanning stage.

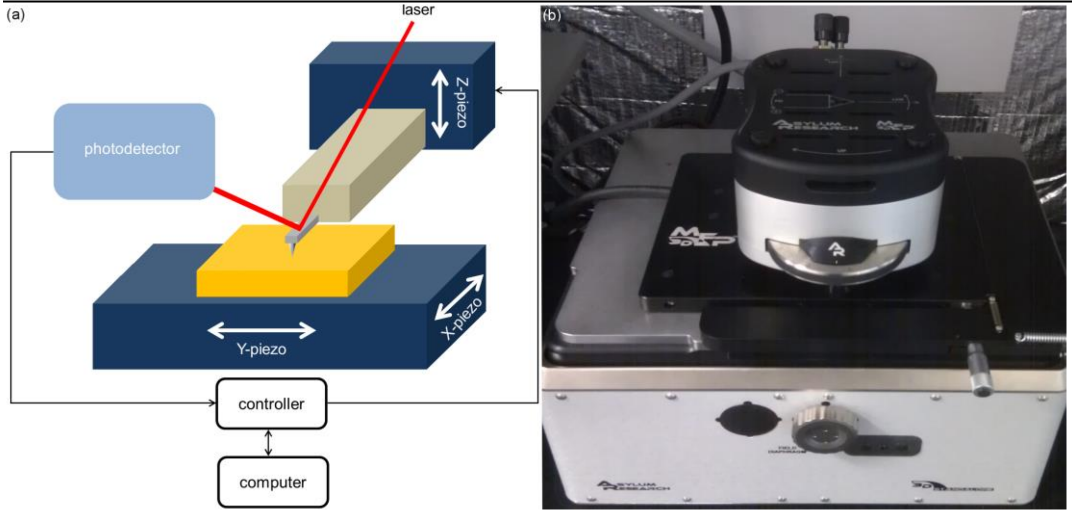

Figure 2.7: (a) Schematic of the AFM, (b) a photograph of AFM head placed above the base.

When the tip approaches the surface it firstly experiences long range attractive forces, such as van der Waals, capillary and electrostatic forces (Figure 2.8). When very near to the surface the net interaction becomes repulsive due to the dominance of repulsive electrostatic interaction between electron clouds. Tip-surface interactions induce bending of the flexible cantilever which is detected in a following way: A laser beam is incident on the cantilever's top surface - which often has a thin layer of reflective materials such as Au or Al - and reflected onto a sensitive photo-detector. The photo-detector is connected with the controller and monitors cantilever deformation. A piezoelectric crystal adjusts the probe height above the investigated surface to change cantilever deflection. This feedback loop allows either constant cantilever deflection, or constant oscillation amplitude to be maintained during a scan, while the information of *z*-piezo voltage as a function of *x*-*y* position is recorded.[252]

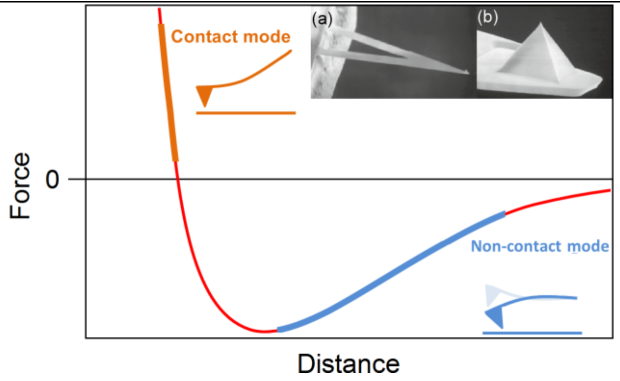

Figure 2.8: Force – distance curve for AFM tip approaching sample surface. The force regimes for tapping and contact modes are highlighted. Inset: Scanning electron microscopy images of (a) 'v' shaped cantilever and (b) pyramidal tip adapted from ref [252].

There are two commonly used AFM working modes: *(i)* contact mode; *(ii)* tapping mode. In this thesis contact mode was used for simultaneous surface morphology and conductivity measurements, whilst tapping mode was used to measure surface morphology only. In contact mode the tip comes into continuous contact with the sample and remains in the regime of repulsive forces at all times. This method can be performed in variable or constant force mode. In variable force mode the *z*-voltage applied to the piezo-electric remains constant and the variation in cantilever deflection is monitored to track sample morphology. This method can only be used for very smooth surfaces. In the constant force mode - which was used in this study - the cantilever deflection is maintained with the feedback loop during the scan. The changes in *z*-piezo voltage are monitored as a function of *x*-*y* position and used to create a 3D image of surface morphology. For contact mode measurements stiff ‘v’ shape AFM tips are used (see Figure 2.8 (a)) which avoids image distortion due to tip deformation (i.e. twisting). The tip acts as an electrode to which voltage is applied and the conductive sample is electrically grounded. The applied voltage is constant (usually in -8 V to 8 V range) and changes in current are recorded.[253] For surface current measurements an Au-coated (with Cr adhesion layer) contact mode AFM probes (TR 400 PB, Budget Sensors, spring constant 0.09 Nm^{-1}, tip radius < 30 nm) were used.

The relatively large repulsive forces used in contact mode cause the risk of sample and/or tip damage. That is why for simple morphology measurement a tapping mode is commonly used. In this mode the cantilever remains in the attractive force regime and oscillates at a value close to its resonant frequency (typically within ~ 5%). As the probe approaches the surface it repeatedly engages and disengages with the surface, which restricts the amplitude of oscillation. The constant amplitude of oscillation is maintained with the *z*-piezo feedback loop, which allows creating the 3D morphology map in a similar manner as in case of contact mode.

The surface topography and conductivity was studied using Asylum Research MFP-3D. For tapping mode Si tips were used (AC240TS, Olympus, spring constant: 1 – 3.8 Ns^{-1}, resonance frequency ~70 kHz, tip radius < 10 nm). MFP-3D software was used to analyse images. Typically 5 × 5 μm or 2 × 2 μm sample areas were scanned. For quantitative comparison of sample roughness R_{rms} was used, which is defined as the a root mean square of the deviations of the surface profile from mean height;

$$R_{rms} = \sqrt{\frac{1}{N}\sum_{i}^{N}\left(Z_i - Z_{avg}\right)^2} \qquad (Eqn.\ 2.05)$$

where; N – number of points, Z_i –height of point i, Z_{avg} – average height of the surface. For roughness measurements typically three 5 × 5 µm scans per sample were performed.

The resolution of an AFM image is limited by the shape of the tip and does not allow for accurate measurements of the width of features with dimensions less than the radius of curvature of the tip (while the height can be measured with sub-nm resolution).

2.3.2 Scanning electron microscopy (SEM)

SEM was used for surface imaging. It provides higher resolution than AFM and enables the imaging of larger areas of sample at a time. However SEM imaging requires the sample to be conductive and doesn’t provide 3-dimensional information about the surface. In SEM an electron beam is accelerated in a high vacuum column and focused so a very small beam spot of few nm in diameter and energy of few keV reaches the sample. The electrons interact with the sample, which results in generation of back scattered electrons, secondary electrons and electromagnetic radiation. Usually SEM is equipped with different detectors which allow collecting complementary information about the sample. Back-scattered electrons provide high contrast between chemically and crystallographically different areas and have been used in this study.

SEM imaging was performed using a ZEISS-SUPRA 55VP operating with an accelerating voltage of 20 kV.

2.3.3 Sheet resistance measurement

Sheet resistance (R_{sheet}) is a commonly used to describe the resistivity of electrodes. In PV devices electrode sheet resistance is a major contributor to R_s, and so affects *FF* and η (see section 1.4.5). The R_{sheet} is defined as:

$$R_{sheet} = \frac{\rho}{d} \qquad \textit{(Eqn. 2.06)}$$

where; ρ is the material resistivity and d is film thickness. Sheet resistance measurements were performed using van der Pauw technique, which can be applied to samples with arbitrary shape, provided the layers are homogeneous, isotropic and have uniform thickness. To perform the measurement the sample is contacted at four points (points 1-4 on Figure 2.9) with four probes that form ohmic contacts with the sample. The probes must be situated at the periphery of the sample and must have a contact area much less than the sample area to minimise measurement errors. A schematic of the measurement setup is shown in Figure 2.9. A constant current is applied between two neighbouring probes, and the potential difference is measured between the remaining two probes. Van der Pauw defined two characteristic resistances:[254]

$R_{12,43}$ – the potential difference between points 3 and 4 divided by the current flowing between 2 and 1,

$R_{14,32}$ – the potential difference between points 2 and 3 divided by the current flowing between 4 and 1.

$R_{12,43}$ and $R_{14,32}$ are related with R_s;[254]

$$\exp\left(-\pi\frac{R_{12,34}}{R_s}\right)+\exp\left(-\pi\frac{R_{14,32}}{R_s}\right)=1 \qquad \text{(Eqn. 2.07)}$$

In case of square samples $R_{12,43} = R_{14,32} = R$ so;

$$R_s = \frac{\pi R}{\ln 2} \qquad \text{(Eqn. 2.08)}$$

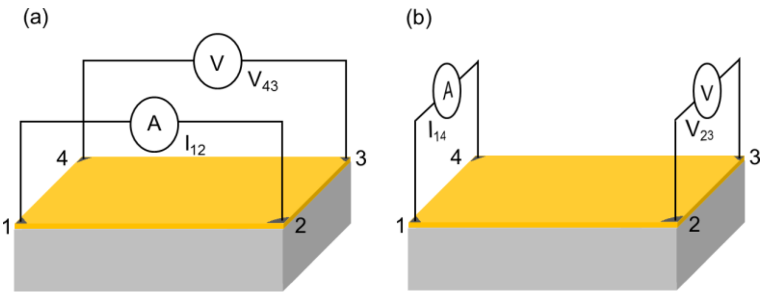

Figure 2.9: Schematic of van der Pauw method measurement.

Sheet resistance measurements were performed on 26 × 26 mm samples, with the contact made in the corners with conductive silver paint. 1 mA was applied using Keithley 2400 and voltage was measured using a multi-meter.

2.3.4 Electronic absorption (ultraviolet-visible light) spectroscopy

The efficiency of OPVs depends on both the incident light intensity and the efficiency with which incident light is absorbed. It is therefore important that the electrode through which light enters the device is as transparent as possible. The variety of photoactive materials used in this study with different architectures of conjugated bonds absorb light across different parts of the 300 – 750 nm region and so the transparency of the electrodes over this range of wavelengths had to be scrutinised each time a new electrode was developed. The far-field transparency depends on three factors; reflectivity, scattering and absorption.

Reflectivity is quantified as;

$$\zeta(\lambda) = \frac{I_r(\lambda)}{I_0(\lambda)} \qquad (\textit{Eqn. 2.09})$$

where; $\varsigma(\lambda)$ is reflectivity, $I_0(\lambda)$ is the incident light intensity and $I_r(\lambda)$ is the intensity of light reflected from the sample. Reflectivity is a particularly strong feature of metal films. For example thick Ag films exhibit over 90% reflectivity at $\lambda > 400$ nm, and thick Au over 90% > 700 nm.[255]

The reflectivity of metal films can be significantly reduced by deviating from a flat film surface.[256] However, light scattering is also increased and since the paths of scattered light deviate from the surface normal scattered light cannot be recorded using a conventional far-field UV-Vis spectrometer. Furthermore, if the scattering features are randomly shaped and distributed light scattering is difficult to predict quantitatively due to the complexity of the system.

In thin metal films light absorption results from the high free electron density. The absorption process is described by Beer-Lambert law, which for solid films takes the following form:

$$T'(\lambda) = \frac{I_t(\lambda)}{I_{0r}(\lambda)} = 10^{-\alpha(\lambda)L} \qquad (Eqn.\ 2.10)$$

where; $T'(\lambda)$ is transmission dependent on wavelength λ, $I_{0r}(\lambda)$ is the incident light intensity reduced by the amount of reflected light, $I_t(\lambda)$ is the intensity of light leaving the sample, $\alpha(\lambda)$ is absorption coefficient, L is penetration depth. Sample absorption can be described as $A(\lambda)$:

$$A(\lambda) = \alpha(\lambda)L \qquad (Eqn.\ 2.11)$$

The far-field transparency, T, measured by the UV-Vis spectrometer is rather complicated superposition of reflection, scattering and absorption and so can only be used to determine how much light passes through the electrode without significantly changing direction. It is defined as the ratio between the light intensity reaching the detector after passing through the sample $I_s(\lambda)$ and the intensity of light reaching the detector after passing through the reference $I_{ref}(\lambda)$:

$$T(\lambda) = \frac{I_s(\lambda)}{I_{ref}(\lambda)} \qquad (Eqn.\ 2.12)$$

The measurements were performed using Perkin-Elmer Lambda 25 spectrometer over the 300 nm – 900 nm range. A schematic of the instrument is given in Figure 2.10. The spectrometer is equipped with deuterium lamp (160 nm – 375 nm) and a tungsten-halogen lamp (350 – 2500 nm). The light is directed onto a monochromator which selects wavelengths with a 1 nm bandwidth. Metal film transmission was measured with the incident light shining on the substrate side, as occurs in an OPV. The transparent supporting substrate was used as the reference. After passing through the sample the light beam is detected and recorded as a function of λ. In the following chapters when a single percentage is given for transparency this corresponds to the mean far-field transparency, referenced to the transparent supporting substrate, over the range 400 nm – 750 nm, unless stated otherwise.

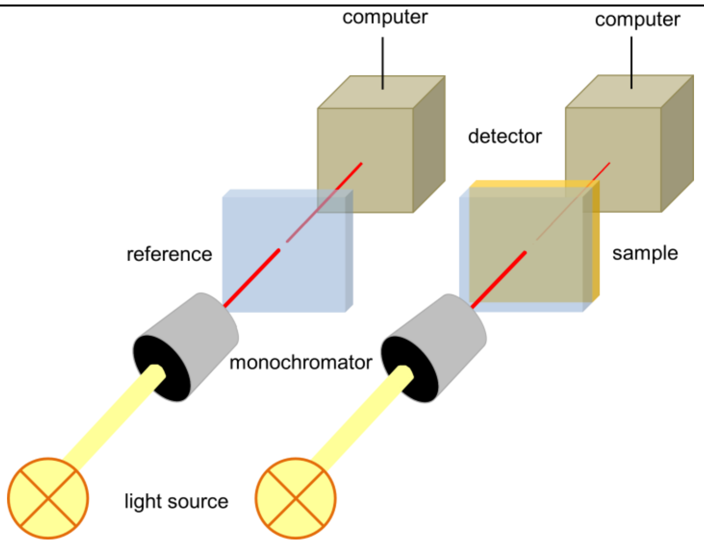

Figure 2.10: A schematic of UV-Vis spectrometer.

2.3.5 X-ray photoelectron spectroscopy (XPS)

XPS is a surface-sensitive technique, in which soft X-rays are used to study the elemental composition and chemical bonding in a sample. It is based on the photoelectric effect described by Einstein in 1905. A photon with an energy of 200-

2000 eV ejects core-level electrons from the sample atoms as depicted in Figure 2.11. The atom is left in the excited state and relaxes to the ground state by dropping an electron from a higher energy level into the vacant state followed by emission of an Auger electron or X-ray photon.[257,258] Koopman's theorem defines the binding energy, E_B, of the emitted photoelectron as the difference between the initial energy state and the final energy state following emission. However the final state energy is lowered due to reduced electron screening and so the measured E_B is higher than the orbital energy.

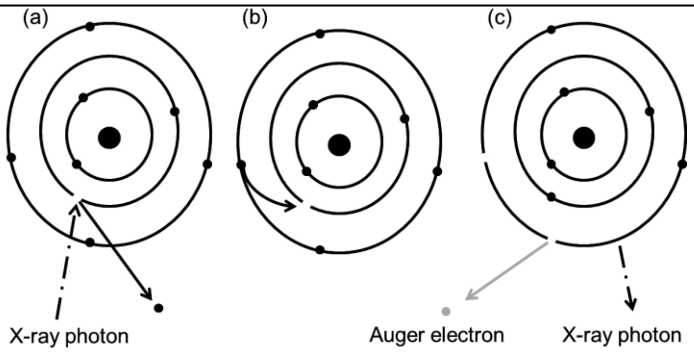

Figure 2.11: A schematic diagram illustrating the processes when an X-ray interacts with an atom: (a) An electron is ejected from a the core atomic orbital.; (b) Relaxation of an electron from a higher lying (or valence) atomic orbital into the vacancy.; (c) Emission of an Auger electron or an X-ray photon.

A monochromatic X-ray source generated by an Al source is incident on the sample and the beam of ejected electrons is collected by the electron analyser, which comprises a collection lens, energy analyser and detector. A schematic energy level diagram of the sample and the detector is shown in Figure 2.12.

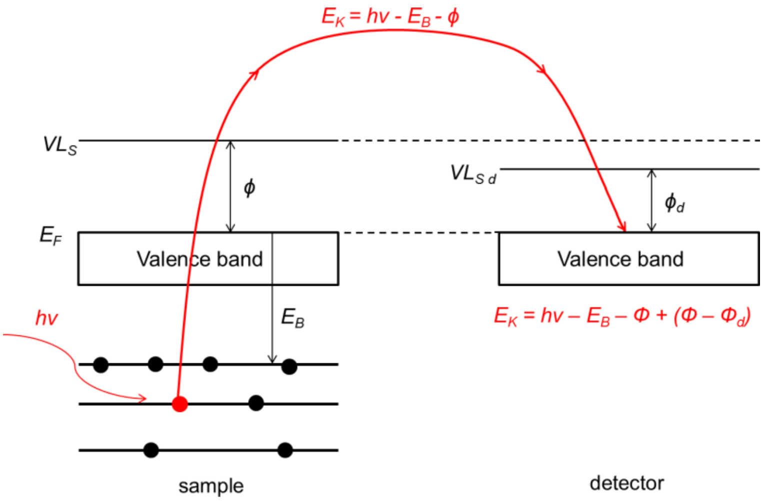

Figure 2.12: The energy level diagram of a conductive sample and a detector.

The absolute kinetic energy (E_k) of the ejected photoelectron is equal to the energy of the X-ray beam reduced by E_B and the ϕ of the solid;

$$E_k = h\nu - E_B - \phi \qquad (Eqn.\ 2.13)$$

where; the photon energy is $h\nu$; ν is the radiation frequency. However, the E_k is measured relative to the vacuum level at the surface of the detector, since the detector has a different work function (ϕ_d) to the sample. The sample is in electrical equilibrium with the detector and the measured E_k of the sample is given by:

$$E_k = h\nu - E_B - \phi + (\phi - \phi_d) = h\nu - E_B - \phi_d \qquad (Eqn.\ 2.14)$$

Since the Fermi level of the detector is aligned with that of the sample the binding energy is measured with respect to the Fermi level.

In practice plots of binding energy rather than E_k are most commonly used, so the zero on the binding energy scale corresponds to the energy of electrons at the

Fermi level in the sample. If the sample is insulating a mono-energetic source of low energy electrons is used to prevent the build-up of positive charge.

The E_B spectrum correlates with the electron configuration in the atoms of the sample. Small shifts in the binding energy result from differences in the electron density distribution around an atom. These changes in peak position in an XPS spectrum provide information about the bonding environment of the atom and are referred to as a *chemical shifts*.

High resolution XPS (HRXPS) measurements were made using a Kratos Axis Ultra. Survey spectra over the binding energy range 1400 to – 10 eV were recorded at an emission angle of 0° to the surface normal using an Al monochromatic X-ray source operated at 15 kV and 5 mA emission. Each analysis area was approximately 700 × 300 μm. The analysis conditions were 160 eV pass energy, 1eV steps, 0.2 sec dwell per step and 1 scan. CasaXPS was used to measure the peak areas with the U.K. National Physical Laboratory intensity calibration and commonly employed sensitivity factors to determine the concentrations of the detectable elements present. Narrowscan spectra of C 1s, N 1s, S 2p and S 2s were taken using 20 eV pass energy, 0.1eV steps, 0.5 sec dwell per step and 1, 1, 2 and 10 scans respectively. The S 2s peak was used for quantification as the S 2p peak was too close to the Si 2s. The peak energies were corrected by referencing to the C 1s hydrocarbon peak at 285 eV and the spectra intensities corrected using a recent calibration using NPL's XPS Intensity Calibration Software. Two, three or four components were used in the fits after a performing a linear background correction in CasaXPS.

2.3.6 Contact potential measurement: The Kelvin probe technique

The Kelvin probe is a non-contact, non-destructive technique with high surface sensitivity used to measure ϕ and changes in surface potential. It is highly surface-sensitive since surface potential is determined by the top atomic /molecule layers.[259] The technique is based on the measurement of potential difference between the sample and a probe of known ϕ brought into a close proximity. A schematic diagram of the Kelvin probe set-up is depicted in Figure 2.13 (d).

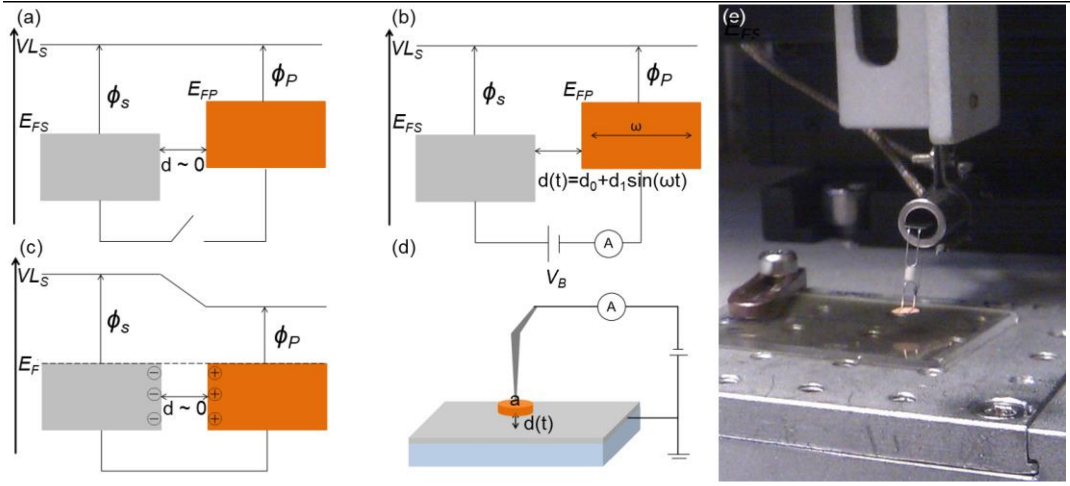

Figure 2.13: Energy level diagram of two metals in a close proximity disconnected (a); connected (b); in a Kelvin probe arrangement (c); schematic diagram of Kelvin probe (d); a photograph of a Kelvin probe above a grounded thin Au film sample (e).

The instrument comprises a metal probe of surface area *a* orientated parallel to the sample surface and electrically connected to the sample. When the probe and the sample are electrically connected charge flows from the one with lower ϕ to that with higher ϕ, until the ϕ difference between probe and sample is compensated and the Fermi levels are aligned. When the probe is brought into close proximity with the sample (0.2 - 2 mm) a parallel plate capacitor is formed of capacitance *C*:

$$C = \frac{Q}{V_{CPD}} = \frac{\varepsilon\varepsilon_0 a}{d} \qquad \textit{(Eqn. 2.15)}$$

$$V_{CPD} = \frac{Qd}{\varepsilon_0 \varepsilon a} \qquad \textit{(Eqn. 2.16)}$$

where; ε is a relative permittivity of the material between electrodes (ε_{air} ~ 1), ε_0 is the electric permittivity of the vacuum, d is the distance between the sample and the probe, Q is the charge and V_{CPD} is the contact potential difference (CPD). The CPD is equal in magnitude to the difference in work function between the sample and the probe. A counter potential is then applied, which is equal to $-V_{CPD}$ when the charge on the probe and sample is nulled. Since it is not possible to measure the electrostatic potential directly, the probe must be oscillated with respect to sample to change the capacitance and so induce an oscillating current in the wire connecting the probe and sample. An oscillating Kelvin probe was first demonstrated in 1932.[260] In this setup, which is now commonly used, a probe oscillates above the surface of the sample at a distance d and at a frequency ω such that;

$$d = d_0 + d\sin(\omega t) \qquad \textit{(Eqn. 2.17)}$$

$$C = \frac{Q}{V_{CPD}} = \frac{\varepsilon\varepsilon_0 a}{d_0 + d_1 \sin(\omega t)} \qquad \textit{(Eqn. 2.18)}$$

The contact potential V_{CPD} is fixed, so if d is changed then Q must change. Since:

$$I = \frac{dQ}{dt} = V_{CPD}\varepsilon_0 \varepsilon a \frac{d}{dt}\frac{1}{d_0 + d_1 \sin(\omega t)} = V_{CPD}\varepsilon_0 \varepsilon a \frac{d_1 \omega \cos(\omega t)}{\left(d_0 + d_1 \sin(\omega t)\right)^2} \qquad \textit{(Eqn. 2.19)}$$

$$V_{CPD} = \frac{I}{\varepsilon_0 \varepsilon a} \frac{\left(d_0 + d_1 \sin(\omega t)\right)^2}{d_1 \omega \cos(\omega t)} \qquad (Eqn.\ 2.20)$$

The alternating current flowing between the sample and probe is directly proportional to V_{CPD}. A backing potential equal to $-V_{CPD}$ must be applied to null this current.[260]

The probe is typically made of chemically stable conductive material such as steel or gold which, under controlled conditions, should have a stable ϕ and hence provide a reliable reading of contact potential difference. However to make measurements of ϕ calibration of the probe is necessary against a sample of known ϕ. This is achieved by measuring the contact potential difference between freshly cleaved, highly oriented pyrolytic graphite (HOPG) and the probe. This material is very inert and has a ϕ of 4.475 eV, as measured using photoelectron spectroscopy.[261] The contact potential difference between the probe and freshly cleaved HOPG is then used as a correction factor when measuring the ϕ of other samples.

In this thesis Kelvin probe measurements were performed in a N_2 filled glove box. The Kelvin probe is mounted next to the evaporation chamber, which allows measurement of the ϕ of freshly evaporated samples minimising the impact of ambient conditions on the sample surface.

2.3.7 X-ray diffraction (XRD)

Crystals comprise repetitive units, or *building blocks*, of atoms, ions or molecules. The shape and size of the three-dimensional repeating unit can be described by six lattice constants; three vectors: *a*, *b* and *c* and three inter-axial angles; *α*, *β* and *γ* defining the crystallographic axis. Taking into account the number and distribution of atoms/ions in the unit cell all symmetry elements in crystals can be described by 230 space groups.

Miller indices (*hkl*) are used to describe crystal planes. They are defined as reciprocals of the fractional intercepts that the crystal plane makes with crystallographic axes (Figure 2.14); That is the plane defined by the Miller indices (hkl) intersects the crystal axes at distances of 1/h, 1/k and 1/l respectively. The distance between two parallel planes with the same (hkl) index is defined as lattice plane spacing d_{hkl}.

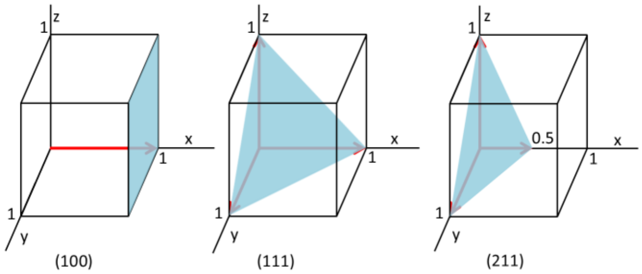

Figure 2.14: Example of some (*hkl*) indices in cubic system.

Crystal structure can be probed using the technique of X-ray diffraction (XRD). An X-ray beam is an electromagnetic wave which are absorbed and scattered by the electrons that surround atom nuclei. X-rays have wavelengths in the range 10 nm to 10^{-3} nm which is comparable to the inter-planar distances in most crystals and so can be diffracted by the crystal lattice. The intensity of the diffracted X-ray beam depends on the arrangement of atoms/molecules in the unit cell and the angle of incidence.[262] Each crystal plane is only partially transparent to the incident X-rays, with part of the incident beam being reflected as depicted in Figure 2.15.

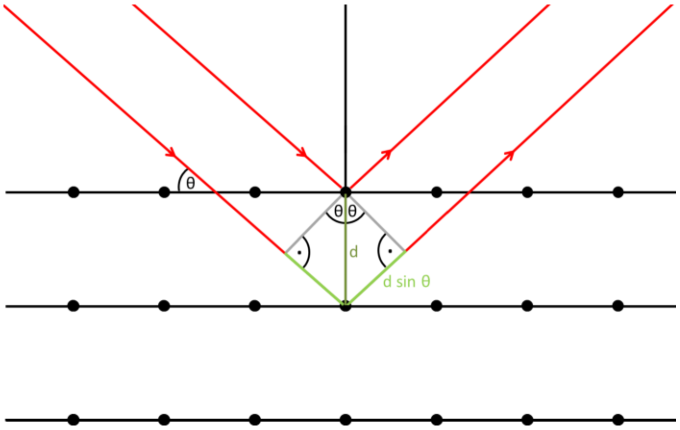

Figure 2.15: A schematic diagram of X-ray diffraction by a crystal.

If the X-rays reflected from two parallel planes at an angle θ to the normal they will constructively interfere when the path difference is a multiple of the incident wavelength, as described by Bragg condition:

$$2d \sin\theta = n\lambda \qquad (Eqn.\ 2.21)$$

where; n is an integer, λ is the wavelength.

XRD spectra are collected using an X-ray diffractometer, which is schematically illustrated in Figure 2.16.

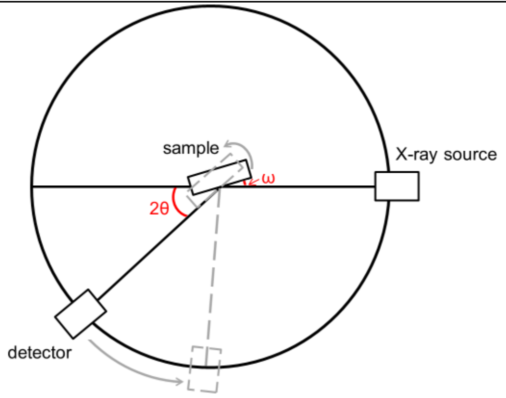

Figure 2.16: A schematic diagram of X-ray diffractometer.

The sample, in a flat-plate form, is placed in the focusing circle. The X-ray source and detector are situated on the circle perimeter. The X-ray source position is fixed and the sample is rotated through an angle ω. The detector is moved along the circle perimeter on the 2θ-axis. For highly crystalline and/or thicker samples the θ-2θ mode is commonly used; in this mode as the sample rotate (with increasing angle $\omega = \theta$) the detector rotate at double angular velocity.[262] However in some cases, such as thin polycrystalline films this method is insufficient to obtain detectable signal strength. Thus, a grazing angle diffraction is applied; it combines Bragg condition with X-ray total external reflection reducing the penetration depth from 1-10 µm to 1-10 nm.[263]

XRD measurements were made using a Siemens D5000 X-ray diffractometer operated in grazing angle or θ-2θ Bragg configuration using Cu (Kα) radiation with a wavelength of 1.542 Å. The voltage was set to 45 kV with a flux of 40 mA. Data was collected in the θ range 30° to 120°, with sampling interval of 0.05° and a time per step of 4 seconds.

2.3.8 Contact angle measurement

Contact angle measurements quantify the adhesive forces between the solid and the liquid by probing the ability of a liquid to spread on a surface. This method often employs water as the probe liquid to estimate the surface hydrophilicity. It is also a useful tool to investigate the wettability of heterogeneous surfaces, e. g. partially covered with monolayers, or to calculate surface energy if several liquids are used.[264]

If a drop of a liquid is placed on a solid surface the interaction between three phases; the liquid, the solid and the vapour is described by three interfacial energies; solid-vapour (γ_{sv}), solid-liquid (γ_{sl}) and liquid-vapour (γ_{lv}) (Figure 2.17). If the energy gained in replacing the solid-vapour interface by a liquid-solid interface exceeds the energy used to form the liquid-vapour interface;

$$\gamma_{sv} - \gamma_{sl} > \gamma_{lv} \qquad \text{(Eqn. 2.22)}$$

complete wetting takes place.[265] Otherwise a drop is formed on the solid surface and its shape is defined by the condition of thermodynamic equilibrium set between all three phases. If the contact angle θ is defined by vectors γ_{sl} and γ_{lv}, as described in Figure 2.17, the conditions for equilibrium is described by Young equation;

$$\gamma_{sv} = \gamma_{sl} + \gamma_{lv}\cos(\theta) \qquad \text{(Eqn. 2.23)}$$

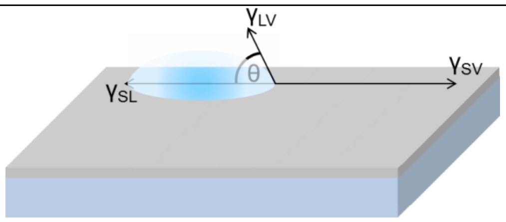

Figure 2.17: A schematic depiction of a drop of liquid on a solid surface with the three interfacial energy vectors shown.

The contact angle is very sensitive to the surface roughness and can be used to investigate composition of microscopically[265] and chemically[266] heterogeneous surfaces.

Contact angle measurements were performed using a Krüss Drop Shape Analyser 100, using the sessile drop method. The HPLC grade water droplets of 0.2 µl volume were deposited on substrates supported on glass with R_{rms} ~ 400 pm.

Chapter 3.

Ultra-thin Transparent Au Electrodes

The work presented in this chapter has been published in:
H. M. Stec, R. Williams, T. S. Jones, R. A. Hatton, *Ultra-thin Transparent Au Electrodes for Organic Photovoltaics fabricated using a Mixed Mono-Molecular Nucleation Layer*, Advanced Functional Materials, **2011,** *21* (9), 1709-1716.

Summary

In this chapter a rapid, solvent free method for the fabrication of highly transparent ultra-thin (~ 8 nm) Au films on glass is described. This is achieved by derivatising the glass surface with a mixed nanolayer of 3-mercaptopropyl(trimethoxysilane) (MPTMS) and 3-aminopropyl(trimethoxysilane) (APTMS) *via* co-deposition from the vapour phase prior to Au deposition by thermal evaporation. The mixed nanolayer modifies the growth kinetics producing highly conductive films (R_{sheet} ~11 Ω sq^{-1}) with a remarkably low root-mean-square roughness (R_{rms} ~ 0.4 nm) that are exceptionally robust towards ultra-sonic agitation in a range of common solvents. By integrating microsphere lithography into the fabrication process a means of tuning the transparency by incorporating a random array of circular apertures into the film is shown. The application of these nanostructured Au electrodes is demonstrated in efficient organic photovoltaic devices where it offers a compelling alternative to indium-tin oxide coated glass.

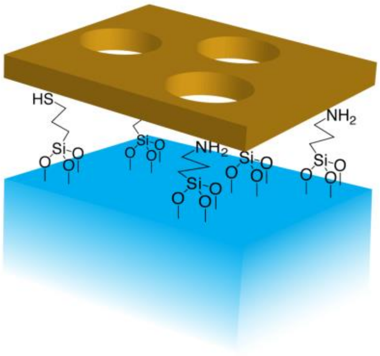

Figure 3.1: A schematic illustration of an ultra-thin Au electrode supported on an APTMS and MPTMS mixed nanolayer derivatised glass substrate with micron-size apertures.

3.1 Introduction

The oldest category of window electrodes is unpatterned thin metal films, which offer the advantages of simplicity, chemical homogeneity and established manufacturing infrastructure for large area roll-to-roll evaporation in the packaging industry.[126,127] The primary drawback of this class of window electrodes is the reduced transparency across the visible and near infra-red spectrum as compared to optimised conducting oxide electrodes.[267] However, optical modelling by O'Connor *et al.* has shown that OPVs fabricated on unpatterned thin metal films on glass have the potential to perform as well as those on conducting oxide coated glass due to micro-cavity effects which help to trap light in the device. [128] Transparent electrodes based on thin metal films have also been successfully employed as the window electrode in organic light-emitting diodes (OLEDs), with Au emerging as a particularly promising metal for this application.[133, 268,269]

The properties of thin (~10 nm) evaporated noble metal films depends on the deposition rate and the substrate material.[132] In particular noble metal films evaporated on glass are very fragile. This is due to poor film quality which results from the intrinsically low energy of adhesion with the substrate.[129] These films are also prohibitively resistive, because the metal atoms aggregate at nucleation sites on the substrate surface forming islands, which only start to coalesce at a film thickness of ~10 nm. To realise robust and conductive films of low thickness on glass an interfacial layer is required, which enhances metal nucleation by interacting strongly with both the substrate and the incoming metal atoms, thereby suppressing surface diffusion and promoting the growth of continuous metal films at low thickness. One established class of adhesive layer for this purpose is the deposition of an ultra-thin (1-10 nm) film of a transition metal such as Ge,[130] Cr or Ta[131]. However, in the context of optically thin metal films this thickness is sufficient to contribute to the film absorption. An alternative approach is to functionalise the substrate surface with a single molecular adhesive layer that is transparent across the visible and near infra-red spectrum.[133] Thiol functionalised silanes have previously been investigated for this purpose, since thiols have a strong affinity for Au and Ag, whilst organosilanes couple with native hydroxyl groups on a variety of substrate materials[134,135] to form strong siloxane bonds. Hatton *et al.*[133] has previously reported the viability of this approach for Au films on glass using a thiol functionalised molecular adhesive layer and demonstrated application in OLEDs. However, that method is not amenable to scale-up because of the requirement to use large quantities of solvent and the tendency for methoxysilanes to polymerise when deposited from solution. [135,136] A few reports have also investigated the possibility of utilising amine functionalised silanes to promote the growth of Au films on silicon and glass, although not for the purposes of fabricating highly transparent films and all using solvent assisted deposition methods.[137,138,139] There were also no reports, to the author’s knowledge, of the use of a mixed amine and thiol terminated organosilanes molecular adhesive layer for this purpose prior to this work. Interestingly, alkyl amines are not an obvious candidate as molecular adhesives for Au films since the Au-N bond is much weaker than the Au-S interaction.[270] The amine silane nanolayer deposition process is however self-catalytic[271] and hence can be utilised to accelerate the process of adhesive layer formation.

3.2 Experimental

3.2.1 Preparation of ultra-thin Au films on glass

Glass substrates were cleaned according to the procedure described in Chapter 2, UV/O_3 treated for 15 minutes and immediately transferred to a dessicator where they were exposed to the vapour of APTMS, MPTMS or APTMS:MPTMS at a background pressure of ≤ 50 mbar for different periods of time (1 to 70 hours). The optimised treatment times for different types of monolayers are as following: APTMS – 1 hour, MPTMS – 20 hours, APTMS:MPTMS – 4 hours. Derivatised substrates were then immediately transferred to the evaporator, where Au was deposited at the rate of 0.1 nm s^{-1}.

3.2.2 Preparation of ultra-thin Au films on glass with micron-sized apertures.

For the preparation of electrodes with micron-sized apertures the above method was modified as follows: Cleaned slides were dipped in 1:80 poly(diallyldimethylammoniumchloride) : H_2O solution, rinsed with water and blow dried with nitrogen. The glass surface was then covered with 2.5 wt.% aqueous solution of 2 µm diameter polystyrene beads and spin-cast at 6000 r.p.m. to form a sub-nanolayer of the beads masking ~ 20% of the glass surface. The substrates were then treated with oxygen plasma for 200 seconds and immediately transferred to a dessicator for MPTMS:APTMS vapour treatment. After Au evaporation the polystyrene beads were easily removed using scotch tape. Residual silane was removed using a 0.2 M solution of tetrabutylammonium fluoride in tetrahydrofuran. Finally, the substrates were rinsed with water and dried with nitrogen.

3.2.3 Substrate characterisation

HRXPS and static water contact angle measurements were employed to characterise the nanolayer density and composition. HRXPS measurements were performed and analysed as described in Chapter 2.

All HRXPS intensities have been corrected by the sensitivity factors. The thickness of the silane nanolayer was estimated from the attenuation of the Si 2s intensity. Using the attenuation length, L, for an "average polymer"; L = 3.57 nm, the thickness t of the nanolayer on clean glass is given by Equation 3.01:

$$t = -L \ln\left(\frac{I_{Si2s}}{I_{Si2s\mathrm{Re}f}}\right) \qquad (Eqn.\ 3.01)$$

where; $I_{Si2sRef}$ is the intensity of the Si 2s peak from a clean glass substrate and I_{Si2s} is the intensity of the Si 2s peak from the sample. Since both molecular adhesives incorporate a Si anchor group this method underestimates the nanolayer thickness. On the other hand this calculation overestimates the thickness of a carbon-based overlayer on a substrate surface if there is any carbon-based surface contamination. It is therefore primarily used as a relative measure of nanolayer density.

The main source of surface contamination comes from airborne hydrocarbons, which are commonly present in the atmosphere and deposit on surfaces even after very brief exposure to the laboratory environment. Sulphur contamination comes from the manufacturing processing of glass substrates, as confirmed by the supplier, and low levels of sulphur containing gases in the atmosphere, such as H_2S, OCS, SO_2, and CS_2.[117]

To determine the contribution of APTMS, MPTMS and hydrocarbon to the overlayer thickness the following method was used: The intensities measured on nanolayer modified glass were corrected for background levels of carbon, sulphur and nitrogen:

$$I_x = I_{x\,sample} - I_{x\,glass} \qquad (Eqn.\ 3.02)$$

where; x = N 1s, S 2s, C 1s. The APTMS:MPTMS ratio in case of sample with mixed nanolayer was estimated using these corrected intensities:

$$APTMS : MPTMS = \frac{I_{N1s}}{I_{S2s}} \qquad (Eqn.\ 3.03)$$

It was assumed that the C:N ratio in APTMS is 3:1 and C:S ratio in MPTMS 3:1. To calculate the intensity contribution to the thickness from hydrocarbon contamination three times the intensities of S 2s and N 1s were subtracted from the intensity of C 1s:

$$I_{hydrocarbon} = I_{C1s} - 3I_{N1s} - 3I_{S2s} \qquad (Eqn.\ 3.04)$$

The fractional contribution of hydrocarbon, APTMS and MPTMS to C 1s peak intensity is given by Equation 3.05:

$$f = \frac{X}{I_{C1s}} \qquad (Eqn.\ 3.05)$$

where; X is $3I_{N\ 1s}$ in case of APTMS, $3I_{S\ 2s}$ in case of MPTMS and $I_{hydrocarbon}$ in case of hydrocarbon. The thickness contribution from APTMS, MPTMS and hydrocarbon was then calculated by multiplying f by the total thickness estimated using Equation 3.01. Crucially, since the measured thickness is an ‘average’ the values given in the results section are indicators of nanolayer density rather than actual thickness.

Static water contact angle measurements were also made, as described in Chapter 2, to estimate sample surface hydrophobicity.

3.2.4 Metal films characterisation

Metal films were characterised using the techniques described in Chapter 2. The conductance measurements were performed using contact mode AFM with a tip bias of +3V.

3.2.5 OPV fabrication and testing

Optimised Au and reference ITO electrodes were incorporated into the bulk heterojunction (BHJ) OPV of structure: electrode / 7.5 nm WO_x / 1:1 P3HT:PCBM spincasted from 40 mg ml^{-1} overall solution in dichlorobenzene / 8 nm BCP / 100 nm Al. Al was deposited through a shadow mask to give individual devices with an area of 0.35 cm^2.

3.3 Results and Discussion

3.3.1 Ultra-thin film fabrication and characterisation

The primary aim of this work was to develop ultra-thin Au film electrodes suitable as the transparent electrode in OPVs. For this application the transparency across the visible and near-infrared spectrum must be maximised whilst minimising the sheet resistance and surface roughness. In order to optimise the silanisation procedure UV/O_3 treated glass substrates were exposed to the vapour of MPTMS and/or APTMS (See Figure 3.2) at reduced pressure (<50 mbar) for different time periods immediately prior to evaporation of Au to form films of the same effective thickness.

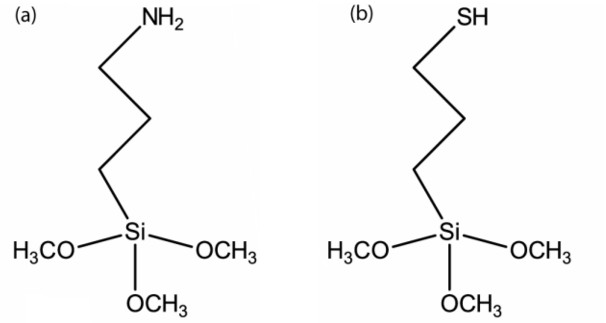

Figure 3.2: The chemical structures of APTMS (a) and MPTMS (b).

The sheet resistance is a key indicator of the continuity of thin metal films[128] and so it was used as an indirect method for determining the optimal silane treatment time. Figure 3.3 shows how the sheet resistance of sub-10 nm films of Au of constant effective thickness depends on the vapour treatment time for the two different molecular adhesives shown in Figure 3.2. It is clear from Figure 3.3 that the effectiveness of APTMS and MPTMS at nucleating the growth of continuous Au films is strongly dependent on the time taken to derivatise the glass substrate.

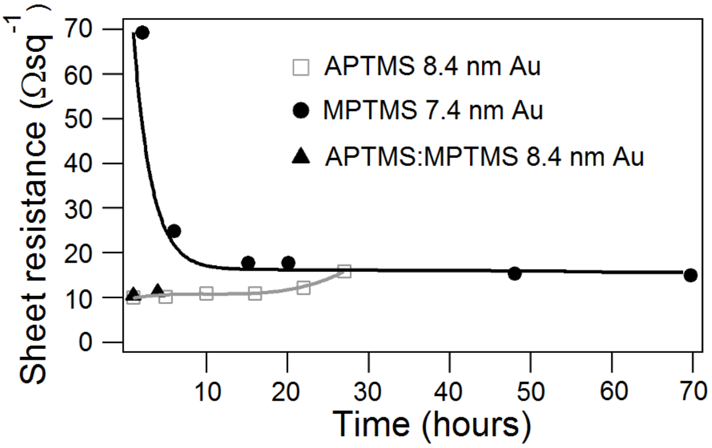

Figure 3.3: Sheet resistance of Au films supported on APTMS, MPTMS and APTMS:MPTMS derivatised glass as a function of vapour treatment time. The thickness of Au on the APTMS and the mixed nanolayer is 8.4 nm. The thickness of Au on the MPTMS nanolayer treated glass is 7.4 nm.

3.3.1.1 MPTMS

The sheet resistance of Au films with an effective thickness of 7.4 nm on MPTMS derivatised glass rapidly decreases with increasing MPTMS deposition time before saturating at ~ 18 Ω sq^{-1} after times greater than 15 hours. This behaviour is consistent with increasing MPTMS coverage of the glass substrate with time, corresponding to an increase in the density of Au nucleation sites responsible for promoting uniform film growth at low thickness.[132, 137] In the absence of a molecular adhesive layer the sheet resistance was > 300 Ω sq^{-1}.

The XPS survey scans of clean glass and MPTMS derivatised glass are shown in Figure 3.4 (a) and (b) respectively. The peak intensities determined from high resolution XPS measurements are given in Table 3.1. Table 3.2 shows the intensity of Si 2s for different samples, the overlayer thickness calculated on the basis of Si peak attenuation and the absolute thickness attributed to APTMS and MPTMS. The effective thickness of the MPTMS nanolayer after 20 hours exposure to MPTMS vapour is estimated to be ~ 0.1 nm. Such a low thickness is indicative of a sub-monolayer since a dense monolayer would have a thickness approaching the height of an MPMS molecule; ~ 0.8 nm.[137] A possible explanation for the low MPTMS surface coverage is that the density of surface hydroxyls to which the MPTMS molecules covalently bind is low, although can't rule out possibility that the coverage increases with increasing time beyond 20 hours. However, as film resistivity doesn't improve for longer times so there is no advantage from a practical perspective.

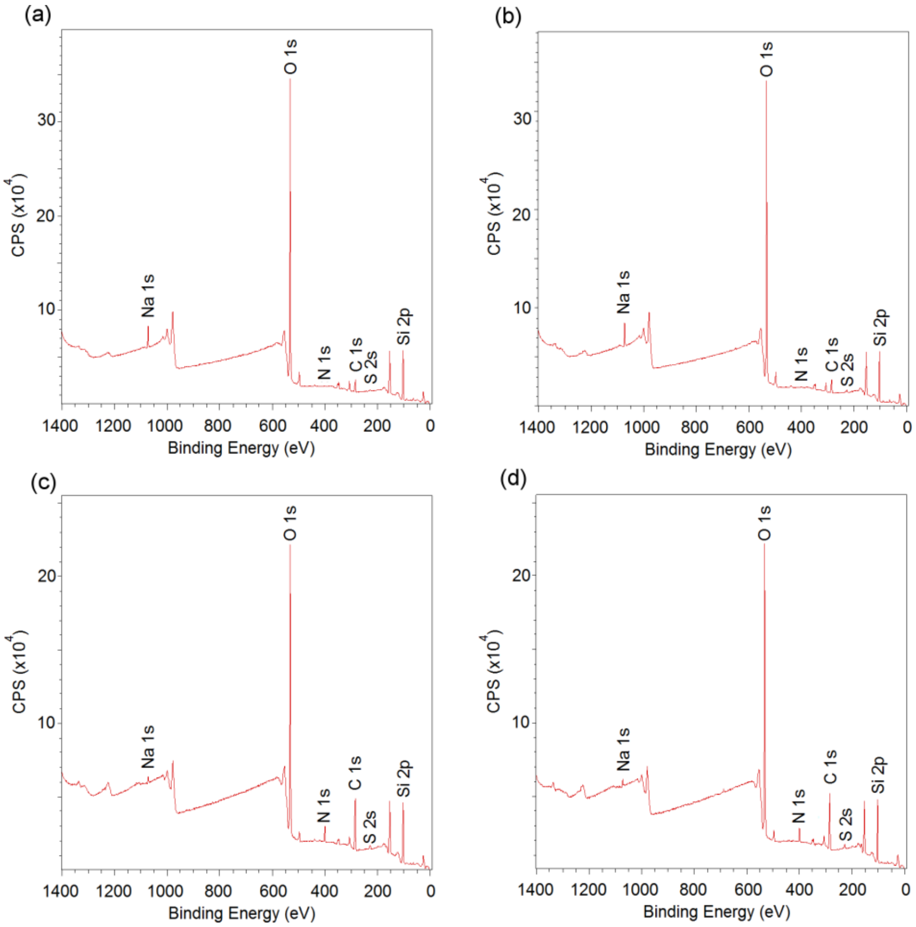

Figure 3.4: XPS survey scans of: (a) clean glass; and glass derivatised with: (b) MPTMS; (c) APTMS; (d) APTMS : MPTMS.

Table 3.1. HRXPS elemental analysis of the nanolayer composition. Peaks intensities associated with C 1s, N 1s and S 2s on bare glass and glass derivatised with MPTMS, APTMS and an APTMS:MPTMS nanolayers corrected by the sensitivity factors.

Sample	C 1s	S 2s	N 1s
		$\times10^4$ [CPS]	
Clean glass	23.1 ± 0.1	2.4 ± 0.1	0.4 ± 0.2
MPTMS	27.3 ± 0.8	3.7 ± 0.1	0.5 ± 0.2
APTMS	66.6 ± 0.4	3.7 ± 0.1	9.5 ± 0.2
APTMS:MPTMS	68.6 ± 0.1	5.0 ± 0.1	9.1 ± 0.1

Table 3.2. Si 2s peak intensity corrected by the sensitivity factor, the total overlayer thickness estimated using the attenuation length for the 'average polymer' and thickness attributed to APTMS and MPTMS.

Glass substrate modification	Si 2s	Total thickness [nm]	APTMS thickness [nm]	MPTMS thickness [nm]
None	103.7 ± 0.1	-	-	-
MPTMS	100.0 ± 0.1	0.13 ± 0.2	-	0.11 ± 0.02
APTMS	81.8 ± 0.1	0.85 ± 0.1	0.53 ± 0.05	-
APTMS:MPTMS	78.4 ± 2.2	1.00 ± 0.1	0.58 ± 0.03	0.17 ± 0.02

The film sheet resistance of 7.4 nm Au film (~18 Ω sq^{-1}) is seven fold larger than that calculated on the basis of the resistivity of bulk Au.[272] This difference most likely results from increased scattering: *(i)* at the surface of the film, since the mean free path of electrons in bulk Au (~36 nm)[273] is a factor of four larger than the film thickness; *(ii)* and at crystal boundaries, since the high density of nucleation sites at the glass surface after treatment with a molecular adhesive promotes the formation of crystallinites with small lateral dimensions. Notably the resistivity of 7.4 nm Au films fabricated on MPTMS derivatised glass (<1.3 $x10^{-5}$ Ω cm) is fractionally lower than those of Hatton *et. al.* [1.4 $x10^{-5}$ Ω cm for a 7 nm thick film][133] and much lower than Dunaway *et al.* [1.6 $x10^{3}$ Ω cm for an 8.4 nm film on MPTMS and 4.2 $x10^{-5}$ Ω cm on APTMS][137] both of whom deposited the molecular adhesive layer with the aid of a solvent. To test the robustness towards standard substrate cleaning procedures films with an effective thickness of 8.4 nm Au were subject to ultra-sonic agitation in three common solvents; namely, 2-propanol, toluene and water. Remarkably films prepared on MPTMS derivatised glass were resistant to scotch tape test and all of the solvent treatments with no significant change in sheet resistance (Table 3.3) or optical properties. Upon UV/O_3 treatment the resistance increased consistent with the oxidation of the uppermost 1 nm of a film of uniform thickness (Table 3.3). Conversely 8.4 nm Au films deposited on the non-treated glass disintegrate upon sonication in water and become insulating when UV/O_3 treated.

Table 3.3. Sheet resistance of 8.4 nm Au films supported on glass substrates derivatised with MPTMS, APTMS and APTMS:MPTMS (for optimised times) before and after ultra-sonic agitation in three common solvents (toluene, water and 2-propanol) and UV/O_3 oxidative treatment.

Molecular adhesive	Untreated	Toluene	Water [Ω sq^{-1}]	2-propanol	UV/O_3
MPTMS	11.3 ± 0.7	12.2 ± 0.8	12.2 ± 0.7	11.3 ± 1.0	13.6 ± 0.8
APTMS	10.4 ± 0.8	11.7 ± 0.8	∞	12.7 ± 0.6	14.5 ± 1.0
APTMS:MPTMS	11.3 ± 1.2	11.7 ± 1.0	11.3 ± 0.8	12.2 ± 1.0	12.2 ± 1.2
None	>300	>400	∞	>300	∞

3.3.1.2 APTMS

Figure 3.3 is indirect evidence that derivatisation of glass with APTMS is more rapid than its thiol analogue, since the resistivity of Au films prepared on glass substrates exposed to APTMS for ≤ 4 hours is comparable to that of Au films deposited onto glass substrates exposed to MPTMS vapour for > 16 hours. The XPS spectrum (Figure 3.4 (c)) shows a significant increase in the intensity of the C 1s and N 1s peaks. From the attenuation of the Si 2s core level peaks in the HRXPS spectra the effective thickness of the nanolayer after 4 hours exposure to APTMS vapour was > 0.8 nm, consistent with the formation of a dense nanolayer of upright APTMS molecules.

The transparency spectra of Au films deposited on different types of nanolayer are shown in Figure 3.5. The discontinuous structure of Au films evaporated directly onto glass without any adhesion layer results in a relatively low mean transparency across the visible spectrum of ~54% due to the high number of scattering centres. A sharp peak in the transparency at ~ 500 nm followed by increased absorption at longer wavelengths is typical of Au particles.[274]

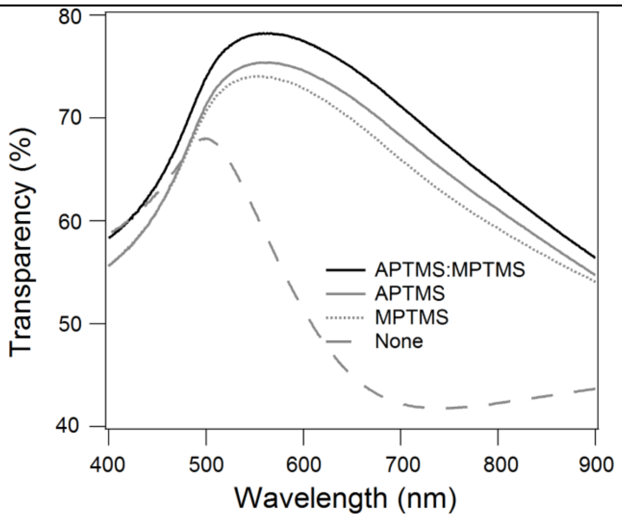

Figure 3.5: Far-field transparency spectra of 8.4 nm Au films deposited onto glass (grey dashed line) and MPTMS (grey dotted line), APTMS (grey solid line) and mixed APTMS:MPTMS (black line) derivatised glass substrates.

The superior transparency of Au films deposited on APTMS derivatised glass (average ~ 70% *vs.* ~ 68% for MPTMS) is tentatively attributed to a reduction in light scattering due to a decrease in the average Au crystalline size resulting from the higher density of surface nucleation sites. A plausible reason for the more rapid derivatisation of the glass surface by APTMS and the formation of a denser layer, as compared to MPTMS, is the previously documented catalysis of the coupling reaction between alkoxysilanes and hydroxyl moieties tethered to solid surfaces by primary amines:[271, 275] In the first instance the amine can hydrogen bond with native surface silanols helping to keep the molecular adhesive at the glass surface for long enough for reaction to occur (Figure 3.6 (b)). The amine will also promote the deprotonation of these surface silanol moieties thus self-catalysing the condensation reaction between them and methoxysilanes moieties attached to the molecular adhesive molecules as depicted in the Figure 3.6 (c). The amine moieties on adjacent APTMS molecules may also catalyse the cross-linking reaction between adjacent APTMS on the glass surface, helping to increase the surface number density.

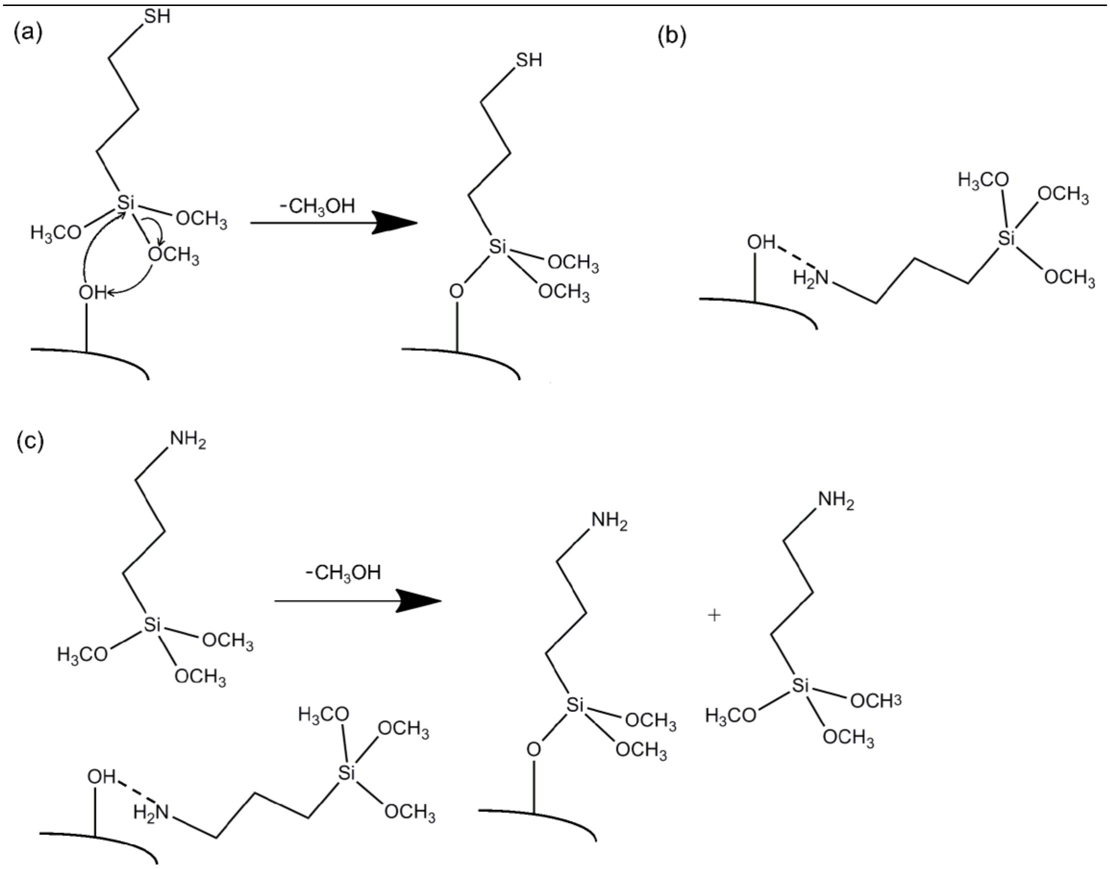

Figure 3.6: The scheme of (a) a siloxane bond formation between MPTMS and surface hydroxyl groups; (b) hydrogen bond between APTMS and surface hydroxyl groups; (c) an amine-catalysed siloxane bond formation between APTMS and surface hydroxyl groups.[271]

Surprisingly the sheet resistance of Au films deposited on amine derivatised glass is lowest for short APTMS deposition times (t < 5 hours) and gradually increases for longer times. To shed light on the reason for this unexpected behaviour the surface roughness of the APTMS derivatised glass before and after deposition of an Au film was measured using AFM. Whilst the roughness of Au films deposited onto APTMS derivatised glass after short APTMS deposition times is initially exceptionally low (~ 0.4 nm), it steadily increases with time, which explains the gradual increase in sheet resistance as a result of increased scattering as shown in Figure 3.7 (a). This increase in roughness cannot however be attributed to polymerisation of the APTMS into aggregates, which is known to occur when glass is derivatised with APTMS from solution,[135] since the roughness of the APTMS derivatised surface does not increase with increasing deposition time. To explain this observation we propose that the high energy amine moieties bury themselves into the nanolayer at high APTMS coverage, presenting the methyl group onto which Au weakly couples to the incoming Au atoms.[276] Static contact angle measurements support this hypothesis since the surface becomes considerably more hydrophobic after t > 5 hours, as evident from the ~ 10° increase in water contact angle (Figure 3.7 (lower)).

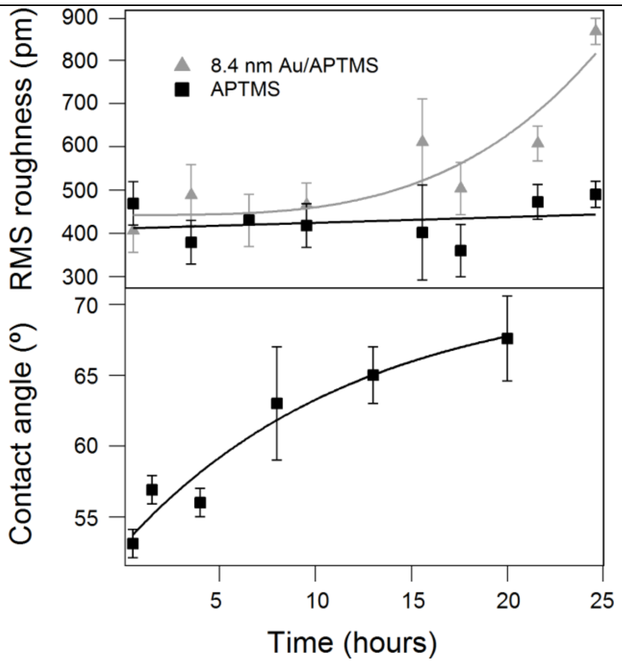

Figure 3.7: Root mean-square roughness of APTMS derivatised glass before (black squares) and after (grey triangles) deposition of an 8.4 nm Au film as a function of APTMS deposition time (upper); static water contact angle *vs.* time of exposure of glass substrates to APTMS vapour (lower).

Unfortunately whilst ultra-thin Au films prepared on APTMS derivatised glass are resistive towards scotch tape test and ultra-sonication in toluene and 2-isopropanol they are not resistant to ultra-sonication in water (Table 3.3). This is indirect evidence that the nature of the bond formed between the tethered amine and the Au overlayer is similar to that between alkylamines adsorbed on Au substrates, since the latter are known to be unstable in polar condensed phases.[270,277] The effectiveness of an APTMS nanolayer as a molecular adhesive for Au films therefore results from the collective action of a large number of relatively weak bonding interactions, rather than a low density of strong bonds as is the case when using MPTMS.

3.3.1.3 APTMS:MPTMS

In order to combine the superior robustness of ultra-thin Au films prepared on MPTMS derivatised glass with the advantage of short derivatisation times when using APTMS the possibility of employing a mixed molecular adhesive layer was investigated. This approach proved to be extremely effective: The sheet resistance of 8.4 nm Au films deposited onto glass exposed to APTMS:MPTMS vapour for only 4 hours was ~ 11 Ω sq^{-1} and remained unchanged after ultra-sonic agitation in toluene, 2-propanol or water (Table 3.3). Furthermore, the transparency of Au films prepared on a mixed nanolayer was superior to that on either single component nanolayer (Figure 3.5), peaking at 77% with the mean value ~ 72%. The R_{rms} of these films was also remarkably low at ~ 0.4 nm and comparable to that of the underlying glass substrate (Figure 3.8 (a)). Taken in conjunction with the homogeneity of the surface conductivity measured using AFM (Figure 3.8 (b)), the conformal nature of the Au film on glass is compelling evidence that the film is of uniform thickness.

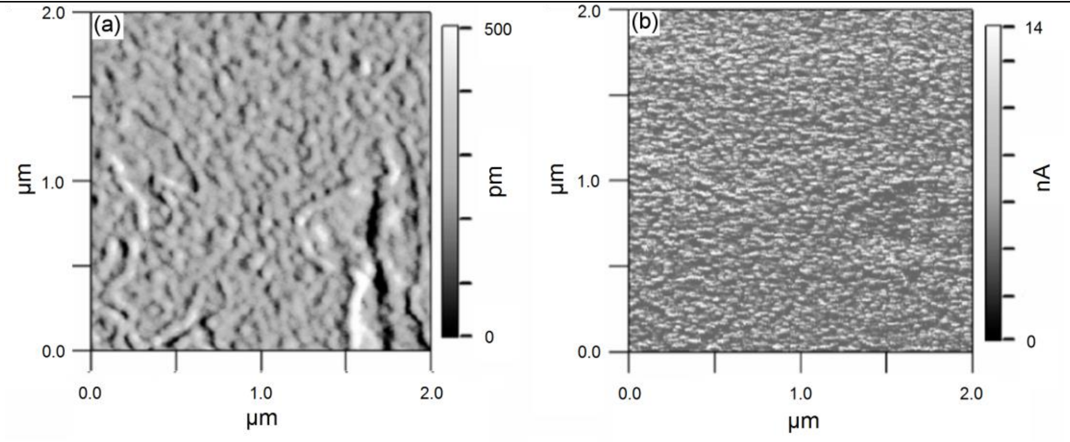

Figure 3.8: AFM images of the surface topography **(a)** and conductivity **(b)** of an 8.4 nm Au film on an MPTMS:APTMS derivatised glass substrate.

Analysis of the cross-section of scored Au films corroborates this conclusion (Figure 3.9). Notably, the measured film thickness is ~ 1 nm thicker than the deposited film thickness, evidence that the nanolayer is not embedded in the Au film, rather that the Au film is supported on top of the nanolayer. From the attenuation of the Si 2s core level peaks in the HRXPS spectra the effective thickness of the mixed nanolayer after 4 hours exposure to the vapour of APTMS and MPTMS is ~1 nm, supporting the conclusion that a high density nanolayer is formed. The composition of the mixed nanolayer was 3.4 (± 0.1):1 APTMS:MPTMS as determined using HRXPS by measuring the ratio of the surface concentration of N to S.

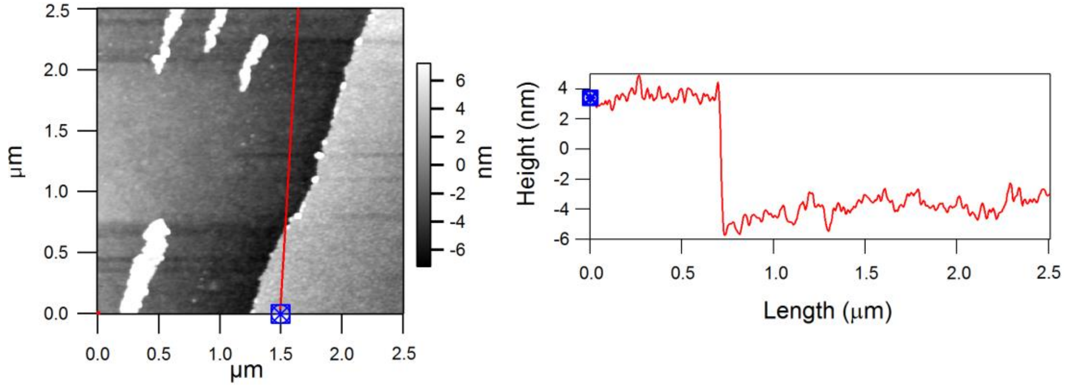

Figure 3.9: AFM morphology (left) and cross-section (right) of a step edge in an 8.4 nm Au supported on APTMS:MPTMS derivatised glass, where the Au film was partially removed by scoring the film mechanically.

The excess of APTMS is consistent with the expected difference in the vapour pressure of these two compounds, since APTMS has the lower boiling point (194 °C *vs.* 212 °C), combined with the ability of APTMS to self-catalyse its reaction with surface hydroxyls. Notably, elemental analysis of the nanolayer composition shown in Table 3.1 also reveals that the percentage of those elements associated with moieties capable of binding to Au (i.e. nitrogen; amine and sulphur; thiol) in the mixed nanolayer is significantly higher than on substrates functionalised with either single component nanolayer. The superior transparency of Au films prepared on mixed nanolayers (Figure 3.5) is therefore tentatively attributed to a reduction in light scattering due to the decrease in the average Au crystalline size that results when the density of surface nucleation sites is higher.

3.3.2. Tuning the optical transparency using micro-sphere lithography

Films supported on all three types of nanolayer have similar transparency spectra with a wide peak at ~ 565 nm. However, due to the high free electron density in metals, the far-field transparency of metal films with a thickness of 7-12 nm is typically 10 - 20% lower than of optimised conducting oxides across the wavelength range 300-900 nm.[65, 133] To increase the transparency of the ultra-thin Au films, and so make them more suitable for application in OPVs, a method for incorporating a random array of micron-sized apertures of controlled density into the film was developed. Using the method schematically illustrated in Figure 3.10 microsphere lithography is integrated with the surface derivatisation process to form well defined circular apertures of controllable size and number density (Figure 3.11 (a) and (b)). Circular apertures with a diameter of ≥ 1 μm allow light of wavelengths less than 900 nm to pass through unhindered.

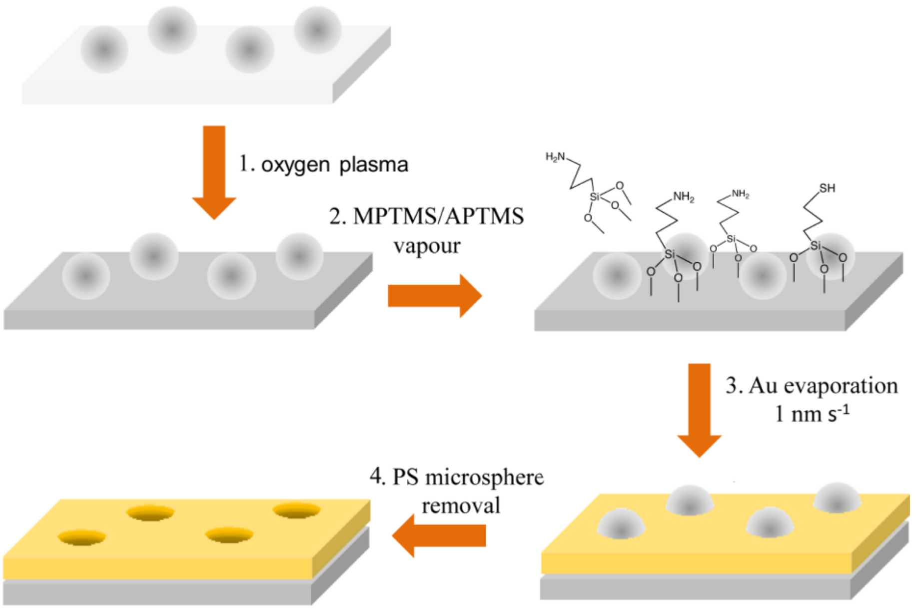

Figure 3.10: Schematic illustration of the integrated processes of ultra-thin Au film fabrication and microsphere lithography.

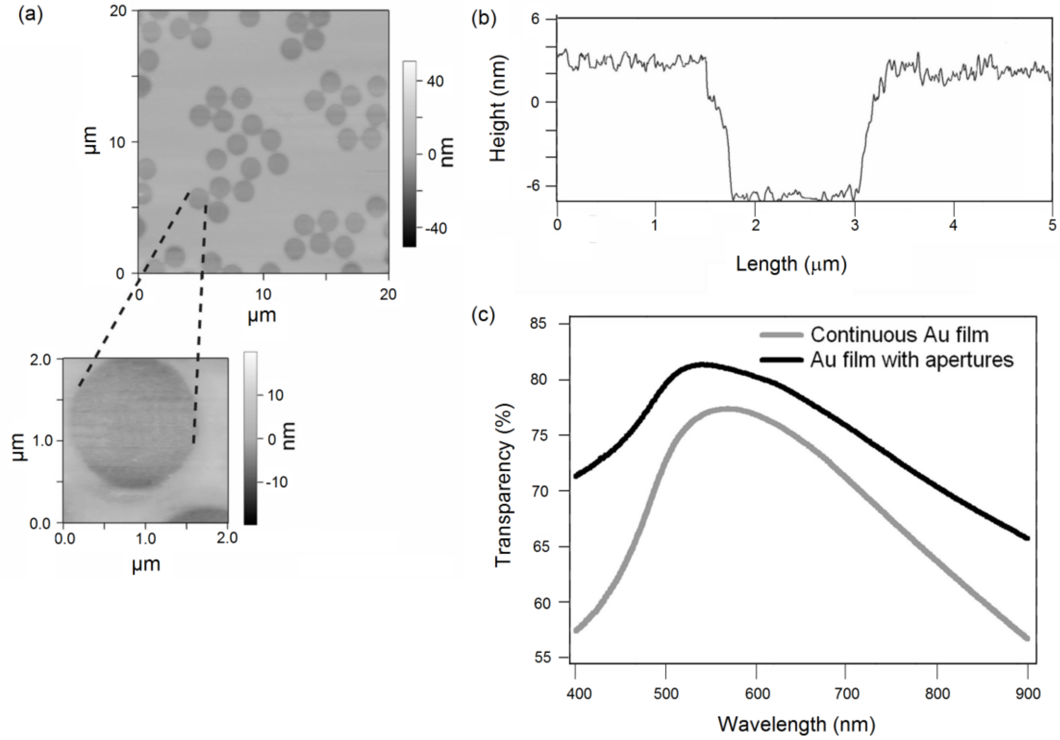

Figure 3.11: (a) - Representative AFM images of circular apertures in an 8.4 nm Au film; (b) - Typical profile of an aperture formed using a 2 µm diameter polystyrene bead; (c) - Far-field transparency of 8.4 nm Au films on APTMS:MPTMS without and with apertures (the aperture area ~ 20% of the film).

In the current context the aim was to increase the far-field transparency across the wavelength range 400-900 nm and so apertures with diameters of 1-2 μm were required. Based on the work of Cravino *et al.*,[278] who investigated the importance of edge effects when measuring the efficiency of small area OPVs, it was expected that apertures with diameters as large as 2 μm can be introduced into the ultra-thin Au film without adversely impacting device performance provided the organic overlayer immediately adjacent to the Au electrode has a conductivity of > 10^{-5} S cm^{-1}. This restriction results from the requirement for charge carriers generated over an aperture to be efficiently transported through the organic overlayer to the Au electrode without adversely impacting device series resistance.[278] Less conductive materials can be accommodated by reducing the aperture size closer to 1 μm. The advantage of using polystyrene microspheres as masks is that they can be easily removed either mechanically or using a solvent. It is also possible to fine-tune the diameter of polystyrene beads prior to molecular adhesive deposition using oxygen plasma treatment, which isotropically etches the polystyrene sphere. In this case the diameter of apertures formed using 2 μm beads is reduced to ~ 1.5 μm using oxygen plasma treatment. Importantly plasma etching retains the circular shape which minimises the increase in the film sheet resistance resulting from loss of material and increased scattering. The ability to reduce the diameter of the beads post-deposition is most important for high bead densities, since it ensures that any bead aggregates do not result in the formation of irregular very large apertures. When ~ 20% of the film was perforated with apertures formed using 2 μm diameter beads (Figure 3.11 (a) and (b)). The far-field transparency across the full range of wavelengths between 400 - 900 nm increased to ~78%, peaking between 495-600 nm at > 80% and with the mean value ~ 78% (Fig. 3.11 (c)). However, the sheet resistance of the 8.4 nm Au film increased from 11 ± 1 Ω sq^{-1} to 27 ± 1 Ω sq^{-1}, which is at the upper limit of what is required for large area applications such as PVs.

3.3.3. Utility as the window electrode in OPVs

To demonstrate the viability of these nano-structured electrodes as a direct replacement for ITO glass in OPVs they were incorporated into devices employing a WO_x hole-extraction layer and a P3HT:PCBM BHJ photoactive layer. The latter is a well characterised photoactive material system for OPVs, capable of delivering power conversion efficiencies (η) of > 4%.[185, 279] WO_x is an efficient hole-extraction material for OPVs[204] although its lateral conductivity is significantly lower than the archetypal hole-extraction material PEDOT:PSS.[278] This combination of hole-extraction layer and photoactive layer is therefore well suited as a test bed to assess the suitability of these electrodes for OPVs. In our laboratory reference OPVs fabricated on ITO glass substrates exhibited η = 3.80 ± 0.20 %.

Figure 3.12 and Table 3.4 show the *J*-*V* characteristics of devices employing different types of electrodes; plane Au electrodes, Au electrodes with micron-sized apertures and ITO coated glass. It is evident that OPVs employing an ultra-thin Au film electrode with and without apertures exhibit a *FF* and V_{oc} comparable to that of OPV devices of the same structure employing an ITO glass electrode. The current density is improved by > 10% if the plane electrode is replaced with the electrode with micron-size apertures. The only significant difference in performance between the latter and ITO electrode is a ~ 10% lower J_{sc} which can be attributed to the difference in far-field transparency. However, with optimisation of the aperture density and diameter we believe that this relatively small difference can be significantly reduced. Notably, the comparable V_{oc} demonstrates that even with a resistive hole-extraction layer such as WO_x, charge carriers generated in regions of the photoactive layer adjacent to optically large apertures in the window electrode can be efficiently extracted to the external circuit.

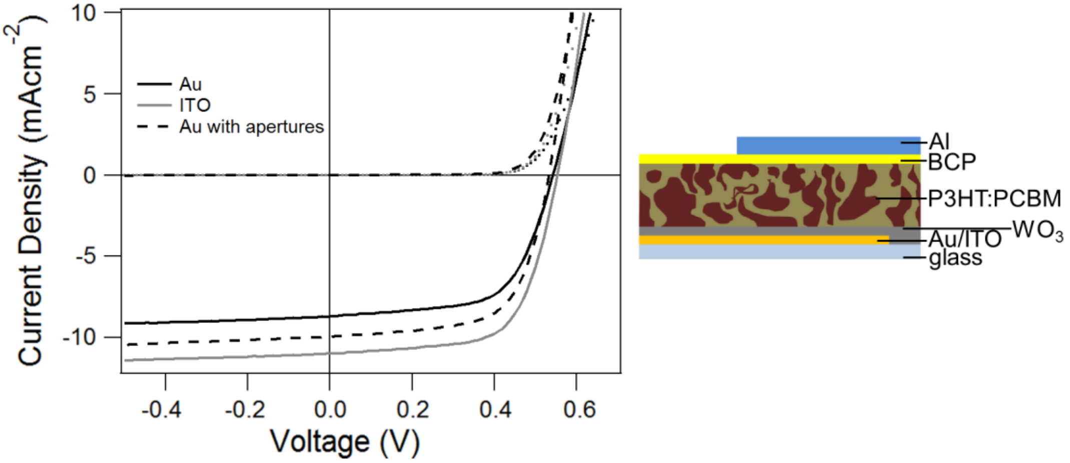

Figure 3.12: *J-V* characteristics and device architecture of OPV with structure: electrode / WO_3 / 1:1 P3HT:PCBM / BCP / Al.

Table 3.4. Typical device characteristics of the OPV test cells studied of structure: Au electrode / WO_3 / P3HT:PCBM / BCP / Al.

Window electrode	Au	Au with apertures	ITO
J_{sc} [mA cm^{-2}]	8.75 ± 0.20	9.90 ± 0 .20	10.70 ± 0.25
V_{oc} [V]	0.54 ± 0.01	0.53 ± 0.01	0.55 ± 0.02
FF	0.64 ± 0.02	0.64 ± 0.02	0.64 ± 0.02
η [%]	3.05 ± 0.20	3.35 ± 0.20	3.80 ± 0.20

3.4 Conclusions

In this chapter the development of a rapid, solvent free method for the fabrication of highly transparent ultra-thin (~ 8 nm) Au films on glass based on co-deposition of a mixed molecular adhesive layer immediately prior to Au thermal evaporation is described. Different type of molecular adhesive were tested: APTMS, MPTMS and mixed APTMS:MPTMS. The protocol for nanolayer preparation was optimised for each adhesive in order to minimise the sheet resistance. The properties of Au films on different types of nanolayer were investigated as well as the density and composition of the nanolayer itself. APTMS:MPTMS mixed nanolayer proved to have properties best suited for OPV application in addition to the shortest preparation time. The resulting films are highly transparent (mean transparency > 70%) and electrically conductive (R_{sheet} ~11 Ω sq^{-1}) with a remarkably low surface roughness and are exceptionally robust towards ultra-sonic agitation in a variety of solvents and UV/O_3 surface treatment. As such they are potentially widely applicable for a range of large area applications, particularly where stable, chemically well-defined, ultra-smooth electrodes are required. By integrating microsphere lithography into the fabrication process the transparency could be improved *via* the incorporation of a random array of circular apertures in the film. The application of these nano-structured Au electrodes is demonstrated in efficient P3HT:PCBM OPVs where it offers a viable alternative to ITO. The difference between the performance of devices employing a plane Au electrode and ITO coated glass; η = 3.80% *vs.* 3.05% is attributed to the lower far field transparency of Au electrode. It is shown that this efficiency gap can be reduced by introducing micron-sized apertures into the film and so improving the far-field transparency of metal electrodes (η = 3.35%), although the increase in transparency is at the expense of sheet resistance and so a balance must be struck.

Chapter 4.

Thermal stability of ultra-thin metal film electrodes

Summary

In this chapter the results of studies investigating the thermal stability of the ultra-thin Au electrodes described in Chapter 3 are reported. The range of Au thicknesses investigated is 3.7 nm – 8.4 nm. It is shown that the low thickness of these films renders them amenable to rapid thermal annealing to realise highly crystalline, transparent and electrically conductive window electrodes. By capping these films with a very thin (~10 nm) transition metal oxide layer their thermal stability can be dramatically improved, whilst at the same time improving their far field transparency. This approach is shown to be equally applicable to optically thin Ag electrodes. These electrodes are demonstrated in 1 cm^2 efficient OPV fabricated using one high temperature processing step.

4.1 Introduction

As it has been shown in Chapter 3, sub-10 nm Au films supported on mixed APTMS:MPTMS nanolayer derivatised glass are remarkably robust towards mechanical abrasion and ultra-sonic agitation in a variety of solvents. They are also very smooth and chemically well-defined, making them well suited as a model electrode for fundamental scientific work. However, for many applications it is also desirable to be able to precisely control the degree of crystallinity of the metal, since the crystal structure determines many of its physical properties.[280,281] Crystallinity strongly depends on the properties of the underlayer, the film thickness, deposition method and processing temperature.[161,282,283] Thermal annealing is an effective means of obtaining a highly crystalline structure after film deposition. Apart from changing the crystallinity of the ultra-thin films, the ability to withstand elevated temperatures increases the number of potential applications of these electrodes, to include applications in inorganic PVs such as copper indium gallium selenide (CIGS)) and DSSC, where the processing temperatures can be as high as 500 °C.[163,284,285] For these reasons this Chapter is dedicated to investigating the properties of the optically thin Au films described in Chapter 3 when annealed.

Intuitively a single layer of organic molecules with a thickness less than 0.8 nm would not be expected to be stable at high temperature, particularly above the temperature at which these molecules are known to desorb or degrade. Encouragingly Wanunu *et al.* have shown that 15 nm Au films on APTMS derivatised glass can be annealed at 200 °C for 20 hours to realise a smooth (111) textured surface with an average transparency across the visible spectrum of 32%.[166] Ghandi *et al.* reported that 50 nm copper films supported on MPTMS derivatised silicon substrates and capped with 150 nm Ta were remarkably resistant to fracture along even after annealing to 700 °C, which resulted in toughening of copper films.[167] In this case the interfacial toughening was shown to arise from thermally activated interfacial siloxane bridging, which suppresses nanolayer desorption.[167] An APTMS nanolayer has also been used as an adhesion layer between silicon capped with SiO_2 layer and 35 nm Cu films and shown to withstand temperature of 220 °C.[286] However the thermal stability of sub-10 nm noble metal films supported on monolayer derivatised substrates has not, to the author's knowledge, been reported.

More generally, ultra-thin films of Au would not be expected to be resistant to elevated temperatures owing to the thermodynamic instability resulting from the high surface to volume ratio, which suppresses the melting point and scales inversely with film thickness.[287] Indeed, Doron-Mor *et al.* have shown that sub 15 nm Au films on MPTMS derivatised glass are not stable to even mild heating.[288] Without an adhesive layer films of Au with equivalent thicknesses (<10 nm) are typically discontinuous with an island like structure and so their properties upon annealing have been investigated mainly in pursuit of the unusual optical properties of such isolated particles.[289,290]

Oxides of metals such as Ti, Mo and W are widely used as interfacial layers in OPV architectures to optimise the interfacial energetics.[200,201,202, 203,204] The high refractive index of these wide band gap metal oxides make them effective as anti-reflecting coating for thin metal film electrodes.[141, 145, 291,] Whilst these oxides can be evaporated under high vacuum onto substrates at room temperature, processing from solution requires an annealing step and so requires that the electrode is resistant to elevated temperature.

4.2 Experimental

4.2.1 Preparation of ultra-thin metal films on glass

In this chapter all Au films were prepared according to the optimised procedure described in Chapter 3. Briefly, clean glass substrates were exposed to APTMS:MPTMS vapour for at least 1 hour (or: for 1 hour to APTMS vapour; 20 hours to MPTMS vapour) at a pressure of $\leq$ 50 mbar prior to Au deposition by evaporation at 0.1 nm s^{-1}. To fabricate Ag films the procedure was modified as follows: After solvent cleaning the substrates were exposed to the vapour of MPTMS for 36 hours, followed by Ag evaporation at the rate 0.1 nm s^{-1}. Rapid annealing of metal films was performed in a N_2 atmosphere for 10 minutes, unless stated otherwise, followed by rapid cooling.

In the case of bi-layer metal:metal oxide films MoO_x and WO_x were evaporated immediately after metal deposition without breaking vacuum. TiO_x layers were formed from a precursor solution spin-cast at 2000 rpm for 60 seconds and annealed at 450 °C under N_2. MoO_x solution precursor was also spin-cast at 2000 rpm for 60 seconds, but annealed in the air at 350 °C.

All thermal annealing of metal:metal oxide bilayer films was performed for 30 minutes.

4.2.2 Metal film characterisation

Metal films were characterised using the techniques described in Chapter 2.

4.2.3 OPV fabrication and testing

To demonstrate that these electrodes are suitable for high temperature applications they were incorporated into BHJ OPVs requiring a high temperature processing step. TiO_x precursor was spin-cast onto 8.4 nm Au, 9 nm Ag and commercial ITO electrodes on glass and annealed at 450 °C for 30 minutes. These bi-layered electrodes were used as platforms to build inverted OPV devices with the structure: electrode / ~ 20 nm TiO_x / 1:3 PCDTBT:$PC_{70}BM$ spincasted from 16 mg ml^{-1} overall solution in chloroform / 7.5 nm WO_x / 100 nm Al. Al was deposited through a shadow mask to give a device area of 1 cm^2.

4.3 Results

4.3.1 Properties of sub-9 nm Au films on APTMS:MPTMS derivatised glass prior to annealing

In chapter 3 it is shown that 8.4 nm Au films deposited on a mixed nanolayer of APTMS:MPTMS derivatised glass have a mean transparency of 72%, a sheet resistance of ~ 11 Ω sq^{-1}, smooth surface (R_{rms} ~ 0.4 nm) and are exceptionally robust towards ultra-sonic agitation in a variety of solvents. In order to increase the transparency of these films to 78%, a random array of 1.5 µm circular apertures covering ~ 20% of the surface was introduced into the film using microsphere lithography, although this improvement was at the expense of the electrode sheet resistance, which increased by approximately a factor of three to ~27 Ω sq^{-1}. This increase is attributed to scattering at the aperture edges and loss of material through which electrons can flow. It is evident from Figure 4.1 that a similar improvement in transparency can be achieved by simply reducing the thickness of the metal film, which has the advantage of reducing Au usage. For example, Au films with a thickness of 5.5 nm Au films have a mean transparency of 77% and a sheet resistance of ~ 22 Ω sq^{-1}.

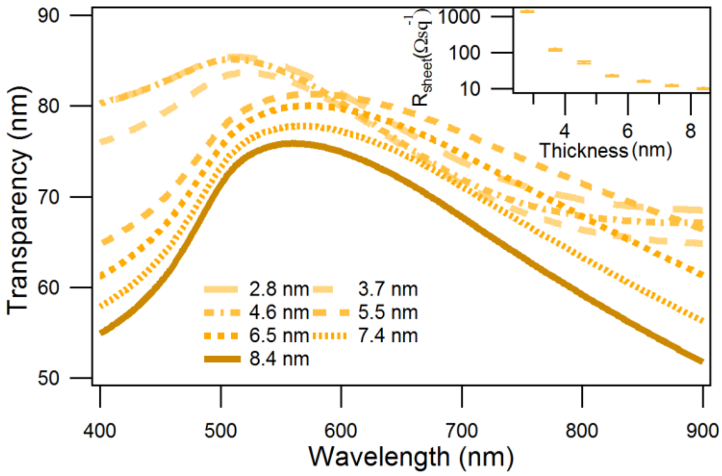

Figure 4.1: The far-field transparency and sheet resistance (inset) of optically thin Au films supported on mixed nanolayer derivatised glass.

It is clear from the inset in Figure 4.1 that whilst the transparency of such films increases approximately linearly by a few percentage points as the film thickness is decreased, the sheet resistance increases exponentially with decreasing thickness. The sheet resistance of films with a thickness much less than 8.4 nm is too high for large area, high current applications such as PVs (where sheet resistance < 15 Ω sq^{-1} is required[160]), although may be sufficient for applications where higher sheet resistances are acceptable. For example the sheet resistance of an Au film with thickness of 3.7 nm is ~120 Ωsq^{-1} with a mean transparency of 78%. The change in shape of the electronic absorption spectra for film thicknesses < 5 nm is indicative of a transition in film morphology from a uniform metal slab to a continuous network of interconnected islands.[288] Films of average thickness lower than 2 nm are not conductive.

4.3.2 Properties of sub-9 nm Au films as a function of annealing temperature

The increase in roughness and loss in conductivity upon annealing is a serious limitation for thin film processing in microelectronics and OPV fabrication where annealing to elevated temperatures is often required.

To investigate how the properties of Au films supported on mixed nanolayer derivatised glass change upon thermal annealing, the sheet resistance of samples was measured as a function of annealing temperature up to 500 °C (Figure 4.2), since the sheet resistance is very sensitive to the degree of film continuity.

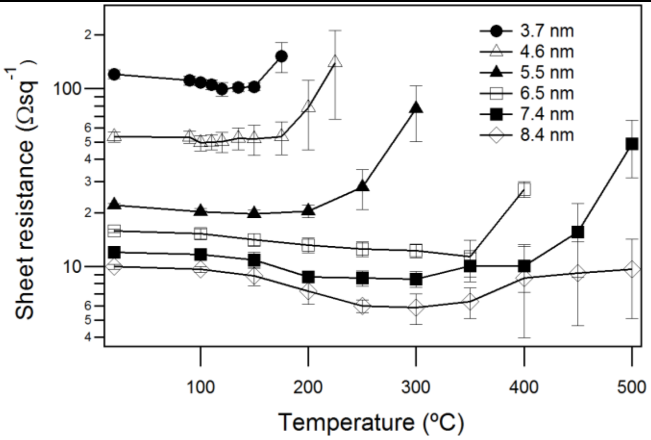

Figure 4.2: Sheet resistance as a function of temperature for Au films of different thickness supported on mixed APTMS:MPTMS nanolayer derivatised glass.

For films with thickness between 3.7 nm and 8.4 nm the temperature at which the films cease to conduct scales with the film thickness. This is consistent with the expectation that as the surface to volume ratio increases, the melting point is reduced[287] and so film thermal stability decreases. Before the onset of film disintegration into discrete islands the sheet resistance initially falls with increasing temperature. This reduction can be attributed to an increase in crystal grain size which reduces the number of grain boundaries at which electron scattering occurs. To verify these changes in the crystallinity as a result of annealing the Au films were investigated using XRD (see Figure 4.3).

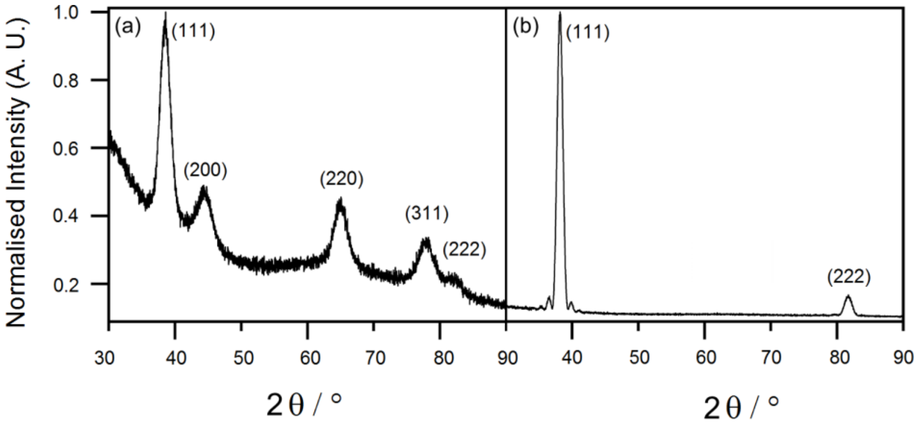

Figure 4.3: XRD spectra: (a) grazing angle of unannealed 8.4 nm Au film, (b) *θ-2θ* spectrum of 8.4 nm Au film annealed to 300 °C.

The XRD measurements show that the as-grown 8.4 nm films are polycrystalline with reflections from a number of different crystal faces; (111), (200), (220), (311) and (222). However, upon annealing at 300 °C for 10 minutes the peaks associated with reflections from the (111) plane dramatically increase in intensity, so much so that the spectra must be gathered at normal incidence. Taken in conjunction with the very flat background this indicates a near perfect (111) textured surface. Furthermore, the presence of the Kiessig fringes on either side of the (111) peak confirms the uniform, defect free structure. Using theses fringes the thickness is computed as 0.78 ± 0.5 nm on the basis of the Sherrer formula.[292] Such a highly oriented structure is unexpected for such short annealing times although is consistent with the suppressed melting point that results from size effects. The loosely packed crystal faces of Au have a lower melting point than the (111) facets,[293] which are known to be '*non-melting*'. That is, melting of the (111) crystal faces at the surface only begins when the bulk (111) Au melting temperature is reached (> 1000 °C)[294] When mobile Au atoms arrive at the site of (111) facet they coalesce, enlarging the (111) crystallite[293] eventually resulting in purely (111) structure. The reduction in sheet resistance can therefore be rationalised in terms of the degree of crystallinity in the film upon annealing, which scales inversely with the extent to which electrons are scattered at crystal boundaries.[295]

The decrease in resistance, observed for all film thicknesses as the anneal temperature is increased, is followed by an increase in resistance. The latter results from the formation of apertures in the films that grow in size and density with increasing temperature due to Ostwald ripening[289] and the volume changes that occur when the film becomes more crystalline. Notably, films with a thickness of 8.4 nm do not fail up to the maximum temperature investigated of 500 °C, which is just below the softening temperature of the glass substrate.[289] Indeed the sheet resistance saturates as a level comparable to that of the unannealed film (~ 11 Ω sq^{-1}). Furthermore, at the optimal annealing temperature of ~ 300 °C the sheet resistance is as low as 6.0 ± 0.5 Ω sq^{-1} only a factor of two greater than that calculated on the basis of the bulk resistivity[272] and a half of the resistance of unannealed films. It is also notable that the onset of hole formation does not begin until 300 °C. Owing to the exceptionally high thermal stability and low sheet resistance of 8.4 nm Au films, films of this thickness were used for subsequent experiments.

In Chapter 3 it is shown that Au films prepared on mixed nanolayer derivatised substrates have a number of advantages over films of the same thickness prepared on single component nanolayers and so it was of interest to see if using a mixed nanolayer also has advantages for the thermal stability. To investigate this the comparative performance of 8.4 nm Au films supported on APTMS, MPTMS and mixed APTMS:MPTMS molecular adhesive layers upon annealing up to 300 °C was investigated (Figure 4.4).

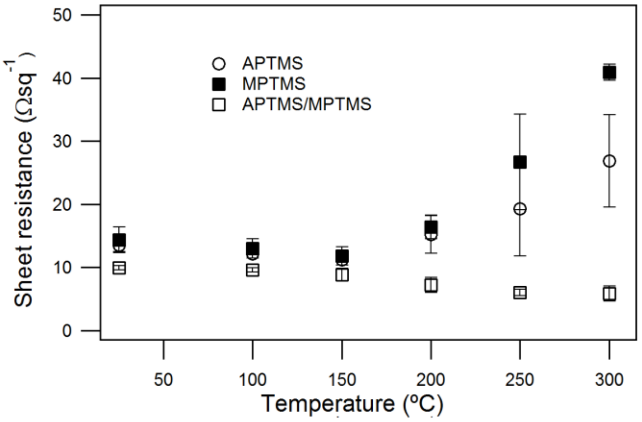

Figure 4.4: Sheet resistance as a function of temperature for 8.4 nm Au films supported on different types of nanolayer.

At room temperature the Au films are continuous and uniform on all three nanolayers. It is evident from Figure 4.4 that in all three cases the sheet resistance decreases with increasing annealing temperature up to a ~ 150 °C. At this temperature apertures begin to form in Au films on APTMS and MPTMS nanolayers, growing in number, density and diameter with increasing temperature until the films disintegrate into individual islands, which result in a rapid increase in sheet resistance. These differences in robustness can be rationalised in terms of the nanolayer coverage and strength of the interaction between the reactive head group and incident Au: For MPTMS modified glass incoming Au atoms bind strongly with the thiol.[270,296] However, in Chapter 3 it is shown that vapour deposition of MPTMS onto glass yields a low surface coverage, since the nanolayer has a thickness well below that expected for a dense monolayer. The results of the XPS study of nanolayer thickness for the different molecular adhesives are summarised in Figure 4.5.

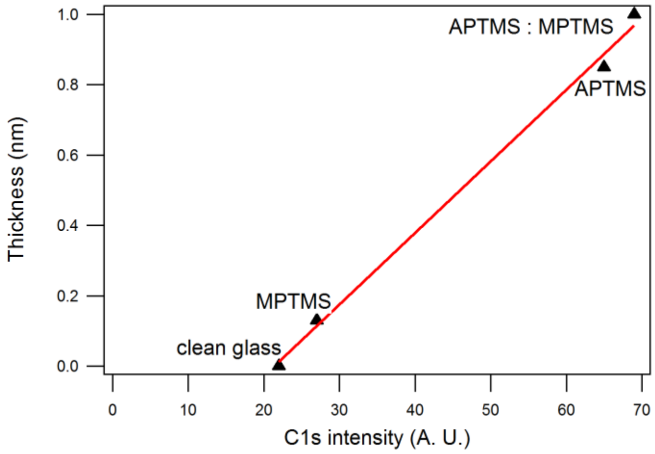

Figure 4.5: Thickness additional to clean glass deduced from Si 2s as a function of C 1s intensity (Experiment and calculation details are provided in Chapter 3).

As a result the low density of anchor points is not sufficient to override the thermodynamic driver to minimise surface energy. Conversely APTMS forms a dense monolayer on glass when deposited from the vapour phase, although the N-Au interaction is known to be a factor of 5 weaker than the Au-S interaction.[270] Whilst this high density of weaker surface binding sites promotes uniform film growth at room temperature, apertures form at temperatures >150 °C resulting in an increase in sheet resistance. The mixed nanolayer therefore offers both a high density of moderate interaction strength Au-N bonds and sufficient density of strong Au-S bonds, which is why Au films supported on a mixed nanolayer are the most robust toward elevated temperature.

4.3.2.1 Morphology of annealed Au films

The evolution of Au film morphology upon annealing was investigated using SEM and AFM. Figures 4.7 show SEM images of the morphology of a typical 8.4 Au film supported on a mixed nanolayer. Consistent with the results of the XRD study it is evident that films deposited at room temperature are polycrystalline, with a very small (< 10 nm) crystallite size, since the images are homogeneous. This is consistent with a picture in which there is a high density of nucleation sites on the substrate surface provided by the mixed molecular nanolayer. Upon annealing 'thermal roughening' is observed due to crystal grain enlargement,[297] as the less stable crystallinites (i.e. those with the highest energy surfaces) melt and provide Au atoms for the growth of (111) crystal faces. Figure 4.6 shows the morphology of 8.4 nm Au films supported on a mixed nanolayer before and after annealing at 300 °C.

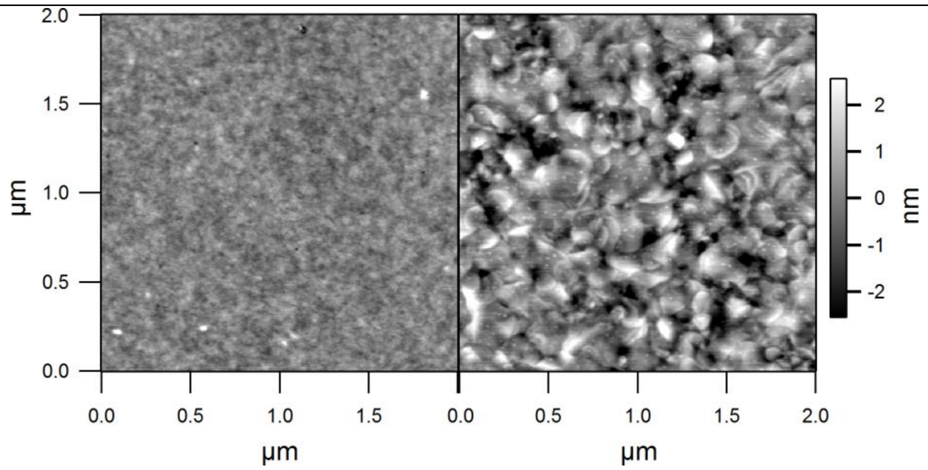

Figure 4.6: AFM morphology of 8.4 nm Au films supported on APTMS:MPTMS nanolayer: Not annealed (left); annealed to 300 °C (right) for 10 minutes.

The smooth surface is transformed into a film of crystallites with diameters of up to a few hundred of nm. This large increase in crystallinity results in a doubling of the surface roughness from 0.4 to 0.8 nm although the absolute value is still very low.

The changes in crystallite size can be also observed as an initial increase in heterogeneity in the SEM images of annealed Au films in Figure 4.7.

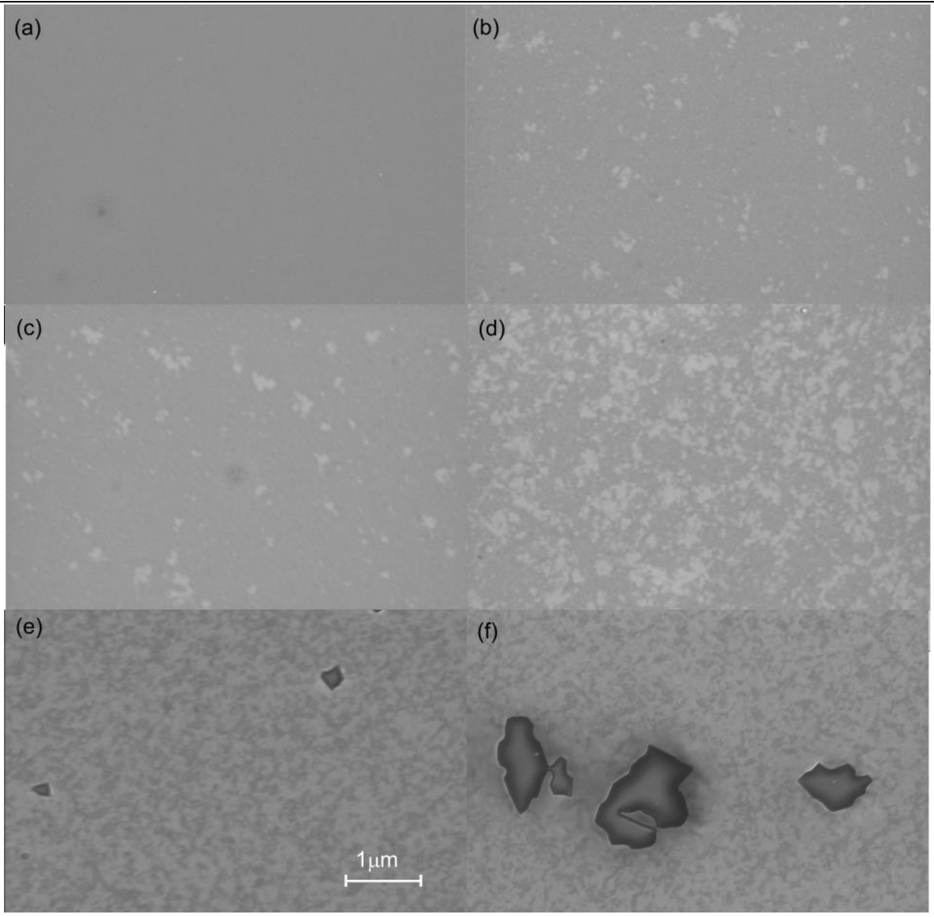

Figure 4.7: SEM images of 8.4 Au films supported on a mixed APTMS:MPTMS nanolayer: Not annealed (a) and annealed to 100 °C (b), 150 °C (c), 200 °C (d), 300 °C (e) and 400 °C (f) for 10 minutes.

The formation of apertures in 8.4 nm thick films supported on mixed nanolayer derivatised glass begins at ~ 300 °C. The formation of apertures upon annealing was also observed in Au films fabricated on APTMS:MPTMS derivatised silicon wafer ruling out the possibility that they result from imperfections on the glass surface (not shown). The size of apertures depends on the size of surrounding crystallities,[298] and hence bigger apertures are obtained in films annealed to higher temperatures (Figure 4.7) since the crystallites are larger. This indicates that apertures form to relieve strain in the film as it reverts to a more dense crystal structure. The surface roughness changes when the first apertures are formed and the thermodynamic driver for crystallisation begins to override film adhesion to the substrate. Importantly, the temperature at which the apertures start to form, is a function of film thickness and the nanolayer density. The latter can be modified by varying the time of exposure to vapour and the back pressure. This is exploited in Chapter 6 where it is desirable to form sub-wavelength apertures.

4.3.2.2 The optical properties of annealed Au films

Since the size distribution and density of apertures can be controlled by the nanolayer type and annealing temperature so can the optical properties of these films. Examples of transparency spectra of Au films of different thickness are shown in Figure 4.8. The transparency spectra of a 3.7 nm Au film (Figure 4.8(a)) show the discontinuous character of this film, even before annealing. However, as the temperature rises the spectrum undergoes significant transformation up to 200 °C, when films disintegrate and the spectrum becomes characteristic for separated Au nanoparticles.[274] Figure 4.8 (b) shows the transparency evolution of an 8.4 nm Au film. The transparency changes uniformly with temperature across the full wavelength range. The peak transparency of these films increases from 75% for unannealed films to 81% for films annealed at 300 °C and then decreases. The holes formed in 8.4 Au film supported on dense APTMS:MPTMS nanolayer are sparse and have typically dimensions of 0.5 – 1 micron. They don’t affect strongly the optical properties of these films, due to the low density of holes and wide size distribution. Larger holes do in fact play a similar role to the large circular apertures described in Chapter 3.

The increase in transparency is comparable to that achieved by using microsphere lithography, but the method is less time-consuming and more suitable for industrial processes. The annealing improves the transparency, conductivity and crystal structure of these films making them ideal model substrates, also suitable for applications requiring high temperature processing (>300°C).

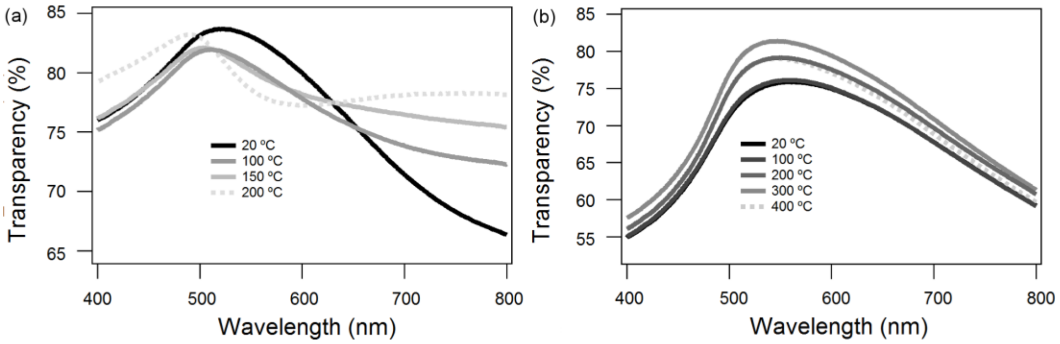

Figure 4.8: The transparency spectra of (a) 3.7 nm Au film and (b) 8.4 nm Au film supported on APTMS:MPTMS nanolayer.

4.3.2.3 Testing the robustness of annealed Au films

Remarkably, Au films with a thickness of 8.4 nm retain their extraordinary robustness upon annealing up to 500 °C: Ultra-sonic agitation in common solvents and scotch tape testing resulted in no significant change in sheet resistance for unannealed and annealed films alike (Table 4.1). This may be explained by interfacial toughening of the Au film/glass interface upon annealing, which has been observed for different SiO_2/nanolayer/Cu systems[165,167, 299] and is attributed to the formation of siloxane linkages.[165, 167]

Table 4.1. Robustness tests of films supported on dense APTMS:MPTMS nanolayer before and after annealing to 500 °C.

Film type	Untreated	Toluene	Water	2-propanol	Scotch tape
			$[\Omega\ sq^{-1}]$		
Room temperature	11.0 ± 0.7	11.2 ± 0.8	12.5 ± 1.0	11.2 ± 0.8	11 ± 1.0
Annealed to 500 °C	9.0 ± 0.5	9.1 ± 0.8	11.0 ± 1.0	9.2 ± 0.6	9.2 ± 0.8

4.3.3 Properties of metal / metal oxide films at elevated temperatures

In the context of an OPV the transparent electrode is often coated with a 5-15 nm thick transition metal oxide layer to optimise interfacial energy level alignment and light coupling into the device. The most commonly used oxides are TiO_x, WO_x, MoO_x, ZnO although V_2O_5 can also be used. Transition metal oxides may be deposited by evaporation[203,204] and/or from solution.[200,201,202] Solution deposition processing typically requires a high temperature post-deposition anneal to drive off the solvent and decompose the organometallic sol from which they are formed. The oxides are typically spin-cast from an alcohol solution of the precursors (e. g. $Ti[OCH(CH_3)_2]$[300,] and $MoO_2(OH)(OOH)$[200,299]). These compounds undergo hydrolysis even at room temperature with the formation of TiO_x and MoO_x. Mild heating (100 – 150 °C) accelerates the evaporation of the solvent which reduce the thickness of the overlayer.[200, 301, 300] The most dramatic changes in film structure occur below 200 °C when a film of amorphous oxide is formed. However, further annealing is known to improve the electrical properties of these films[200] and promote crystallisation and crystallite sintering. For example, TiO_x is often annealed at 450 °C in the context of DSSCs at which temperature the anatase and rutile start to crystallise.[300] As shown previously, ultra-thin Au electrodes can withstand temperatures up to 300 °C before the onset of aperture formation. To investigate if the continuity of these films can be preserved at higher temperatures when buried beneath an oxide layer, 8.4 nm Au films supported on an APTMS:MPTMS nanolayer with thin overlayers of TiO_x, MoO_x and WO_x were tested. The layers of TiO_x and MoO_x were spin-cast from solution. WO_x was evaporated under high vacuum. All three oxides were deposited according to established procedures reported in the literature with thicknesses of ~ 10 nm and annealed at 500 °C under nitrogen together with an 8.4 nm Au reference electrodes. The morphologies of these films before and after annealing are depicted in Figure 4.9.

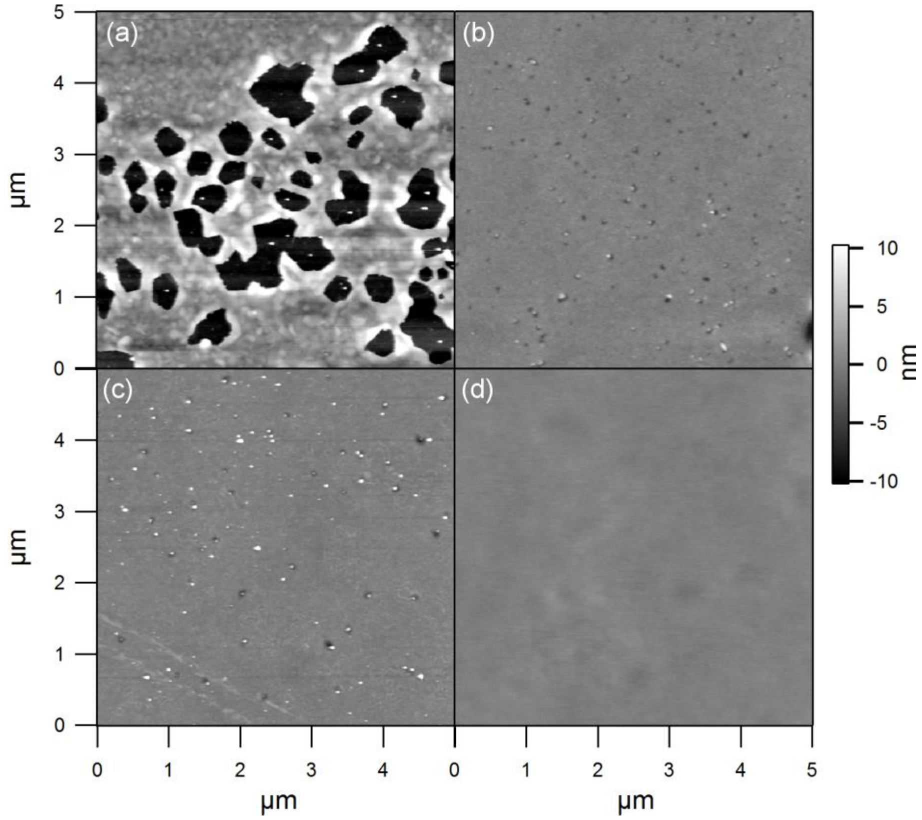

Figure 4.9: AFM morphologies of 8.4 nm Au films without an overlayer (a); and with overlayers of: MoO_x (b); WO_x (c) and TiO_x (d) all annealed to 500 °C for 30 minutes.

As expected, the uncapped film shows a high density of holes of different diameters. Conversely, films with MoO_x and WO_x are smooth with an R_{rms} ~1 nm, whilst films with a TiO_x overlayer have a very smooth surface comparable to that of unannealed Au (R_{rms} ~ 0.4 nm) and are defect-free. Since MoO_x can also be evaporated, the robustness of 8.4 nm Au / 10 nm MoO_x with an evaporated MoO_x was also tested. Au films capped with an evaporated MoO_x layer were not as robust as those capped with the other three types of oxide layer. When annealed at temperatures above 400 °C the film catastrophically breaks down (Figure 4.10).

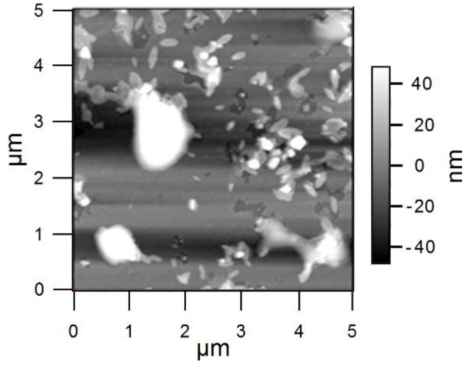

Figure 4.10: AFM morphologies of 8.4 nm Au film with evaporated MoO_x overlayer annealed to 500 °C.

Collectively these results indicate that a thin oxide layers deposited from solution are very effective at making optically thin Au films more robust towards elevated temperature. This is attributed to the gradual hardening of these films through solvent loss, and the mobility of the oxide particles immediately after deposition, which helps to minimise strain in the oxide overlayer.

The sheet resistance of films with an oxide overlayer annealed to 500 °C is ~7 Ω sq^{-1}. Such a low resistance is the lowest value for this thickness, and was previously only achieved for films without an oxide overlayer when annealed at 300

°C, where the conductivity is enhanced as a result of the increase in crystallinity without the deleterious influence of forming apertures. To test if apertures do actually form in Au films buried underneath the oxide overlayer when annealed to 500 ^{o}C but are obscured by the oxide, the following experiment was performed: An 8.4 nm Au film was deposited onto two APTMS:MPTMS nanolayer derivatised glass substrates. Both films were annealed at 500 °C which resulted in aperture formation (Figure 4.11 (a)). One of these annealed films (with apertures) along with one previously unannealed film (without apertures) was then covered with a TiO_x overlayer. Both films were then annealed at 500 °C and their morphology was examined using AFM. The apertures formed during the first annealing step are still well-pronounced (Figure 4.11 (b)), indicating that the TiO_x overlayer is of uniform thickness and does not hide the apertures. If the aperture formed underneath the TiO_x they would be evident as indentations. However the film which was not annealed prior to TiO_x deposition is smooth and remains aperture free (Figure 4.11 (c)) which indicates that 8.4 nm Au film annealed with TiO_x overlayer retain intact continuity up to 500 °C.

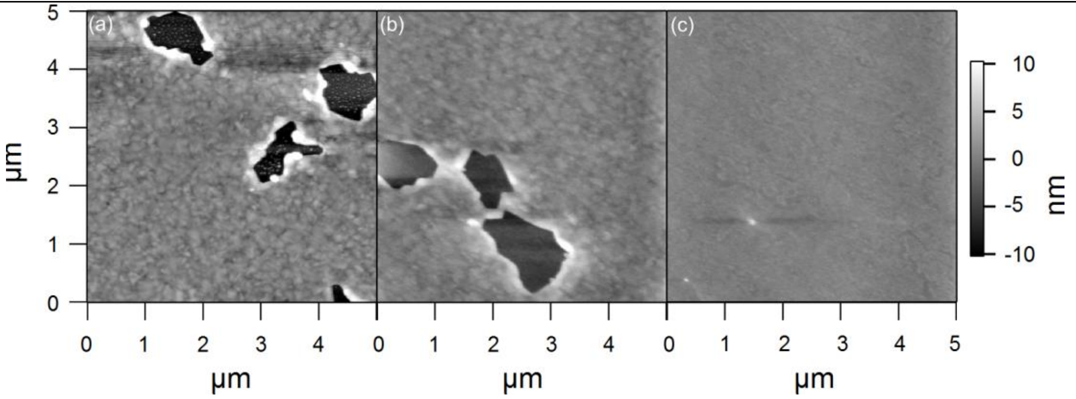

Figure 4.11: AFM morphology of: (a) 8.4 nm Au film annealed to 500 °C; (b) 8.4 nm Au film annealed to 500 °C and then again with TiO_x overlayer; (c) 8.4 nm Au films annealed to 500 °C with TiO_x overlayer.

Apart from the very low sheet resistance and ultra-smooth surface these films show also excellent optical properties, due to the anti-reflective role played by the oxide overlayer, which increases in the mean transparency of the metal / metal oxide bi-layers as compared to the metal films without an oxide overlayer: MoO_x - ~71%, WO_3 – ~73%, TiO_x – ~76%, compared to ~ 65% before annealing (Figure 4.12). Importantly this improvement narrows the gap between these metal electrodes and ITO coated glass (mean transparency ~85%) without adding an extra processing step to OPV fabrication. It is also notable that the shape of the absorption spectra with a thin oxide layer is very similar to that of the unannealed metal film, which is further evidence that the metal film is continuous after annealing.

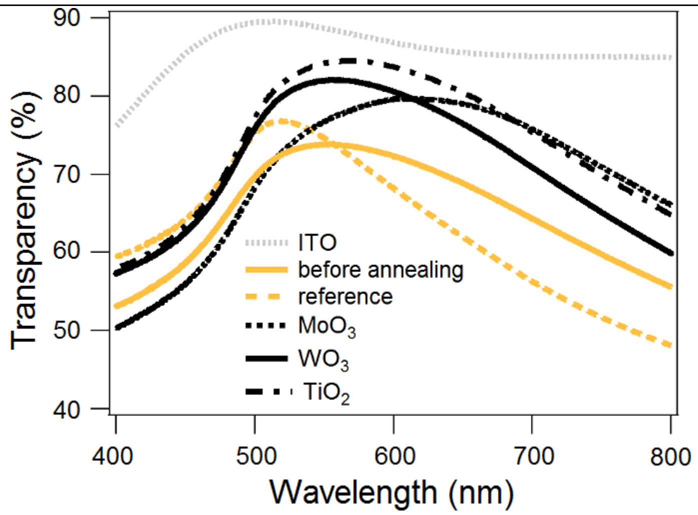

Figure 4.12: Far-field transparency spectra of 8.4 nm Au films supported on APTMS:MPTMS with and without different oxide overlayers annealed to 500 °C; for comparison the spectrum of a not annealed Au film and ITO on glass is also shown.

The transparency at 600 nm of thin Au films on glass, in the air, with different oxide overlayer has been simulated using MacLeod software. The simulated transparencies as a function of thickness of Au and TiO_x/MoO_x/WO_x oxide are presented in Figure 4.13: The results remain in good agreement with experiment and can be used for further optimisation of the optical properties of thin metal films.

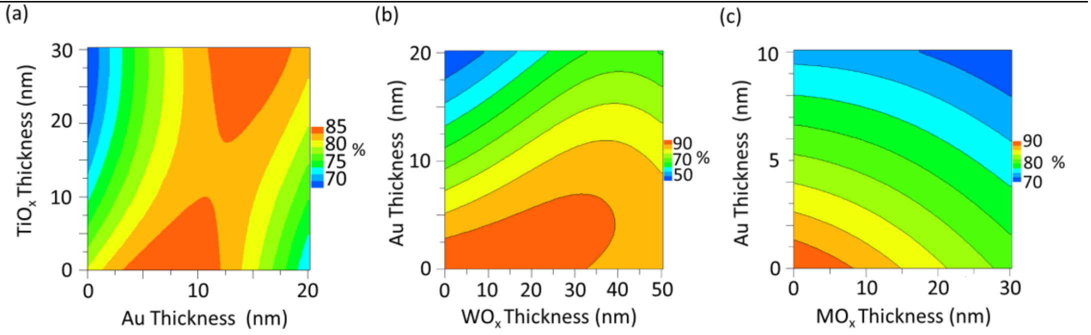

Figure 4.13: Calculated contour plots of transmittance for metal/metal oxide bi-layer on glass upon variation of layer thicknesses. The simulations were performed for different oxides; (a) TiO_x; (b) WO_x; (c) – MoO_x.

4.3.4 Thermal stability of optically thin Ag films capped with an oxide overlayer

Ag is another technologically important noble metal, which offers the advantage of lower cost as compared with Au. Ag is the most widely used metal in conventional silicon PV and is also known for strong plasmonic effect which has been investigated in Chapter 6. It was therefore interesting to see if thin oxide overlayers could also be used to improve the robustness of optically thin Ag films towards high temperature.

Ag films were deposited on MPTMS derivatised glass. Due to the low density of MPTMS molecules attached to the glass surface when deposited from the vapour phase there are few crystallite nucleation centres for the evaporated metal, and so the film forms from large Ag islands which require more material to coalesce and form uniform conductive films. This is manifested by a greater percolation thickness of Ag films (>7 nm) which is evident from the change in shape of the transparency spectra for films with an effective thickness between 5 nm and 7 nm (Figure 4.14). Ag films of thickness above 10 nm have a very low sheet resistance (< 10 Ω sq^{-1}), which increases exponentially with reduced thickness.

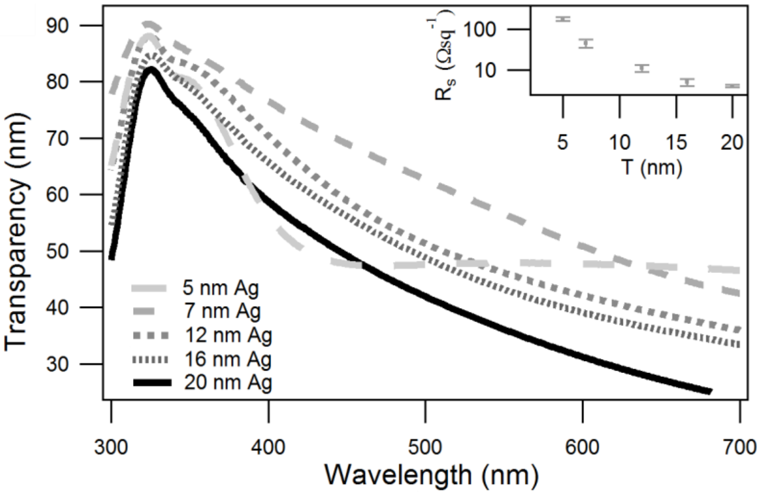

Figure 4.14: The far field transparency and sheet resistance (insets) of Ag films supported on MPTMS derivatised glass (derivatisation time: 36 hours).

To demonstrate the versatility of the oxide overlayer approach to improving metal film robustness towards high temperature 9 nm Ag electrodes were covered with ~ 10 nm TiO_x overlayer and annealed to 500 °C. There was no change in sheet resistance (~6 Ωsq^{-1}) and the transparency was improved (Figure 4.15).

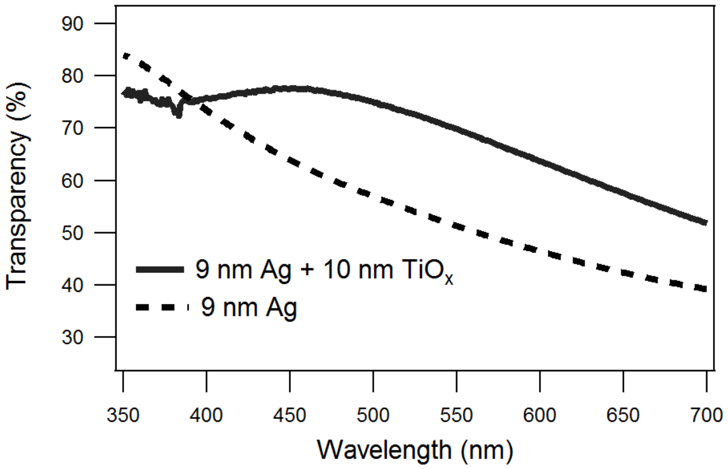

Figure 4.15: The far field transparency of 9 nm Ag films with and without TiO$_x$ overlayer.

4.3.5 OPV studies

The proven stability of 8.4 nm Au films towards annealing at temperatures up to 500 °C when capped with a thin oxide overlayer opens the door to the application of these window electrodes for optoelectronic devices requiring a high temperature processing step in their fabrication. To demonstrate this, efficient inverted OPVs, based on a PCDTBT:PC$_{70}$BM BHJ were fabricated, employing a thin ~ 10 nm TiO$_x$ electron extracting layer. 8.4 nm Au and 9 nm Ag film electrodes capped with TiO$_x$ overlayer were annealed at 450 °C for 30 minutes to realise transparent, air-stable electron-extracting electrodes that are indium free and exceptionally smooth. Identical devices employing ITO glass as the window electrode were fabricated as a reference.

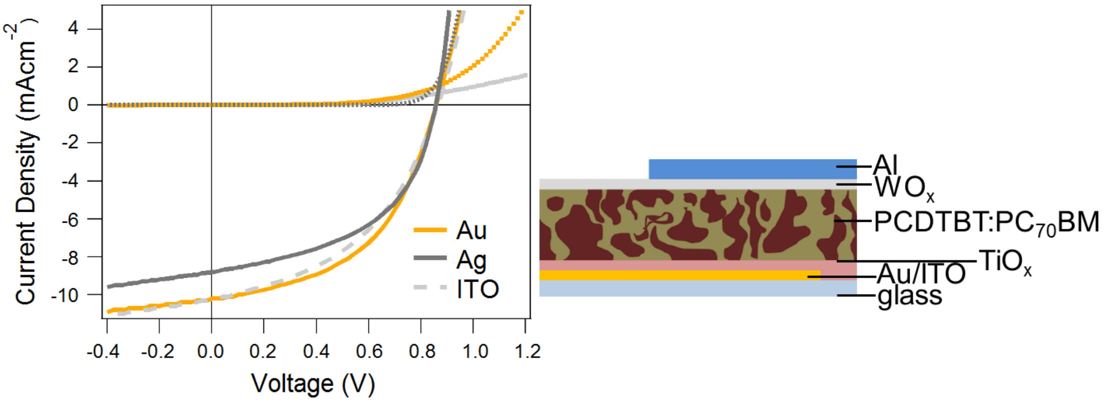

Figure 4.16: The *J-V* characteristic of devices of structure: electrode (Au, Ag or ITO on glass) / TiO_x / PCDTBT:PC_{70}BM / WO_x / Al under 1 sun solar illumination.

OPVs employing Au, Ag and ITO electrodes exhibited η of 4.4 ± 0.2%, 3.8 ± 0.2% and 4.3 ± 0.1% respectively (Figure 4.16). Notably there is no difference in J_{sc} between devices employing ITO and Au electrodes. Whilst the Au electrode is less transparent on average than ITO glass, the absorption spectrum of PCDTBT:PC_{70}BM BHJ is well matched to the broad transparency window in the Au/TiO_x electrode where the difference in transparency between the electrodes is small. Optical modelling performed by O'Connor *et al.* has shown that OPVs employing thin metal film transparent electrodes may outperform those with ITO due to improved light absorption resulting from microcavity effects.[128] The lower transparency of Ag films in the longer wavelength range results in a reduced J_{sc} by ~ 2 mAcm^{-2}. The steeper gradient near to the open-circuit condition is consistent with the lower resistivity of the metal film electrodes. Also the shunt resistance in ITO cells is lower, which may be accounted for by the fact that the metal electrodes are smoother and so there are likely to be fewer filamentary shorts.

4.4 Conclusions

In this chapter the properties of thin Au films on nanolayer derivatised glass have been studied, showing that the coalescence thickness is only 5.5 nm. The protocol for fabricating these films has also been adapted to another technologically important noble metal: Ag. Thin Ag films have been fabricated on MPTMS monolayer modified glass. The coalescence thickness for Ag is between 5 and 7 nm. Ag films showed comparable sheet resistance to Au but lower transparency due to the high reflectivity of Ag for wavelengths above 400 nm.

The properties of Au films prepared according to the procedure reported herein are dramatically improved as compared to those previously reported in the literature. Moderate annealing improved the transparency and conductivity of whole investigated range of Au film thicknesses (3.7 nm to 8.4 nm). For example the transparency of 8.4 nm Au films increase by ~5% after annealing to 300 °C and the sheet resistance decreases from 12 to 6 Ω sq^{-1}, which is only ~ 3 Ω sq^{-1} higher than for bulk Au. The thermal energy induces growth of (111) crystallites of size increasing with temperature, which eventually leads to formation of apertures surrounded by Au crystallinites. The temperature, at which the apertures start to form, is thickness dependent and is manifested by rapid increase in sheet resistance and deviation in the shape of transparency spectrum, caused by scattering effects.

It has been shown that the robustness of thin Au films towards elevated temperature can be greatly improved by capping it with a thin oxide overlayer. The properties of sub-10 nm Au films capped with a thin metal (Mo, Ti, W) oxide overlayer were investigated, proving them to be good protective layers up to 500 °C. Moreover, oxide overlayers improve the far-field transparency of these metal films due to their high refractive index. This approach is better than putting micron-sized apertures into the film using microsphere lithography (Chapter 3), since metal oxides are employed in OPV architectures as interfacial layers, and so this step doesn't add complexity to OPV fabrication and it increases transparency without compromising sheet resistance. 9 nm Ag films have also proved to be compatible with TiO_x processing; they retain low sheet resistance and show improved transparency after oxide deposition and annealing.

Au and Ag electrodes have been incorporated into efficient PCDTBT:$PC_{70}BM$ solar cells with a TiO_x electron transporting layer requiring high temperature processing. The efficiency of devices employing Au and ITO are comparable, which opens the door to the widespread utilisation of these window electrodes in fundamental research and a broad range of applications including DSSC, inorganic PVs and infra-red reflective glass.

Chapter 5.

Metal window electrodes on flexible substrates

The work presented in this chapter has been published in:
H. M. Stec, R. A. Hatton, *Widely Applicable Coinage Metal Window Electrodes on Flexible Polyester Substrates Applied to Organic Photovoltaics*, ACS Applied Materials & Interfaces, **2012**, *4* (11), 6013-6020.

Summary

In this chapter the molecular adhesive method for the fabrication of ultra-thin Au films on glass described in Chapter 3 is translated to the technologically important flexible substrates PET and PEN, and extended to the lower cost coinage metals Ag and Cu. A molecular adhesive layer of APTMS and MPTMS was chosen for these metals since the nitrogen in primary amines is known to coordinate with Cu,[302] Ag[303] and Au[304] *via* its lone pair, and thiols are known to bind to all coinage metals *via* a strong covalent linkage.[296] Since PET and PEN have no native surface hydroxyl groups onto which these silanes can covalently bind, a method is described for introducing them onto the surface of these plastics prior to APTMS:MPTMS deposition, which does not increase the substrate roughness. It is shown that the power conversion efficiency of 1 cm^2 OPVs employing 8 nm Ag and Au films as the hole-extracting window electrode exhibit performance comparable to those on ITO, with the advantage that they are resistant to repeated bending through a small radius of curvature. These results combined with lifetime studies show the superior properties of these metal electrodes. Unexpectedly OPVs employing Cu and bilayer Cu:Ag electrodes exhibit inferior performance due to a lower V_{oc} and FF.

Measurements of the interfacial energetics made using the Kelvin probe technique provide insight into the physical reason for this difference.

5.1 Introduction

Conducting oxides, such as ITO and fluorine doped tin oxide, are universally employed as the transparent electrodes in the current generation of OPVs. However conducting oxides are not relevant as a material for truly flexible organic electronics since they are inherently brittle and so fail catastrophically upon bending. [100,101] Additionally, in order to achieve a low sheet resistance (i.e. $< 15\ \Omega\ \text{sq}^{-1}$)[91, 160] ITO must be annealed at temperatures ≥ 300 °C,[98] a process that is incompatible with low cost, highly transparent flexible plastic substrates such as PEN and PET. As a result the sheet resistance of commercially available ITO films supported on plastic substrates is typically $> 35\ \Omega\ \text{sq}^{-1}$, which is 3-4 times higher than on glass.[305,306] Further problems associated with the use of conducting oxides is the high cost of patterning oxide films, the chemically ill-defined nature of the surface and the relatively high surface roughness, which adversely impact the stability of the electrode contact with the adjacent organic layer.[96, 97, 307] The complexity of ITO and other conducting oxides also makes it difficult to investigate the science of electrode - organic semiconductor contacts in organic optoelectronic devices.[83] It is now widely recognised that the electrode interfaces are critical determinants of the performance of OPVs and that there is a great deal yet to be understood about organic semiconductor / electrode contacts, particularly regarding the process of charge carrier extraction.[89, 308] As a result window electrodes that bridge the gap between model substrates required for fundamental science and truly flexible window electrodes for practical applications are highly desirable. In the absence of a commercially available alternative, ITO supported on PET is however the only benchmark against which new, flexible window electrodes can be compared.

For the full potential of OPVs to be realised they must be fabricated on flexible substrates to enable rapid roll-to-roll fabrication, although there are very few reports relating to the use of unpatterned metal films on flexible substrates as the window electrode for OPV. Kim *et al.* have recently demonstrated OPVs fabricated on 15 nm thick Au wrinkled electrodes on PET with a cell area of 0.18 cm^2 and a power conversion efficiency of 1.8%.[140] Yambem *et al.* have demonstrated small area OPV employing flexible 19 nm Ag electrodes evaporated onto PET with power conversion efficiency of 2.3%.[123] Optically thin Cu films sandwiched between oxide layers are also emerging as a promising electrode materials for OPVs; Perez Lopez *et al.* have recently demonstrated 18 nm Cu films sandwiched between the MoO_x layers in 0.22% efficient OPVs on glass,[141] although unpatterned copper films have not yet been used as window electrodes in flexible OPV.

Another reason why optically-thin metal films on flexible substrates are not widely used as the window electrode in OPV is that they can be extremely fragile. For example, Wu *et al.* reported that 20 nm thick Cu films prepared by sputtering onto flexible poly(dimethylsiloxane) fail catastrophically when bent through an 8 mm radius,[119] which is caused by poor adhesion between the metal and the substrate. To address this problem on rigid substrates the substrate surface can be modified with a methoxysilane adhesive layer prior to metal deposition as described in Chapter 3 of his thesis. This approach has not been previously used to prepare optically thin films of other coinage metals, nor has it been applied to plastic substrates. The reason for the latter is the absence of native surface groups onto which silanes can covalently bind on most technologically important plastics and the limitation imposed by the requirement for solvent orthogonality when chemically modifying plastics from solution.

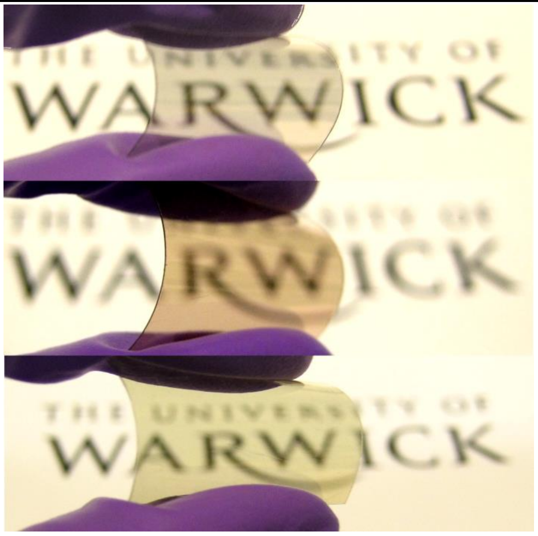

Figure 5.1: Photographs of 8 nm Ag (top), Cu (middle) and Au (bottom) on APTMS:MPTMS derivatised PET substrates.

5.2 Experimental

5.2.1 Preparation of ultra-thin metal films on plastic

PET - and PEN were cleaned using the standard procedure described in Chapter 2. After acetone vapour treatment substrates were UV/O_3 treated for 4 minutes unless stated otherwise. The substrates were immediately transferred to a dessicator where they were exposed to the vapour of APTMS:MPTMS at 50 mbar for 4 hours before loading into an evaporator for Au, Cu and Ag deposition. The metal deposition rate was 0.1 nm s^{-1}.

5.2.2 Substrate characterisation

To characterise the chemical composition of the plastic substrate surface before and after oxidative treatment and after chemical modification with an APTMS:MPTMS nanolayer, high resolution X-ray photoelectron spectroscopy (HRXPS) was employed. HRXPS measurements were performed and analysed as described in Chapter 2.

Static water contact angle measurements were made to probe sample surface hydrophobicity as described in Chapter 2.

5.2.3 Metal film characterisation

Metal films were characterised using the techniques described in Chapter 2.

5.2.4 OPV fabrication and testing

ITO coated PET with a sheet resistance 45 Ωsq^{-1} was cleaned in the same manner as the PEN and PET substrates. Two types of devices were fabricated: *(i)* solution processed BHJ with the structure: electrode / 10 nm MoO_x / 1:3 PCDTBT:$PC_{70}BM$ spincasted from 16 mg ml^{-1} overall solution in chloroform / 8 nm BCP / 100 nm Al; and (ii) small molecule bilayer OPVs with the structure: electrode / 1 nm perylene-3,4,9,10-tetracarboxylic-3,4,9,10-dianhydride (PTCDA) / 43 nm pentacene / 40 nm C_{60} / 8 nm BCP / 100 nm Al. Bending tests were conducted on ~1 cm^2 OPVs; Devices were repeatedly bent over a 4 mm radius of curvature.

5.3 Results and discussion

5.3.1 Electrode fabrication

PEN and PET are widely regarded as the substrates of choice for flexible organic optoelectronics due to their high transparency, good mechanical properties and resistance to oxygen and water vapour penetration.[120, 309,310] The substitution of phenylene ring in PET with the bulkier naphthalene in PEN imparts a higher melting point and increases absorption below 380 nm, thereby simultaneously improving thermal stability and filtering out UV photons which are suspected of degrading organic semiconductors.[238] The weak adhesion between coinage metal films deposited by vacuum evaporation and these plastics results in poor film quality. For example, Au films with an effective thickness of 8 nm on PET have a sheet resistance of 31 Ω sq^{-1}, which is a factor of 3 higher than that achieved using the method reported herein and is arguably too high for OPV applications. Furthermore upon 10 minutes ultra-sonic agitation in water this increases to 40 Ω sq^{-1}. When Cu films of the same thickness on PET are subject to an identical test they fail completely. The effect of brief ultra-sonic agitation in various solvents on 8 nm Cu and Au films prepared by vacuum deposition directly onto PET and PEN substrates is summarised in Table 5.1.

Table 5.1. Sheet resistance of 8 nm Au and Cu films supported on untreated PEN and PET substrates before and after ultra-sonic agitation in three common solvents: toluene, water and 2-propanol.

Substrate	Untreated	Toluene [Ω sq^{-1}]	Water	2-propanol
Au/PEN	25.0 ± 2	29 ± 3	50 ± 5	30 ± 2
Au/PET	31 ± 2	31 ± 2	40 ± 5	31 ± 2
Cu/PEN	18 ± 2	25 ± 2	>600	25 ± 2
Cu/PET	16 ± 2	21 ± 2	Not conductive	23 ± 2

To improve the robustness of optically thin films of these metals on plastic substrates and promote uniform film growth at low thickness we have explored the possibility of chemically modifying the surface of PEN and PET substrates using a mixed monolayer of APTMS and MPTMS. Compatibility with flexible substrates is only possible because the monolayer is deposited from the vapour phase, which circumvents complexity that results from the frequent incompatibility of these plastics with solvents. Whilst APTMS and MPTMS couple to glass substrates *via* native surface hydroxyl groups, no such groups exist at the surface of PET or PEN and so it is necessary to introduce surface hydroxyl moieties without undermining the mechanical integrity of the surface. Oxidative treatments such as oxygen plasma[311] and UV/O_3[242] can be used to form reactive oxygen containing moieties at the surface of plastics, although for the current purpose the latter method was found to be most suitable since it is less aggressive than plasma oxidation and does not increase the surface roughness, which remained unchanged at R_{rms} = 1.5 nm ± 0.2 nm for treatment times of < 5 min.

The incorporation of hydrophilic moieties at the intrinsically hydrophobic polymer surface drastically alters its hydrophilicity and so the optimal oxidation time was determined by measuring the static water contact angle as a function of UV/O_3 treatment time. It is evident from Figure 5.2 that the increase in surface hydrophilicity begins to saturate after 4 minutes.

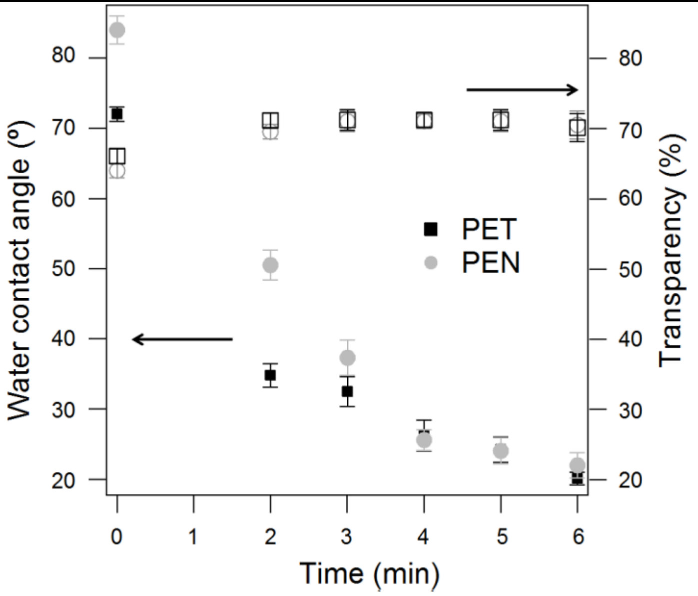

Figure 5.2: Static water contact angle of PET and PEN films and average transparency of 8 nm Au films supported on mixed nanolayer derivatised PET and PEN as a function of UV/O_3 treatment time.

After this period the maximum transparency of 8 nm Au films evaporated on APTMS:MPTMS treated substrates is achieved. This change results from an increase in the density of oxygen containing moieties at the surface, which was verified using HRXPS (Table 5.2).

Table 5.2. C 1s and O 1s HRXPS survey scan summaries before and after UV/O_3 treatment of PET and PEN expressed as atomic percentages (**Columns 2 and 3**); **Column 4 (Blue):** Proportion of C 1s peak assigned to C-OH, -C-O-C- and COO-C bonding environments.

	C 1s [%]	O 1s [%]	C 1s (alcohol, ester, ether) / C1s
PEN	78.8 ± 0.1	21.1 ± 0.1	0.14
PET	72.8 ± 0.1	27.2 ± 0.1	0.21
PEN UV/O_3 treated	69.9 ± 0.2	29.7 ± 0.2	0.22
PET UV/O_3 treated	68.1 ± 0.1	31.9 ± 0.1	0.24

The proportion of the C 1s core level peak assigned to C-OH, -C-O-C- and COO-C increased by ~ 3% on PET and ~ 8% on PEN. By measuring the ratio of the N 1s to S 2s peak areas in the HRXPS spectra, the ratio of APTMS to MPTMS was determined to be 3.52 ± 0.03 on PET and 3.43 ± 0.03 on PEN. Notably the optimised derivatisation time and composition of the resulting mixed monolayer is very similar to that reported in Chapter 3. This similarity demonstrates the versatility of this approach for the preparation of ultra-thin Au films on very different substrates.

The requirement for both UV/O_3 treatment and APTMS:MPTMS vapour treatment is evident from Figure 5.3; the far-field transparency of an 8.4 nm Au film on PEN is highest when the substrate has been UV/O_3 and APTMS:MPTMS vapour treated. It is also clear that the optical properties of optimised Au films on PEN are essentially identical to those on glass.

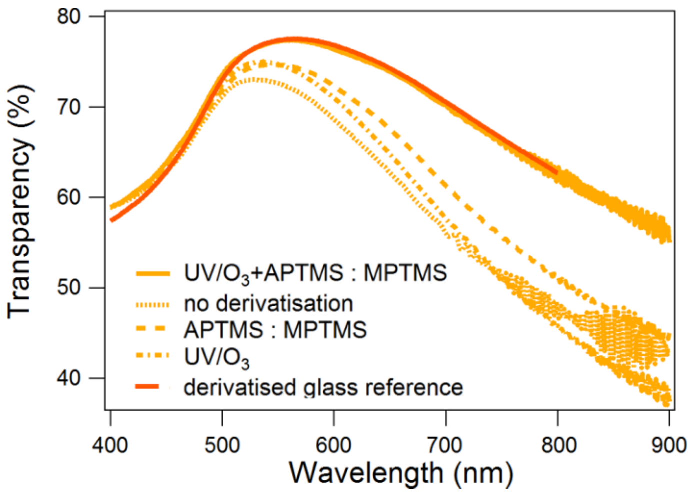

Figure 5.3: Far-field transparency spectra of 8.4 nm Au films on derivatised and non-derivatised PEN. An 8.4 nm Au film on glass nanolayer derivatised according to the optimised procedure given in Chapter 3 is also shown for comparison.

Figure 5.4 shows how the sheet resistance and mean transparency of Au films supported on nanolayer derivatised PET and PEN depends on the metal thickness. It is evident from Figure 5.4 that the properties of Au films on PET and PEN are essentially identical.

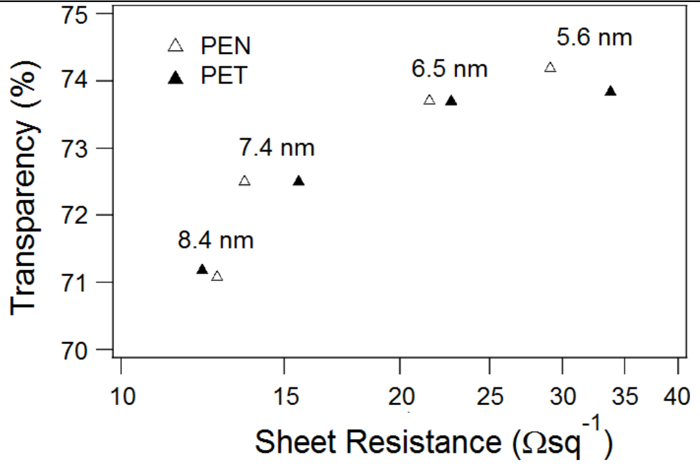

Figure 5.4: Graph summarising mean optical transparency as a function of sheet resistance for different thicknesses of Au on UV/O_3 treated PET and PEN derivatised with an APTMS:MPTMS nanolayer.

It is evident from Figure 5.5 that the roughness of 8 nm Au, Ag and Cu films fabricated on PET is very low (≤ 1.6 nm) and comparable to that of the underlying plastic, consistent with the formation of metal films of uniform thickness. Whilst the sheet resistance is 4-5 times higher than that calculated on the basis of the bulk resistivity of the metals in each case,[272] it is comparable to that of optimised ITO films on glass and thus low enough for use in OPVs.

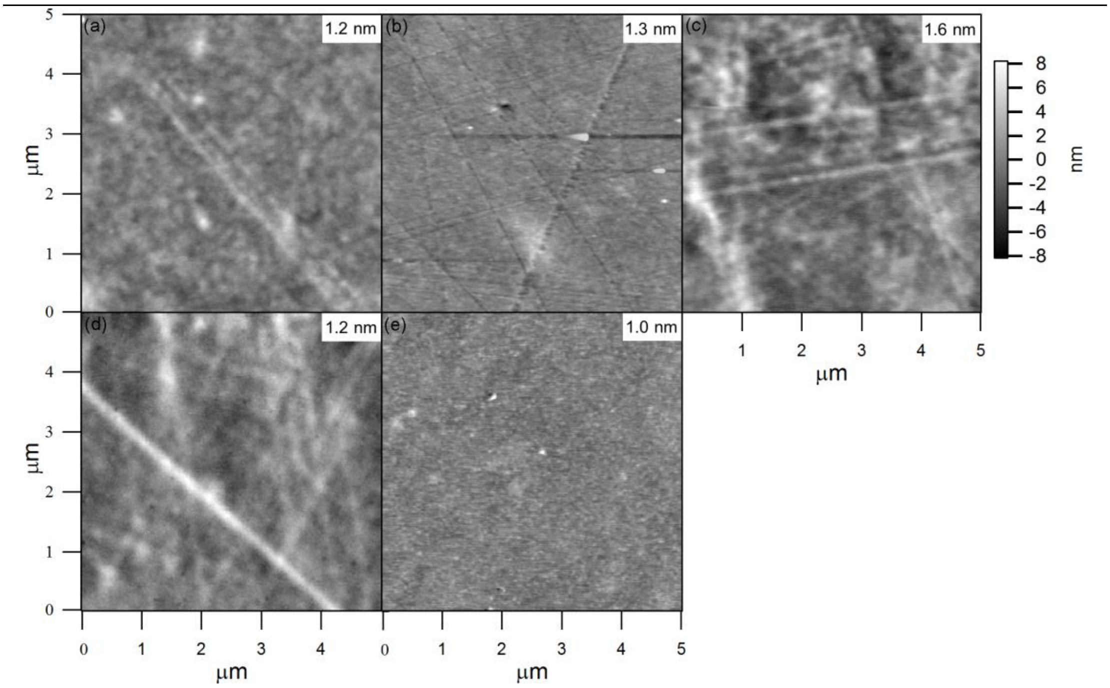

Figure 5.5: Representative AFM images of 8 nm metal films supported on APTMS:MPTMS derivatised PET: (a) Au ; (b) Ag ; (c) Cu ; (d) Cu:Ag 3:1; and (e) UV/O_3 treated PET. Typical R_{rms} for each substrate is given in the top right corner of each image.

The film robustness towards standard substrate cleaning procedures was tested by ultra-sonic agitation in three common solvents; namely, 2-propanol, toluene, and water. Remarkably these films were resistant to all of these solvent treatments with no significant change in sheet resistance (Table 5.3).

Table 5.3. Sheet resistance of 8 nm Au, Cu, Ag, Cu:Ag 3:1 films supported on PEN and PET substrates derivatised with an APTMS:MPTMS nanolayer before and after ultra-sonic agitation in three common solvents: toluene, water and 2-propanol.

Substrate	Untreated	Toluene	Water	2-propanol
		[Ω sq^{-1}]		
Au/PEN	12 ± 2	13± 3	13 ± 2	13 ± 3
Au/PET	12 ± 2	13 ± 2	14 ± 2	13 ± 2
Cu/PET	11 ± 3	11 ± 3	13 ± 3	11 ± 3
Ag/PET	9 ± 2	10 ± 2	12 ± 4	10 ± 2
Cu:Ag/PET	14 ± 3	14 ± 3	16 ± 3	15 ± 3

5.3.2 Effect of annealing

OPVs are typically annealed to 100-200 °C post-fabrication to realise optimal phase separation and/or crystallisation of the organic semiconductor layer.[312,313] For this reason the effect of annealing the substrate electrode at 200 °C is also reported. Due to the low film thickness the melting point of these metals is suppressed and so heating at 200 °C for only 10 minutes is sufficient to realise a 10 - 30% reduction in sheet resistance, depending on the metal (Table 5.4), without significantly altering film topography.

Table 5.4. Sheet resistance of 8 nm metal electrodes on derivatised PET before and after annealing to 200 °C.

	Au	Ag	Cu/Ag 3:1	Cu/Ag 2:6	Cu
			[Ω sq^{-1}]		
RT	12 ± 2	9 ± 2	14 ± 3	11 ± 2	11 ± 3
200 °C	9 ± 2	8 ± 2	11 ± 2	8 ± 2	8 ± 2

These films have a lower sheet resistance than most other unpatterned metal films of the same thickness on glass and plastic substrates reported to date.[128, 145, 314,315,291,316,317,318] The notable exception is the 6 nm Ag films sandwiched between MoO_x layers reported by Sergeant *et. al.*,[65] who achieved 6.2 Ω sq^{-1} by evaporating Ag onto MoO_x coated glass substrates held at -5 °C, although MoO_x/Ag/MoO_x films fabricated in our laboratory were not robust towards ultra-sonic agitation in water. The reduction in sheet resistance upon annealing is attributed to an increase in film crystallinity which reduces the number of grain boundaries and defects at which electrons are scattered, since it is known that annealing much thicker Au films on glass increases the crystal grain size.[161, 166] Importantly, annealing reduces the sheet resistance of all the single component films and the 2 nm Cu : 6 nm Ag bilayer films to ≤ 9 Ω sq^{-1}, which represents a significant further improvement.

Wanunu *et al.* have previously reported highly crystalline 15 nm Au films on glass with a mean transparency (across the 300 nm – 700 nm range) of 32% and demonstrated application as a versatile, chemically well-defined substrate for surface science.[166] Since the Au films fabricated here offer the advantage of; *(i)* flexibility; *(ii)* more than twice the far-field transparency; *(iii)* and half the Au usage, the possibility of achieving the high degree of crystallinity reported by Wanunu *et. al.* in a much shorter time frame was investigated. Au films with thicknesses in the range 5.6 nm to 8.4 nm were annealed up to 200 °C for 10 minutes. The changes in sheet resistance of Au films of different thicknesses upon annealing and changes in XRD spectrum of 8 nm Au film before and after annealing to 200 °C are shown in Figure 5.6.

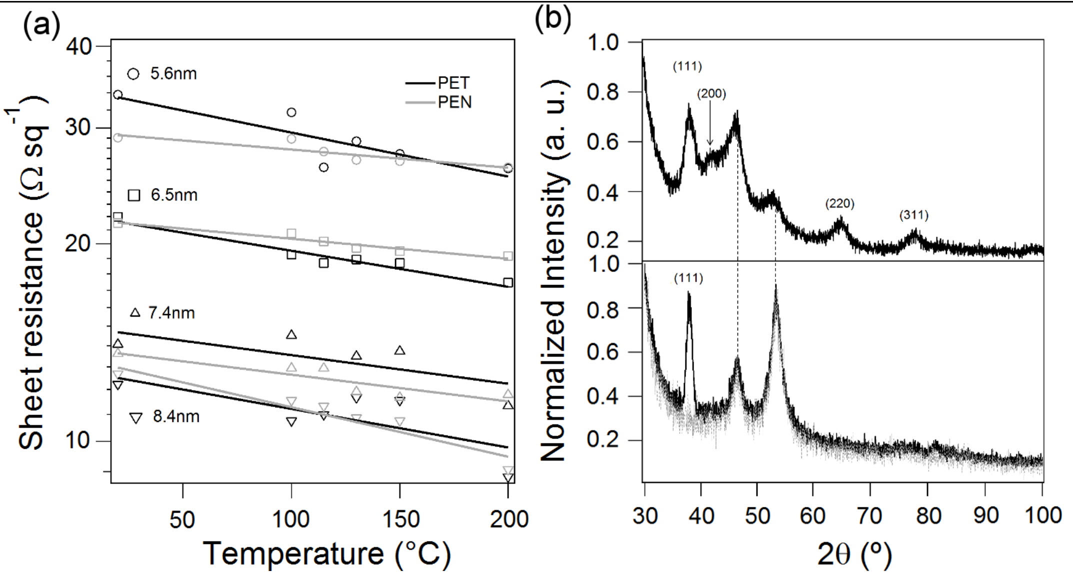

Figure 5.6: (a) Graph showing changes in sheet resistance with annealing temperature for different Au film thickness; (b) **(Upper)** Grazing incidence XRD spectrum of an 8.4 nm Au film supported on APTMS:MPTMS derivatised PET; **(Lower)** θ-2θ XRD spectra of PET (grey) and 8.4 nm Au film supported on APTMS:MPTMS derivatised PET (black) after annealing at 200 °C for 10 minutes.

It is evident from Figure 5.6 (a) that the largest percentage reduction in sheet resistance upon brief thermal annealing at 200 °C is achieved for the thickest Au films: 8.4 nm, which exhibit a 25% decrease from 12 ± 2 Ω sq^{-1} to 9 ± 2 Ω sq^{-1} without any significant change in R_{rms} (1.5 nm ± 0.2 nm *vs.* 1.3 nm ± 0.1 nm) or transparency. Grazing angle XRD spectrum of Au films on PET prior to annealing shows weak reflections from the Au (111), (200), (220) and (311) crystal planes (Figure 5.6 (b)). Upon annealing at 200 °C for 10 minutes an intense Au (111) reflection emerges such that it is no longer necessary to record the spectrum at grazing angle. This dramatic change is direct evidence that the surface reverts almost entirely to the (111) crystallographic face rendering these electrodes both chemically and structurally well-defined. This transformation is remarkable in that it occurs so rapidly and renders these electrodes near perfect for organic optoelectronics, bridging the gap between model substrates required for fundamental science and truly flexible window electrodes for various applications. Films with thicknesses ≤ 6.5 nm undergo significant transformation upon annealing with the transparency decreasing in the middle of the visible spectrum and increasing in the red/near-infra red region (Figure 5.7). This change correlates with a change in the film morphology with the formation of a random array of sub-micron-sized holes. This phenomenon is discussed in detail in Chapter 6.

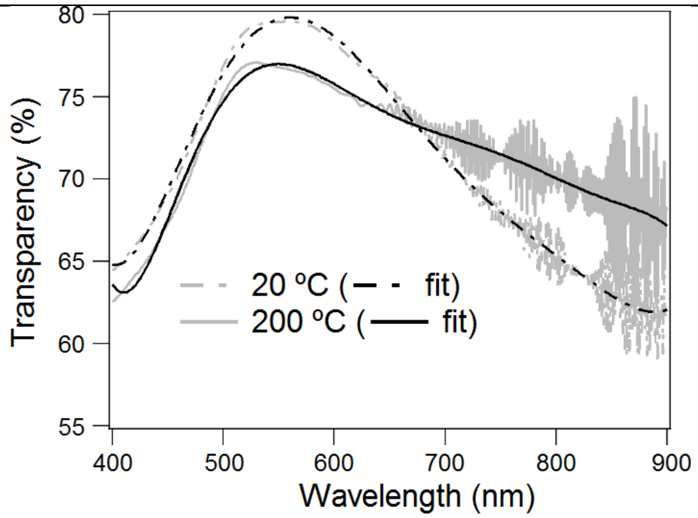

Figure 5.7: Transparency spectra for 6.5 nm Au film on PEN before and after annealing to 200°C for 10 minutes.

5.3.3 Tuning the transparency by the choice of metal

It is evident from Figure 5.8 (a) that the far-field transparency of the Ag, Cu and Au films is significantly different, with Au films offering the highest mean transparency (71% (Au) *vs.* 61% (Ag) and 62% (Cu)) across the visible spectrum. Ag and Cu films are most transparent at opposite ends of the visible spectrum and so to realise an electrode with broad band transparency at a lower materials cost than Au, bilayer Ag and Cu were fabricated with the Cu layer buried beneath the Ag layer to protect it against oxidation. It is clear from Figure 5.8 (b) that this approach works best for 1:1

Cu:Ag films: Whilst the mean transparency of Cu (4 nm): Ag (4 nm) films (65%) is 7% lower than Au electrodes of the same thickness it is higher than that of the pure Ag (61%) or Cu (62%) films of the same thickness with a broader band transparency.

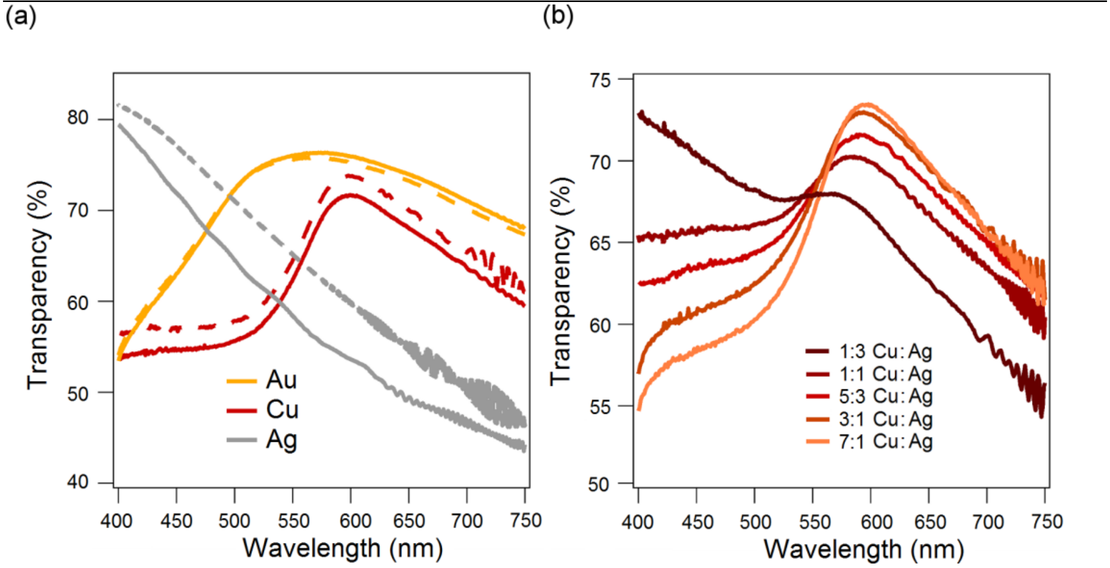

Figure 5.8: (a) Transparency spectra of 8 nm coinage metal on nanolayer derivatised PET (solid line) and PEN (dashed line) (b) Transparency spectra of 8 nm Cu:Ag bilayer films with different Cu:Ag ratios supported on APTMS:MPTMS derivatised PET.

5.3.4 Device fabrication and testing

To demonstrate the viability of these electrodes as a drop-in replacement for ITO in flexible OPVs they were incorporated into solution processed OPVs with the structure: hole-extracting electrode / 10 nm MoO_x / PCDTBT:$PC_{70}BM$ / 8 nm BCP / 100 nm Al. In this device structure the BCP layer serves as an exciton blocking layer at the contact with the electron extracting electrode. MoO_x is a widely used hole-extraction material for OPVs and is doped *n*-type by gap states resulting from partial filling of unoccupied 4d orbitals of Mo atoms neighbouring oxygen vacancies.[210] Its functionality stems from its exceptionally high ϕ,[319] which results in spontaneous ground-state charge transfer from the HOMO of the organic semiconductor and the Fermi level of the electrode which pins these energy levels close to one another on either side of the oxide layer.[198, 210] Charge transport across the oxide layer is mediated either by the gap states themselves[210] or *via* electron transport in the conduction band[198] depending on the degree of *n*-type doping. PCDTBT:PC$_{70}$BM harvests light across almost the entire visible spectrum and so is ideally suited to investigate the applicability of window electrodes with a strongly wavelength dependent transparency across the visible spectrum.

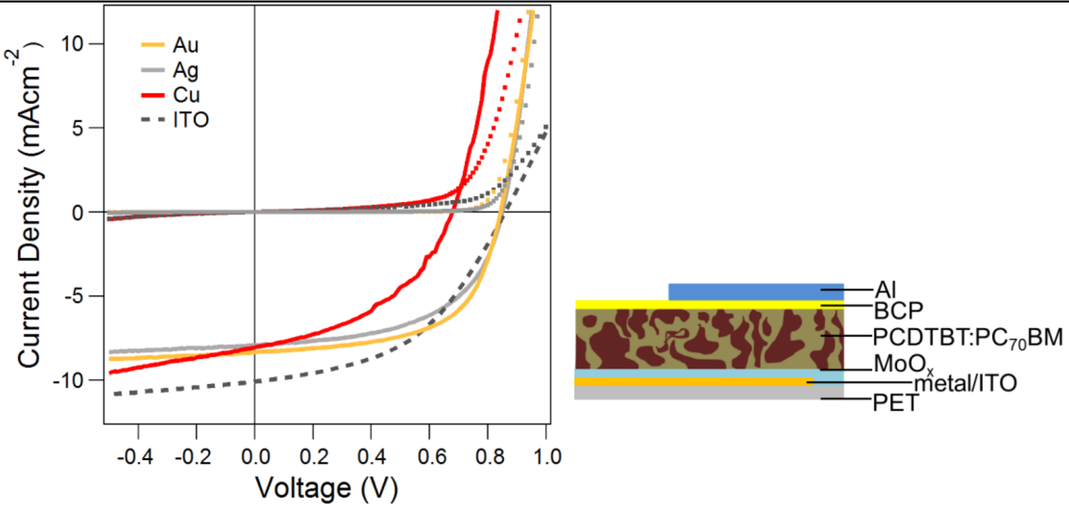

Figure 5.9: (a) *J*-*V* characteristics of OPV in the dark (dotted lines) and under 1 sun simulated solar illumination (solid lines) with structure: 8 nm metal electrode on APTMS:MPTMS derivatised PET (or ITO coated PET)/ 10 nm MoO$_x$ / 1:3 PCDTBT:PC$_{70}$BM / 8 nm BCP / 100 nm Al.

Typical *J*-*V* characteristics of 1 cm^2 PCDTBT:PC$_{70}$BM devices are shown in Figure 5.9 (a). To a first approximation J_{sc} scales with the electrode transparency: Ag (T = 61%, J_{sc} = 7.7 ± 0.1 mA cm^2); Cu (T = 62%, J_{sc} = 8.1 ± 0.1 mA cm^2); Au (T = 71%, J_{sc} = 8.45 ± 0.15 mA cm^2); ITO (T = 81%, J_{sc} = 9.60 ± 0.40 mA cm^2). The difference in J_{sc} between devices employing Ag and Cu electrodes, as compared to

Au, is smaller than expected on the basis of transparency alone. This is attributed to micro-cavity effects,[65] since Ag has a higher reflectivity than Au across the visible spectrum.[255] Crucially the efficiency (η) of OPVs fabricated on Ag and Au electrodes, 3.70% ± 0.15 and 4.25% ± 0.20 respectively, is comparable to that of devices using ITO electrodes, 4.10% ± 0.15, due to the higher *FF*; (Ag) 0.55 ± 0.03, (Au) 0.60 ± 0.01 and (ITO) 0.45 ± 0.03. The origin of this improvement is the lower cell series resistance, which is evident from the gradient of the *J*-*V* characteristic at *J* = 0 and results from the lower sheet resistance of the metal electrodes (9-12 Ω sq^{-1}) as compared to ITO (45 Ω sq^{-1}) on PET.

To demonstrate the generality of this result, wholly vacuum deposited 1 cm^2 OPVs based on a pentacene/C_{60} heterojunction were also fabricated on Au and ITO electrodes on PET and PEN (Figure 5.10 & Table 5.5).

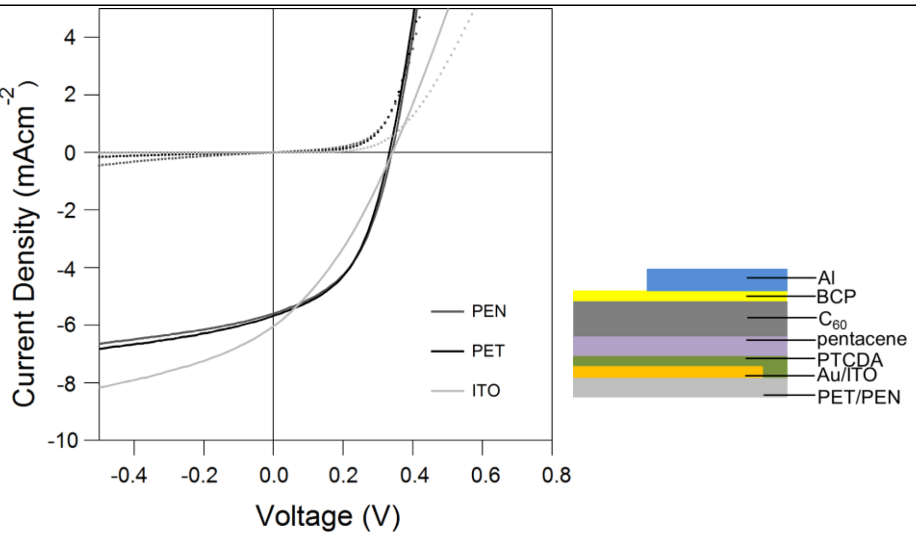

Figure 5.10: *J*-*V* characteristics of OPVs in the dark (dotted lines) and under 1 sun simulated solar illumination (solid lines) with structure: 8 nm Au on APTMS:MPTMS derivatised PET or PEN (or ITO PET) / 1 nm PTCDA / 43 nm pentacene / 40 nm C_{60} / 8 nm BCP / 100 nm Al.

Table 5.5. Summary of the key device performance characteristics and calculated series resistance (R_s) for OPVs with a device structure; electrode (8 nm Au or ITO) / PTCDA / pentacene / C_{60} / BCP / Al.

	PEN	PET	ITO
J_{sc} [mA cm-2]	5.85 ± 0.15	5.70 ± 0.5	5.90 ± 0.20
V_{oc} [V]	0.33 ± 0.01	0.33 ± 0.01	0.33 ± 0.01
FF	0.43 ± 0.04	0.46 ± 0.01	0.31 ± 0.03
η [%]	0.83 ± 0.05	0.85 ± 0.03	0.64 ± 0.07
R_{sheet} [Ωcm^2]	8.7 ± 0.5	9.0 ± 0.5	45.5 ± 2.0

Au electrodes were used since they exhibit the best performance of the metal electrodes in solution processed OPVs. In molecular OPV it is well known that relatively small differences in the nature of the substrate electrode can be critical determinants of device performance, since the growth mode of molecular semiconductors often exhibits a strong dependence on substrate surface energy and morphology.[320] For this reason a 1 nm layer of PTCDA was deposited onto the substrate electrode prior to deposition of the 43 nm pentacene donor layer. A 1 nm PTCDA interlayer is sufficiently thin to be transparent to hole transport across the interface[321] and is known to adopt the same orientation on both ITO[321] and Au[322] substrates. AFM images of 43 nm pentacene films grown on these different electrodes with a PTCDA interlayer confirms that the pentacene film morphology is essentially identical (Figure 5.11) and so any difference in device performance is unlikely to result from a difference in the morphology of the pentacene layer.

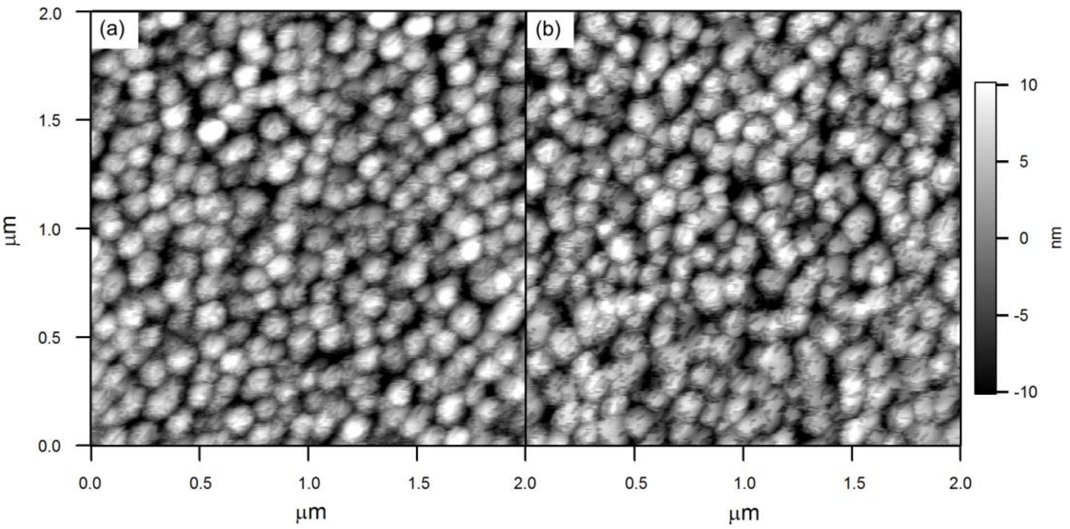

Figure 5.11: AFM images showing topography of 43 nm pentacene films supported on 1 nm PTCDA on ITO/PET **(a)** and Au/PEN **(b)**.

The ϕ of freshly evaporated Au and freshly UV/O_3 treated ITO was measured using the Kelvin probe technique to be 4.90 ± 0.05 eV and 5.40 ± 0.15 eV respectively. After deposition of a 1 nm film of PTCDA this reduced to 4.60 ± 0.05 eV and 4.9 ± 0.1 eV respectively. Sharma *et al.* have shown that the performance of pentacene/C_{60} based OPVs is not affected by differences in the ϕ of the hole-extracting electrode over this range and so any difference in device performance cannot be attributed to the differences in the interfacial energetics.[323] Devices on 8 nm Au on PET and PEN exhibit η = 0.85 ± 0.03% and 0.83 ± 0.05% respectively. Again, the primary reason for the increased η in devices fabricated on ultra-thin Au electrodes is the higher *FF*, which results from the lower device series resistance (Table 5.5). This result serves to highlight the importance of electrode sheet resistance in large area OPVs, clearly demonstrating that increasing the transparency at the expense of the sheet resistance is a false economy for large area applications.

5.3.4.1 The 8 nm Cu electrode

It is evident from Figure 5.9 that the performance of OPVs on Cu electrodes is inferior to that on Ag and Au due to the lower V_{oc} and *FF*. The latter results from a lower shunt resistance as is evident from the steeper gradient of the *J-V* characteristic at $V = 0$. The reason for the lower V_{oc} is the earlier onset of dark current injection under forward bias which is indicative of a smaller built-in potential. Interestingly this correlates with the ϕ of the electrodes measured immediately prior to device fabrication using a Kelvin probe; Cu: 4.52 ± 0.03eV; Ag: 4.87 ± 0.01eV; Au: 4.85 ± 0.01eV, since the ϕ of the Cu electrode is 0.25 - 0.30 eV lower than the Ag or Au electrodes. However, this simplistic explanation does not take account of the important role played by the MoO_x layer, which should align the E_f of the electrode close to the HOMO in PCDTBT so that the difference in ϕ between these electrodes does not translate to a difference in built-in potential.

To gain further insight into the interfacial energetics, measurements of the change in energy between the electrode E_f and the vacuum level at the surface (VL_s) were made as a function of MoO_x layer thickness using a Kelvin probe (See Figure 5.12). This energy difference, ε_f^{vac}, corresponds to the ϕ of the oxide when the film thickness is sufficient for E_f alignment to be established across the interface.[31] If thermodynamic equilibrium is not achieved then ε_f^{vac} corresponds to the ϕ of the metal electrode with a modified surface potential.[31, 89] This technique has been used extensively to probe interfacial energetics at electrode – organic semiconductor interfaces and has the advantage over photoelectron spectroscopy that it can be used to investigate the change in potential across relatively thick films of wide band gap materials.[31, 89]

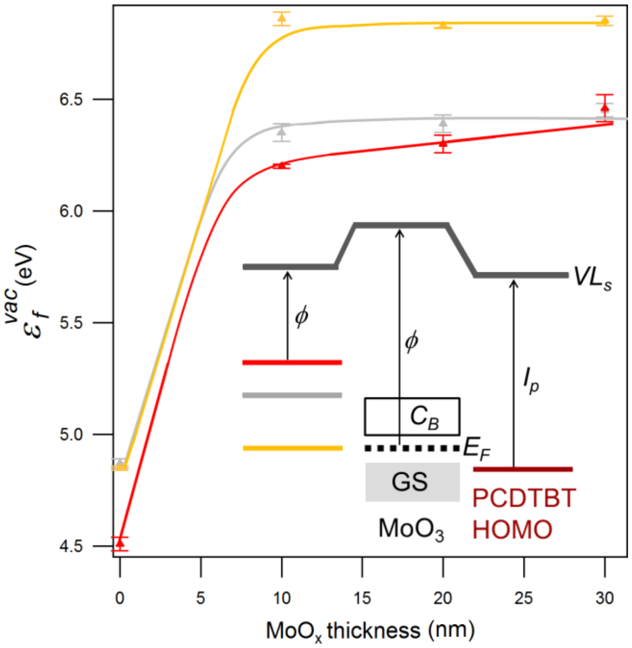

Figure 5.12: The variation in ε_f^{vac} across MoO$_x$ layers deposited onto Au, Ag and Cu electrodes as function of MoO$_x$ thickness.

For the thickness of MoO$_x$ used in devices (10 nm) the change in ε_f^{vac} is different on all three substrates indicating that E_f alignment is not achieved across at least two of the three interfaces. In those cases the thin oxide layer simply modifies the surface potential of the substrate electrode such that it has a ϕ much greater than the ionisation potential of PCDTBT (5.35 eV[324]). Since ε_f^{vac} on the Au electrode exhibits the largest change and remains constant with increasing layer thickness at a value equal to the ϕ of MoO$_x$ reported in the literature; 6.9 eV,[198, 210] it is likely that thermodynamic equilibrium has been achieved across this interface. This result is in excellent agreement with measurements of the interfacial energetics between Au substrates and MoO$_x$ by Seki *et al.*[210] using photoelectron spectroscopy. Under these circumstances E_f of the Au electrode is aligned closely to the HOMO of PCDTBT, which ensures that the built-in electric field in the diode is maximised. As a result the onset of hole-injection under forward bias is delayed as much as possible, ensuring that V_{oc} is maximised. By extension, at the interface between the 10 nm MoO_x layer and Ag and Cu electrodes there is sub-optimal energy level alignment. Since it is reasonable to assume that the HOMO of PCDTBT is always pinned to the E_f of the MoO_x[210] the performance of OPVs employing both Ag and Cu electrodes should be inferior to that achieved using Au electrodes due to the smaller built-in potential, which results in an earlier onset of dark current injection. Whilst it is clear from Figure 5.9 that this is the case for the Cu electrode it does not hold true for the Ag electrode. The measurements of the energetics at the metal electrode / MoO_x interface cannot therefore be rationalised in terms of a well-defined interface. Instead, it is necessary to account for the possibility that Ag and Cu diffuse into the thin MoO_x overlayer.[141, 325] Indeed the very low thickness of these metal films suppresses the temperature at which metal diffusion occurs, which is why these films are amenable to rapid annealing at 200 °C. Ag is known to diffuse less aggressively into oxide overlayers[325] and so it is plausible that those Ag atoms that do diffuse into the MoO_x function as *n*-type dopants, much like Mo atoms, moving the E_f closer to the conduction band edge and thus reducing the ϕ of the oxide. This hypothesis offers an explanation as to why ε_f^{vac} at the Ag/MoO_x interface converges to a lower ϕ than MoO_x on Au. It also offers a plausible explanation as to why OPVs employing an Ag electrode have the same V_{oc} as those using an Au electrode, since the ϕ of Ag doped MoO_x (~ 6.4 eV, from Fig. 5.12) is still sufficiently high to align the electrode E_f (~4.9 eV below VL_s) with the HOMO of PCDTBT (5.35 eV below VL_s) [324]. Conversely Cu is known to diffuse very aggressively into metal oxides including MoO_x[141] and so it is possible that filamentary strands of metallic Cu extend along the grain boundaries all the way through the 10 nm MoO_x layer, thereby undermining it electronic functionality. This would explain why ε_f^{vac} does not saturate with increasing MoO_x thickness, but continues to increase towards that of MoO_x on Au. It would also explain the early onset of dark current injection under forward bias, since the ϕ of Cu is too low for the E_f of the electrode to align closely with the HOMO in PCDTBT. The deterioration in *FF* can also be rationalised in terms of this hypothesis since the role of the oxide layer in reducing filamentary short circuits is undermined.[205, 326]

5.3.4.2 Bilayer Cu : Ag electrodes

To explore the potential of tuning the optical properties of these metal film electrodes bilayer Cu:Ag electrodes were fabricated with different relative thicknesses. In principle these electrodes also offered a path to circumventing the aforementioned problem with Cu electrodes, since the Ag forms the interface with the MoO_x hole-extraction layer. The total metal thickness was kept at 8 nm and the bilayer Cu:Ag thickness ratio was 1:0, 3:1, 1:3 and 0:1. It is clear from the *J-V* characteristics, shown in Figure 5.13, that when the Ag layer thickness is 2 nm the electrode essentially behaves as if it were Cu only. Increasing the Ag thickness to 6 nm results in a relatively small improvement in both V_{oc} and *FF*, which falls well short of that achieved on Ag alone. Pitts *et al.*[327] have shown that Cu can diffuse at room temperature through Ag overlayers as thick as 11 nm. These results can therefore also be rationalised in terms of the diffusion of Cu into the MoO_x layer and serve to highlight the challenges associated with the using Cu electrodes in OPV.

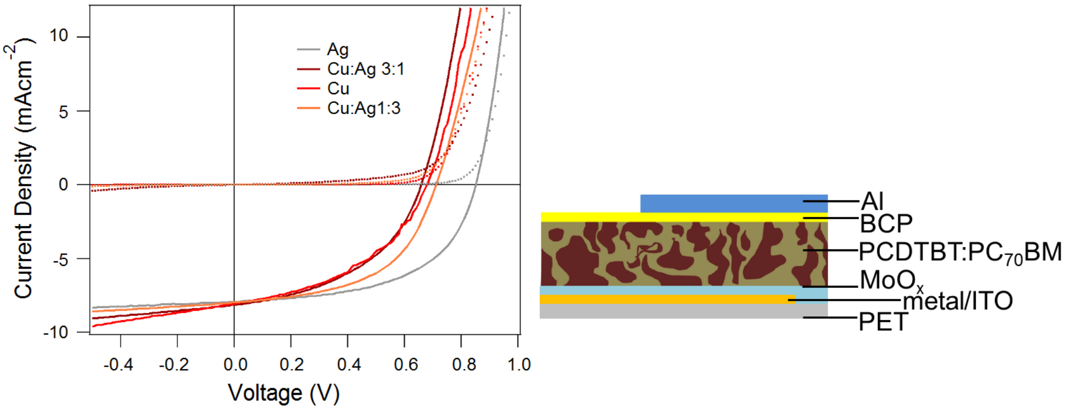

Figure 5.13: *J-V* characteristics of OPVs in the dark (dotted lines) and under 1 sun simulated solar illumination (solid lines) with the structure: 8 nm metal electrode on APTMS:MPTMS derivatised PET / 10 nm MoO$_x$ / 1:3 PCDTBT:PC$_{70}$BM / 8 nm BCP / 100 nm Al.

5.3.4.3 OPV durability testing (bending and lifetime tests)

Device lifetime is a critical factor when considering the commercial potential of any PV technology and it is known that the operational lifetime of OPV is limited if chemically unstable (metastable) electrodes such as ITO are used.[328] Specifically , the ITO/organic semiconductor interface is known to be susceptible to photo-induced degradation leading to a gradual deterioration in charge extraction efficiency across the interface.[329] Figure 5.14 shows how the key characteristics of 1 cm^2 pentacene / C$_{60}$ OPVs, employing Au and ITO electrodes, change under prolonged illumination. The performance of devices with Au electrodes remains virtually unchanged after 2.5 hours, whilst identical devices employing ITO electrodes lose over 50% of their efficiency.

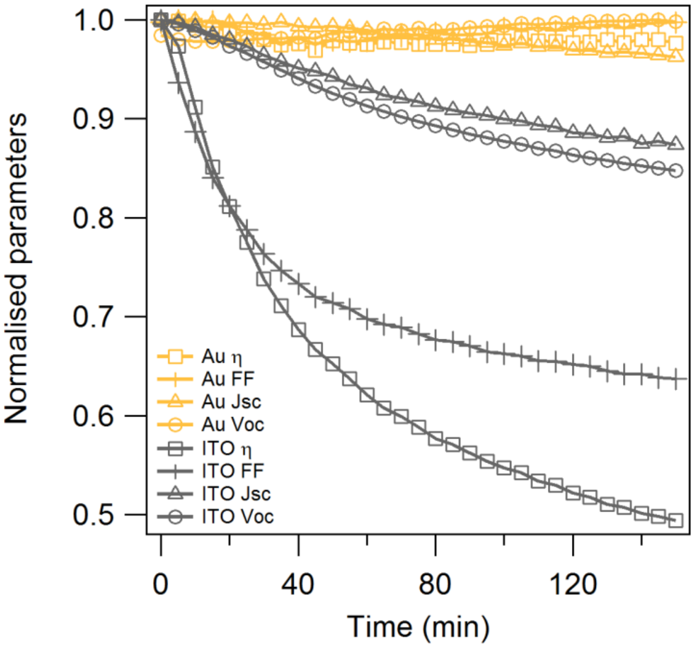

Figure 5.14: J_{sc}, V_{oc}, FF and η of 1 cm^2 OPVs as a function of illumination time, for the bilayer device with the structure: electrode / pentacene / C_{60} / BCP / electrode.

Finally, it is widely considered that for OPVs to realise their full commercial potential they must be fabricated on flexible substrates. Figure 5.15 (a) and (b) shows how the efficiency of 1 cm^2 solution processed and small molecule OPVs fabricated on ITO and metal electrodes on PET perform as a function of the number of bend cycles through a radius of curvature of 4 mm. The performance of devices with an ITO electrode deteriorates rapidly. This is because conducting oxide electrodes such as ITO are inherently brittle and so susceptible to cracking when bent. In contrast the performance of both solution processed and vacuum deposited OPVs with metal electrodes is practically unchanged even after 100 bend cycles, opening the door to the realisation of truly flexible OPVs.

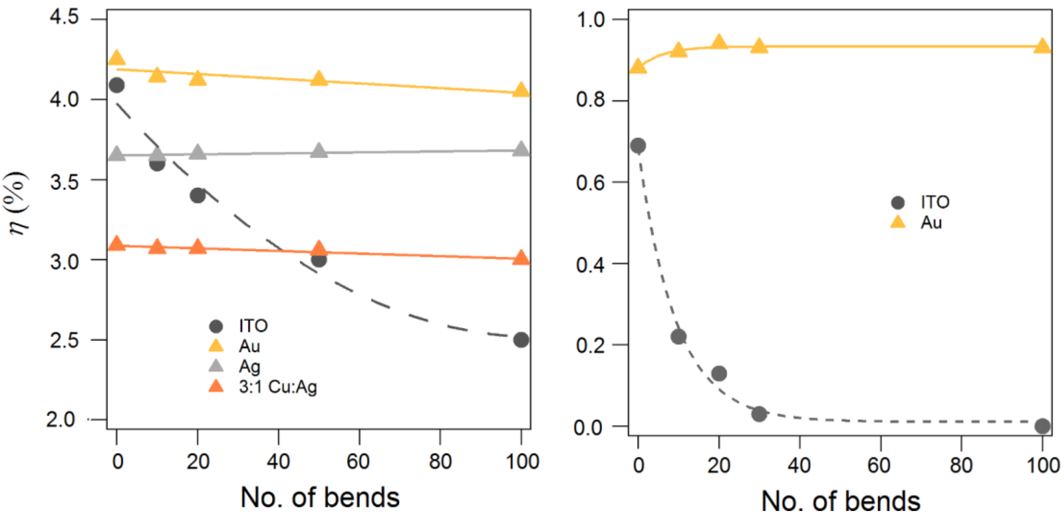

Figure 5.15: Power conversion efficiency as a function of number of bend cycles for; (a) - PCDTBT:$PC_{70}BM$ based OPV with Au/PET (yellow triangles), Cu/PET (brown triangles), Ag/PET (grey triangles) or ITO/PET (closed circles) as the substrate window electrode.; (b) C_{60} / pentacene based OPV with Au/PET (yellow triangles) and ITO/PET (closed circles) electrodes.

5.4. Conclusions

The key findings of this Chapter are:

1. 8 nm films of the coinage metals Cu, Ag and Au can be fabricated on the technologically important substrates PET and PEN to realise highly electrically conductive, low R_{rms} and exceptionally robust window electrodes. The key to the realisation of these electrodes is the chemical derivatisation of the plastic surface with a mixed monolayer of thiol and amine methoxysilanes co-deposited from the vapour phase.

2. Owing to the low thickness of these metal films their melting point is suppressed so that brief heating at only 200 °C can be used to reduce the sheet resistance to $\leq 9\ \Omega\ \mathrm{sq}^{-1}$. Annealing Au electrodes at 200 °C for only 10 minutes causes the surface to revert almost entirely to the (111) face rendering it ideal as a widely applicable electrode for fundamental science and practical application alike.

To the author's knowledge the properties of these electrodes in terms of robustness and sheet resistance are superior to almost all unpatterned metal film electrodes of the same thickness on plastic substrates reported to date.

3. The performance of ~ 4% efficient 1 cm^2 OPVs on Ag and Au electrodes is comparable to that on commercial ITO electrodes on flexible plastic substrates. The disadvantage of the lower transparency of the metal electrodes, as compared to ITO, is off-set by the advantage of much lower sheet resistance.

4. 1 cm^2 OPVs fabricated on 8 nm metal window electrodes are robust towards repeated bending through a radius of curvature of 4 mm opening the door to the realisation of truly flexible OPVs. In contrast, ITO coated plastic substrates deteriorate rapidly upon repeated bending. Devices employing ITO electrodes undergo fast deterioration under illumination while devices with metal electrodes remain stable.

5. Cu offers a path to low cost transparent electrodes and can be combined with Ag to tune the optical transparency. However, even when buried beneath a 6 nm Ag layer and a 10 nm MoO_x hole-extraction layer OPVs with Cu electrodes do not perform as well as Ag or Au electrodes of the same thickness. On the basis of device studies and measurements of the energetics at the metal electrode / MoO_x interface this is attributed to diffusion of Cu into the MoO_x layer which undermines it functionality as a high work function interlayer.

Chapter 6.

Plasmon-active nano-aperture window electrodes

The work presented in this chapter has been published in:
H. M. Stec, R. A. Hatton, *Plasmon-Active Nano-Aperture Window Electrodes for Organic Photovoltaics*, Advanced Energy Materials, **2013,** *3* (2), 193-199.

Summary

This chapter describes a method for the fabrication of optically thin Au and Ag films with a high density of non-symmetric sub-wavelength apertures on glass and plastic substrates without the complexity of a lithographic step. It is shown that these films are remarkably robust, have a sheet resistance low enough for OPV applications and support surface plasmon resonances, which couple strongly with visible light concentrating it near to the electrode surface. The two key steps in the realisation of these electrodes are: *(i)* Chemical modification of the substrate surface prior to metal deposition to tune the strength of adhesion between the substrate and the metal film; *(ii)* Following metal deposition of the metal the film is briefly annealed to form a random array of nano-sized apertures with a high number density. It is shown that the efficiency of model BHJ and bilayer OPVs is greatly increased as compared to identical devices utilising aperture-free electrodes and these electrodes actually outperform ITO as the window electrode in flexible OPVs. In addition to presenting compelling evidence that this functionality results from surface plasmon mediated light concentration effects, this work demonstrates that the sub-wavelength apertures need not have a uniform shape or have a particularly tight size distribution and may

have dimensions more than one order of magnitude smaller than the wavelength of the light being collected.

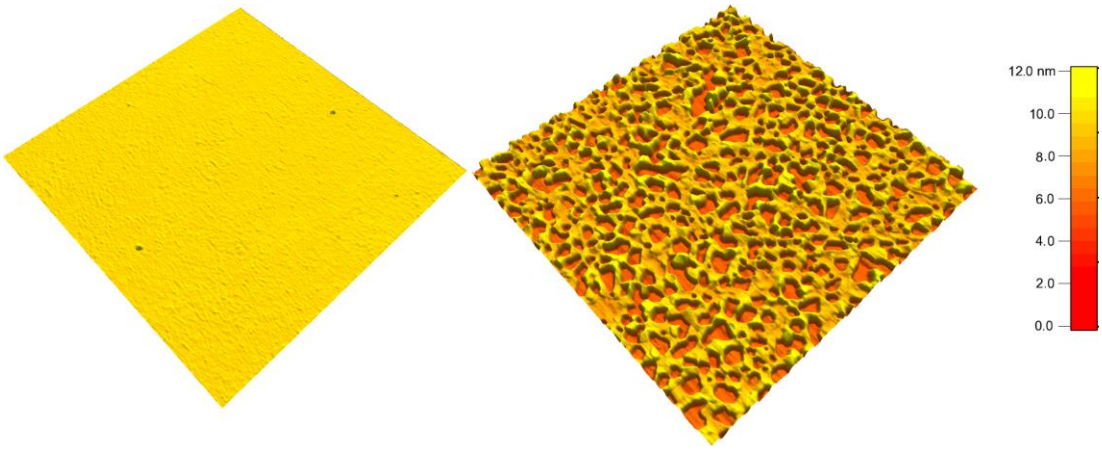

Figure 6.1: 3D AFM topographs of Au electrodes (lateral scale 5 µm × 5 µm); flat metal electrode (left); modified, plasmon-active electrode (right).

6.1 Introduction

To date the most efficient OPVs are based on the BHJ concept where co-deposited electron-donor and electron-acceptor type organic semiconductors spontaneously phase-separate into domains with dimensions comparable to the exciton diffusion length in each material to realise a large area interpenetrating heterojunction.[184, 330,331] This architecture helps to address the exciton diffusion bottleneck that occurs in bi-layer OPVs as a result of the short exciton diffusion length in organic semiconductors.[75, 142, 171] However, recombination losses during charge carrier transport through the complex network of donor and acceptor phases can limit the thickness of the photoactive layer to less than optimal for light absorption.[75, 142] By analogy the very short mean free path of charge carriers in amorphous silicon and quantum dot photovoltaics, resulting from the high defect density, also imposes a limitation on the thickness of the semiconductor layer.[64, 332] Conversely, more generally it is desirable to reduce the semiconductor thickness in photovoltaics without adversely impacting device efficiency in order to reduce material costs, increase fabrication speed and reduce electrical losses.[64]

It is possible to increase light absorption without increasing the thickness of the photoactive layer using light trapping strategies including microcavity effect,[65] the use of optical spacers[66] and structures to scatter the incident light.[64, 143, 333] Alternatively plasmonic phenomena, which has been firstly demonstrated by Ebessen *et al.* in opaque Ag film with sub-wavelength apertures,[334] can be exploited to concentrate the optical field in the photoactive layer using plasmon-active metal nano-structures,[146, 335] or to increase the effective path length through the photoactive layer either using metal nano-structures as scattering elements or to trap the incident light in surface plasmon polaritons at the photoactive layer - metal electrode interface.[64, 147] For these purposes Au and Ag are the most widely used metals since they support surface plasmon resonances that couple strongly with visible light and are relatively stable towards oxidation. To date plasmonics have been exploited in OPVs in two ways: (*i*) Incorporation of plasmon active metal nanoparticles with diameters < 100 nm either at the electrode interfaces[148] or dispersed within the photoactive layer itself;[149] *(ii)* Utilisation of electrodes comprising networks of plasmon-active metal nanowires[147] or metal films patterned with arrays of apertures with sizes in the range 80-300 nm[150,151] or gratings.[152] To date, most research into the application of plasmonics in OPV has focused on *(i)*, although due to the low thickness of the semiconducting layer in (< 200 nm) integrating metal nanoparticles or nanowires into these devices increases the risk of short-circuiting.[153] Approach *(ii)* has the advantage that the nano-structured metal serves as both a light concentrating element and collector of charge carriers. The majority of studies have focused on the use of regular periodic structures[154,155] and so modelling can be used to predict the structure – property relation as so identify optimised designs.[152,156] However, the techniques used in the research laboratory to fabricate dense ordered arrays of structures with dimensions < 300 nm, such as ion-beam milling,[154, 156] cannot be cost effectively scaled to large areas. A random array of sub-wavelength apertures is more amenable to scaling than a periodic array, although more difficult to model. Indeed, the possible plasmon activity in metal films with a high density of randomly arranged apertures becomes increasingly complex as the film becomes optically thin (i.e. < 15 nm) since efficient coupling between surface plasmon polaritons on the front and back of the metal film can occur[336] as well as significant ordinary transmission of light. These effects are in addition to coupling between adjacent apertures[157] and the effect of light concentration at aperture edges,[158] which are features of optically thick metal films with a random array of sub-wavelength apertures.

The first report of plasmon-active metal film electrodes in OPVs was by Reilly *et al.*, who have shown that OPVs employing a Ag metal electrode with a random arrangement of circular apertures outperform identical devices without apertures in the electrode.[150] In that work the Ag electrode was relatively thick (30 nm) and the random array of circular apertures was formed using nanosphere lithography. Whilst the relative improvement in performance was large, 1.03% to 1.22%, the absolute performance was at least a factor of three lower than that achieved using a conventional ITO electrode. Reilly *et al.* have also shown that using lithography to form 92 nm diameter apertures over 20% of the surface of a 40 nm thick Ag film results in a 150% increase in sheet resistance.[159] As a result, forming a high number density of apertures using this technique in a much thinner – and thus more transparent - metal film would render the sheet resistance too high for OPV applications. A further disadvantage of microsphere lithography is the need to remove 100% of the microspheres prior to device fabrication. It is therefore clear that this class of window electrode must firstly be shown to demonstrate the potential to perform as well as conducting oxide electrodes in efficient OPV. Then, for practical implementation, low cost, scalable methodologies for the fabrication of optically thin metal electrodes with a high density of sub-wavelength apertures and low sheet resistance must be forthcoming. Finally, to help guide the design of these electrodes for OPV it is useful to determine whether the sub-wavelength apertures need to have a tight size and shape distribution or whether this design principle can be relaxed.

6.2 Experimental

6.2.1 Fabrication of nano-aperture metal films on glass and plastic substrates

Nano-aperture electrodes were fabricated by chemical modification of the substrate surface prior to metal deposition to tune the strength of adhesion between the substrate and the metal film. On glass substrates this was achieved using a sub-monolayer coverage of APTMS:MPTMS. On plastic substrates this was achieved by controlling the extent to which the surface is oxidised prior to metal deposition, since surface oxidation introduces reactive surface groups (as discussed in Chapter 5). This was followed by metal deposition and a thermal annealing step to form a random array of nano-sized apertures with a high number density. The importance of modifying the surface of the substrate with '*sticky*' surface groups prior to metal deposition, either by addition of a molecular adhesive layer or formation of ‘adhesive’ moieties directly on the surface is two-fold: *(i)* It enables a high degree of control over aperture formation by increasing the thermal stability of the films.; *(ii)* It ensures that once the apertures are formed the resulting nano-structured electrode adhere strongly to the substrate.

The optimised electrode fabrication procedures were: glass, PEN and PET substrates were cleaned according to the procedure described in Chapter 2 followed by 15 minutes UV/O_3 treatment for glass and or 5 minutes UV/O_3 treatment for plastic substrates respectively. Glass slides were then immediately transferred to a dessicator where they were exposed to the vapour of APTMS or APTMS:MPTMS at 150 mbar for 1 hour (unless stated otherwise) before transferring to the evaporator for Au deposition. PET and PEN substrates were transferred to the evaporator for Ag deposition immediately after UV/O_3 treatment. To obtain the nanostructured morphology Au and Ag films were annealed at 350 °C and 200 °C respectively, for 10 minutes in a N_2 atmosphere, unless stated otherwise.

6.2.2 Substrate characterisation

The chemically modified substrates were investigated using high resolution HRXPS and static contact angle measurements.

Static contact angle measurements were made using high purity water with a drop size of 0.2 µl to estimate the APTMS:MPTMS monolayer coverage on glass substrates subjected to vapour treatment under different conditions. In the case of a heterogeneous surface composed of well-defined patches or regions of two different materials the surface heterogeneity can be estimated using the Cassie equation:[265]

$$\cos\theta = f\cos\theta_1 + (1-f)\cos\theta_2 \qquad \textit{(Eqn. 6.01)}$$

where; θ_1, θ_2 are the contact angles measured on single component surfaces of 1 and 2 respectively and f is the fractional surface coverage of component 1 on a surface of component 2. However for materials that are heterogeneous at the molecular level the Israelachvili-Gee equation is more appropriate:[266]

$$(1+\cos\theta)^2 = f(1+\cos\theta_1)^2 + (1-f)(1+\cos\theta_2)^2 \qquad \textit{(Eqn. 6.02)}$$

6.2.3 Metal film characterisation

Metal films were characterised using the techniques described in Chapter 2. AFM images of the surface topography of films with a random array of apertures were analysed for aperture coverage, density and size distribution using WSxM software.[337]

6.2.4 OPV fabrication and testing

The ITO coated glass and PEN substrates were cleaned in the same manner as the glass and plastic substrates. The electrodes were incorporated into two different OPV architectures:

(1) BHJ devices with the structure: hole-extracting electrode / MoO_x / 1:3 PCDTBT:$PC_{70}BM$ spincasted from 16 mg ml^{-1} overall solution in chloroform / 8 nm BCP / 100 nm Al;

(2) Small molecule bilayer devices with the structure: hole-extracting electrode / 5 nm MoO_x / 14 nm SubPc / 40 nm C_{60} / 8 nm BCP / 100 nm Al.

In both cases Al was deposited through a shadow mask to give a device area of 6 mm^2.

6.3 Results and discussion

6.3.1 Control over aperture formation in Au and Ag films

As described in previous chapters smooth and conductive metal films of sub-10 nm thickness can be prepared on glass and plastic surfaces derivatised with a molecular nanolayer that binds to both the substrate and evaporated metal. In Chapter 3 an optimised protocol for the preparation of uniform Au films on glass using a mixed nanolayer of APTMS and MPTMS is described. This method is not suitable for the formation of the plasmon-active electrodes reported in this chapter since the Au film binds too strongly to the glass and so upon thermal annealing only very large (micron-sized) and sparsely distributed apertures form (**Figure 6.2 (a) and Figure 6.3(a)**). This is because the nanolayer deposition protocol described in Chapter 3 forms dense nanolayers equivalent to 100 % surface coverage, as determined using HRXPS and static contact angle measurements. However, the molecular adhesion layer can be modified to tune the strength of adhesion between the substrate and metal film by varying the surface coverage, since the strength of adhesion is proportional to the density of reactive moieties at the substrate surface, to which the metal can bind.

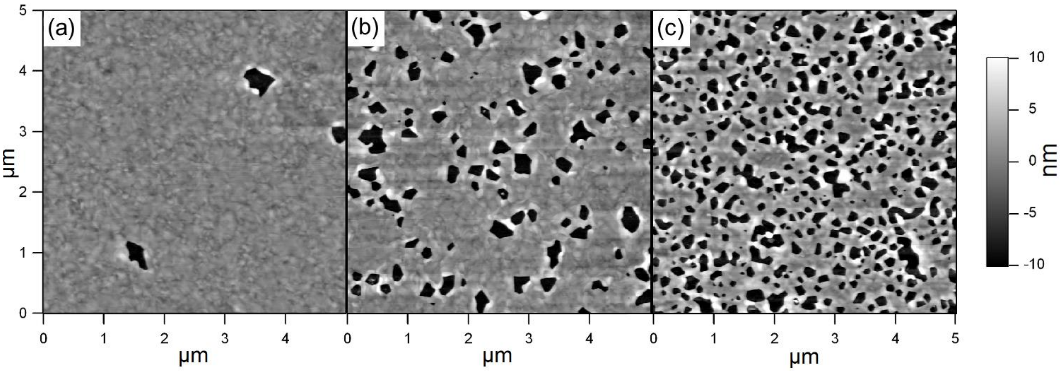

Figure 6.2: Morphology of 8.4 nm Au films on APTMS:MPTMS derivatised glass annealed at 350 °C for 10 minutes measured using an AFM. The nanolayer derivatisation time was 45 minutes and the vacuum pressure in the deposition chamber was: **(a)** 50 mbar; **(b)** 100 mbar; **(c)** 150 mbar.

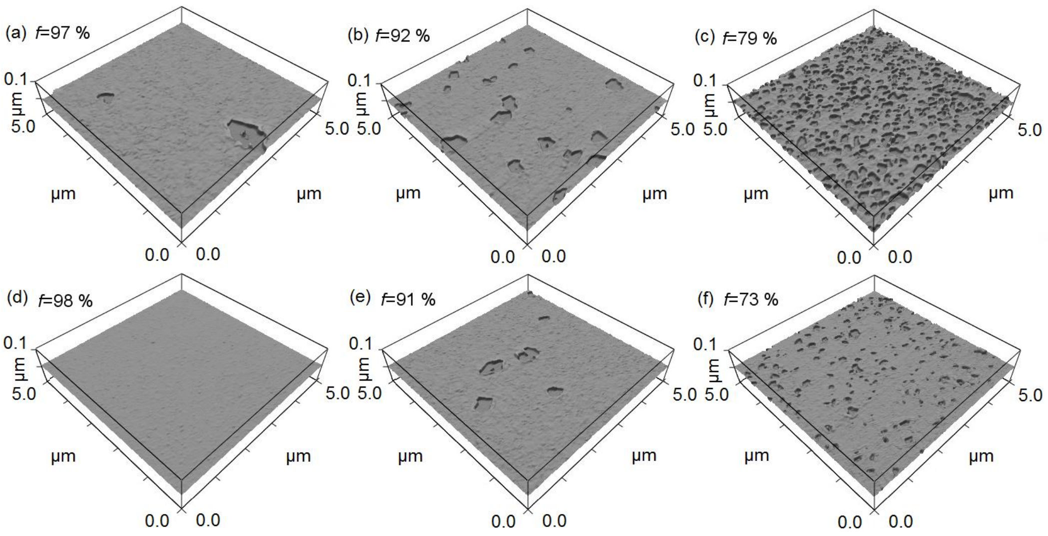

Figure 6.3: (a-c) Morphology of 8.4 nm Au films supported on APTMS:MPTMS nanolayer derivatised glass post-annealing at 400 °C for 10 minutes. The glass substrates were all exposed to APTMS:MPTMS vapour for 60 minutes at **different vacuum pressures**: (a) 50 mbar; (b) 100 mbar; (c) 200 mbar. **(d-f)** Morphology of 8.4 nm Au films supported on APTMS:MPTMS nanolayer derivatised glass post-annealing at 300 °C for 10 minutes. The glass substrates were all exposed to APTMS:MPTMS at 100 mbar vacuum pressure for **different times**: (d) 100 minutes; (e) 60 minutes; (f) 30 minutes. *f* – indicates the nanolayer coverage calculated using Israelachvili-Gee equation.

In order to realise Au films with a high number density of sub-wavelength apertures after brief annealing, the nanolayer surface coverage must be reduced, either by changing the derivatisation time or vapour pressure. Figures 6.2 and 6.3 illustrate the effect of changing the pressure at which the nanolayer is deposited and the nanolayer derivatisation time. Importantly, the former corresponds to a *decrease* in APTMS:MPTMS vapour pressure since the background gas pressure is higher. Nanolayer surface coverage under different deposition conditions was determined from static contact angle measurements using the Cassie equation[265] and Israelachvili-Gee equation.[266] The latter is more suitable whenever the size of chemically heterogeneous patches approaches atomic dimensions[266] (Table 6.1). It is clear from Figures 6.2 – 6.4 that there is a strong correlation between aperture coverage and nanolayer coverage, which shows that controlling the nanolayer surface coverage is an extremely effective means of tuning the morphology of the Au film on top.

Table 6.1. Monolayer coverage calculated using the Cassie[265] and Israelachvili-Gee[266] equations from water contact angle measurements. Monolayers were prepared according to the same protocols used in preparation of Au films depicted in Figure 6.2 and 6.3.

	Nanolayer Coverage [%)]	
Sample	Cassie equation [± 3%]	Israelachvili-Gee equation [± 3%]
6.2 (a)	94	95
6.2 (b)	87	89
6.2 (c)	77	80
6.3 (a)	96	97
6.3 (b)	91	92
6.3 (c)	79	79
6.3 (d)	97	98
6.3 (e)	90	91
6.3 (f)	69	73

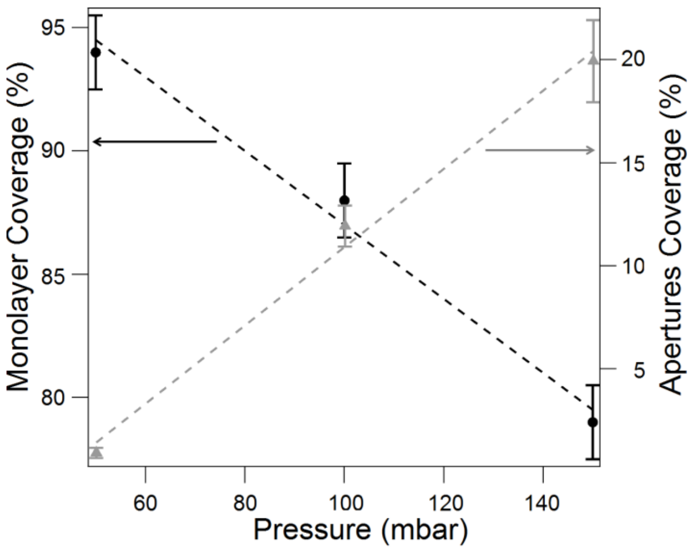

Figure 6.4: Graph of APTMS:MPTMS surface coverage calculated using Israelachvili-Gee equation and corresponding aperture coverage in Au film as a function of the vacuum pressure in the APTMS:MPTMS deposition vessel. The metal film is 8.4 nm Au annealed to 350 °C for 10 minutes to form apertures.

6.3.2 The influence of the annealing time of Au film structure

Whilst rapid thermal annealing is a convenient way to form apertures, the stability of these films towards extended periods of high temperature annealing is also of interest.[288, 338] Figure 6.5 shows the morphology of 8.4 nm Au films supported on MPTMS:APTMS nanolayer annealed at 300 °C for different periods of time and rapidly cooled.

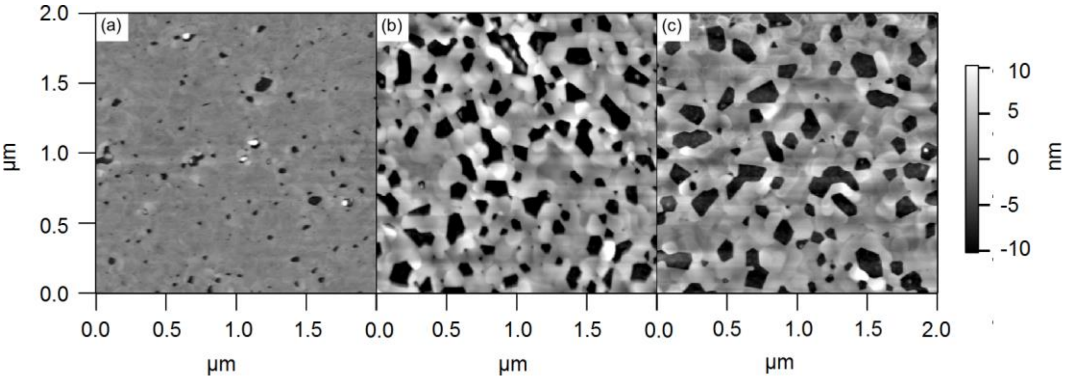

Figure 6.5: AFM morphology of 7.4 nm Au films supported on APTMS:MPTMS nanolayer (150 mbar, 1 hour) annealed at 300 °C for 3 minutes (a), 10 minutes (b), 120 minutes (c).

The apertures start to form very soon after the sample is subjected to the high temperature (Figure 6.5 (a)). Notably the apertures have well-defined straight edges, consistent with the formation of crystallites of comparable dimensions to the aperture size. On average films annealed to for 120 minutes retain the same number density and size of apertures as annealed for 10 minutes only, although their edges become more uniform and well-defined resulting in a R_{rms} close to 2 nm (as compared to ~ 3 nm after 10 minutes).

6.3.3 Au films supported on single type of nanolayer

Since in this chapter the aim was to reduce the strength of adhesion between the metal film and the glass substrate in a controlled way, the possibility of forming a random array of apertures in Au films supported on a nanolayer of APTMS only was investigated. It is evident from the SEM images in Figure 6.6 that this is the case, although the onset of aperture formation begins at a lower temperature than on films supported on a mixed nanolayer and the nano-structured films are much less stable towards ultra-sonic agitation.

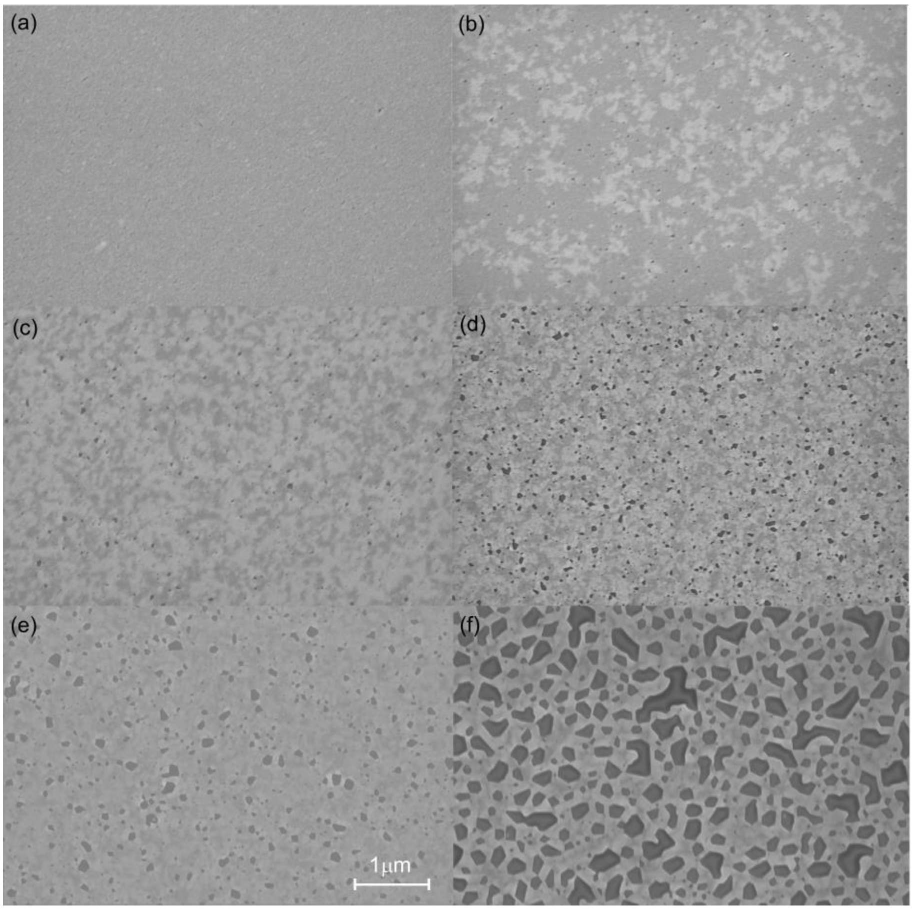

Figure 6.6: SEM images of 8.4 Au films supported on mixed APTMS nanolayer (50 mbar, 1 hour); not annealed film (a); film annealed to 100 °C (b); 130 °C (c); 170°C (d); 200°C (e) and 240°C (f).

6.3.4 Ag films

In an extension of the molecular adhesive approach for the chemical derivatisation of glass, optically thin (11 nm) films of Ag with a random array of apertures were fabricated on the technologically important plastic substrates PET and PEN. Since in Chapter 5 it is shown that APTMS and MPTMS bind to UV/O_3 treated plastic substrates and Ag, a mixed nanolayer could also have been used for the preparation of Ag films on plastic, as for Au on glass. However, it was found that Ag would bind sufficiently strongly to freshly UV/O_3 treated PET and PEN for the formation of apertures and so this simplified protocol was used for the preparation of Ag films on plastic substrates in this chapter. Notably, UV/O_3 treatment is not as effective as APTMS:MPTMS monolayer treatment for the fabrication of Ag and Au films without apertures. For example, the sheet resistance of 8 nm Ag on APTMS:MPTMS derivatised PET and 8 nm Ag on UV/O_3 treated PET is 9 ± 2 Ω sq^{-1} and 12 ± 1 Ω sq^{-1} respectively. Using UV/O_3 treatment the strength of adhesion between the metal film and the substrate can be tuned by altering the UV/O_3 treatment time and/or UV light intensity. The reactive groups formed at the plastic surface and the nature of their interaction with Ag is discussed in section 6.3.5.2 of this chapter.

9 nm Ag films supported on UV/O_3 treated PET substrates with sparse apertures are formed upon annealing to 150 °C and film became discontinuous around 200 °C (see Figure 6.7 (a) and (b)). Films of the same thickness supported on MPTMS derivatised glass, described in section 4.3.4, disintegrate at only 100 °C. This clearly indicates the importance of reactive groups formed on the surface of UV/O_3 treated plastic, and absent on the surface of glass, in metal/substrate adhesion improvement. However thicker Ag films supported on MPTMS derivatised glass offer the possibility to tune the aperture size as shown in Figure 6.7 (c) – (f).

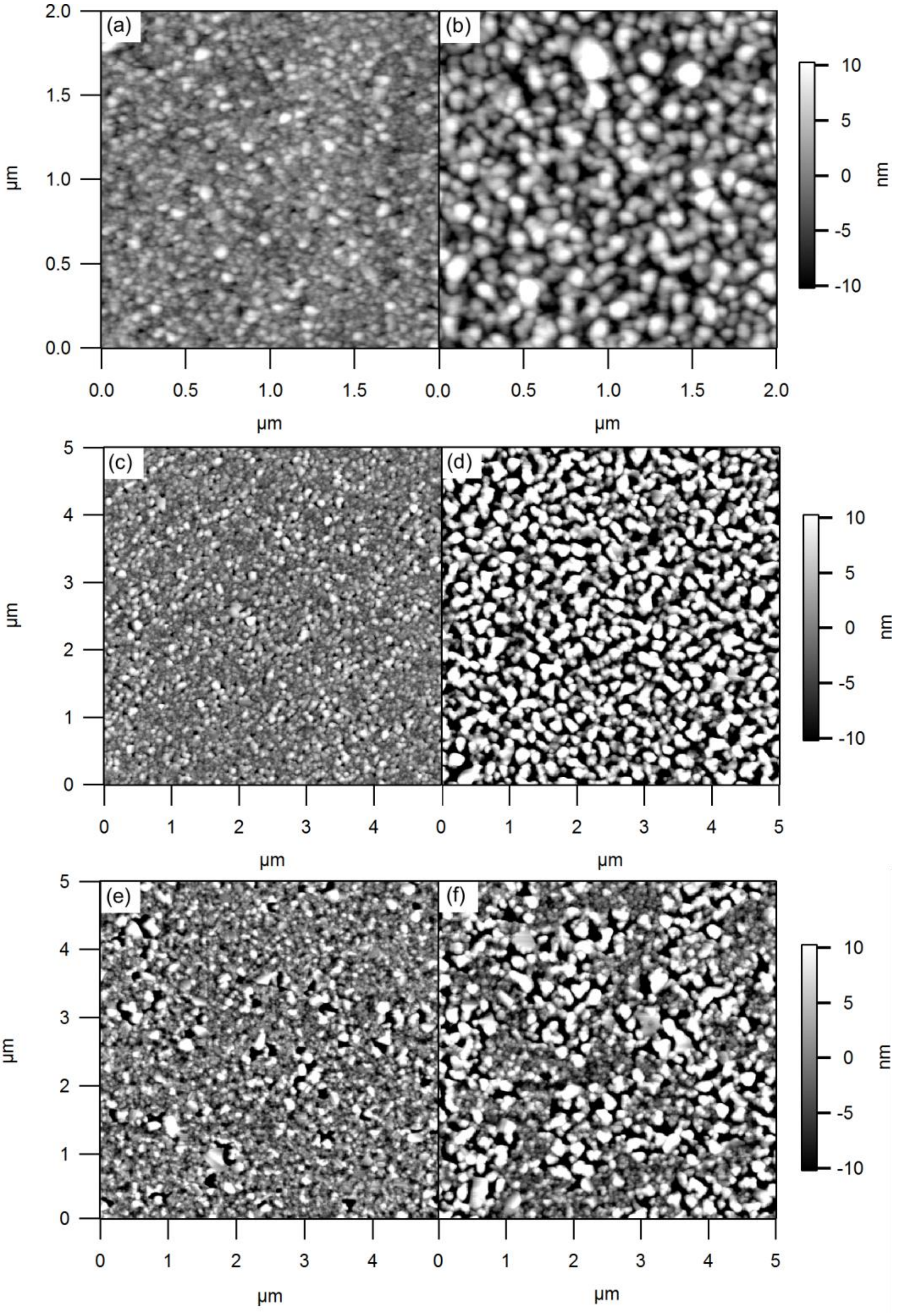

Figure 6.7: (a-b) Morphology of 9 nm Ag films supported on UV/O_3 treated PET post-annealing at 150 °C (a) and 200 °C (b) for 10 minutes. **(c-d)** Morphology of 13 nm Ag films supported on MPTMS derivatised glass post-annealed at 100 °C (c) and 150 °C (d) for 10 minutes. **(e-f)** Morphology of 15 nm Ag films supported on MPTMS derivatised glass post-annealed at 150 °C (e) and 200 °C (f) for 10 minutes.

6.3.5 Nanostructured Au and Ag electrodes

For further investigations nano-structured films meeting the following criteria were chosen: *(i)* a high density of apertures; *(ii)* a large reduction in far-field transparency – indicative of strong coupling between the incident light and the metal film; *(iii)* no significant change in sheet resistance as compared with flat films. 8.4 nm Au films were deposited on APTMS:MPTMS derivatised glass (150 mbar 1 hour ~ 80% monolayer coverage) and annealed to 350 °C, 11 nm Ag films deposited on 5 min UV/O_3 treated PET annealed to 200 °C. Prior to aperture formation by thermal annealing the 8.4 nm Au on glass and 11 nm Ag films on plastic substrate are continuous (Figure 6.8 (a) and (c)) and robust towards ultra-sonic agitation in a variety of solvents (Table 6.2). Subsequent annealing for 10 minutes results in the formation of a random array of non-uniformly shaped apertures (Figures 6.8 (b) and (d)), which however induce only moderate increase in sheet resistance.

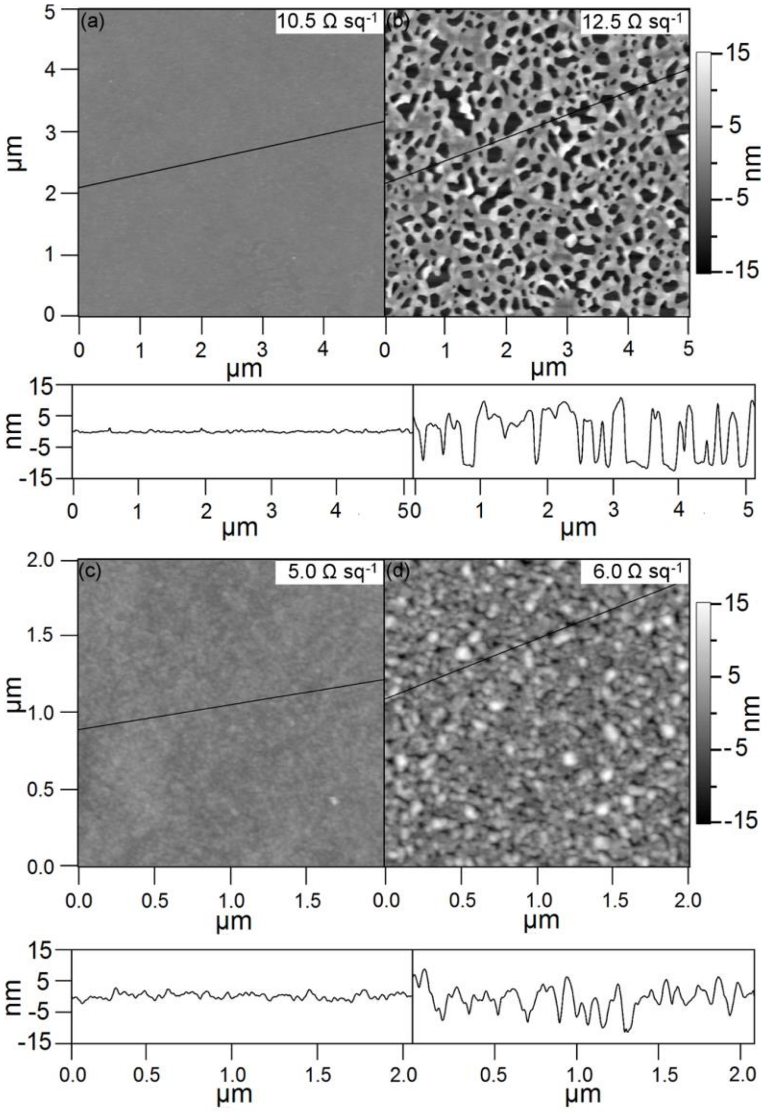

Figure 6.8: AFM topographs and cross-section of: (**Upper**) 8.4 nm Au films supported on APTMS:MPTMS derivatised glass before **(a)** and after **(b)** annealing at 350 °C.; (**Lower**) 11 nm Ag films on UV/O_3 treated PET before **(c)** and after **(d)** annealing at 200 °C.

Crucially the size and number density of the apertures does *not* change if the annealing time is extended beyond 10 minutes, although there is a slight decrease in surface roughness as the aperture edges are softened, as shown in Figure 6.5. The depth of the apertures measured using an AFM is comparable to that of the deposited film thickness, which is evidence that the apertures extend all the way through the metal film in both cases.

Table 6.2. Sheet resistance of 8.4 Au films and 11 nm Ag films pre- and post-annealing before and after ultra-sonic agitation in three common solvents (toluene, water and 2-propanol).

Sample	Untreated	Toluene [Ω sq^{-1}]	Water	2-propanol
Au (pre- anneal)	10.5 ± 1.0	11.0 ±1.0	12.5 ± 1.0	11.0 ± 1.0
Au (post -anneal at 350 °C)	12.5 ± 2.0	12.5 ± 2.0	16.0 ± 3.0	12.5 ± 2.0
Ag (pre- anneal)	5.0 ± 1.0	5.0 ± 1.0	6.0 ± 1.0	5.0 ± 1.0
Ag (post-anneal at 200 °C)	6.0 ± 1.0	6.0 ± 1.0	7.0 ± 1.0	6.0 ± 1.0

6.3.5.1 Au

In this study the Au films are optimised to have a random array of apertures with diameters in the range 80-250 nm peaking at ~ 100 nm since this range of symmetric aperture sizes have shown promise for light concentration[150, 151, 339,340] and collection in OPVs.[150, 151] Aperture size analysis, performed using WSxM software,[337] is shown in Figure 6.9. The aperture number density and area coverage is ~ 20 per μm^2 and ~ 20% respectively. The film thickness, 8.4 nm, was selected because the sheet resistance prior to aperture formation is ~ 10 Ω sq^{-1}, which is low enough for OPV applications. Upon brief thermal annealing to form apertures the sheet resistance increases by only 20% from 10.5 ± 0.5 Ω sq^{-1} to 12.5 ± 2 Ω sq^{-1}. The reason for such a small increase is two-fold: *(i)* The metal that forms the continuous film prior to annealing is simply re-distributed rather than being omitted, as is the case with lithography, so the thickness of the remaining metal is fractionally greater than that prior to annealing.; *(ii)* At the same time the metal network also becomes more crystalline and so its resistivity is reduced. The latter is evident from the straight edges of the apertures (Figure 6.8 (a)).

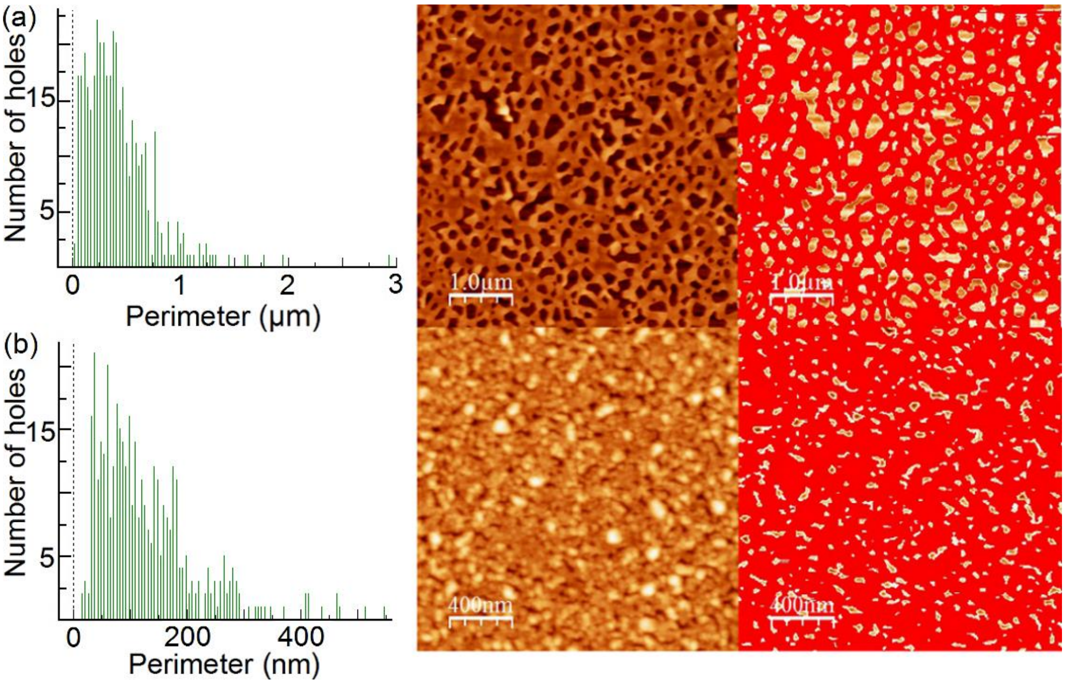

Figure 6.9: Perimeter distribution of apertures in **(a)** Au and **(b)** Ag films analysed using WSxM 5.0 Develop 5.2.[337]

6.3.5.2 Ag

For the preparation of optically thin Ag films on the flexible substrates PET and PEN, brief UV/O_3 treatment was used to form reactive oxygen containing moieties directly on the plastic surface. Core level HRXPS measurements (Figure 6.10 and Table 6.3) show that upon UV/O_3 treatment both hydroxyl and carboxylic acid moieties are formed, in addition to an increase in the prevalence of esters. Since carboxylic acids are known to bind to Ag surfaces[341] it is tentatively suggested that they are responsible for the improvement in interfacial adhesion: 11 nm Ag films evaporated onto untreated PET and PEN substrates have a sheet resistance of 10 ± 2 Ω sq^{-1}, peak transparency of ~73% in 400 – 750 nm range, and R_{rms} of ~ 3 nm. Upon 15 minutes ultra-sonic agitation in water the sheet resistance increased by 50%. Conversely 11 nm Ag films evaporated onto PET and PEN pre-treated with UV/O_3

exhibit half the sheet resistance (5 ± 1 Ω sq^{-1}), a 5% increase in peak transparency (~78%) and one third of the surface roughness (~ 1 nm). Furthermore, the sheet resistance remained unchanged after 15 minutes ultra-sonic agitation in water. Apertures do not form in 11 nm films on PET below 150 °C and the upper annealing temperature, 200 °C, is limited by the plastic substrate. This restriction on the upper annealing temperature limited the size of the apertures formed to an order of magnitude smaller than the wavelength of the incident light at ~ 30 nm. Aperture size analysis is provided in Figure 6.9 (b). The aperture density and coverage area in investigated Ag films is ~ 100 per μm^2 and ~ 15% respectively.

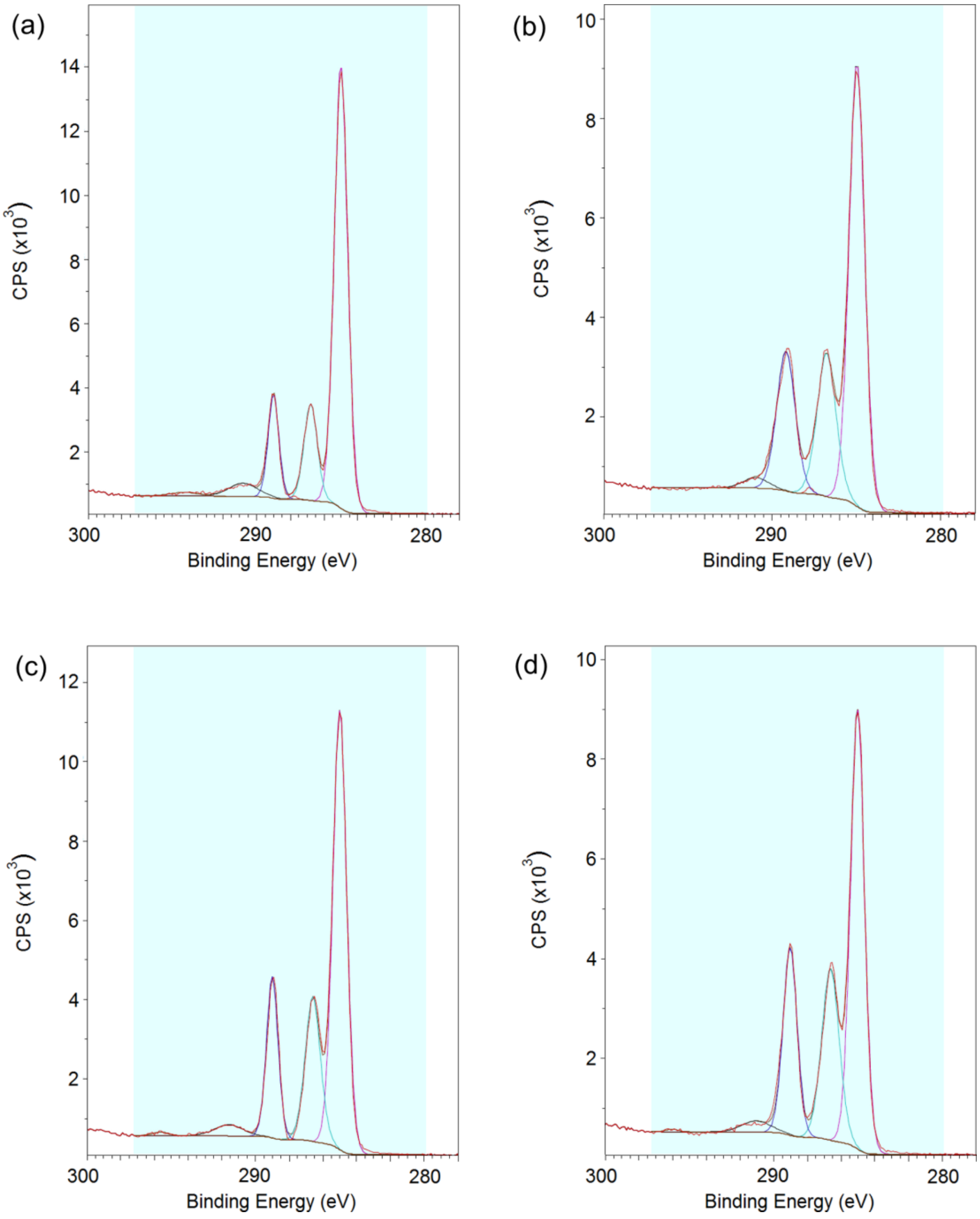

Figure 6.10: HRXPS: C 1s of PEN (a and b) and PET (c and d) before (a and c) and after (b and d) UV/O_3 treatment.

For practical application films with apertures must be mechanically robust. Au and Ag films with apertures fabricated according the procedure described herein are robust towards ultra-sonic agitation in a variety of solvents as shown in Table 6.2 and are stable under ambient conditions in direct sunlight. The transparency, sheet resistance and morphology remain unchanged after exposure to air and sunlight for one week. Longer term durability testing was not performed.

Table 6.3. (a) HRXPS peak intensities for C 1s and O 1s on PET and PEN substrates before and after UV/O_3 treatment; **(b)** Assignment of peaks.

(a)

Substrate	C 1s [%]	O 1s [%]
PET	72.8 ± 0.1	27.2 ± 0.1
PET UV/O_3	68.1 ± 0.1	31.9 ± 0.1
PEN	78.8 ± 0.1	21.1 ± 0.1
PEN UV/O_3	69.9 ± 0.2	29.7 ± 0.2

(b)

Substrate	Hydrocarbon [%]	Alcohol, ether [%]	Carbonyl [%]	Acid, ester [%]
PET	57.3	21.4	0.0	17.9
PET UV/O_3	50.7	24.4	0.1	21.7
PEN	67.5	14.4	0.2	12.6
PEN UV/O_3	55.2	22.0	0.3	20.5

6.3.3 Transparency

To demonstrate application of these nano-structured electrodes in OPVs, Au electrodes on glass and Ag electrodes on PET with and without apertures, as shown in Figure 6.8, were fabricated. Notably, unlike all other metal electrodes with apertures reported to date for use in OPVs, the sub-wavelength apertures in both electrodes have significant variance in size and shape. It is clear from Figure 6.11 that the far field transparency of the Au and Ag electrodes prior to annealing (i.e. without apertures) is much lower than that of the ITO electrodes on glass and plastic across most of the range between 400-900 nm. The effect of annealing is to further reduce the far-field transparency of both films since the nano-structured films support surface plasmon resonances which couple strongly with the incident light (Figure 6.11 (grey solid lines)).

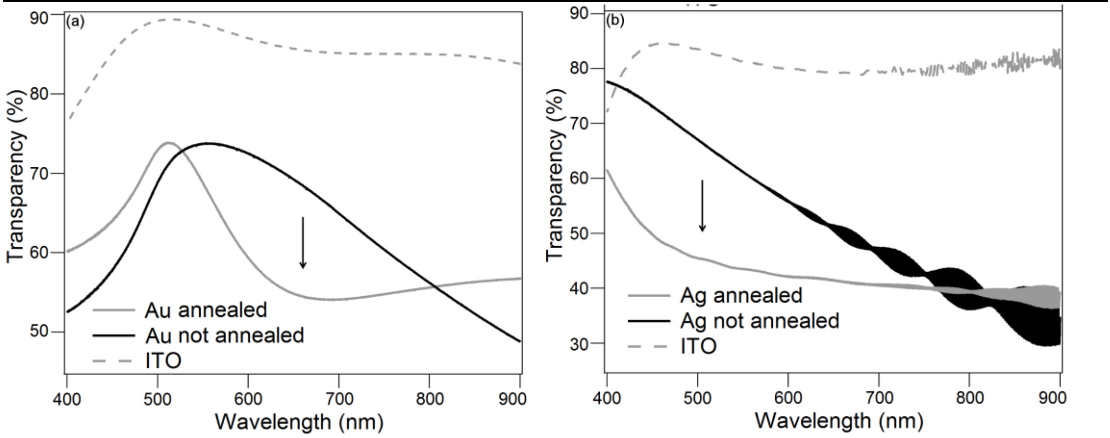

Figure 6.11: Far-field transparency spectra for: **(a)** 8.4 nm Au on APTMS:MPTMS derivatised glass before and after annealing at 350 °C, and commercial ITO coated glass.; **(b)** 11 nm Ag film on UV/O_3 treated PET before and after annealing at 200°C, and commercial ITO coated PET. The reference material was a UV/O_3 treated glass plate or PEN/PET film.

6.3.6 Device fabrication and testing

These nano-structured electrodes were employed as a drop-in-replacement for the ITO hole–extracting electrode in BHJ OPVs with the structure: hole-extracting electrode / *x* nm MoO_x / PCDTBT:$PC_{70}BM$ / 8 nm BCP / 100 nm Al. MoO_x is an efficient hole-extraction material for OPVs, giving best performance for 5 nm thickness, although maintaining good performance for significantly thicker layers up to 20 nm.[342] PCDTBT:$PC_{70}BM$ harvests light across the entire visible spectrum and so is ideally suited to investigate plasmon enhanced light harvesting effects across the wavelength range 300-750 nm. By changing the MoO_x thickness it is possible to determine the range over which light concentration effects extend from the electrode surface. The J_{sc} of devices with the optimal MoO_x thickness of 5 nm on Au and Ag electrodes *without* apertures was ~ 25% lower than on ITO glass, consistent with the lower transparency of unpatterned metal electrodes. At a thickness of 5 nm the MoO_x layer is expected to be thin enough for the photoactive layer to benefit from light concentration in the vicinity of the electrode due to plasmonic effects[64] whilst being thick enough to prevent exciton quenching by the electrode.[343,344] In Table 6.4 the performance of OPVs fabricated on Au and Ag electrodes with apertures (N – nanostructured electrode) is compared to identical devices fabricated on electrodes without apertures (P – planar electrode) for MoO_x thickness varying from 5 to 20 nm. To exclude the effect of changes in optical geometry brought about by changing the MoO_x thickness only devices employing MoO_x layers of the same thickness are compared directly.

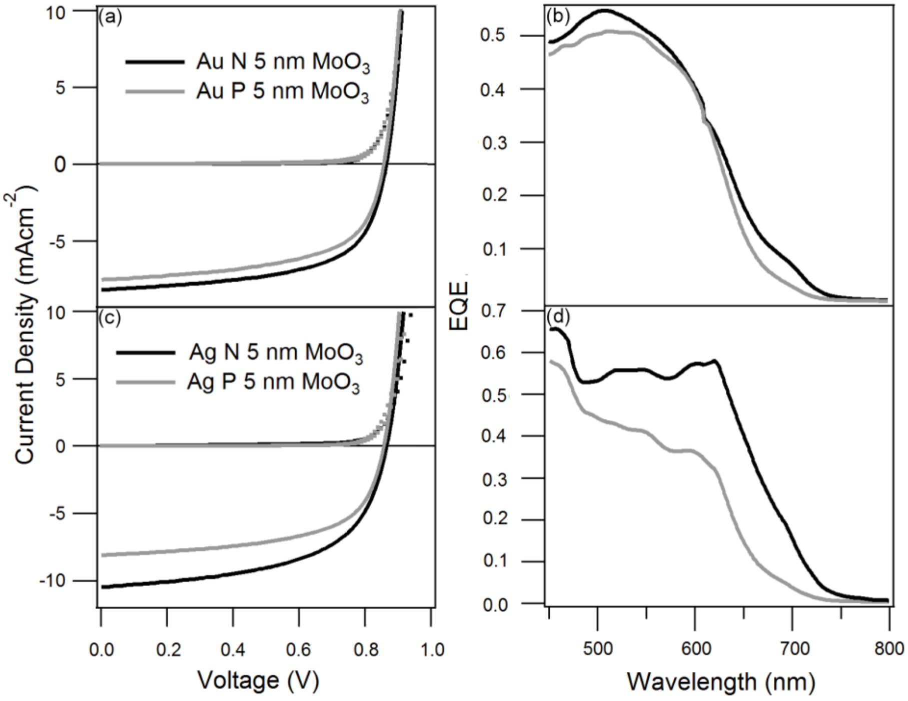

Figure 6.12: *J-V* characteristics (a and c) and associated *EQE* spectra (b and d) of hole-extracting electrode / MoO_x (5 nm) / PCDTBT:$PC_{70}BM$ / BCP / Al OPVs employing Au (upper) and Ag (lower) window electrodes with (N) and without (P) apertures.

Table 6.4. Key OPV performance characteristics under 1 sun simulated solar illumination with device architecture: hole-extracting electrode / *x* nm MoO_x / PCDTBT:$PC_{70}BM$ / BCP / Al. The metal electrode is either planar (P) or nano-structured (N). Table: **(a)** hole-extracting electrode = 8.4 nm Au; **(b)** hole-extracting electrode = 11 nm Ag on PEN.

(a)

MoO_x (nm)	*5 N*	*5 P*	*10 N*	*10 P*	*20 N*	*20 P*
J_{sc} [mA cm^{-2}]	8.55 ± 0.15	7.60 ± 0.10	7.90 ± 0.30	8.15 ± 0.20	7.65 ± 0.20	7.85 ± 0.20
V_{oc} [V]	0.85 ± 0.01	0.85 ± 0.02	0.86 ± 0.01	0.85 ± 0.02	0.87 ± 0.01	0.87 ± 0.01
FF	0.59 ± 0.03	0.53 ± 0.05	0.64 ± 0.01	0.61 ± 0.01	0.61 ± 0.01	0.60 ± 0.01
η [%]	4.30 ± 0.30	3.40 ± 0.40	4.35 ± 0.30	4.50 ± 0.30	4.10 ± 0.15	4.05 ± 0.15

(b)

MoO_x (nm)	*5 N*	*5 P*	*10 N*	*10 P*	*20 N*	*20 P*
J_{sc} [mA cm^{-2}]	10.60±0.25	8.25 ± 0.40	8.35 ± 0.20	8.20 ± 0.30	7.80 ± 0.50	7.45 ± 0.60
V_{oc} [V]	0.86 ±0.02	0.84 ± 0.02	0.85 ± 0.03	0.85 ± 0.01	0.85 ± 0.02	0.85 ± 0.02
FF	0.56 ± 0.03	0.55 ± 0.03	0.57 ± 0.03	0.58 ± 0.03	0.57 ± 0.02	0.59 ± 0.03
η [%]	5.10 ± 0.30	3.80 ± 0.35	4.05 ± 0.30	4.05 ± 0.40	3.80 ± 0.50	3.75 ± 0.60

It is evident from Table 6.4 that for OPVs employing the same MoO_x thickness neither V_{oc} nor *FF* are adversely affected when sub-wavelength apertures are introduced into the hole-extracting electrode. This also holds true for the bi-layer OPVs fabricated as part of this study (discussed below) which employ a sub-phthalocyanine electron-donor layer and demonstrates that voltage losses associated with extracting photo-generated holes from regions immediately above apertures are not significant. In devices with a 5 nm MoO_x layer the J_{sc} is significantly higher in

OPVs employing an electrode with apertures (28% higher for Ag and 13% higher for Au) despite the far lower transparency (Figure 6.11). This result can be rationalised in terms of strong coupling between the incident light and the photo-active layer mediated by plasmon excitons localised on the apertures and/or surface plasmon polaritons. For a MoO_x thickness of 10 nm or more the J_{sc} of devices with apertures is comparable to those without apertures. This strong dependence of the enhancement in J_{sc} on the separation between the electrode and the photoactive layer is consistent with the short-range over which plasmon mediated light concentration effects operate.[64,339] The EQE spectra also provide evidence for plasmon enhanced light absorption, since the photocurrent enhancement is wavelength dependent and the EQE is enhanced at wavelengths where the electrode transparency is particularly low: namely 675 nm and 625 nm for Au and Ag electrodes respectively. The increase in J_{sc} is most pronounced in devices employing Ag electrodes. The optical constants of Ag make it the metal of choice for the optimisation of surface plasmon polariton mediated light-trapping[345] which offers a plausible explanation for this result. However, this difference could also be attributed to the much higher number density of apertures and/or smaller mean aperture size. Importantly from a technological perspective the 28% increase in J_{sc} when using the nano-structured Ag electrode, from 8.25 ± 40 mA cm^{-2} to 10.60 ± 0.25 mA cm^{-2} is so large that it exceeds J_{sc} in identical OPVs employing an ITO electrode (10.25 ± 0.15 mA cm^{-2}). Notably the FF is also improved (0.56 ± 0.03 *vs.* 0.52 ± 0.02) due to the lower sheet resistance of the Ag electrodes (5 ± 1 Ω sq^{-1} *vs.* 45 Ω sq^{-1}), which translates to a large improvement in η from 4.58% to 5.10%.

To demonstrate the wider applicability of these nano-structured window electrodes they were incorporated into bilayer OPVs fabricated by vacuum deposition based on a SubPc / C_{60} heterojunction. The device structure is: hole-extracting electrode / 5 nm MoO_x / 14 nm SubPc / 40 nm C_{60} / 8 nm BCP / Al. The SubPc layer is only 14 nm in thickness, but is located adjacent to the plasmon-active electrode and so is well placed to benefit from light concentration and trapping effects at the electrode surface. The *J-V* characteristics (Figure 6.13 and Table 6.5) clearly show an increase in photocurrent, which is again greatest for the Ag electrode. The EQE spectra for OPVs on nanostructured Au are consistent with those measured for PCDTBT:PC_{70}BM, exhibiting a broad absorption enhancement between 400-580 nm and no enhancement at 580-620 nm. The EQE spectra for OPVs on nanostructured Ag electrodes are also broadly consistent with those measured for PCDTBT:PC_{70}BM in that there are significant increases in photocurrent generation between 450-600 nm.

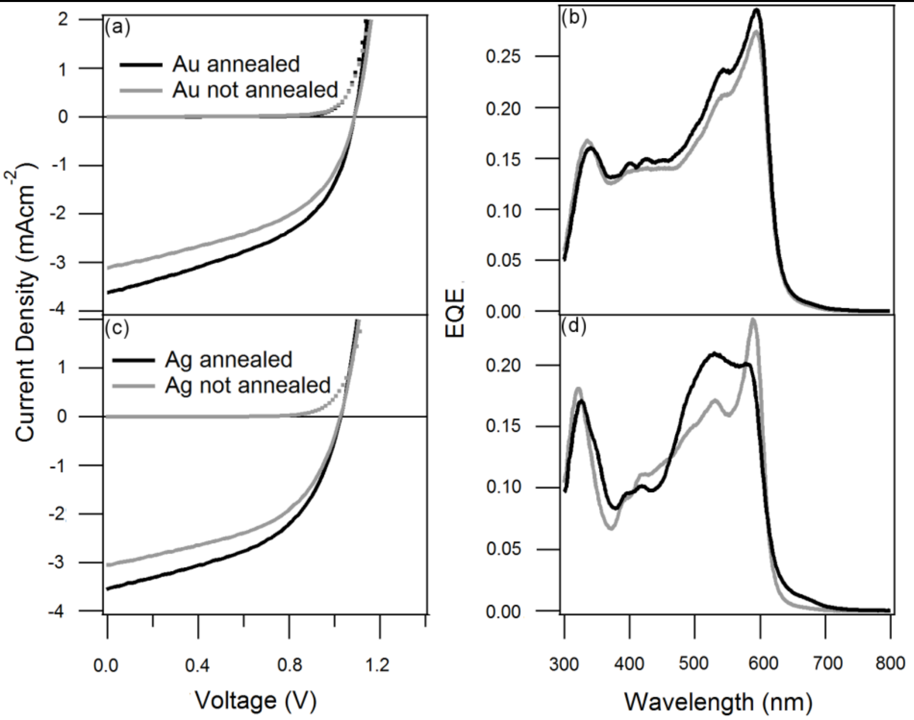

Figure 6.13: *J-V* characteristics and EQE spectra of different devices SubPc/C_{60} devices on Au (a), (b) and Ag (c), (d) electrodes.

Table 6.5. Key OPV performance characteristics under 1 sun simulated solar illumination with device architecture: hole-extracting electrode / 5 nm MoO_x / 14 nm SubPc / 40 nm C_{60} / 8 nm BCP / 100 nm Al. The metal electrode is either planar (P) or nano-structured (N).

(a)

Electrode: Au	P	N
J_{sc} [mA cm-2]	3.30 ± 0.15	3.50 ± 0.15
V_{oc} [V]	1.09 ± 0.01	1.09 ± 0.01
FF	0.48 ± 0.01	0.48 ± 0.01
η [%]	1.67 ± 0.10	1.80 ± 0.10

(b)

Electrodes: Ag	P	N
J_{sc} [mA cm-2]	3.00 ± 0.10	3.50 ± 0.15
V_{oc} [V]	1.03 ± 0.01	1.03 ± 0.01
FF	0.50 ± 0.01	0.51 ± 0.01
η [%]	1.55 ± 0.10	1.80 ± 0.10

6.4 Conclusions

In this Chapter a lithography-free approach to fabricating optically thin noble metal electrodes with a dense array of nano-sized apertures is reported. This method has three key advantages over lithographic methods: *(i)* It is inherently less complex since there is no requirement for the positioning or removal of a mask.; *(ii)* It is a non-contact method and so the risk of imparting debris to the surface is minimal.; *(iii)* The introduction of apertures does not incur a large increase in sheet resistance as compared to unpatterned films. These electrodes are shown to be remarkably robust towards aggressive ultra-sonic agitation in a variety of solvents and, when employed as the window electrode in bulk-heterojunction and bilayer OPVs, increase η by coupling strongly with the incident light and concentrating it in the photoactive layer near to the electrode surface. As a direct replacement for ITO electrode in flexible OPV device efficiency is improved from 4.6% to 5.1% demonstrating that these electrodes have both a mechanical and efficiency advantage over conducting oxide window electrodes.

Finally, to help guide the design of these electrodes for OPV it is useful to determine whether the sub-wavelength apertures need to have a tight size and shape distribution or whether this design principle can be relaxed.

Chapter 7.

Understanding the improvement in OPV efficiency using a sub-1 nm Au film at the hole-extracting electrode / organic semiconductor interface

Summary

This Chapter shows how the electrodes developed in Chapter 3 can be used to investigate a fundamental question of importance in OPV research. It represents work in progress and is included to illustrate the direction for future work.

The efficiency of OPVs can be dramatically improved by incorporating a sub-1 nm Au layer at the interface between the hole-extracting electrode and the donor layer, although it is not understood why. This chapter investigates this phenomenon in pursuit of a complete explanation for the effectiveness of such a small amount of Au at this interface, exploiting the model Au electrode described in Chapter 3. The significantly different nature of thin Au electrodes, as compared to the conducting oxide electrodes used in all previous reports on this subject also demonstrates the versatility of this approach to non-oxide electrodes for the first time.

7.1 Introduction

It is known that an ultra-thin, typically sub-1 nm, discontinuous Au layer at the interface between the conducting oxide transparent electrode and the organic semiconductor in OPVs has a remarkably beneficial effect on device performance,[346,347,348,349] without significantly changing the transparency[349] or roughness[346] of the electrode. Cattin *et al.* have shown, using two separate methods (SEM image analysis and XPS peak shape analysis), that for an Au film thickness of 0.5 nm the coverage of the oxide surface is ~ 15% with an average particle size of 4.8 – 7.5 nm^2, increasing to ~ 35% coverage for a film thickness of 1.5 nm.[350] Importantly, the results were essentially the same for both ITO and ZnO substrates. It is surprising that such a low surface coverage should be so effective as an interfacial layer since buffer layers used in OPVs, such as TiO_2, MoO_3 and PEDOT:PSS are typically continuous.

The improvement in OPV performance has been observed in small molecule architectures and with different conducting oxides (namely, fluorine doped tin oxide, aluminium doped zinc oxide and ITO) serving as the transparent electrode.[346, 349, 351, 347, 350] However, it is achieved exclusively with Au as an interfacial layer. The same device architectures with sub-1nm films of other metals exhibit comparable (e. g. Ag) or inferior (e. g. Pt) efficiency as compared to the reference.[349] The efficiency improvement when using Au results from a large improvement in J_{sc} and *FF*.[346, 349,347] and is usually attributed to: (*i*) the high ϕ of Au (5.1 eV) which, it is argued, improves the energy level alignment at the electrode – organic semiconductor interface;[346, 349, 351] (*ii*) and/or favourable changes in the semiconductor layer growth mode on the Au modified oxide, resulting in an improvement in hole-extraction efficiency.[349] However this does not explain why other high ϕ metals, such as Pt, are not equally effective, nor does it account for the fact that when Au forms a contact with a donor type organic semiconductor there is invariably a large negative vacuum level shift (due to the *push-back* effect – see section 1.3) which has the effect of reducing the Au ϕ.

A number of different studies have shown that absorption in the photoactive layer can be enhanced due to plasmonic scattering or near field enhancement caused by localised surface plasmon resonances.[64, 148, 352,353] However in this case the Au nanoparticles are too small to efficiently scatter visible light and because they are uncapped, quenching competes with any beneficial effect of enhanced light absorption.[354]

Understanding why sub-1 nm Au films are so effective in this context is made difficult by the complex nature of the conducting oxide electrodes used in OPV research. Ternary conducting oxides, such as ITO, are meta-stable and chemically ill-defined with a relatively high surface roughness. The surface chemistry is also difficult to control and depends strongly on the deposition method and applied cleaning procedures resulting in variability in ϕ and difficulties in obtaining reproducible electrical performance.[355,356] Furthermore, the plasma etching and UV/O_3 treatments, that are commonly used as standard surface cleaning methods, introduce an extra complexity since they increase the oxidation state of the upper most surface of the electrode rendering it more insulating than the bulk.[357,358] Whilst this layer is thin enough to be transparent to the flow of electrons across the interface (~1 nm) it is responsible for the change in surface potential that gives rise to the increase in the ϕ of conducting oxides when treated with UV/O_3 or oxygen plasma.[359,360,5]

The Au electrode described in Chapter 3 is a '*model*' window electrode, with a homogeneous smooth surface and is chemically well-defined. It therefore offers an opportunity to study the phenomenon of improved efficiency in OPVs using sub-1 nm Au overlayer by removing the complexity associated with conducting oxide electrodes. A brief UV/O_3 treatment of Au results in the formation of an ultra-thin

AuO_x layer mimicking the surface of conducting oxide electrodes after plasma or UV/O_3 treatment. Importantly this oxide layer is self-limiting at ~1 nm and the exact thickness can be inferred from the change in film resistance as described in Chapter 3. Importantly, Rentenburger *et al.*[361] and Cacialli *et al.*[362] have separately shown that the oxide nanolayer formed at the surface of Au electrodes is stable when buried beneath an organic semiconductor.

7.2 Experimental

7.2.1 Fabrication of Au/AuO_x/sub-1nm Au electrodes

8.4 nm Au electrodes on glass were prepared according to the procedure described in Chapter 3. The electrodes were UV/O_3 treated for 15 minutes immediately prior to evaporation of an ultra-thin Au overlayer.

7.2.2 Electrode characterisation

Metal films were characterised using the techniques described in Chapter 2.

7.2.3 OPV fabrication and testing

The electrodes were incorporated into OPVs with the structure: Au / AuO_x / Au electrode / BHJ / 8 nm BCP / 100 nm Al where the BHJ was P3HT:PCBM (1:1 P3HT:PCBM spincasted from 40 mg ml^{-1} overall solution in dichlorobenzene) or PCDTBT:$PC_{70}BM$ (1:3 PCDTBT:$PC_{70}BM$ spincasted from 16 mg ml^{-1} overall solution in chloroform).

7.3 Results and discussion

7.3.1 Electrode characterisation

8.4 nm Au electrodes supported on mixed APTMS:MPTMS derivatised glass have a sheet resistance of 11.5 Ω sq^{-1} ± 1.0 Ω sq^{-1}. In such thin films the resistivity is thickness dependant and higher than in bulk Au. This is because the film thickness is lower than the electron mean free path in the bulk and so there is scattering from the film surfaces as discussed in Chapter 3. After 15 minutes UV/O_3 treatment a thin layer of AuO_x is formed and the sheet resistance increases to 13 Ω sq^{-1}. From this increase it is possible to estimate the oxide layer thickness to be ~ 1 nm, assuming that the AuO_x layer is insulating. Ordinarily AuO_x is known to be unstable and undergoes reduction to Au.[361, 363,360] Consistent with this after 48 hours the sheet resistance of films stored under N_2 or in air returned to that before oxidation. This process of gradual reduction is not however observed when the oxide is buried beneath an organic semiconductor layer where the oxide remains stable for at least few days.[361] The ultra-thin AuO_x oxide layer is therefore stable enough for the purpose of this experiment since devices were fabricated within minutes of the oxidation step.

Figure 7.1 (a) shows SEM micrographs of 1 nm Au evaporated onto a UV/O_3 treated 8.4 nm Au electrode. As previously shown in Chapter 3 these electrodes have a very low surface roughness (R_{rms} <0.4 nm) and uniform polycrystalline structure, which is why there is very little contrast in the SEM image (Figure 7.1 (a) **inset**). UV/O_3 treatment of the electrode renders the Au electrode surface hydrophilic, hence the thin Au overlayer forms nanoparticles similar to those formed on conducting oxide electrodes, which correspond to the bright patches on the SEM micrographs (Figure 7.1 (a)). The surface coverage has been estimated with WSxM software to be

~ 25% coverage of the electrode surface, which is in good agreement with the work of Cattin *et al.*[350] For comparison, Figure 1(b) – (d) shows SEM images of 1 nm Cu, Ag and Al deposited on UV/O_3 treated Au from which it is clear that there is a lower density of much larger patches of metal – significantly different to those formed by Au.

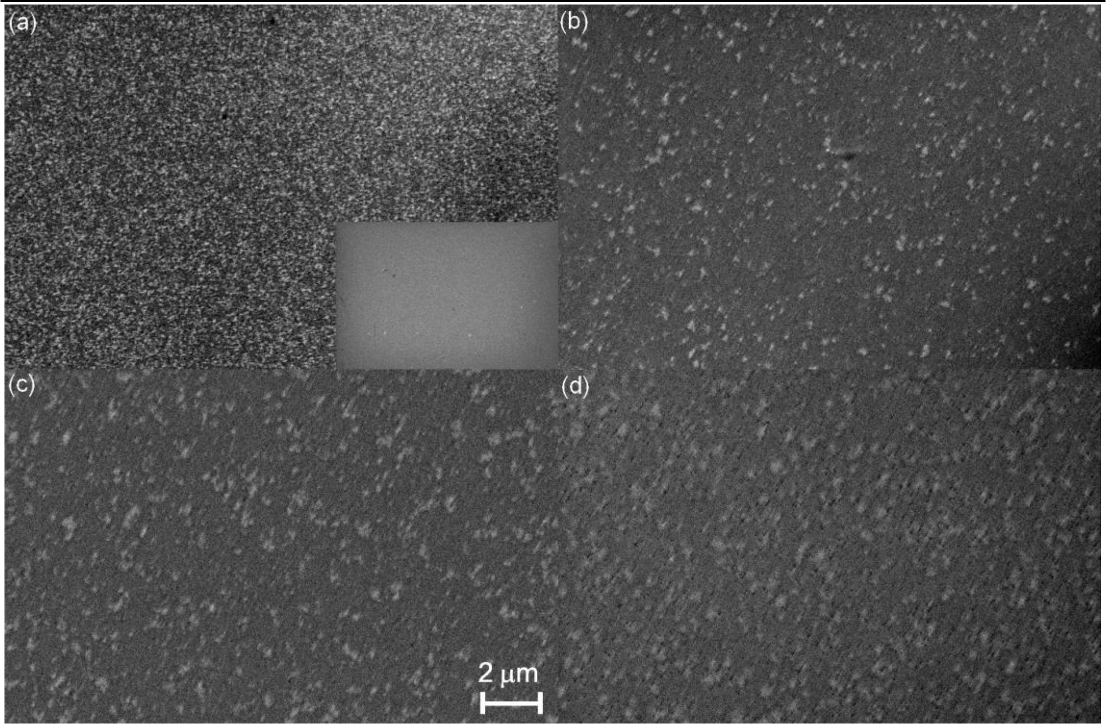

Figure 7.1: SEM micrograph of 1 nm of (a) Au; (b) Ag; (c) Cu; (d) Al on UV/O_3 treated 8.4 nm Au film supported on APTMS:MPTMS derivatised glass. **Inset in (a):** UV/O_3 treated 8.4 nm Au without a sub-1 nm metal overlayer.

The evolution of the ϕ as a function of Au overlayer thickness on freshly UV/O_3 treated Au and ITO electrodes is shown in Figure 7.2. The reduction in ϕ of the oxidised Au electrode with increasing Au thickness, and convergence to a value of ~ 5 eV, is consistent with the lower ϕ of Au (5.0-5.1eV) as compared to AuO_x

(5.4-5.6 eV).[361,360] The unchanging ϕ of the ITO substrate is consistent with fact that ϕ of freshly UV/O_3 treated ITO is comparable to that of Au.

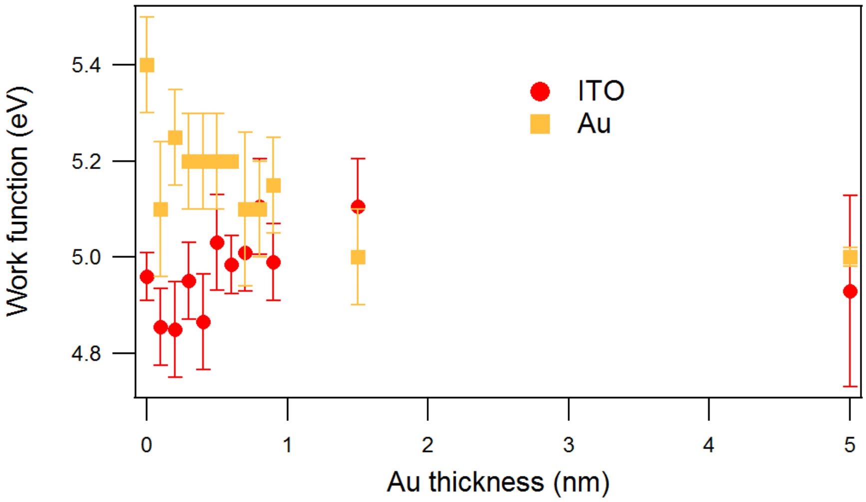

Figure 7.2: The ϕ of freshly UV/O_3 treated Au and ITO electrodes as a function of Au overlayer thickness.

7.3.2 Device fabrication and testing

After fabrication the oxidised Au electrodes with and without a sub-1 nm Au overlayer were immediately incorporated into OPVs with the structure: electrode / P3HT:PCBM / BCP / Al. The OPV characteristics are summarised Figure 7.3. The trend in OPV efficiency is in good agreement with the results presented by Bernede *et al.* for CuPc :C_{60} bilayer OPVs using an ITO electrode:[349] V_{oc} gradually decreases with increasing Au overlayer thickness, whilst FF and J_{sc} are dramatically improved in the presence of ultra-thin Au, reaching peak value for Au thickness of 0.3-0.6 nm for FF and 0.8-0.9 nm for J_{sc}.

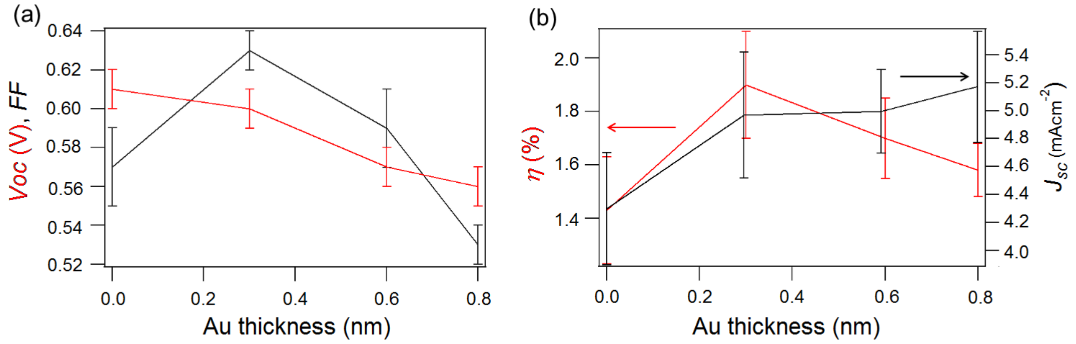

Figure 7.3: Variation of the typical cell performance of OPV with structure: Au / AuO$_x$ / Au *x* nm / 1:1 P3HT:PCBM / BCP / Al as a function of *x*.

The same trend is observed when the P3HT:PCBM is replaced with PCDTBT:PC$_{70}$BM blend, although the latter had a very high failure rate as compared to devices fabricated using P3HT:PCBM and conventional oxide interlayers such as those used in Chapter 5 and 6. The reason for this is not yet clear.

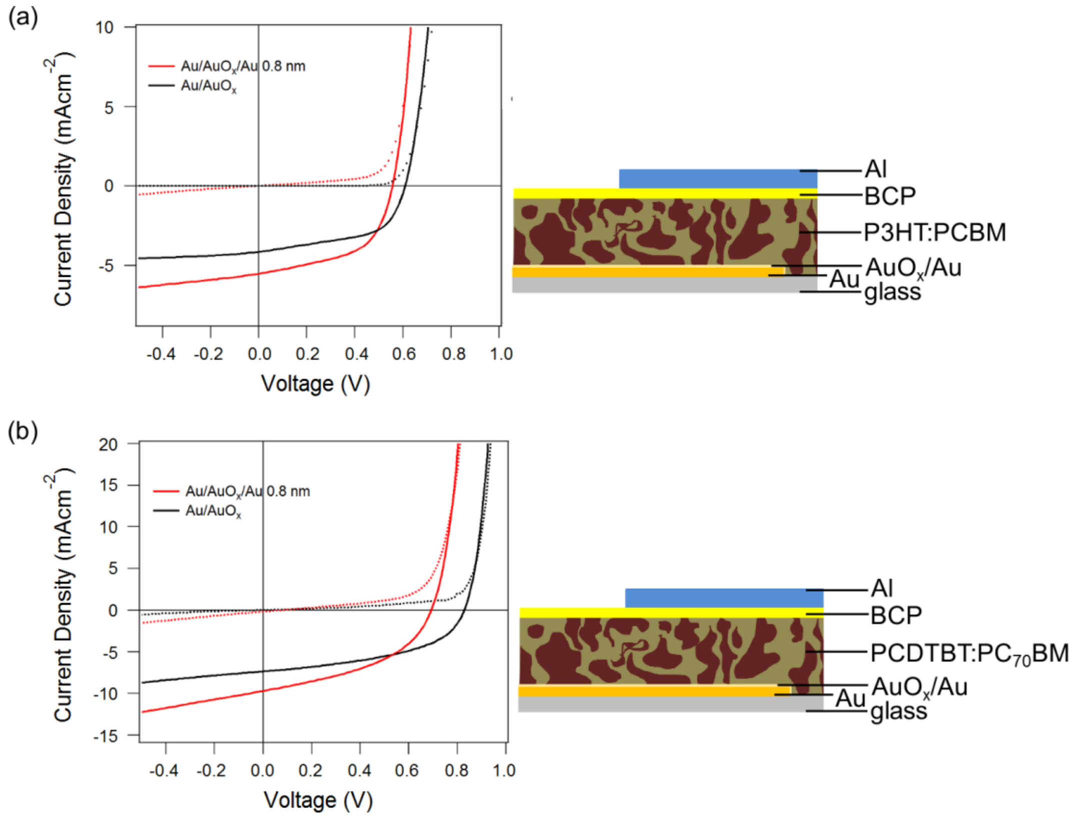

Figure 7.4: *J-V* characteristics of Au/AuO$_x$/Au (0 or 0.8 nm) / P3HT:PCBM (typical) (a) PCDTBT:PC$_{70}$BM (best) (b) / BCP / Al.

In the literature the main factor used to explain the improvement in efficiency of OPVs with an ultra-thin Au interlayer is better energy alignment between the electrode Fermi level and the HOMO of the adjacent organic semiconductor.[349, 351,348] This explanation does not however account for the following points:

1. The improvement in performance is not observed using metals with comparable or higher ϕ than Au, such as Pt or Ni.[349]

2. Whilst it is true that the ϕ of conductive oxides is typically lower than that of Au prior to oxidation ~ 4.5 eV,[349] the oxygen plasma/UV/O_3 treatment used as a standard cleaning procedure, enrich the oxide surface with oxygen,[357, 358] which increases the ϕ increase to > 5.0 eV,[5] which is comparable to that of Au (Figure 7.2).

3. The fact that ϕ of evaporated Au is effectively reduced by as much as 0.5 – 1 eV upon contact with most donor type organic semiconductors due to the *push-back* effect is not accounted for.

4. The optimal surface coverage of Au is very low, at only ~ 15 %.[350]

5. V_{oc} typically decreases in OPVs using a sub-1 nm Au interlayer.

It is possible to understand the reduction in V_{oc} in terms of measurements of the interfacial energy level alignment reported in the literature: When donor-type organic semiconductors come in contact Au there is always a negative vacuum level shift. For P3HT this means that the barrier to hole injection from the Au Fermi level to the HOMO of P3HT is 0.35 eV. At the interface between PCBTBT there is an 0.33 eV negative vacuum level shift.[364] This means that in both cases the HOMO of the donor and the Fermi level of the electrode are poorly aligned and so the built-in electric field is not maximised, hence V_{oc} is lower than the maximum achievable because of the earlier onset of the dark current.

One possible explanation for the improvement in J_{sc} and FF is that of geometric electric field enhancement. Pegg and Hatton have recently shown that conducting nano-protrusions at the surface of a flat conductor can facilitate the extraction of holes in OPV *via* a purely geometric effects by concentrating the electric field.[365] To see if this offers a possible explanation in this case, where there is a thin insulating layer at the electrode surface, we have conducted the simulations described in following section.

7.3.3 Electric Model

The electric field in the vicinity of Au nano-islands at the surface of an otherwise smooth oxide coated electrode was simulated using the COMSOL Multiphysics software. The electric field strength (F) between parallel plate electrodes was simulated in 3-dimensional space, with an electrode separation of 60 nm, which is corresponding to the thickness of PCDTBT:PC$_{70}$BM BHJ layer. A potential difference of 0.5 V, which is typical of the built-in field in OPV near to the short circuit condition, was applied between the electrodes. The structure simulated is as following; (1) bulk metal electrode; (2) very thin resistive overlayer; (3) hemispherical metallic island (4) conducting polymer. Two sets of simulations were performed. The first keeps the conductivity of the oxide overlayer fixed and varies the layer thickness. The second keeps the oxide layer thickness fixed at1 nm as in the case of freshly UV/O_3 treated Au and ITO[357, 358] and varies the conductivity. The permittivity of AuO_x is assumed to be 16.[366] The conductivity of AuO_x depends strongly on the Au:O ratio[367] and changes over time due to oxide instability.[368] Also the electrical properties of ITO depends strongly on the oxygen content[369,370,371] and so the conductivity of the thin oxide layer formed upon UV/O_3 treatment is very difficult to predict. Considering the conductivity of other metal oxides; $Ag_2O \sim 10^{-4}$ Sm^{-1}, AgO ~ 4×10^{-4} Sm^{-1},[372] $WO_x \sim 10^{-4}$ Sm^{-1}, $CuO_x \sim 10^{-2}$ Sm^{-1} [373] a conductivity of 10^{-3} Sm^{-1} has been assumed for the first set of simulations. The effect of changing the conductivity in the range 10^{-10} to 10^{-3} Sm^{-1} has also been investigated in the second set. The metallic islands are assumed to have a hemispherical shape – which helps to minimise their surface energy – with radius 1 – 1.5 nm as calculated on the basis on results of Cattin *et al.* [350] The permittivity of the conducting polymer is assumed to be ~ 3.5[374,188] and its conductivity is assumed to be ~ 10^{-8} Sm^{-1}.[375] The model was set-up so that a custom physics controlled extra-fine triangular mesh. The results of the simulation are given in Figures 7.5 and 7.6.

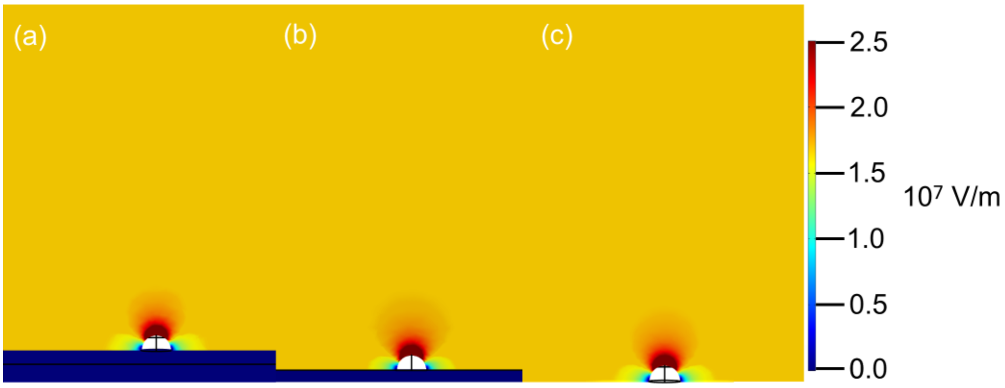

Figure 7.5: The electric field distribution in the vicinity of hemispherical Au nanoparticle of radius 1.5 nm on 3 nm (a), 0.5 nm (b), 0 nm (c) thick oxide layer with conductivity 10^{-3} Sm^{-1}.

It is clear from Figure 7.5 that the electric field in the region above the nanoparticles is enhanced as compared to the bulk field and that the radius of the enhanced field region is greater than the radius of the metal hemisphere. Due to relatively low resistivity of the interlayer, there is a little difference between architectures with and without oxide interlayer (Figure 7.5). This result is consistent with the simulations of Pegg *at al.* for metal nanoparticles at the surface of a flat metal electrode and means that the nano-particles should be very effective at extracting photo-generated charge carrier to the external circuit.[365]

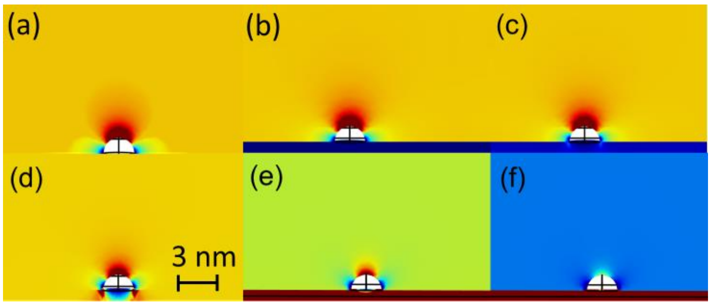

Figure 7.6: The electric field distribution for hemisphere of radius 1.5 nm without oxide (a) and on 1 nm oxide with conductivity: (b) 10^{-3} Sm^{-1}; (c) 10^{-7} Sm^{-1}; (d) 10^{-8} Sm^{-1}; (e) 10^{-9} Sm^{-1}; (f) 10^{-10} Sm^{-1}.

It is evident from Figure 7.6 that for more resistive oxide layers a region of enhanced electric field above the nanoparticles is still achieved with the advantage that the volume of reduced field at the particle sides is decreased. Notably the bulk field is reduced when the oxide layer becomes very insulating because the built-in potential is distributed across the polymer layer and thin oxide layer according to their resistance.

To mimic the real structure of electrodes simulations including a number of Au nanoparticles have been performed (Figure 7.7). Geometric field enhancement is known to be very sensitive to the proximity of adjacent protrusions,[365] due to field screening effects, which corroborates with experimental results, where the strongest improvement is achieved for Au layer ≤ 1 nm, [349, 350] where the coverage is <30%.[350]

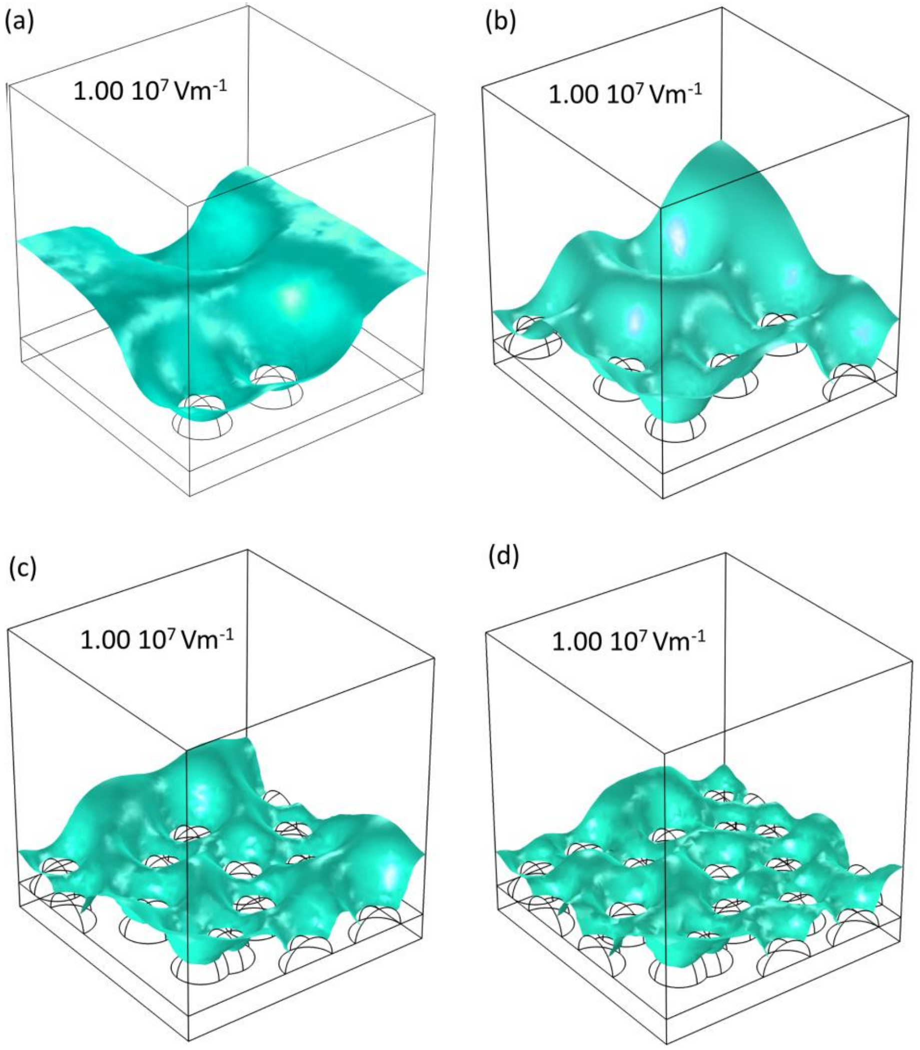

Figure 7.7: Iso-surface of electric field strength above metal electrode with 1 nm oxide overlayer of conductivity 10^{-3} Sm^{-1} and 1 nm radius hemispherical islands of coverage; (a) 10%; (b) 20%;p (c) 40% (d) 60%. The scale: 10 nm × 10 nm × 10 nm.

The results of the simulation show the adverse effect of electric field screening. The thin resistive layer plays an important role in promoting the growth of small and separated Au islands needed for geometric electric field enhancement, which, based on the SEM images in Figure 7.1 seems to be unique for Au among the investigated metals. The resistive nano-layer may also amplify the effect of field enhancement, however this is difficult to determine due to the unknown conductivity of the oxide interlayer. For coverage of > 30% the field enhancement is supressed and other effects detrimental for OPV performance, such as exciton quenching and transparency decrease, start to adversely affect OPV performance, so improvement is observed in architectures employing only very thin ~ 1 nm Au layers.

7.3.4 Future Work

To better understand the origin of the improvement in OPV operation upon introducing a sub-1 nm Au layer further investigations are necessary.

- The ill-defined nature of the thin oxide interlayer could be understood better if an oxide of known properties was introduced. The application of different materials with a range of conductivities and controllable thickness could shed light on the importance of the insulating layer in metal island field enhancement.
- A capping self-assembled monolayer could be introduced to avoid the reduction in FF and V_{oc}.
- Different OPV architectures and tests to determine if the Au layer indeed affects the morphology of the organic layer and so the OPV performance.

Chapter 8

Conclusions

The work presented in this thesis has focused on the development ultra-thin metal film electrodes for OPVs with the aim of boosting device performance, lowering the cost and/or extending the range of potential applications. By developing and modifying methods of controlling adhesion between the metal and the supporting substrate and post-deposition treatments, the properties of thin metal films have been optimised and improved for application as the window electrode in OPVs.

8.1. Ultra-thin Au electrodes on glass

Firstly a new method for fabricating highly transparent ultra-thin (~ 8 nm) Au films on glass has been described. The method is based on co-deposition of a mixed molecular adhesive layer of amine and thiol terminated silanes from the vapour phase immediately prior to Au thermal evaporation. Films supported on a mixed nanolayer proved to have properties better suited for OPV application than those supported on single component nanolayers (either amine or thiol terminated silanes) in addition to the shortest preparation time. The resulting films are highly transparent (mean transparency > 70%) and electrically conductive (R_{sheet} ~11 Ω sq^{-1}) with a remarkably low surface roughness and are exceptionally robust towards ultra-sonic agitation in a variety of solvents and UV/O_3 surface treatment. By integrating microsphere lithography into the fabrication process the transparency is improved *via* the incorporation of a random array of circular apertures into the film. The application of these nano-structured Au electrodes has been demonstrated in efficient P3HT:PCBM OPVs where it offers a viable alternative to ITO coated glass. The relatively small difference between the performance of devices employing a plane Au electrode and ITO coated glass; η = 3.8 ± 0.2 % *vs.* 3.0 ± 0.2 % is attributed to the lower far field transparency of Au electrode. It has been shown that this efficiency gap can be reduced by introducing micron-sized apertures into the film which improve the far-field transparency of metal electrodes (η = 3.4 ± 0.2 %), although the increase in transparency is at the expense of sheet resistance and so a balance must be struck.

8.2 Thermal stability of ultra-thin metal film electrodes

In the second results chapter the protocol for fabricating thin Au films has been successfully adapted to another technologically important noble metal: namely, Ag. The coalescence thickness for Ag on a molecular nanolayer is shown to be between 5 and 7 nm, which is comparable to that of Au. Ag films have comparable sheet resistance to Au films of the same thickness, but lower transparency due to the high reflectivity of Ag for wavelengths above 400 nm.

It is also shown that moderate annealing improves the transparency and conductivity of Au film with thicknesses in the range: 3.7 nm to 8.4 nm. For example, the transparency of 8.4 nm Au films increases by ~ 5% after annealing to 300 °C and the sheet resistance decreases from 12 Ω sq^{-1} to 6 Ω sq^{-1}, which is only ~ 3 Ω sq^{-1} higher than that expected for bulk Au. Moderate heating induces growth of (111) crystallites of size increasing with temperature, which eventually leads to formation of apertures surrounded by Au crystallinites. The temperature at which the apertures start to form is thickness dependent and is manifested by a rapid increase in sheet resistance and change in the shape of the transparency spectrum, caused by scattering effects.

It has been shown that the robustness of thin Au films towards elevated temperature can be greatly improved by capping with a thin oxide overlayer. The properties of sub-10 nm Au films capped with a thin metal (Mo, Ti, W) oxide overlayer were investigated, proving them to be good protective layers up to 500 °C. Moreover, oxide overlayers improve the far-field transparency of these metal films due to their high refractive index.

Au and Ag electrodes have been incorporated into efficient PCDTBT:$PC_{70}BM$ solar cells with a TiO_x electron transporting layer requiring high temperature processing (500 ˚C). The power conversion efficiency of OPVs employing Au and ITO is comparable (4.4 ± 0.2% and 4.3 ± 0.1%), while the efficiency of OPVs employing Ag is fractionally lower (3.8 ± 0.2%) which opens the door to the widespread utilisation of these window electrodes in fundamental research and a broad range of applications including DSSC, inorganic PVs and infra-red reflective glass.

8.3 Metal window electrodes on flexible substrates

The third results chapter describes how 8 nm films of the coinage metals Cu, Ag and Au can be fabricated on the technologically important substrates PET and PEN, to realise highly electrically conductive, low R_{rms} and exceptionally robust window electrodes. The key to the realisation of these electrodes is the chemical derivatisation of the oxidised plastic surface with a mixed monolayer of thiol and amine methoxysilanes co-deposited from the vapour phase.

Owing to the low thickness of these metal films their melting point is suppressed so that brief annealing at only 200 °C can be used to reduce the sheet resistance to ≤ 9 Ω sq^{-1}. Annealing Au electrodes at 200 °C for only 10 minutes causes the surface to revert almost entirely to the (111) face rendering it ideal as a widely applicable electrode for fundamental science and practical application alike.

The performance of 1 cm^2 PCDTBT:$PC_{70}BM$ OPVs on Ag (3.70% ± 0.15) and Au (4.25% ± 0.20) electrodes is shown to be comparable to that on commercial ITO coated PET (4.10% ± 0.15). The disadvantage of the lower transparency of the metal electrodes, as compared to ITO, is off-set by the advantage of much lower sheet resistance. Importantly, 1 cm^2 OPVs fabricated on 8 nm metal window electrodes are robust towards repeated bending through a radius of curvature of 4 mm opening the door to the realisation of truly flexible OPVs. In contrast, ITO coated plastic substrates deteriorate rapidly upon repeated bending. As a result OPVs employing ITO electrodes undergo fast deterioration upon bending whilst devices with metal electrodes remain stable.

It is shown that Cu offers a path to low cost transparent electrodes and can be combined with Ag to tune the optical transparency. However, even when buried beneath a 6 nm Ag layer and a 10 nm MoO_x hole-extraction layer OPVs with Cu electrode does not perform as well as Ag or Au electrodes of the same thickness. On the basis of device studies and measurements of the energetics at the metal electrode / MoO_x interface this is attributed to diffusion of Cu into the MoO_x layer which undermines it functionality as a high work function interlayer.

8.4 Plasmon-active nano-aperture window electrodes

To further boost the device efficiency a lithography-free approach to fabricating optically thin plasmon-active noble metal electrodes with a dense array of nano-sized apertures has been developed. This method has three key advantages over lithographic methods: *(i)* It is inherently less complex since there is no requirement for the positioning or removal of a mask.; *(ii)* It is a non-contact method and so the risk of imparting debris to the surface is minimal.; *(iii)* The introduction of apertures does not incur a large increase in sheet resistance as compared to unpatterned films. These electrodes are shown to be remarkably robust towards aggressive ultra-sonic agitation in a variety of solvents and, when employed as the window electrode in bulk-heterojunction and bilayer OPVs, increase η by coupling strongly with the incident light and concentrating it in the photoactive layer near to the electrode surface. As a direct replacement for ITO electrode in flexible OPV PCTBTB:$PC_{70}BM$ device efficiency is improved from 4.6 ± 0.1 % (ITO on PET) to 5.1% ± 0.3 (plasmon-active Ag on PET) demonstrating that these electrodes have both a mechanical and efficiency advantage over conducting oxide window electrodes.

8.5 Transparent Au films as *'model'* electrodes

The Au electrode described in the first results chapter (Chapter 3) of this thesis is a '*model*' window electrode, with a homogeneous smooth surface and is chemically well-defined. It therefore offers an opportunity to study the phenomenon of improved efficiency in OPVs using sub-1 nm Au electrode overlayer, by removing the complexity associated with conducting oxide electrodes. A brief UV/O_3 treatment of Au results in the formation of an ultra-thin AuO_x layer mimicking the surface of conducting oxide electrodes after plasma or UV/O_3 treatment.

The BHJ devices with PCDTBT:$PC_{70}BM$ and P3HT:PCBM showed similar improvement in performance upon introducing sub-1nm Au overlayer on oxidised Au electrode as observed in literature for conducting oxide electrodes. To investigate this phenomenon the electric field strength in the device has been simulated using

COMSOL Multiphysics software. The preliminary results indicate that the improvement in device performance should be attributed to enhanced field region above the Au nanoparticles present on the electrode surface, facilitating the extraction of photo-generated charge carriers to the external circuit and is most efficient when the Au coverage is less than 30 %.

References

1. http://www.eia.gov/forecasts/ieo/ Accessed December, 2012.
2. G. Maggio; G. Cacciola, *Fuel* **2012,** 98, 111-123.
3. I. S. Nashawi; A. Malallah; M. Al-Bisharah, *Energy & Fuels* **2010,** 24, 1788-1800.
4. http://www.un-energy.org/sites/default/files/share/une/ren21_gsr2011.pdf Accessed December, 2012.
5. J. S. Kim; M. Granstrom; R. H. Friend; N. Johansson; W. R. Salaneck; R. Daik; W. J. Feast; F. Cacialli, *J. Appl. Phys.* **1998,** 84, (12), 6859-6870.
6. Q. Volker, *Renewable energy and climate change*, Wiley: Chichester, 2010.
7. http://www.map.ren21.net/GSR/GSR2012_low.pdf Accessed January, 2013.
8. http://unisolar.com.ua/wp-content/uploads/2012/02/EPIA-market-report-2011.pdf Accessed December, 2012.
9. K. Kawajiri; T. Oozeki; Y. Genchi, *Environ. Sci. Technol.* **2011,** 45, (20), 9030-9035.
10. http://www.renewableenergyworld.com/rea/news/article/2012/03/germanys-official-2011-solar-pv-stats-where-growth-is-happening Accessed November, 2012.
11. P. Peumans; S. Uchida; S. R. Forrest, *Nature* **2003,** 425, (6954), 158-162.
12. M. Riede; C. Uhrich; J. Widmer; R. Timmreck; D. Wynands; G. Schwartz; W. M. Gnehr; D. Hildebrandt; A. Weiss; J. Hwang; S. Sundarraj; P. Erk; M. Pfeiffer; K. Leo, *Adv. Funct. Mater.* **2011,** 21, (16), 3019-3028.
13. G. D. Sharma; J. A. Mikroyannidis; S. S. Sharma; M. S. Roy; K. R. J. Thomas, *Org. Electron.* **2012,** 13, (4), 652-666.
14. A. Tada; Y. Geng; Q. Wei; K. Hashimoto; K. Tajima, *Nat. Mater.* **2011,** 10, (6), 450-455.
15. D. H. Wang; K. H. Park; J. H. Seo; J. Seifter; J. H. Jeon; J. K. Kim; J. H. Park; O. O. Park; A. J. Heeger, *Adv. Energy Mater.* **2011,** 1, (5), 766-770.
16. Z. M. Beiley; E. T. Hoke; R. Noriega; J. Dacuna; G. F. Burkhard; J. A. Bartelt; A. Salleo; M. F. Toney; M. D. McGehee, *Adv. Energy Mater.* **2011,** 1, (5), 954-962.
17. Y. F. Lim; Y. Shu; S. R. Parkin; J. E. Anthony; G. G. Malliaras, *J. Mater. Chem.* **2009,** 19, (19), 3049-3056.
18. P. Sullivan; A. Duraud; I. Hancox; N. Beaumont; G. Mirri; J. H. R. Tucker; R. A. Hatton; M. Shipman; T. S. Jones, *Adv. Energy Mater.* **2011,** 1, (3), 352-355.
19. T. Ameri; G. Dennler; C. Lungenschmied; C. J. Brabec, *Energy Environ. Sci.* **2009,** 2, (4), 347-363.
20. S. R. Forrest, *Nature* **2004,** 428, (6986), 911-918.
21. N. Espinosa; M. Hosel; D. Angmo; F. C. Krebs, *Energy Environ. Sci.* **2012,** 5, (1), 5117-5132.
22. A. McEvoy;; T. Markvart;; L. Castaner, *Practical Hanbook of Photovoltaics Fundamentals and Applications*, Elsevier: Walham, USA, 2012.
23. C. Kittel, *Introduction to Solid state physics*, Wiley: Hoboken, USA, 2005.
24. J. R. Hook, H. E. Hall, *Solid State Physics*, John Wiley & Sons Ltd.: Chichester, 1997.
25. J. Nelson, *Physics of solar cells*, Imperial College Press: London, 2008.
26. B. P. Rand; J. Genoe; P. Heremans; J. Poortmans, *Prog. Photovoltaics* **2007,** 15, (8), 659-676.

27. H. X. Zhou; L. Q. Yang; W. You, *Macromolecules* **2012,** 45, (2), 607-632.

28. R. M. Silverstein, Bassler, G. Clayton, Morril, Terence C., *Spectrometric Identification of organic compounds*, John Wiley & Sons: Chichester, 1981.

29. J. Mei; K. Ogawa; Y.-G. Kim; N. C. Heston; D. J. Arenas; Z. Nasrollahi; T. D. McCarley; D. B. Tanner; J. R. Reynolds; K. S. Schanze, *ACS Appl. Mater. Interface* **2009,** 1, (1), 150-161.

30. J. Ku; Y. Lansac; Y. H. Jang, *J. Phys. Chem. C* **2011,** 115, (43), 21508-21516.

31. H. Ishii; K. Sugiyama; E. Ito; K. Seki, *Adv. Mater.* **1999,** 11, (8), 605-625.

32. L. L. E. Gutmann Felix, *Organic Semiconductors*, John Wiley & Sons, Inc.: Berkeley, USA, 1967.

33. D. Nabok; P. Puschnig; C. Ambrosch-Draxl; O. Werzer; R. Resel; D.-M. Smilgies, *Phys. Rev. B* **2007,** 76, (23).

34. R. Matsubara; M. Sakai; K. Kudo; N. Yoshimoto; I. Hirosawa; M. Nakamura, *Org. Electron.* **2011,** 12, (1), 195-201.

35. S. Braun; W. R. Salaneck; M. Fahlman, *Adv. Mater.* **2009,** 21, (14-15), 1450-1472.

36. Y. Tanaka; K. Kanai; Y. Ouchi; K. Seki, *Org. Electron.* **2009,** 10, (5), 990-993.

37. F. Amy; C. Chan; A. Kahn, *Org. Electron.* **2005,** 6, (2), 85-91.

38. S.-S. Sun; L. R. Dalton, *Introduction to Organic Electronics and Optoelectronic Materials and Devices*, CRC Press: New York, USA, 2008.

39. B. A. Gregg; M. C. Hanna, *J. Appl. Phys.* **2003,** 93, (6), 3605-3614.

40. X. Y. Zhu; Q. Yang; M. Muntwiler, *Accounts Chem. Res.* **2009,** 42, (11), 1779-1787.

41. L. W. Tu; W. C. Kuo; K. H. Lee; P. H. Tsao; C. M. Lai; A. K. Chu; J. K. Sheu, *Appl. Phys. Lett.* **2000,** 77, (23), 3788-3790.

42. M. Burgelman; B. Minnaert, *Thin Solid Films* **2006,** 511, 214-218.

43. B. Gil; D. Felbacq; S. F. Chichibu, *Phys. Rev. B* **2012,** 85, (7), 075205.

44. E. I. Haskal; Z. Shen; P. E. Burrows; S. R. Forrest, *Phys. Rev. B* **1995,** 51, (7), 4449-4462.

45. I. H. Campbell; T. W. Hagler; D. L. Smith; J. P. Ferraris, *Phys. Rev. Lett.* **1996,** 76, (11), 1900-1903.

46. M. Knupfer, *Appl. Phys. A-Mater. Sci. Process.* **2003,** 77, (5), 623-626.

47. E. M. Conwell; H. A. Mizes, *Phys. Rev. B* **1995,** 51, (11), 6953-6958.

48. O. Mikhnenko, *Singlet and Triplet Excitons in Organic Semiconductors*, PhD thesis, University of Groningen, Polymer Insitute, 2011.

49. B. Marc, *The Electronic and Optical Properties of Amorphous Organic Semiconductors*, PhD thesis, Princeton, 2001.

50. G. R. Hutchison; M. A. Ratner; T. J. Marks, *J. Am. Chem. Soc.* **2005,** 127, (48), 16866-16881.

51. D. H. Dunlap; P. E. Parris; V. M. Kenkre, *Phys. Rev. Lett.* **1996,** 77, (3), 542-545.

52. L. Bozano; S. A. Carter; J. C. Scott; G. G. Malliaras; P. J. Brock, *Appl. Phys. Lett.* **1999,** 74, (8), 1132-1134.

53. L. Kronik; Y. Shapira, *Surf. Sci. Rep.* **1999,** 37, (1-5), 1-206.

54. C. J. Fall; N. Binggeli; A. Baldereschi, *Phys. Rev. B* **2000,** 61, (12), 8489-8495.

55. N. E. Singh-Miller; N. Marzari, *Phys. Rev. B* **2009,** 80, (23), 235407.

56. J. Hwang; A. Wan; A. Kahn, *Mater. Sci. Eng. R.* **2009,** 64, (1-2), 1-31.

57. C. D. Wang; W. C. H. Choy, *Sol. Energy Mater. Sol. Cells* **2011,** 95, (3), 904-908.

58. W. J. Potscavage; A. Sharma; B. Kippelen, *Accounts Chem. Res.* **2009,** 42, (11), 1758-1767.

59. K. Sugiyama; H. Ishii; Y. Ouchi; K. Seki, *J. Appl. Phys.* **2000,** 87, (1), 295-298.

60. S. R. Day; R. A. Hatton; M. A. Chesters; M. R. Willis, *Thin Solid Films* **2002,** 410, (1-2), 159-166.

61. R. J. Davis; M. T. Lloyd; S. R. Ferreira; M. J. Bruzek; S. E. Watkins; L. Lindell; P. Sehati; M. Fahlman; J. E. Anthony; J. W. P. Hsu, *J. Mater. Chem.* **2011,** 21, (6), 1721-1729.

62. R. Pandey; R. J. Holmes, *Appl. Phys. Lett.* **2012,** 100, (8).

63. P. Schilinsky; C. Waldauf; C. J. Brabec, *Appl. Phys. Lett.* **2002,** 81, (20), 3885-3887.

64. H. A. Atwater; A. Polman, *Nat. Mater.* **2010,** 9, (3), 205-213.

65. N. P. Sergeant; A. Hadipour; B. Niesen; D. Cheyns; P. Heremans; P. Peumans; B. P. Rand, *Adv. Mater.* **2012,** 24, (6), 728-732.

66. A. Roy; S. H. Park; S. Cowan; M. H. Tong; S. Cho; K. Lee; A. J. Heeger, *Appl. Phys. Lett.* **2009,** 95, (1).

67. H. Hoppe; N. S. Sariciftci, *J. Mater. Res.* **2004,** 19, (7), 1924-1945.

68. P. M. Beaujuge; C. M. Amb; J. R. Reynolds, *Accounts Chem. Res.* **2010,** 43, (11), 1396-1407.

69. S. R. Scully; M. D. McGehee, *J. Appl. Phys.* **2006,** 100, (3), 034907.

70. O. V. Mikhnenko; H. Azimi; M. Scharber; M. Morana; P. W. M. Blom; M. A. Loi, *Energy Environ. Sci.* **2012,** 5, (5), 6960-6965.

71. S. Athanasopoulos; E. Hennebicq; D. Beljonne; A. B. Walker, *J. Phys. Chem. C* **2008,** 112, (30), 11532-11538.

72. Y. Terao; H. Sasabe; C. Adachi, *Appl. Phys. Lett.* **2007,** 90, (10), 103515.

73. S. Yoo; B. Domercq; B. Kippelen, *Appl. Phys. Lett.* **2004,** 85, (22), 5427-5429.

74. H. Najafov; B. Lee; Q. Zhou; L. C. Feldman; V. Podzorov, *Nat. Mater.* **2010,** 9, (11), 938-943.

75. P. W. M. Blom; V. D. Mihailetchi; L. J. A. Koster; D. E. Markov, *Adv. Mater.* **2007,** 19, (12), 1551-1566.

76. H. van Eersel; R. A. J. Janssen; M. Kemerink, *Adv. Funct. Mater.* **2012,** 22, (13), 2700-2708.

77. P. Heremans; D. Cheyns; B. P. Rand, *Accounts Chem. Res.* **2009,** 42, (11), 1740-1747.

78. V. D. Mihailetchi; L. J. A. Koster; J. C. Hummelen; P. W. M. Blom, *Phys. Rev. Lett.* **2004,** 93, (21), 216601.

79. P. Peumans; A. Yakimov; S. R. Forrest, *J. Appl. Phys.* **2003,** 93, (7), 3693-3723.

80. W. Tress; A. Petrich; M. Hummert; M. Hein; K. Leo; M. Riede, *Appl. Phys. Lett.* **2011,** 98, (6), 063301.

81. J. L. Bredas; J. E. Norton; J. Cornil; V. Coropceanu, *Accounts Chem. Res.* **2009,** 42, (11), 1691-1699.

82. R. Steim; F. R. Kogler; C. J. Brabec, *J. Mater. Chem.* **2010,** 20, (13), 2499-2512.

83. L.-J. Pegg; S. Schumann; R. A. Hatton, *ACS Nano* **2010,** 4, (10), 5671-5678.

84. C. F. Lin; B. H. Lin; S. W. Liu; W. F. Hsu; M. Zhang; T. L. Chiu; M. K. Wei; J. H. Lee, *Phys. Chem. Chem. Phys.* **2012,** 14, (11), 3837-3842.
85. A. Maurano; R. Hamilton; C. G. Shuttle; A. M. Ballantyne; J. Nelson; B. O'Regan; W. M. Zhang; I. McCulloch; H. Azimi; M. Morana; C. J. Brabec; J. R. Durrant, *Adv. Mater.* **2010,** 22, (44), 4987-4992.
86. D. Cheyns; J. Poortmans; P. Heremans; C. Deibel; S. Verlaak; B. P. Rand; J. Genoe, *Phys. Rev. B* **2008,** 77, (16), 165332.
87. N. C. Giebink; G. P. Wiederrecht; M. R. Wasielewski; S. R. Forrest, *Phys. Rev. B* **2010,** 82, (15), 155305.
88. C. Zhang; S.-W. Tong; C.-Y. Jiang; E.-T. Kang; D. S. H. Chan; C. Zhu, *IEEE T. Electron Dev.* **2010,** 57, (2), 397-405.
89. R. M. Cook; L.-J. Pegg; S. L. Kinnear; O. S. Hutter; R. J. H. Morris; R. A. Hatton, *Adv. Energy Mater.* **2011,** 1, (3), 440-447.
90. B. P. Rand; D. P. Burk; S. R. Forrest, *Phys. Rev. B* **2007,** 75, (11), 115327.
91. D. S. Hecht; L. B. Hu; G. Irvin, *Adv. Mater.* **2011,** 23, (13), 1482-1513.
92. J. S. Kim, M. Granstrom, R. H. Friend, N. Johansson, W. R. Salaneck, R. Daik, W. J. Feast, F. Cacialli, *J. Appl. Phys.* **1998,** 84, 6859-6870.
93. P. K. Manoj; B. Joseph; V. K. Vaidyan; D. S. D. Amma, *Ceram. Int.* **2007,** 33, (2), 273-278.
94. A. M. Gheidari; F. Behafarid; G. Kavei; M. Kazemad, *Mat. Sci. Eng. B-Solid* **2007,** 136, (1), 37-40.
95. L. J. Meng; J. Gao; M. P. Dos Santos; X. Wang; T. Wang, *Thin Solid Films* **2008,** 516, (7), 1365-1369.
96. N. R. Armstrong; P. A. Veneman; E. Ratcliff; D. Placencia; M. Brumbach, *Accounts Chem. Res.* **2009,** 42, (11), 1748-1757.
97. S. D. Yambem; K. S. Liao; N. J. Alley; S. A. Curran, *J. Mater. Chem.* **2012,** 22, (14), 6894-6898.
98. E. Fortunato; D. Ginley; H. Hosono; D. C. Paine, *MRS Bull.* **2007,** 32, (3), 242-247.
99. D. H. Kim; M. R. Park; H. J. Lee; G. H. Lee, *Appl. Surf. Sci.* **2006,** 253, (2), 409-411.
100. R. Paetzold; K. Heuser; D. Henseler; S. Roeger; G. Wittmann; A. Winnacker, *Appl. Phys. Lett.* **2003,** 82, (19), 3342-3344.
101. K. Chiba; A. Futagami, *Appl. Phys. Lett.* **2008,** 93, (1), 013114.
102. J. Kalowekamo; E. Baker, *Sol. Energy* **2009,** 83, (8), 1224-1231.
103. T. Minami; T. Miyata, *Thin Solid Films* **2008,** 517, (4), 1474-1477.
104. T. M. Brown; J. S. Kim; R. H. Friend; F. Cacialli; R. Daik; W. J. Feast, *Appl. Phys. Lett.* **1999,** 75, (12), 1679-1681.
105. C. J. M. Emmott; A. Urbina; J. Nelson, *Sol. Energy Mater. Sol. Cells* **2012,** 97, 14-21.
106. J. Weickert; H. Y. Sun; C. Palumbiny; H. C. Hesse; L. Schmidt-Mende, *Sol. Energy Mater. Sol. Cells* **2010,** 94, (12), 2371-2374.
107. Z. Xiong; C. Liu, *Org. Electron.* **2012,** 13, (9), 1532-1540.
108. K. Kawano; R. Pacios; D. Poplavskyy; J. Nelson; D. D. C. Bradley; J. R. Durrant, *Sol. Energy Mater. Sol. Cells* **2006,** 90, (20), 3520-3530.
109. E. Vitoratos; S. Sakkopoulos; E. Dalas; N. Paliatsas; D. Karageorgopoulos; F. Petraki; S. Kennou; S. A. Choulis, *Org. Electron.* **2009,** 10, (1), 61-66.
110. G. Latini; L. W. Tan; F. Cacialli; S. R. P. Silva, *Org. Electron.* **2012,** 13, (6), 992-998.

111. Y. H. Kim; C. Sachse; M. L. Machala; C. May; L. Muller-Meskamp; K. Leo, *Adv. Funct. Mater.* **2011,** 21, (6), 1076-1081.
112. J. S. Yeo; J. M. Yun; S. S. Kim; D. Y. Kim; J. Kim; S. I. Na, *Semicond. Sci. Technol.* **2011,** 26, (3), 034010.
113. M. W. Rowell; M. A. Topinka; M. D. McGehee; H. J. Prall; G. Dennler; N. S. Sariciftci; L. B. Hu; G. Gruner, *Appl. Phys. Lett.* **2006,** 88, (23), 233506.
114. H. X. Chang; G. F. Wang; A. Yang; X. M. Tao; X. Q. Liu; Y. D. Shen; Z. J. Zheng, *Adv. Funct. Mater.* **2010,** 20, (17), 2893-2902.
115. C. Feng; K. Liu; J. S. Wu; L. Liu; J. S. Cheng; Y. Y. Zhang; Y. H. Sun; Q. Q. Li; S. S. Fan; K. L. Jiang, *Adv. Funct. Mater.* **2010,** 20, (6), 885-891.
116. L. B. Hu; H. S. Kim; J. Y. Lee; P. Peumans; Y. Cui, *ACS Nano* **2010,** 4, (5), 2955-2963.
117. J. L. Elechiguerra; L. Larios-Lopez; C. Liu; D. Garcia-Gutierrez; A. Camacho-Bragado; M. J. Yacaman, *Chem. Mater.* **2005,** 17, (24), 6042-6052.
118. B. Stahlmecke; F. J. M. zu Heringdorf; L. I. Chelaru; M. Horn-von Hoegen; G. Dumpich; K. R. Roos, *Appl. Phys. Lett.* **2006,** 88, (5), 053122.
119. H. Wu; L. B. Hu; M. W. Rowell; D. S. Kong; J. J. Cha; J. R. McDonough; J. Zhu; Y. A. Yang; M. D. McGehee; Y. Cui, *Nano Lett.* **2010,** 10, (10), 4242-4248.
120. Y. Galagan; J. Rubingh; R. Andriessen; C. C. Fan; P. W. M. Blom; S. C. Veenstra; J. M. Kroon, *Sol. Energy Mater. Sol. Cells* **2011,** 95, (5), 1339-1343.
121. M. G. Kang; L. J. Guo, *Adv. Mater.* **2007,** 19, (10), 1391-1396.
122. S. K. Hau; H. L. Yip; J. Y. Zou; A. K. Y. Jen, *Org. Electron.* **2009,** 10, (7), 1401-1407.
123. S. D. Yambem; K. S. Liao; S. A. Curran, *Sol. Energy Mater. Sol. Cells* **2011,** 95, (11), 3060-3064.
124. A. Kumar; Z. Hong; S. Sista; Y. Yang, *Adv. Energy Mater.* **2011,** 1, (1), 124-131.
125. C. J. Brabec; S. Gowrisanker; J. J. M. Halls; D. Laird; S. Jia; S. P. Williams, *Adv. Mater.* **2010,** 22, (34), 3839-3856.
126. H. Klauk, *Organic Electronics*. Viley-VCH: Stuttgart, Germany, 2008.
127. J. Lange; Y. Wyser, *Packag. Technol. Sci.* **2003,** 16, (4), 149-158.
128. B. O'Connor; C. Haughn; K. H. An; K. P. Pipe; M. Shtein, *Appl. Phys. Lett.* **2008,** 93, (22), 223304.
129. D. S. Lin, *J. Phys. D Appl. Phys.* **1971,** 4, (12), 1977-1992.
130. L. Vj; N. P. Kobayashi; M. S. Islam; W. Wu; P. Chaturvedi; N. X. Fang; S. Y. Wang; R. S. Williams, *Nano Lett.* **2009,** 9, (1), 178-182.
131. J. C. Hoogvliet; W. P. van Bennekom, *Electrochim. Acta* **2001,** 47, (4), 599-611.
132. D. L. Allara; A. F. Hebard; F. J. Padden; R. G. Nuzzo; D. R. Falcone, *J. Vac. Sci. Technol. A.* **1983,** 1, (2), 376-382.
133. R. A. Hatton; M. R. Willis; M. A. Chesters; D. Briggs, *J. Mater. Chem.* **2003,** 13, (4), 722-726.
134. T. J. Horr; P. S. Arora, *Colloid Surface A* **1997,** 126, (2-3), 113-121.
135. E. T. Vandenberg; L. Bertilsson; B. Liedberg; K. Uvdal; R. Erlandsson; H. Elwing; I. Lundstrom, *J. Colloid Int. Sci.* **1991,** 147, (1), 103-118.
136. M. Hu; S. Noda; Y. Tsuji; T. Okubo; Y. Yamaguchi; H. Komiyama, *J. Vac. Sci. Technol. A.* **2002,** 20, (3), 589-596.
137. D. J. Dunaway; R. L. McCarley, *Langmuir* **1994,** 10, (10), 3598-3606.
138. P. Moberg; R. L. McCarley, *J. Electrochem. Soc.* **1997,** 144, (6), L151-L153.
139. S. L. Caston; R. L. McCarley, *J. Electroanal. Chem.* **2002,** 529, (2), 124-134.

140. J. B. Kim; P. Kim; N. C. Pegard; S. J. Oh; C. R. Kagan; J. W. Fleischer; H. A. Stone; Y.-L. Loo, *Nat. Photonics* **2012,** 6, (5), 327-332.

141. I. Perez-Lopez; L. Cattin; D. T. Nguyen; M. Morsli; J. C. Bernede, *Thin Solid Films* **2012,** 520, (20), 6419-6423.

142. K. M. Coakley; M. D. McGehee, *Chem. Mater.* **2004,** 16, (23), 4533-4542.

143. H. K. Yu; W. J. Dong; G. H. Jung; J. L. Lee, *ACS Nano* **2011,** 5, (10), 8026-8032.

144. J. Lee; S. Y. Kim; C. Kim; J. J. Kim, *Appl. Phys. Lett.* **2010,** 97, (8), 083306.

145. K. Hong; K. Kim; S. Kim; I. Lee; H. Cho; S. Yoo; H. W. Choi; N. Y. Lee; Y. H. Tak; J. L. Lee, *J. Phys. Chem. C* **2011,** 115, (8), 3453-3459.

146. D. M. Schaadt; B. Feng; E. T. Yu, *Appl. Phys. Lett.* **2005,** 86, (6), 063106.

147. M. G. Kang; T. Xu; H. J. Park; X. G. Luo; L. J. Guo, *Adv. Mater.* **2010,** 22, (39), 4378-4383.

148. J.-L. Wu; F.-C. Chen; Y.-S. Hsiao; F.-C. Chien; P. Chen; C.-H. Kuo; M. H. Huang; C.-S. Hsu, *ACS Nano* **2011,** 5, (2), 959-967.

149. D. H. Wang; D. Y. Kim; K. W. Choi; J. H. Seo; S. H. Im; J. H. Park; O. O. Park; A. J. Heeger, *Angew. Chem. Int. Edit.* **2011,** 50, (24), 5519-5523.

150. T. H. Reilly; J. van de Lagemaat; R. C. Tenent; A. J. Morfa; K. L. Rowlen, *Appl. Phys. Lett.* **2008,** 92, (24), 243304.

151. W. A. Luhman; S. H. Lee; T. W. Johnson; R. J. Holmes; S. H. Oh, *Appl. Phys. Lett.* **2011,** 99, (10), 103306.

152. M. A. Sefunc; A. K. Okyay; H. V. Demir, *Opt. Express* **2011,** 19, (15), 14200-14209.

153. L. Hu; H. Wu; Y. Cui, *MRS Bull.* **2011,** 36, (10), 760-765.

154. N. C. Lindquist; W. A. Luhman; S. H. Oh; R. J. Holmes, *Appl. Phys. Lett.* **2008,** 93, (12), 123308.

155. J. W. Menezes; J. Ferreira; M. J. L. Santos; L. Cescato; A. G. Brolo, *Adv. Funct. Mater.* **2010,** 20, (22), 3918-3924.

156. L. Martin-Moreno; F. J. Garcia-Vidal; H. J. Lezec; K. M. Pellerin; T. Thio; J. B. Pendry; T. W. Ebbesen, *Phys. Rev. Lett.* **2001,** 86, (6), 1114-1117.

157. A. E. Ostfeld; D. Pacifici, *Appl. Phys. Lett.* **2011,** 98, (11), 113112.

158. T. Rindzevicius; Y. Alaverdyan; B. Sepulveda; T. Pakizeh; M. Kall; R. Hillenbrand; J. Aizpurua; F. J. G. de Abajo, *J. Phys. Chem. C* **2007,** 111, (3), 1207-1212.

159. T. H. Reilly; R. C. Tenent; T. M. Barnes; K. L. Rowlen; J. van de Lagemaat, *ACS Nano* **2010,** 4, (2), 615-624.

160. W. I. Jeong; J. Lee; S. Y. Park; J. W. Kang; J. J. Kim, *Adv. Funct. Mater.* **2011,** 21, (2), 343-347.

161. Y. Golan; L. Margulis; I. Rubinstein, *Surf. Sci.* **1992,** 264, (3), 312-326.

162. M. Bar; S. Nishiwaki; L. Weinhardt; S. Pookpanratana; O. Fuchs; M. Blum; W. Yang; J. D. Denlinger; W. N. Shafarman; C. Heske, *Appl. Phys. Lett.* **2008,** 93, (24), 244103.

163. X. Feng; K. Shankar; O. K. Varghese; M. Paulose; T. J. Latempa; C. A. Grimes, *Nano Lett.* **2008,** 8, (11), 3781-3786.

164. J. J. Senkevich; G. R. Yang; T. M. Lu, *Colloid Surface A* **2002,** 207, (1-3), 139-145.

165. A. M. Caro; S. Armini; O. Richard; G. Maes; G. Borghs; C. M. Whelan; Y. Travaly, *Adv. Funct. Mater.* **2010,** 20, (7), 1125-1131.

166. M. Wanunu; A. Vaskevich; I. Rubinstein, *J. Am. Chem. Soc.* **2004,** 126, (17), 5569-5576.

167. D. D. Gandhi; M. Lane; Y. Zhou; A. P. Singh; S. Nayak; U. Tisch; M. Eizenberg; G. Ramanath, *Nature* **2007,** 447, (7142), 299-U2.

168. S. Schumann; S. A. F. Bon; R. A. Hatton; T. S. Jones, *Chem. Commun.* **2009**, (42), 6478-6480.

169. A. M. Peiro; P. Ravirajan; K. Govender; D. S. Boyle; P. O'Brien; D. D. C. Bradley; J. Nelson; J. R. Durrant, *J. Mater. Chem.* **2006,** 16, (21), 2088-2096.

170. I. Gur; N. A. Fromer; M. L. Geier; A. P. Alivisatos, *Science* **2005,** 310, (5747), 462-465.

171. R. R. Lunt; N. C. Giebink; A. A. Belak; J. B. Benziger; S. R. Forrest, *J. Appl. Phys.* **2009,** 105, (5), 053711.

172. K. J. Bergemann; S. R. Forrest, *Appl. Phys. Lett.* **2011,** 99, (24), 243303.

173. K. L. Mutolo; E. I. Mayo; B. P. Rand; S. R. Forrest; M. E. Thompson, *J. Am. Chem. Soc.* **2006,** 128, (25), 8108-8109.

174. M. W. B. Wilson; A. Rao; J. Clark; R. S. S. Kumar; D. Brida; G. Cerullo; R. H. Friend, *J. Am. Chem. Soc.* **2011,** 133, (31), 11830-11833.

175. P. Sullivan; T. S. Jones, *Org. Electron.* **2008,** 9, (5), 656-660.

176. C. Goh; R. J. Kline; M. D. McGehee; E. N. Kadnikova; J. M. J. Frechet, *Appl. Phys. Lett.* **2005,** 86, (12), 122110.

177. P. Kohn; S. Huettner; U. Steiner; M. Sommer, *ACS Macro Letters* **2012,** 1, (10), 1170-1175.

178. C. H. Woo; B. C. Thompson; B. J. Kim; M. F. Toney; J. M. J. Frechet, *J. Am. Chem. Soc.* **2008,** 130, (48), 16324-16329.

179. K. M. Coakley; B. S. Srinivasan; J. M. Ziebarth; C. Goh; Y. X. Liu; M. D. McGehee, *Adv. Funct. Mater.* **2005,** 15, (12), 1927-1932.

180. Y. Kim; S. Cook; S. M. Tuladhar; S. A. Choulis; J. Nelson; J. R. Durrant; D. D. C. Bradley; M. Giles; I. McCulloch; C. S. Ha; M. Ree, *Nat. Mater.* **2006,** 5, (3), 197-203.

181. T. Erb; U. Zhokhavets; G. Gobsch; S. Raleva; B. Stuhn; P. Schilinsky; C. Waldauf; C. J. Brabec, *Adv. Funct. Mater.* **2005,** 15, (7), 1193-1196.

182. C. R. McNeill; J. J. M. Halls; R. Wilson; G. L. Whiting; S. Berkebile; M. G. Ramsey; R. H. Friend; N. C. Greenham, *Adv. Funct. Mater.* **2008,** 18, (16), 2309-2321.

183. J. Jo; S. I. Na; S. S. Kim; T. W. Lee; Y. Chung; S. J. Kang; D. Vak; D. Y. Kim, *Adv. Funct. Mater.* **2009,** 19, (15), 2398-2406.

184. A. M. Ballantyne; T. A. M. Ferenczi; M. Campoy-Quiles; T. M. Clarke; A. Maurano; K. H. Wong; W. M. Zhang; N. Stingelin-Stutzmann; J. S. Kim; D. D. C. Bradley; J. R. Durrant; I. McCulloch; M. Heeney; J. Nelson; S. Tierney; W. Duffy; C. Mueller; P. Smith, *Macromolecules* **2010,** 43, (3), 1169-1174.

185. M. Reyes-Reyes; K. Kim; D. L. Carroll, *Appl. Phys. Lett.* **2005,** 87, (8), 083506.

186. S. Alem; T.-Y. Chu; S. C. Tse; S. Wakim; J. Lu; R. Movileanu; Y. Tao; F. Belanger; D. Desilets; S. Beaupre; M. Leclerc; S. Rodman; D. Waller; R. Gaudiana, *Org. Electron.* **2011,** 12, (11), 1788-1793.

187. C. H. Peters; I. T. Sachs-Quintana; J. P. Kastrop; S. Beaupre; M. Leclerc; M. D. McGehee, *Adv. Energy Mater.* **2011,** 1, (4), 491-494.

188. K. K. H. Chan; S. W. Tsang; H. K. H. Lee; F. So; S. K. So, *Org. Electron.* **2012,** 13, (5), 850-855.

189. S. Wakim; S. Beaupre; N. Blouin; B. R. Aich; S. Rodman; R. Gaudiana; Y. Tao; M. Leclerc, *J. Mater. Chem.* **2009,** 19, (30), 5351-5358.

190. A. Haugeneder; M. Neges; C. Kallinger; W. Spirkl; U. Lemmer; J. Feldmann; U. Scherf; E. Harth; A. Gugel; K. Müllen, *Phys. Rev. B* **1999,** 59, (23), 15346-15351.

191. E. Martin, *Zn-Phthalocyanine / C60 Solar Cells*, Master Thesis, Johannes Kepler Universität Linz, Linz, 2005.

192. D. S. Qin; P. Gu; R. S. Dhar; S. G. Razavipour; D. Y. Ban, *Phys. Status Solidi A-Appl. Mat.* **2011,** 208, (8), 1967-1971.

193. C. W. Chu; V. Shrotriya; G. Li; Y. Yang, *Appl. Phys. Lett.* **2006,** 88, (15), 153504.

194. S. M. Tuladhar; D. Poplavskyy; S. A. Choulis; J. R. Durrant; D. D. C. Bradley; J. Nelson, *Adv. Funct. Mater.* **2005,** 15, (7), 1171-1182.

195. G. Li; V. Shrotriya; J. S. Huang; Y. Yao; T. Moriarty; K. Emery; Y. Yang, *Nat. Mater.* **2005,** 4, (11), 864-868.

196. F. J. Zhang; Z. L. Zhuo; J. Zhang; X. Wang; X. W. Xu; Z. X. Wang; Y. S. Xin; J. Wang; W. H. Tang; Z. Xu; Y. S. Wang, *Sol. Energy Mater. Sol. Cells* **2012,** 97, 71-77.

197. Y. Sun; G. C. Welch; W. L. Leong; C. J. Takacs; G. C. Bazan; A. J. Heeger, *Nat. Mater.* **2012,** 11, (1), 44-48.

198. M. Kroeger; S. Hamwi; J. Meyer; T. Riedl; W. Kowalsky; A. Kahn, *Appl. Phys. Lett.* **2009,** 95, (12), 123301.

199. H. Peisert; A. Petr; L. Dunsch; T. Chasse; M. Knupfer, *ChemPhysChem* **2007,** 8, (3), 386-390.

200. C. Girotto; E. Voroshazi; D. Cheyns; P. Heremans; B. P. Rand, *ACS Appl. Mater. Interface* **2011,** 3, (9), 3244-3247.

201. W. T. Wu; W. P. Liao; J. S. Chen; J. J. Wu, *ChemPhysChem* **2010,** 11, (15), 3306-3312.

202. T. Kuwabara; T. Nakayama; K. Uozumi; T. Yamaguchi; K. Takahashi, *Sol. Energy Mater. Sol. Cells* **2008,** 92, (11), 1476-1482.

203. C. Tao; S. P. Ruan; G. H. Xie; X. Z. Kong; L. Shen; F. X. Meng; C. X. Liu; X. D. Zhang; W. Dong; W. Y. Chen, *Appl. Phys. Lett.* **2009,** 94, (4), 043311.

204. S. Han; W. S. Shin; M. Seo; D. Gupta; S. J. Moon; S. Yoo, *Org. Electron.* **2009,** 10, (5), 791-797.

205. M. G. Varnamkhasti; H. R. Fallah; M. Mostajaboddavati; R. Ghasemi; A. Hassanzadeh, *Sol. Energy Mater. Sol. Cells* **2012,** 98, 379-384.

206. A. K. K. Kyaw; X. W. Sun; C. Y. Jiang; G. Q. Lo; D. W. Zhao; D. L. Kwong, *Appl. Phys. Lett.* **2008,** 93, (22), 221107.

207. C. Tao; S. P. Ruan; X. D. Zhang; G. H. Xie; L. Shen; X. Z. Kong; W. Dong; C. X. Liu; W. Y. Chen, *Appl. Phys. Lett.* **2008,** 93, (19), 193307.

208. S. H. Mohamed; A. Anders, *Surf. Coat. Tech.* **2006,** 201, (6), 2977-2983.

209. A. Georg; W. Graf; V. Wittwer, *Sol. Energy Mater. Sol. Cells* **1998,** 51, (3-4), 353-370.

210. K. Kanai; K. Koizumi; S. Ouchi; Y. Tsukamoto; K. Sakanoue; Y. Ouchi; K. Seki, *Org. Electron.* **2010,** 11, (2), 188-194.

211. J. Huang; J. S. Yu; H. Lin; Y. D. Jiang, *J. Appl. Phys.* **2009,** 105, (7), 073105.

212. B. P. Rand; J. Li; J. G. Xue; R. J. Holmes; M. E. Thompson; S. R. Forrest, *Adv. Mater.* **2005,** 17, (22), 2714-2718.

213. H. Gommans; B. Verreet; B. P. Rand; R. Muller; J. Poortmans; P. Heremans; J. Genoe, *Adv. Funct. Mater.* **2008,** 18, (22), 3686-3691.

214. J. P. Hong; A. Y. Park; S. Lee; J. Kang; N. Shin; D. Y. Yoon, *Appl. Phys. Lett.* **2008,** 92, (14), 143311.

215. P. E. C. Franken; V. Ponec, *Surf. Sci.* **1975,** 53, (DEC), 341-350.

216. D. W. Zhao; P. Liu; X. W. Sun; S. T. Tan; L. Ke; A. K. K. Kyaw. *Appl. Phys. Lett.* **2009,** 95, (15), 153304.

217. D. M. F. Chapin, C. S., Pearson, G. L, *J. Appl. Phys.* **1954,** 25, 676-677.

218. M. A. Green; K. Emery; Y. Hishikawa; W. Warta; E. D. Dunlop, *Prog. Photovoltaics* **2012,** 20, (1), 12-20.

219. B. Sopori, *Handbook of Photovoltaic Science and Engineering*. John Wiley & Sons Ltd.: Chichester, 2003.

220. F. Dimroth, *Phys. Status Solidi C* **2006**, 3, 373-379.

221. B. Oregan; M. Gratzel. *Nature* **1991,** 353, (6346), 737-740.

222. M. M. Noor; M. H. Buraidah; S. N. F. Yusuf; M. A. Careem; S. R. Majid; A. K. Arof, *Int. J. Photoenergy* **2011**, 960487.

223. H. N. Tian; X. C. Yang; R. K. Chen; A. Hagfeldt; L. C. Sun, *Energy Environ. Sci.* **2009,** 2, (6), 674-677.

224. L. Y. Han; A. Islam; H. Chen; C. Malapaka; B. Chiranjeevi; S. F. Zhang; X. D. Yang; M. Yanagida, *Energy Environ. Sci.* **2012,** 5, (3), 6057-6060.

225. P.-L. Ong; I. A. Levitsky, *Energies* **2010,** 3, (3), 313-334.

226. G. A. Chamberlain; P. J. Cooney, *Chem. Phys. Lett.* **1979,** 66, (1), 88-94.

227. A. K. Ghosh; T. Feng, *J. Appl. Phys.* **1973,** 44, (6), 2781-2788.

228. A. K. Ghosh; D. L. Morel; T. Feng; R. F. Shaw; C. A. Rowe, *J. Appl. Phys.* **1974,** 45, (1), 230-236.

229. D. L. Morel; A. K. Ghosh; T. Feng; E. L. Stogryn; P. E. Purwin; R. F. Shaw; C. Fishman, *Appl. Phys. Lett.* **1978,** 32, (8), 495-497.

230. G. A. Chamberlain, *Sol. Cells* **1983,** 8, (1), 47-83.

231. C. W. Tang, *Appl. Phys. Lett.* **1986,** 48, (2), 183-185.

232. H. W. Kroto; J. R. Heath; S. C. Obrien; R. F. Curl; R. E. Smalley, *Nature* **1985,** 318, (6042), 162-163.

233. N. S. Sariciftci; L. Smilowitz; A. J. Heeger; F. Wudl, *Science* **1992,** 258, (5087), 1474-1476.

234. M. Hiramoto; H. Fujiwara; M. Yokoyama, *Appl. Phys. Lett.* **1991,** 58, (10), 1062-1064.

235. G. Yu; J. Gao; J. C. Hummelen; F. Wudl; A. J. Heeger, *Science* **1995,** 270, (5243), 1789-1791.

236. M. Helgesen; R. Sondergaard; F. C. Krebs, *J. Mater. Chem.* **2010,** 20, (1), 36-60.

237. H. Kobayashi; T. Ishida; Y. Nakato; H. Tsubomura, *J. Appl. Phys.* **1991,** 69, (3), 1736-1743.

238. M. S. Ryu; H. J. Cha; J. Jang, *Sol. Energy Mater. Sol. Cells* **2010,** 94, (2), 152-156.

239. J. R. Vig, *J. Vac. Sci. Technol. A.* **1985,** 3, (3), 1027-1034.

240. S. K. So; W. K. Choi; C. H. Cheng; L. M. Leung; C. F. Kwong, *Appl. Phys. A-Mater. Sci. Process.* **1999,** 68, (4), 447-450.

241. R. J. Klein; D. A. Fischer; J. L. Lenhart, *Langmuir* **2008,** 24, (15), 8187-8197.

242. A. E. Ozcam; K. Efimenko; C. Jaye; R. J. Spontak; D. A. Fischer; J. Genzer, *J. Electron Spectrosc.* **2009,** 172, (1-3), 95-103.

243. D. Bax; J. Agterdenbos; A. Saakes, *Anal. Chim. Acta* **1990,** 233, (2), 321-324.

244. S. Bhattacharya; A. Datta; J. M. Berg; S. Gangopadhyay, *J. Microelectromech. Syst.* **2005,** 14, (3), 590-597.

245. C. K. O'Sullivan; G. G. Guilbault. *Biosens. Bioelectron.* **1999,** 14, (8-9), 663-670.

246. G. Z. Sauerbrey, *J. Physik* **1959,** 155, 206 - 212.

247. S. R. Forrest, *Chem. Rev.* **1997,** 97, (6), 1793-1896.

248. S. Kowarik; A. Gerlach; F. Schreiber, *J. Phys.-Condens. Mat.* **2008,** 20, (18), 184005.

249. J. Liu; Y. J. Shi; Y. Yang, *Adv. Funct. Mater.* **2001,** 11, (6), 420-424.

250. Y. A. Makarova; A. V. Kharitonov, *Distribution of energy in the solar spectrum and the solar constant*, National Aeronautics and Space Administration: Washington, USA, 1974.

251. G. Binnig; C. F. Quate; C. Gerber, *Phys. Rev. Lett.* **1986,** 56, (9), 930-933.

252. R. Bowen; N. Hilal, *Atomic Force Microscopy in Process Ingineering*. Elsevier Ltd.: Oxford, 2009.

253. A. Alexeev; J. Loos; M. M. Koetse, *Ultramicroscopy* **2006,** 106, (3), 191-199.

254. L. J. van der Pauw, *Philips Res. Rep.* **1958,** 13, (1), 1-9.

255. D. Malacara, B. J. Thompson, *Handbook of Optical Engineering*. Marcel Dekker Inc.: New York, USA, 2001.

256. S. K. Kim; H. S. Ee; W. Choi; S. H. Kwon; J. H. Kang; Y. H. Kim; H. Kwon; H. G. Park, *Appl. Phys. Lett.* **2011,** 98, (1), 011109.

257. J. C. Vickerman; I. S. Gilmore, *Surface Analysis The principial techniques*, John Wiley & Sons Ltd: Chichester, 2009.

258. C. D. Wagner; W. M. Riggs; L. E. Davis; J. F. Moulder; G. E. Muilenberg, *Handbook of X-ray Photoelectron Spectroscopy*, Ed. Heyden & Son Ltd: Eden Praire, USA, 1979.

259. http://www.kelvinprobe.com/index.html Accessed July, 2012.

260. W. A. Zisman, *Rev. Sci. Instrum.* **1932,** 3, 367-368.

261. W. N. Hansen; G. J. Hansen, *Surf. Sci.* **2001,** 481, (1-3), 172-184.

262. Y. W. E. M. K. Shinodo, *X-ray Diffraction Crystallography*, Springer: Berlin, Germany, 2011.

263. . http://sergey.gmca.aps.anl.gov/pub/stepanov_smolenice_1997.pdf Accessed July, 2012.

264. S. A. Paniagua; P. J. Hotchkiss; S. C. Jones; S. R. Marder; A. Mudalige; F. S. Marrikar; J. E. Pemberton; N. R. Armstrong, *J. Phys. Chem. C* **2008,** 112, (21), 7809-7817.

265. A. B. D. Cassie, *Discuss. Faraday Soc.* **1948,** 3, 11-16.

266. J. N. Israelachvili; M. L. Gee, *Langmuir* **1989,** 5, (1), 288-289.

267. S. D. Yambem; A. Haldar; K.-S. Liao; E. P. Dillon; A. R. Barron; S. A. Curran, *Sol. Energy Mater. Sol. Cells* **2011,** 95, (8), 2424-2430.

268. M. G. Helander; Z. B. Wang; M. T. Greiner; Z. W. Liu; J. Qiu; Z. H. Lu, *Adv. Mater.* **2010,** 22, (18), 2037-2040.

269. Z. B. Wang; M. G. Helander; J. Qiu; D. P. Puzzo; M. T. Greiner; Z. M. Hudson; S. Wang; Z. W. Liu; Z. H. Lu, *Nat. Photonics* **2011,** 5, (12), 753-757.

270. F. Chen; X. Li; J. Hihath; Z. Huang; N. Tao, *J. Am. Chem. Soc.* **2006,** 128, (49), 15874-15881.

271. K. C. Vrancken; K. Possemiers; P. Vandervoort; E. F. Vansant, *Colloid Surface A* **1995,** 98, (3), 235-241.

272. J. F. Schakelford, *Introduction to Material Science for Engineers*. MacMillan: New York, USA, 1992.

273. D. Canchal-Arias; P. Dawson, *Surf. Sci.* **2005,** 577, (2-3), 95-111.

274. S. Link; M. A. El-Sayed, *J. Phys. Chem. B* **1999,** 103, (21), 4212-4217.
275. K. M. R. Kallury; P. M. Macdonald; M. Thompson, *Langmuir* **1994,** 10, (2), 492-499.
276. P. R. Moses; L. M. Wier; J. C. Lennox; H. O. Finklea; J. R. Lenhard; R. W. Murray, *Anal. Chem.* **1978,** 50, (4), 576-585.
277. C. J. Xu; L. Sun; L. J. Kepley; R. M. Crooks; A. J. Ricco, *Anal. Chem.* **1993,** 65, (15), 2102-2107.
278. A. Cravino; P. Schilinsky; C. J. Brabec, *Adv. Funct. Mater.* **2007,** 17, (18), 3906-3910.
279. W. L. Ma; C. Y. Yang; X. Gong; K. Lee; A. J. Heeger, *Adv. Funct. Mater.* **2005,** 15, (10), 1617-1622.
280. A. Ulman; J. E. Eilers; N. Tillman, *Langmuir* **1989,** 5, (5), 1147-1152.
281. M. J. Ford; C. Masens; M. B. Cortie, *Surf. Rev. Lett.* **2006,** 13, (2-3), 297-307.
282. C. Gatel; E. Snoeck, *Surf. Sci.* **2006,** 600, (13), 2650-2662.
283. Z. Q. Sun; J. G. Lu; X. P. Song, *Vacuum* **2010,** 85, (2), 297-301.
284. D. B. Mitzi; M. Yuan; W. Liu; A. J. Kellock; S. J. Chey; V. Deline; A. G. Schrott, *Adv. Mater.* **2008,** 20, (19), 3657-3662.
285. S. Merdes; R. Mainz; J. Klaer; A. Meeder; H. Rodriguez-Alvarez; H. W. Schock; M. C. Lux-Steiner; R. Klenk, *Sol. Energy Mater. Sol. Cells* **2011,** 95, (3), 864-869.
286. T. Asher; A. Inberg; E. Glickman; N. Fishelson; Y. Shacham-Diamand, *Electrochim. Acta* **2009,** 54, (25), 6053-6057.
287. K. Dick; T. Dhanasekaran; Z. Y. Zhang; D. Meisel, *J. Am. Chem. Soc.* **2002,** 124, (10), 2312-2317.
288. I. Doron-Mor; Z. Barkay; N. Filip-Granit; A. Vaskevich; I. Rubinstein, *Chem. Mater.* **2004,** 16, (18), 3476-3483.
289. T. Karakouz; D. Holder; M. Goomanovsky; A. Vaskevich; I. Rubinstein, *Chem. Mater.* **2009,** 21, (24), 5875-5885.
290. G. Gupta; D. Tanaka; Y. Ito; D. Shibata; M. Shimojo; K. Furuya; K. Mitsui; K. Kajikawa, *Nanotechnology* **2009,** 20, (2), 025703.
291. G. H. Jung; K. Hong; W. J. Dong; S. Kim; J.-L. Lee, *Adv. Energy Mater.* **2011,** 1, (6), 1023-1028.
292. A. Leuthe; H. Riegler, *J. Phys. D Appl. Phys.* **1992,** 25, (12), 1786-1797.
293. M. E. Lauer; R. Jungmann; J. H. Kindt; S. Magonov; J.-H. Fuhrhop; E. Oroudjev; H. G. Hansma, *Langmuir* **2007,** 23, (10), 5459-5465.
294. P. Carnevali; F. Ercolessi; E. Tosatti, *Phys. Rev. B* **1987,** 36, (12), 6701-6704.
295. J. E. Dominguez; L. Fu; X. Q. Pan, *Appl. Phys. Lett.* **2002,** 81, (27), 5168-5170.
296. P. E. Laibinis; G. M. Whitesides; D. L. Allara; Y. T. Tao; A. N. Parikh; R. G. Nuzzo, *J. Am. Chem. Soc.* **1991,** 113, (19), 7152-7167.
297. E. S. Carmichael; M. Gruebele, *J. Phys. Chem. C* **2009,** 113, (11), 4495-4501.
298. L. T. Banner; A. Richter; E. Pinkhassik, *Surf. Interface Anal.* **2009,** 41, (1), 49-55.
299. S. Garg; A. Jain; C. Karthik; B. Singh; R. Teki; V. S. Smentkowski; M. W. Lane; G. Ramanath, *J. Appl. Phys.* **2010,** 108, (3), 034317.
300. J. Y. Kim; S. H. Kim; H. H. Lee; K. Lee; W. L. Ma; X. Gong; A. J. Heeger, *Adv. Mater.* **2006,** 18, (5), 572-576.
301. C. S. Kim; S. S. Lee; E. D. Gomez; J. B. Kim; Y. L. Loo. *Appl. Phys. Lett.* **2009,** 94, (11), 113302.

302. K. D. Karlin; P. L. Dahlstrom; J. R. Hyde; J. Zubieta, *J. Chem. Soc. Chem. Comm.* **1980**, (19), 906-908.
303. A. L. Pickering; D. L. Long; L. Cronin, *Inorg. Chem.* **2004,** 43, (16), 4953-4961.
304. R. C. Hoft; M. J. Ford; A. M. McDonagh; M. B. Cortie, *J. Phys. Chem. C* **2007,** 111, (37), 13886-13891.
305. K. H. Choi; J. A. Jeong; J. W. Kang; D. G. Kim; J. K. Kim; S. I. Na; D. Y. Kim; S. S. Kim; H. K. Kim, *Sol. Energy Mater. Sol. Cells* **2009,** 93, (8), 1248-1255.
306. M. M. Hamasha; T. Dhakal; K. Alzoubi; S. Albahri; A. Qasaimeh; S. Lu; C. R. Westgate, *J. Disp. Technol.* **2012,** 8, (7), 383-388.
307. C. Jonda; A. B. R. Mayer; U. Stolz; A. Elschner; A. Karbach, *J. Mater. Sci.* **2000,** 35, (22), 5645-5651.
308. L. M. Chen; Z. Xu; Z. R. Hong; Y. Yang, *J. Mater. Chem.* **2010,** 20, (13), 2575-2598.
309. S. Ito; N. L. C. Ha; G. Rothenberger; P. Liska; P. Comte; S. M. Zakeeruddin; P. Pechy; M. K. Nazeeruddin; M. Gratzel, *Chem. Commun.* **2006**, (38), 4004-4006.
310. S. Logothetidis; A. Laskarakis; D. Georgiou; S. Amberg-Schwab; U. Weber; K. Noller; M. Schmidt; E. Kuecuekpinar-Niarchos; W. Lohwasser, *Eur. Phys. J.-Appl. Phys.* **2010,** 51, (3), 33203.
311. Y. Nakamura; Y. Suzuki; Y. Watanabe, *Thin Solid Films* **1996,** 291, 367-369.
312. G. D. Wei; R. R. Lunt; K. Sun; S. Y. Wang; M. E. Thompson; S. R. Forrest, *Nano Lett.* **2010,** 10, (9), 3555-3559.
313. J. S. Moon; C. J. Takacs; Y. M. Sun; A. J. Heeger, *Nano Lett.* **2011,** 11, (3), 1036-1039.
314. H. Cho; C. Yun; J. W. Park; S. Yoo, *Org. Electron.* **2009,** 10, (6), 1163-1169.
315. D. S. Ghosh; T. L. Chen; V. Pruneri, *Appl. Phys. Lett.* **2010,** 96, (9), 091106.
316. M. Zhang; T. L. Chiu; C. F. Lin; J. H. Lee; J. K. Wang; Y. F. Wu, *Sol. Energy Mater. Sol. Cells* **2011,** 95, (9), 2606-2609.
317. S. Wilken; T. Hoffmann; E. von Hauff; H. Borchert; J. Parisi, *Sol. Energy Mater. Sol. Cells* **2012,** 96, (1), 141-147.
318. S. Lim; D. Han; H. Kim; S. Lee; S. Yoo, *Sol. Energy Mater. Sol. Cells* **2012,** 101, 170-175.
319. M. T. Greiner; M. G. Helander; W.-M. Tang; Z.-B. Wang; J. Qiu; Z.-H. Lu, *Nat. Mater.* **2012,** 11, (1), 76-81.
320. L. Li; W. Hu; H. Fuchs; L. Chi, *Adv. Energy Mater.* **2011,** 1, (2), 188-193.
321. P. Sullivan; T. S. Jones; A. J. Ferguson; S. Heutz, *Appl. Phys. Lett.* **2007,** 91, (23), 233114.
322. L. Romaner; D. Nabok; P. Puschnig; E. Zojer; C. Ambrosch-Draxl, *New J. Phys.* **2009,** 11, 053010.
323. A. Sharma; A. Haldi; W. J. Potscavage; P. J. Hotchkiss; S. R. Marder; B. Kippelen, *J. Mater. Chem.* **2009,** 19, (30), 5298-5302.
324. H. N. Yi; S. Al-Faifi; A. Iraqi; D. C. Watters; J. Kingsley; D. G. Lidzey, *J. Mater. Chem.* **2011,** 21, (35), 13649-13656.
325. T. Winkler; H. Schmidt; H. Fluegge; F. Nikolayzik; I. Baumann; S. Schmale; T. Weimann; P. Hinze; H.-H. Johannes; T. Rabe; S. Hamwi; T. Riedl; W. Kowalsky, *Org. Electron.* **2011,** 12, (10), 1612-1618.
326. F. Z. Dahou; L. Cattin; J. Garnier; J. Ouerfelli; M. Morsli; G. Louarn; A. Bouteville; A. Khellil; J. C. Bernede, *Thin Solid Films* **2010,** 518, (21), 6117-6122.
327. J. R. Pitts; A. W. Czanderna; T. M. Thomas, *J. Vac. Sci. Technol. A.* **1986,** 4, (3), 1671-1674.

328. H. Aziz; Z. D. Popovic, *Chem. Mater.* **2004,** 16, (23), 4522-4532.

329. Q. Wang; G. Williams; H. Aziz, *Org. Electron.* **2012,** 13, (10), 2075-2082.

330. C. E. Small; S. Chen; J. Subbiah; C. M. Amb; S.-W. Tsang; T.-H. Lai; J. R. Reynolds; F. So, *Nat. Photonics* **2012,** 6, (2), 115-120.

331. T. Y. Chu; S. Alem; P. G. Verly; S. Wakim; J. P. Lu; Y. Tao; S. Beaupre; M. Leclerc; F. Belanger; D. Desilets; S. Rodman; D. Waller; R. Gaudiana, *Appl. Phys. Lett.* **2009,** 95, (6), 063304.

332. D. Derkacs; S. H. Lim; P. Matheu; W. Mar; E. T. Yu, *Appl. Phys. Lett.* **2006,** 89, (9), 093103.

333. C. Battaglia; J. Escarre; K. Soederstroem; M. Charriere; M. Despeisse; F.-J. Haug; C. Ballif, *Nat. Photonics* **2011,** 5, (9), 535-538.

334. T. W. Ebbesen; H. J. Lezec; H. F. Ghaemi; T. Thio; P. A. Wolff, *Nature* **1998,** 391, (6668), 667-669.

335. X. H. Li; W. C. H. Choy; L. J. Huo; F. X. Xie; W. E. I. Sha; B. F. Ding; X. Guo; Y. F. Li; J. H. Hou; J. B. You; Y. Yang, *Adv. Mater.* **2012,** 24, (22), 3046-3052.

336. C. Sonnichsen; A. C. Duch; G. Steininger; M. Koch; G. von Plessen; J. Feldmann, *Appl. Phys. Lett.* **2000,** 76, (2), 140-142.

337. I. Horcas; R. Fernandez; J. M. Gomez-Rodriguez; J. Colchero; J. Gomez-Herrero; A. M. Baro, *Rev. Sci. Instrum.* **2007,** 78, (1), 013705.

338. A. Serrano; O. R. de la Fuente; M. A. Garcia. *J. Appl. Phys.* **2010,** 108, (7).

339. T. Rindzevicius; Y. Alaverdyan; A. Dahlin; F. Hook; D. S. Sutherland; M. Kall, *Nano Lett.* **2005,** 5, (11), 2335-2339.

340. J. Wenger; D. Gerard; J. Dintinger; O. Mahboub; N. Bonod; E. Popov; T. W. Ebbesen; H. E. Rigneault, *Opt. Express* **2008,** 16, (5), 3008-3020.

341. A. Ulman, *Chem. Rev.* **1996,** 96, (4), 1533-1554.

342. I. Hancox; P. Sullivan; K. V. Chauhan; N. Beaumont; L. A. Rochford; R. A. Hatton; T. S. Jones, *Org. Electron.* **2010,** 11, (12), 2019-2025.

343. A. Kotiaho; R. Lahtinen; A. Efimov; H.-K. Metsberg; E. Sariola; H. Lehtivuori; N. V. Tkachenko; H. Lemmetyinen, *J. Phys. Chem. C* **2010,** 114, (1), 162-168.

344. B. P. Rand; P. Peumans; S. R. Forrest, *J. Appl. Phys.* **2004,** 96, (12), 7519-7526.

345. M. A. Green; S. Pillai, *Nat. Photonics* **2012,** 6, (3), 130-132.

346. B. Kouskoussa; M. Morsli; K. Benchouk; G. Louarn; L. Cattin; A. Khelil; J. C. Bernede, *Phys. Status Solidi A-Appl. Mat.* **2009,** 206, (2), 311-315.

347. A. Godoy; L. Cattin; L. Toumi; F. R. Diaz; M. A. del Valle; G. M. Soto; B. Kouskoussa; M. Morsli; K. Benchouk; A. Khelil; J. C. Bernede, *Sol. Energy Mater. Sol. Cells* **2010,** 94, (4), 648-654.

348. K. Schulze; C. Uhrich; R. Schueppel; K. Leo; M. Pfeiffer; E. Brier; E. Reinold; P. Baeuerle, *Adv. Mater.* **2006,** 18, (21), 2872-2875.

349. J. C. Bernede; L. Cattin; M. Morsli; Y. Berredjem, *Sol. Energy Mater. Sol. Cells* **2008,** 92, (11), 1508-1515.

350. L. Cattin; S. Tougaard; N. Stephant; S. Morsli; J. C. Bernede, *Gold Bull.* **2011,** 44, (4), 199-205.

351. J. C. Bernede; Y. Berredjem; L. Cattin; M. Morsli, *Appl. Phys. Lett.* **2008,** 92, (8), 083304.

352. E. Kymakis; E. Stratakis; E. Koudoumas; C. Fotakis, *IEEE T. Electron Dev.* **2011,** 58, (3), 860-864.

353. K. R. Catchpole; A. Polman, *Opt. Express* **2008,** 16, (26), 21793-21800.

354. X. Chen; L. Zuo; W. Fu; Q. Yan; C. Fan; H. Chen, *Sol. Energy Mater. Sol. Cells* **2013,** 111, 1-8.
355. N. R. Armstrong; C. Carter; C. Donley; A. Simmonds; P. Lee; M. Brumbach; B. Kippelen; B. Domercq; S. Y. Yoo, *Thin Solid Films* **2003,** 445, (2), 342-352.
356. C. Donley; D. Dunphy; D. Paine; C. Carter; K. Nebesny; P. Lee; D. Alloway; N. R. Armstrong, *Langmuir* **2002,** 18, (2), 450-457.
357. W. J. Song; S. K. So; D. Y. Wang; Y. Qiu; L. L. Cao, *Appl. Surf. Sci.* **2001,** 177, (3), 158-164.
358. B. L. Low; F. R. Zhu; K. R. Zhang; S. J. Chua, *Thin Solid Films* **2002,** 417, (1-2), 116-119.
359. M. Ishii; T. Mori; H. Fujikawa; S. Tokito; Y. Taga, *J. Lumines.* **2000,** 87-9, 1165-1167.
360. J. S. Kim; F. Cacialli; M. Granstrom; R. H. Friend; N. Johansson; W. R. Salaneck; R. Daik; W. J. Feast, *Synthetic Met.* **1999,** 101, (1-3), 111-112.
361. S. Rentenberger; A. Vollmer; E. Zojer; R. Schennach; N. Koch, *J. Appl. Phys.* **2006,** 100, (5), 053701.
362. T. M. Brown; G. M. Lazzerini; L. J. Parrott; V. Bodrozic; L. Burgi; F. Cacialli, *Org. Electron.* **2011,** 12, (4), 623-633.
363. H. C. Tsai; E. Hu; K. Perng; M. K. Chen; J. C. Wu; Y. S. Chang, *Surf. Sci.* **2003,** 537, (1-3), L447-L450.
364. S. Cho; J. H. Seo; G. H. Kim; J. Y. Kim; H. Y. Woo, *J. Mater. Chem.* **2012,** 22, (39), 21238-21241.
365. L.-J. Pegg; R. A. Hatton, *ACS Nano* **2012,** 6, (6), 4722-4730.
366. M. M. Lohrengel; J. W. Schultze, *Electrochim. Acta* **1976,** 21, (11), 957-965.
367. F. Machalett; K. Edinger; J. Melngailis; M. Diegel; K. Steenbeck; E. Steinbeiss, *Appl. Phys. A-Mater. Sci. Process.* **2000,** 71, (3), 331-335.
368. R. Pascova; J. Kourtev, *Thin Solid Films* **2011,** 519, (11), 3448-3456.
369. S. Honda; M. Watamori; K. Oura, *Thin Solid Films* **1996,** 282, (1-2), 206-208.
370. V. Christou; M. Etchells; O. Renault; P. J. Dobson; O. V. Salata; G. Beamson; R. G. Egdell, *J. Appl. Phys.* **2000,** 88, (9), 5180-5187.
371. W. F. Wu; B. S. Chiou, *Semicond. Sci. Technol.* **1996,** 11, (2), 196-202.
372. N. R. C. Raju; K. J. Kumar; A. Subrahmanyam, *J. Phys. D Appl. Phys.* **2009,** 42, (13), 135411.
373. B. N. Roy; T. Wright, *Cryst. Res. Technol.* **1996,** 31, (8), 1039-1044.
374. Y. Shang; Q. Li; L. Meng; D. Wang; Z. Shuai, *Appl. Phys. Lett.* **2010,** 97, (14), 143511.
375. J. Obrzut; K. A. Page, *Phys. Rev. B* **2009,** 80, (19), 195211.